Daya Bay Project

Physics Proposal

Working Copy August 31, 2006

Daya Bay Collaboration

Beijing Normal University
Xinheng Guo, Naiyan Wang, Rong Wang

Brookhaven National Laboratory
Mary Bishai, Milind Diwan, Jim Frank, Richard Hahn, Kelvin Li, Laurence Littenberg, David Jaffe, Steve Kettell, Brett Viren, Minfang Yeh

California Institute of Technology
Christopher Jillings, Jianglai Liu, Christopher Mauger, Robert McKeown

Charles Unviersity
Zdenek Dolezal, Rupert Leitner, Viktor Pec, Vit Vorobel

China Institute of Atomic Energy
Long Hou, Xichao Ruan, Biao Xing, Zouying Zhou

Chinese University of Hong Kong,
Ming-Chung Chu, Antony Luk, Wah-Kai Ngai

Illinois Institute of Technology
Christopher White

Institute of High Energy Physics
Jun Cao, Hesheng Chen, Mingjun Chen, Jinyu Fu, Mengyun Guan, Jin Li, Xiaonan Li, Jinchang Liu, Haoqi Lu, Yusheng Lu, Yuqian Ma, Xiangchen Meng, Yaxuan Sun, Ruiguang Wang, Yifang Wang, Zheng Wang, Zhimin Wang, Liangjian Wen, Zhizhong Xing, Changgen Yang, Zhiguo Yao, Liang Zhan, Jiawen Zhang, Zhiyong Zhang, Weili Zhong, Honglin Zhuang

Iowa State University
Kerry Whistnant, Bing-Lin Young

Joint Institute for Nuclear Research
Yuri A. Gornushkin, Igor Nemchenok, Alexander Olshevski

Kurchatov Institute
Vladimir N. Vyrodov

Lawrence Berkeley National Laboratory and University of California at Berkeley
Bill Edwards, Kam-Biu Luk

Nanjing University
Shenjian Chen, Tingyang Chen, Guobin Gong, Ming Qi

Nankai University
Shengpeng Jiang, Xuqian Li, Ye Xu

National Chiao-Tung University
Guey-Lin Lin

National Taiwan University
Yee Hsiung

National United University
Chung-Hsiang Wang

Princeton University
Changguo Lu, Kirk T. McDonald

Rensselaer Polytechnic Institute
John Cummings, Johnny Goett, Jim Napolitano, Paul Stoler

Shenzhen Univeristy
Yu Chen, Hanben Niu, Lihong Niu

Sun Yat-Sen (Zhongshan) University
Zhibing Li

Tsinghua University
Shaomin Chen, Hui Gong, Guanghua Gong, Li Liang, Beibei Shao, Qiong Su, Tao Xue, Ming Zhong

University of California at Los Angeles
Vahe Ghazikhanian, Huanzhong Huang, Chuck Whitten, Steve Trentalange

University of Hong Kong,
K.S. Cheng, Talent T.N. Kwok, Maggie K.P. Lee, John K.C. Leung, Jason C.S. Pun, Raymond H.M. Tsang, Heymans H.C. Wong

University of Houston
Michael Ispiryan, Kwong Lau, Bill Mayes, Larry Pinsky, Guanghua Xu

University of Illinois at Urbana-Champaign
S. Ryland Ely, Jen-Chieh Peng

University of Wisconsin
Karsten M. Heeger

Virginia Tech University
Jonathan Link

Executive Summary

Recent discoveries in neutrino physics have shown that the Standard Model of particle physics is incomplete. The observations of oscillations of neutrinos have unequivocally demonstrated that the masses of neutrinos are nonzero. The smallness of the neutrino masses ($<$1 eV) and the surprisingly large mixing angles provide important clues and constraints to extensions of the Standard Model.

One of the three mixing angles θ_{13} is small and has not yet been determined; the current experimental bound is $\sin^2 2\theta_{13} < 0.10$. It is important to measure this angle to provide further insight on how to extend the Standard Model. The value of θ_{13} is also vital to resolving the neutrino mass hierarchy ambiguity and to attempts to measure CP violation in the lepton sector.

We propose to measure this mixing angle by using antineutrinos from nuclear reactors in Daya Bay, China. The Day Bay Nuclear Power Plant is one of the most prolific sources of antineutrinos in the world. We plan to deploy large antineutrino detectors, in an experimental hall about 1800 m from the reactors, inside the adjacent mountain. The overburden will suppress the background to an insignificant level. The statistics will reach 0.2% in three years of running. To mitigate and control systematic errors to a comparable level, we will also deploy detectors in experimental halls near the reactors. All the experimental halls are interconnected via a horizontal tunnel, which will provide opportunities to calibrate the far detectors in the near experimental halls.

This proposal details our current design of the Daya Bay experiment that can reach a sensitivity of 0.01 or better in $\sin^2 2\theta_{13} < 0.10$.

Contents

List of Figures

List of Tables

1 Physics

Neutrino oscillations are an ideal tool for probing neutrino mass. This intriguing phenomenon depends on three mixing angles. The goal of the Daya Bay experiment is to determine the last unknown neutrino mixing angle θ_{13} with a sensitivity of 0.01 in $\sin^2 2\theta_{13}$, an order of magnitude better than the current limit. This section provides an overview of neutrino oscillations, the key features of reactor neutrino experiments, and the Daya Bay experiment.

1.1 Neutrino Oscillation

The last decade has seen tremendous advances in our understanding of the neutrino sector [1]. There is now robust evidence for neutrino flavor conversion from solar, atmospheric, reactor and accelerator experiments. The only consistent explanation for these results is that neutrinos have mass and that the mass eigenstates are not the same as the flavor eigenstates (neutrino mixing). Neutrino oscillations depend only on mass-squared differences and neutrino mixing angles. The mass-squared difference scale probed by an experiment depends on the ratio L/E, where L is the baseline distance (source to detector) and E is the neutrino energy. Solar and long-baseline reactor experiments are sensitive to one mass-squared difference scale, while atmospheric, short-baseline reactor and long-baseline accelerator experiments are sensitive to a larger mass-squared difference scale. To date only disappearance experiments have convincingly indicated the existence of neutrino oscillations.

The SNO experiment [2] measures high-energy ^{8}B solar neutrinos via charged current (CC), neutral current (NC) and elastic scattering (ES) reactions. The CC reaction is sensitive only to electron neutrinos whereas the NC reaction is sensitive to the total active solar neutrino flux (ν_e, ν_μ and ν_τ). Elastic scattering has both CC and NC components and therefore serves as a consistency check. The neutrino flux indicated by the CC data is about one-third of that given by the NC data, and the NC data also agrees with the standard solar model prediction for the ^{8}B neutrino flux. Since only $\nu_{\rm e}$'s are produced in the sun, the SNO data can only be explained by flavor transmutation $\nu_e \rightarrow \nu_\mu$ and/or ν_τ. Super-Kamiokande has also measured the ES flux $\phi_{\rm ES}$ for the ^{8}B neutrinos [3] and their data agree with the SNO results.

Radiochemical experiments can also measure lower-energy solar neutrinos, in addition to ^{8}B neutrinos. The Homestake experiment [4] is sensitive to ^{7}Be and pep neutrinos using neutrino capture on ^{37}Cl. The SAGE, GALLEX and GNO experiments [5] are sensitive to all sources of solar neutrinos, including the dominant pp neutrinos, using neutrino capture on ^{71}Ga. A global fit to all solar neutrino data yields a unique region in oscillation parameter space, known as the Large Mixing Angle (LMA) solution.

The KamLAND experiment [6], which measured electron anti-neutrinos from reactors with an L/E sensitive to the mass-squared difference indicated by the solar neutrino data, observed a flux deficit is consistent with neutrino oscillations. Furthermore, KamLAND has also observed a spectral distortion in oscillation probability that can only be explained by neutrino oscillations. The oscillation parameters indicated by KamLAND agree with the LMA solution, as they should if CPT is conserved. Since they were done in completely different environments, the combination of solar neutrino and KamLAND data rules out exotic scenarios such as nonstandard neutrino interactions or neutrino magetic moment [1].

Super-Kamiokande atmospheric-neutrino induced μ-like events show a depletion at long distance compared to the theoretical predictions, while the e-like events agree with the non-oscillation expectation [7]. The detailed energy and zenith angle distributions for both electron and muon events agree with the oscillation predictions if the predominant oscillation channel is $\nu_\mu \rightarrow \nu_\tau$. More recently, the long baseline accelerator experiments K2K [8] and MINOS [9] have measured ν_μ survival that is consistent with the atmospheric neutrino data. The mass-squared difference indicated by the atmospheric neutrino data is about 30 times larger than that obtained from the fits to solar data. The existence of two independent mass-squared difference scales means that three neutrinos are required to explain both the solar and atmospheric data.

The Chooz [10] and Palo Verde [11], which measured the survival of reactor anti-electron neutrinos

at an L/E sensitive to the mass-squared difference indicated by the atmospheric neutrino data, found no evidence for oscillations, consistent with the lack of ν_e involvement in the atmospheric neutrino oscillations. However, ν_e oscillations for this mass-squared difference are still allowed at roughly the 10% level or less.

There exists another set of neutrino oscillation data from the LSND short-baseline accelerator experiment [12], which found evidence of the oscillation $\bar{\nu}_\mu \rightarrow \bar{\nu}_\mathrm{e}$. A large region allowed by the LSND data has been ruled out by the KARMEN experiment [13] and astrophysical measurements [14]. The remaining allowed region is currently being tested by the MiniBooNE experiment [15]. If confirmed, the LSND signal would require the existence of new physics beyond the standard three-neutrino oscillation scenario.

1.1.1 Neutrino Mixing

For N flavors, the neutrino mass matrix consists of N mass eigenvalues, $N(N-1)/2$ mixing angles, $N(N-1)/2$ CP phases for Majorana neutrinos or $(N-1)(N-2)/2$ CP phases for Dirac neutrinos. The mass matrix is diagonalized by the mixing matrix which transforms the mass eigenstates to the flavor eigenstates. For three flavors, the Maki-Nakagawa-Sakata-Pontecorvo [16] mixing matrix which transforms the mass eigenstates (ν_1, ν_2, ν_3) to the flavor eigenstates (ν_e, ν_μ, ν_τ) can be parameterized as

$$\begin{pmatrix} 1 & 0 & 0 \\ 0 & C_{23} & S_{23} \\ 0 & -S_{23} & C_{23} \end{pmatrix} \begin{pmatrix} C_{13} & 0 & \hat{S}^*_{13} \\ 0 & 1 & 0 \\ -\hat{S}_{13} & 0 & C_{13} \end{pmatrix} \begin{pmatrix} C_{12} & S_{12} & 0 \\ -S_{12} & C_{12} & 0 \\ 0 & 0 & 1 \end{pmatrix} \begin{pmatrix} e^{i\phi_1} & & \\ & e^{i\phi_2} & \\ & & 1 \end{pmatrix} \quad (1)$$

$$= \begin{pmatrix} C_{12}C_{13} & C_{13}S_{12} & \hat{S}^*_{13} \\ -S_{12}C_{23} - C_{12}\hat{S}_{13}S_{23} & C_{12}C_{23} - S_{12}\hat{S}_{13}S_{23} & C_{13}S_{23} \\ S_{12}S_{23} - C_{12}\hat{S}_{13}C_{23} & -C_{12}S_{23} - S_{12}\hat{S}_{13}C_{23} & C_{13}C_{23} \end{pmatrix} \begin{pmatrix} e^{i\phi_1} & & \\ & e^{i\phi_2} & \\ & & 1 \end{pmatrix} \quad (2)$$

where $C_\mathrm{jk} = \cos\theta_\mathrm{jk}$, $S_\mathrm{jk} = \sin\theta_\mathrm{jk}$, $\hat{S}_{13} = e^{i\delta_\mathrm{CP}} \sin\theta_{13}$. The ranges of the mixing angles and the phases are: $0 \leq \theta_{jk} \leq \pi/2$, $\delta_\mathrm{CP} \geq 0, \phi_1, \phi_2 \leq 2\pi$. The neutrino oscillation phenomenology is independent of the Majorana phases ϕ_1 and ϕ_2, which affect only *neutrinoless* double β decay experiments.

For three flavors, oscillation experiments can only determine three mixing angles θ_{12}, θ_{13}, θ_{23}, two mass-square differences, $\Delta m^2_{21} = m^2_2 - m^2_1$, $\Delta m^2_{31} = m^2_3 - m^2_1$, and one CP phase angle δ_CP. It should note that Δm^2_{31}= Δm^2_{21}+Δm^2_{32}.

1.1.2 Current Knowledge of Mixing Parameters

Various solar, atmospheric, reactor, and accelerator neutrino experimental data have been analyzed to determine the mixing parameters separately and in global fits. In the three-flavor framework there is a general agreement on solar and atmospheric parameters. In particular for global fits in the 2σ range, the solar parameters Δm^2_{21} has been determined to within 9% and $\sin^2\theta_{12}$ within 18%, while the atmospheric parameter $|\Delta m|^2_{32}$ within 26% and $\sin^2\theta_{23}$ within 41%. Due to the absence of a signal, the global fits on θ_{13} are upper bounds which vary significantly from one fit to another. The sixth parameter, i.e., the CP phase angle δ_CP, is inaccessible to the present and near future oscillation experiments.

We quote the result of a recent global fit in 2σ range [17]:

$$\Delta m^2_{21} = 7.92(1.00 \pm 0.09) \times 10^{-5}\,\mathrm{eV}^2 \qquad \sin^2\theta_{12} = 0.314(1.00^{+0.18}_{-0.15}) \quad (3)$$

$$|\Delta m^2_{32}| = 2.4(1.00^{+0.21}_{-0.26}) \times 10^{-3}\,\mathrm{eV}^2 \qquad \sin^2\theta_{23} = 0.44(1.00^{+0.41}_{-0.22}) \quad (4)$$

$$\sin^2\theta_{13} = (0.9^{+2.3}_{-0.9}) \times 10^{-2} \quad (5)$$

A collection of fits of $\sin^2\theta_{13}$ with different inputs as given in [17] is reproduced in Fig. 1.1. Note that fits involving solar or atmospheric data separately have $\theta_{13} = 0$ coinciding with the minima of the chi-square. However global analyses taking into account both solar and atmospheric effects show chi-square minima at non-vanishing value of θ_{13}. More fits on θ_{13} under different inputs can be found in another very

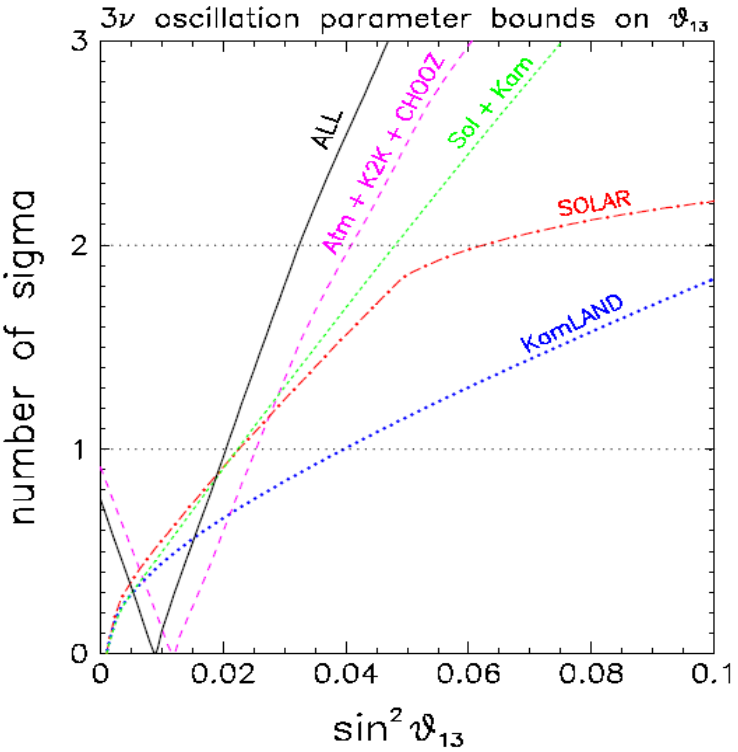

Fig. 1.1. Global fits to $\sin^2\theta_{13}$, taken from [17].

recent global fit [18], in which the fits of other oscillation parameters overlap significantly with the above results even at 1σ, signifying the convergence to a set of accepted values of neutrino oscillation parameters, in Δm^2_{21}, $|\Delta m^2_{32}|$, $\sin^2\theta_{12}$, and $\sin^2\theta_{23}$.

At 2σ, the upper bound of θ_{13} extracted from Eq. 5 is about 10°. This corresponds to a value of $\sin^2 2\theta_{13}$ of 0.12, which should be compared to the upper limit of 0.17 at 90% C.L. obtained by Chooz (to be discussed in Sec. 1.3.5). We can conclude that unlike θ_{12} and θ_{23} the mixing angle θ_{13} is relatively small.

1.2 Mixing Angle θ_{13}

As one of the six neutrino mass parameters measurable in neutrino oscillations, θ_{13} is important in its own right and for further studies of neutrino oscillations. In addition, θ_{13} is important in theoretical model building of the neutrino mass matrix which can serve as a guide to the theoretical understanding of physics beyond the standard model. We elaborate these points below:

On the experimental side:

- The mixing matrix element which provides the information on the CP phase angle $\delta_{\rm CP}$ appears always in the combination $U_{e3} = \sin\theta_{13}e^{-i\delta_{\rm CP}}$. If θ_{13} vanishes then it is not possible to probe leptonic CP violation in oscillation experiments.

- The future generation of neutrino oscillation experiments has several important goals to achieve: to measure more accurately the mixing angles and mass-squared differences, to probe the matter effect, to determine the hierarchy of neutrino masses, and very importantly to determine the CP phase. The association of θ_{13} with $\delta_{\rm CP}$ as described above indicate that we need to know the value of θ_{13} to a sufficient accuracy in order to design the future generation of experiments to measure $\delta_{\rm CP}$. The

matter effect, which can be used to determine the mass hierarchy, also depends on the size of θ_{13}. If $\theta_{13} > 0.01$, then the design of future oscillation experiments can be a straightforward extension of current experiments [19]. However, for smaller θ_{13} new experimental technologies are likely required to carry out the same sets of measurements.

On the theoretical side:

- A vanishing θ_{13} indicates that the neutrino system is not a genuine 3-flavor mixing. Together with the large mixing angles θ_{12} and θ_{23} (possibly maximal) it poses a serious challenge to the theoretical understanding of the physics of neutrinos. On the other hand their precise values can serve as a guide in the construction of the neutrino mass matrix, which, in turn, will have strong implications in the model building of physics beyond the standard model.

- The actual value of θ_{13}, together with the question whether or not θ_{23} is maximal, can put strong constraints on theoretical models in grand unification models. In general, if θ_{13} is not too small i.e., close to the upper bound of the existing limit of $\sin^2 2\theta_{13} \approx 0.1$ and $\theta_{23} \neq \frac{\pi}{2}$, the neutrino mass matrix does not have to have any special features (sometimes referred to as anarchy models) to give rise to large mixing angles, and the smaller value of θ_{13} as compared with the other mixing angles, e.g., $\sin^2 2\theta_{13} \approx 0.1$, can be understood as a numerical accident. However, for much smaller value of θ_{13}, say, an order of magnitude smaller than the current upper bound, e.g., $\sin^2 2\theta_{13} \leq 0.01$, a special symmetry on the neutrino mass matrix will be required. More discussions and references can be found in references [20] and [21]

- As an example of the special symmetry feature needed, the investigation of Mohapatra [22] shows that for $\theta_{13} \leq \frac{\Delta m^2_{\rm sol}}{\Delta m^2_{\rm atm}} \approx 0.03$ a μ and τ lepton flavor exchange symmetry is required for a theoretical explanation. It disfavors a quark-lepton unification type theory based on models of $SU_c(4)$ or $SO(10)$. For a larger value of θ_{13}, it leaves open the question of quark-lepton unification.

1.3 Determining θ_{13} with Nuclear Reactors

1.3.1 Energy Spectrum and Flux of Reactor Antineutrinos

A nuclear power plant derives power from the fission of uranium and plutonium isotopes (mostly ^{235}U and ^{239}Pu) which are packed into rods in the core or the reactor. The fission produces daughters, many of which beta decay because they are neutron rich, Each fission produces on average approximately 200 MeV of released energy and six antineutrinos. The majority of the antineutrinos have very low energies; about 70% of the antineutrinos have energies below 1.8 MeV, the threshold of the inverse beta-decay reaction to be discussed in Section 1.3.2. A 3 $\mathrm{GW_{th}}$ reactor emits 6×10^{20} antineutrinos per second with antineutrino energies up to 8 MeV.

Many reactor neutrino experiments to date have been carried out at pressurized water reactors (PWRs). The neutrino flux and energy spectrum of a PWR depend on several factors: the total thermal power of the reactor, the fraction of each fissile isotope in the fuel, the fission rate of each fissile isotope, and the energy spectrum of neutrinos of the individual fissile isotopes.

The antineutrino yield is proportional to the thermal power, while other thermal parameters such as the temperature, pressure and the flow rate of the cooling water, play negligible role. The reactor thermal power is measured continuously by the power plant with a typical precision of (1–2)%.

Fissile materials are continuously consumed while new fissile isotopes are bred from other isotopes in the fuel (mainly ^{238}U) by fast neutrons. Since the neutrino energy spectra are slightly different for the four main isotopes, the fission composition and its evolution over time are therefore critical to the determination of the neutrino flux and energy spectrum. From the average thermal power and the effective energy released

per fission [23], the average number of fissions per second of each isotope can be calculated as a function of time. Fig. 1.2 shows the results of computer simulation of the Palo Verde reactor cores [24].

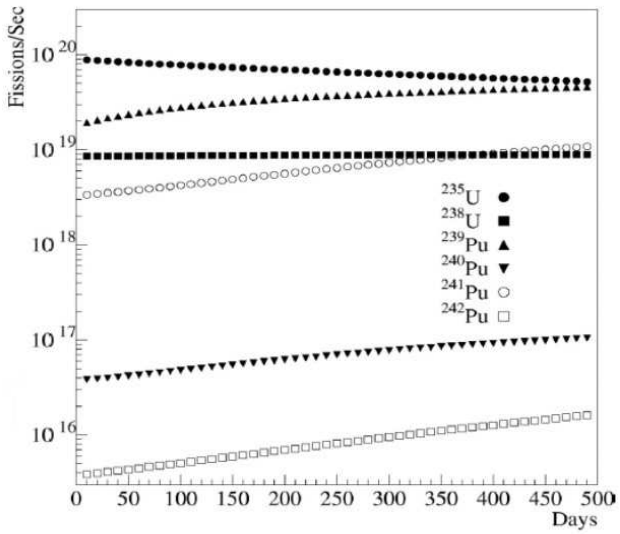

Fig. 1.2. Fission rate of each isotope as a function of time from a Monte Carlo simulation [24].

It is common for a nuclear power plant to replace some of the fuel rods in the reactor periodically as the fuel is used up. Typically, a reactor core will have 1/3 of its fuel changed every 18 months. At the beginning of each refueling cycle, 69% of the fissions are from ^{235}U, 21% from ^{239}Pu, 7% from ^{238}U, and 3% from ^{241}Pu. During operation the fissile isotopes ^{239}Pu and ^{241}Pu are bred continuously from ^{238}U. Toward the end of the fuel cycle, the fission rates from ^{235}U and ^{239}Pu are about equal. The average ("standard") fuel composition is 58% of ^{235}U, 30% of ^{239}Pu, 7% of ^{238}U, and 5% ^{241}Pu [25].

The energy spectrum of the $\bar{\nu}_e$ emitted from the fission reaction depends on the fuel composition. The composite antineutrino spectrum is a function of the time-dependent contributions of the various fissile isotopes to the fission process. The Bugey 3 experiment compared three different models of the antineutrino spectrum with its measurement. Good agreement was observed with the model that made use of the ILL $\bar{\nu}_e$ spectra [28]. The ILL measured spectra for isotopes ^{235}U, ^{239}Pu, and ^{241}Pu are shown in Fig. 1.3. However, there is no data for ^{238}U; only the theoretical prediction is used. The possible discrepancy between the predicted and the real spectra should not lead to significant errors since the contribution from ^{238}U is never higher than 8%. The overall normalization error of the ILL measured spectra is 1.9%. A global shape uncertainty is also introduced by the conversion procedure.

A widely used three-parameter parametrization of the antineutrino spectrum for the four main isotopes, as shown in Fig. 1.4, can be found in [26].

1.3.2 Inverse Beta-Decay Reaction

The reaction employed to detect the $\bar{\nu}_e$ from a reactor is the inverse beta decay $\bar{\nu}_e + p \rightarrow e^+ + n$. The total cross section of this reaction, neglecting terms of order E_ν/M, is

$$\sigma_{tot}^{(0)} = \sigma_0(f^2 + 3g^2)E_e^{(0)}p_e^{(0)}, \tag{6}$$

where $E_e^{(0)} = E_\nu - (M_n - M_p)$ is the positron energy when neutron recoil energy is neglected, and $p_e^{(0)}$ is the positron momentum. The weak coupling constants are $f = 1$ and $g = 1.26$, and σ_0 is related to the

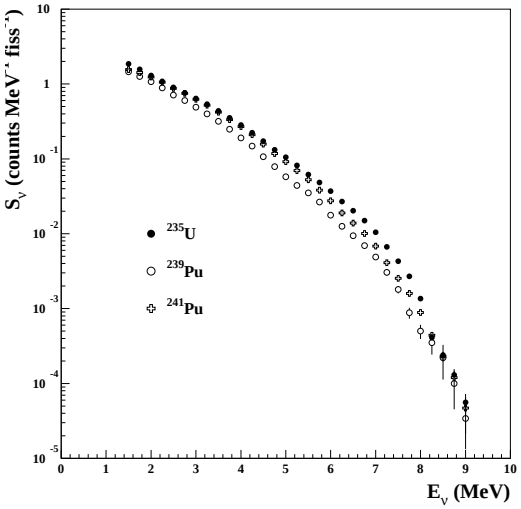

Fig. 1.3. Yield of antineutrinos per fission for the listed isotopes. These are determined by converting the corresponding measured β spectra [28].

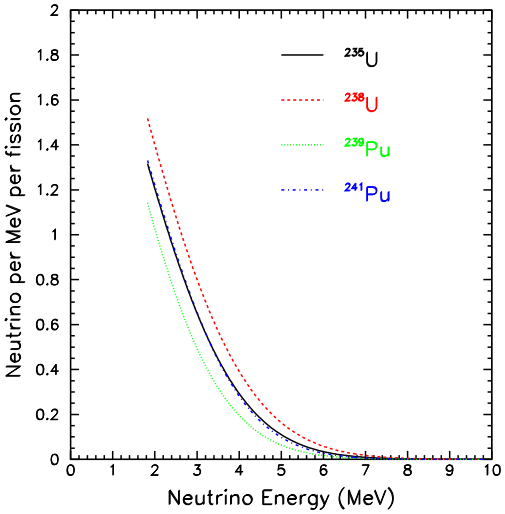

Fig. 1.4. Antineutrino energy spectrum for four isotopes following the parametrization of Vogel and Engel [26].

Fermi coupling constant G_F, the Cabibbo angle θ_C, and an energy-independent inner radiative correction. The inverse beta decay has a threshold energy in the laboratory frame $E_\nu = [(m_{\rm n} + m_{\rm e})^2 - m_{\rm p}^2]/2m_{\rm p}$ = 1.806 MeV. The leading-order expression for the total cross section is

$$\sigma_{tot}^{(0)} = 0.0952 \times 10^{-42} cm^2 E_e^{(0)} p_e^{(0)}, \tag{7}$$

where $E_e^{(0)}$ and $p_e^{(0)}$ are in units of MeV. Vogel and Beacom [29] have recently extended the calculation of the inverse beta decay total cross section and angular distribution to order $1/M$. Fig. 1.5 shows the comparison of the total cross sections obtained in the leading order and the next-to-leading order calculations. Noticeable differences are present for high neutrino energies. We adopt the order $1/M$ formula for the cross-section calculation. In fact, the calculated cross section can be related to neutron life time, whose error is only 0.2%.

The expected recoil neutron energy spectrum, weighted by the antineutrino energy spectrum and the $\bar{\nu}_e + p \rightarrow e^+ + n$ cross section, is shown in Fig. 1.6. Due to the low antineutrino energy relative to the mass of the nucleon, the recoil neutron has low kinetic energy. While the positron angular distribution is slightly backward peaked in the laboratory frame, the angular distribution of the neutrons is strongly forward peaked, as shown in Fig. 1.7.

1.3.3 Observed Antineutrino Rate and Spectrum at Short Distance

The observed antineutrino spectrum in the liquid scintillator at short baseline is a product of the reactor antineutrino spectrum and the cross section of inverse beta decay. Fig. 1.8 shows the differential antineutrino energy spectrum, the total cross section of the inverse beta-decay reaction, and the expected count rate as a function of the antineutrino energy. The differential energy distribution is the sum of the antineutrino spectra of all the radio-isotopes. It is thus sensitive to the variation of thermal power and composition of the nuclear fuel.

By integrating over the energy of the antineutrino, the number of events can be determined. With one-tonne of liquid scintillator, a typical rate is about 100 antineutrinos per day per GW$_{\rm th}$ at 100 m from the reactor. The highest count rate occurs at $E_\nu \sim 4$ MeV.

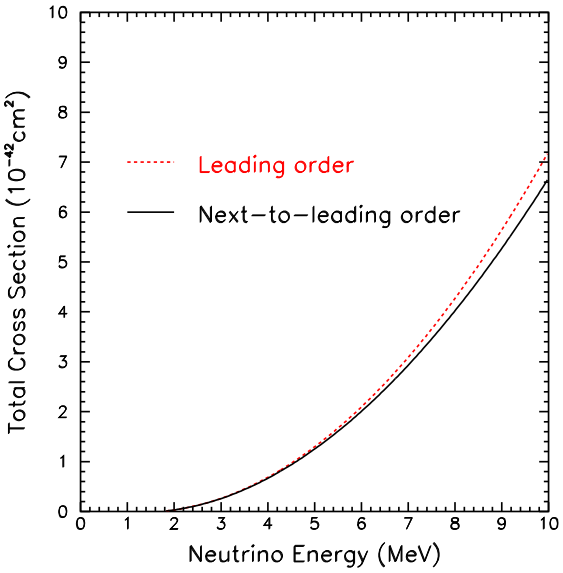

Fig. 1.5. Total cross section of the inverse beta decay calculated in leading order and next-to-leading order.

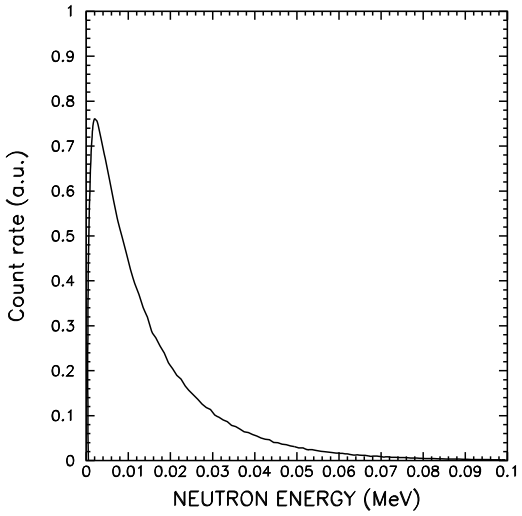

Fig. 1.6. Recoil neutron energy spectrum from inverse beta decay weighted by the antineutrino energy spectrum.

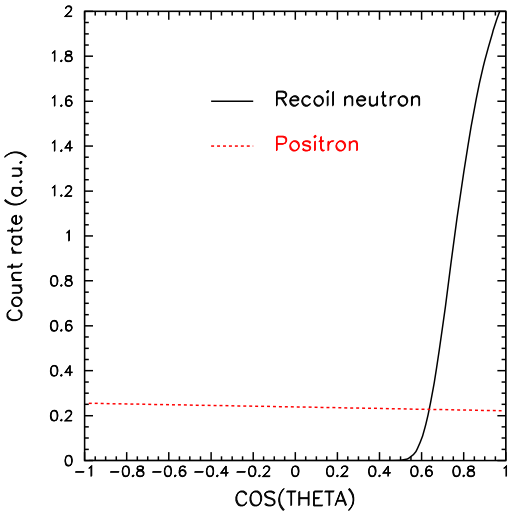

Fig. 1.7. Angular distributions of the positrons and recoil neutrons in the laboratory frame.

1.3.4 Reactor Antineutrino Disappearance Experiments

In a nuclear reactor experiment the measured quantity is the survival probability for $\bar{\nu}_e \rightarrow \bar{\nu}_e$ at a short baseline of the order of hundreds of meters to about a couple hundred kilometers with the $\bar{\nu}_e$ energy from about 1.8 MeV to 8 MeV. The matter effect is totally negligible and so the vacuum formula for the survival

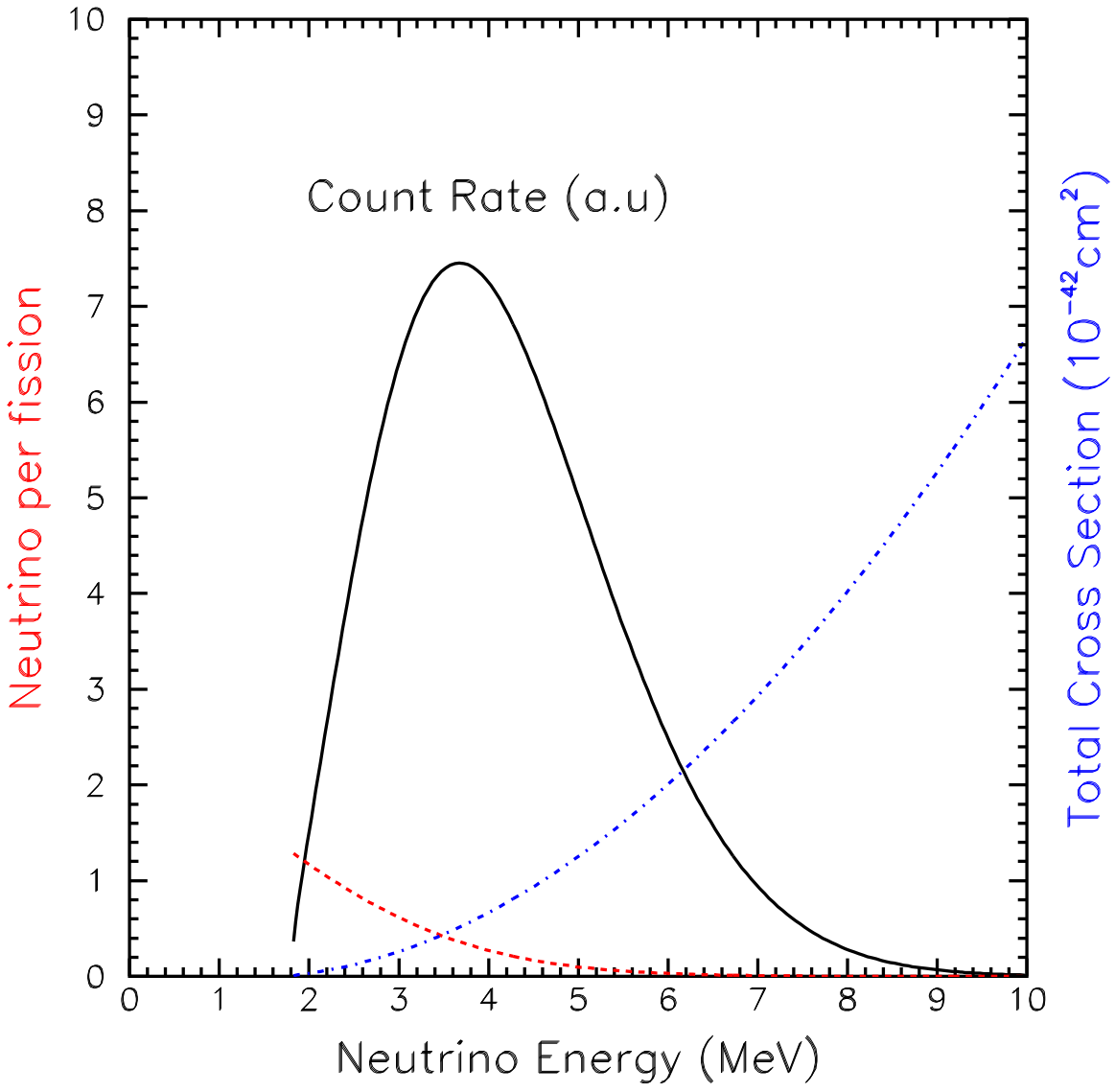

Fig. 1.8. Antineutrino energy spectrum, total cross section of inverse beta decay, and count rate as a function of the antineutrino energy.

probability is valid. In the standard notation of Eq. (2), this probability has a simple expression

$$P_{\rm sur} = 1 - C_{13}^4 \sin^2 2\theta_{12} \sin^2 \Delta_{21} - C_{12}^2 \sin^2 2\theta_{13} \sin^2 \Delta_{31} - S_{12}^2 \sin^2 2\theta_{13} \sin^2 \Delta_{32}, \quad (8)$$

where

$$\begin{aligned} \Delta_{\rm jk} &\equiv 1.267 \Delta m^2_{\rm jk}({\rm eV}^2) \times 10^3 \frac{L({\rm km})}{E({\rm MeV})}, \quad (9) \\ \Delta m^2_{\rm jk} &\equiv m^2_{\rm j} - m^2_{\rm k}. \end{aligned}$$

L is the baseline in km, E the neutrino energy in MeV, and $m_{\rm j}$ the j-th neutrino mass in eV. The $\nu_{\rm e} \to \nu_{\rm e}$ survival probability is also given by Eq. (8) when CPT is not violated. Eq. (8) is independent of the CP phase angle $\delta_{\rm CP}$ and the mixing angle θ_{23}.

To obtain the value of θ_{13}, the depletion of $\bar{\nu}_{\rm e}$ has to be extracted from the experimental $\bar{\nu}_{\rm e}$ disappearance probability below the μ production threshold,

$$\begin{aligned} P_{\rm dis} &\equiv 1 - P_{\rm sur} \\ &= C_{13}^4 \sin^2 2\theta_{12} \sin^2 \Delta_{21} + C_{12}^2 \sin^2 2\theta_{13} \sin^2 \Delta_{31} + S_{12}^2 \sin^2 2\theta_{13} \sin^2 \Delta_{32}\,. \quad (10) \end{aligned}$$

Since θ_{13} is known to be less than 10°, we define the term that is insensitive to θ_{13} as

$$P_{12} = C_{13}^4 \sin^2 2\theta_{12} \sin^2 \Delta_{21} \approx \sin^2 2\theta_{12} \sin^2 \Delta_{21}\,. \quad (11)$$

Then the part of the disappearance probability directly related to θ_{13} is given by

$$\begin{aligned} P_{13} &\equiv P_{\rm dis} - P_{12} \\ &= +C_{12}^2 \sin^2 2\theta_{13} \sin^2 \Delta_{31} + S_{12}^2 \sin^2 2\theta_{13} \sin^2 \Delta_{32} \quad (12) \end{aligned}$$

The above discussion shows that in order to obtain θ_{13} we have to subtract the θ_{13}-insensitive contribution P_{12} from the experimental measurement of $P_{\rm dis}$. To see their individual effect, we plot P_{13} in Fig. 1.9 together with $P_{\rm dis}$ and P_{12} as a function of the baseline from 100 m to 250 km. The neutrino energy is integrated from 1.8 to 8 MeV. We also take $\sin^2 2\theta_{13} = 0.10$, which will be used for illustration in most of the discussions in this section. The other parameters are taken to be

$$\theta_{12} = 34^\circ, \quad \Delta m^2_{21} = 7.9 \times 10^{-5} {\rm eV}^2, \quad \Delta m^2_{31} = 2.5 \times 10^{-3} {\rm eV}^2. \quad (13)$$

The behavior of the curves in Fig. 1.9 are quite clear from their definitions, Eqs. (10), (11), and (12). Below a couple kilometers P_{12} is very small, and P_{13} and $P_{\rm dis}$ track each other well. Beyond the first minimum P_{13} and $P_{\rm dis}$ deviate from each other more and more as L increases when P_{12} becomes dominant in $P_{\rm dis}$.

In the range of baseline that is insensitive to P_{12}, at the first maximum, $P_{\rm dis}$ is close to $P_{13}|_{\rm Max} \simeq \sin^2 2\theta_{13}$. This suggests that the measurement can be best performed at the first oscillation maximum of P_{13}. Since the location of the maximum of P_{13} is determined by $\Delta m^2_{31} \approx \Delta m^2_{32}$ and the energy of the anti-neutrino, the best possible distance $L_{\rm far}$ for the far detector is determined by taking advantage of the energy spread of the $\bar{\nu}_{\rm e}$ beam so as to provide a range of values of L/E.

In Fig. 1.10 P_{13} integrated over E from 1.8 to 8 MeV is shown as a function of $L_{\rm far}$ for three values of Δm^2_{32} that cover the allowed range of Δm^2_{32} in 2σ as given in Eq. 4. The curves show that P_{13} is sensitive to Δm^2_{32}. For $\Delta m^2_{32} = (1.8,\ 2.4,\ 2.9) \times 10^{-3}$ eV^2, the oscillation maxima correspond to a baseline of 2.5 km, 1.9 km, and 1.5 km, respectively. From this simple study, placing the far detector between 1.5 km and 2.5 km from the reactor looks to be a good choice.

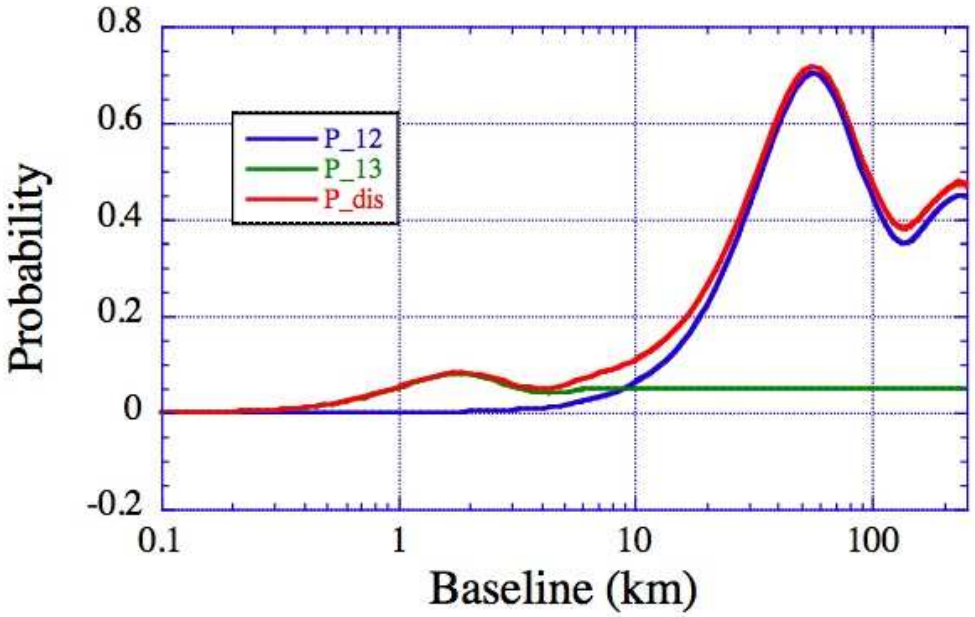

Fig. 1.9. Disappearance probability as a function of the baseline. The values of the mixing parameters are given in Eq. 13. P_{12} is the slowly rising blue curve. P_{13} is the green curve that has a maximum near 2 km. The total disappearance probability $P_{\rm dis}$ is the red curve.

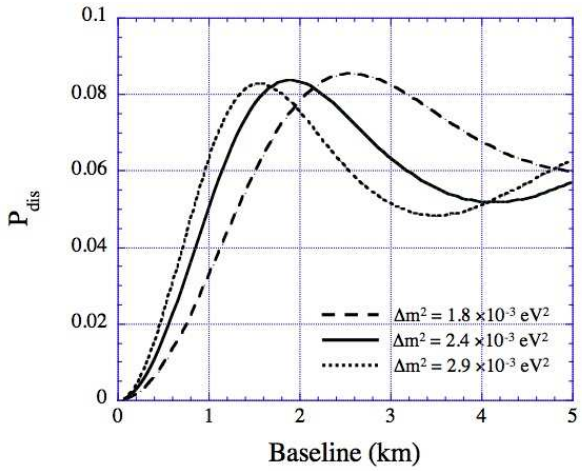

Fig. 1.10. Integrated P_{13} as a function of the baseline $L_{\rm far}$. The three curves covers the 2σ range in Δm^2_{32} given in Eq. 4.

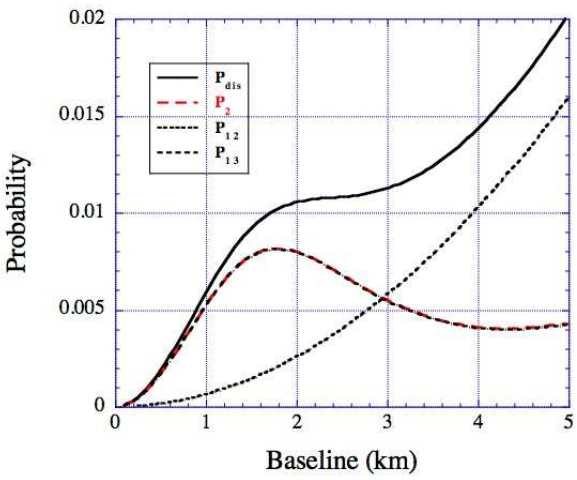

Fig. 1.11. Size of $P_{\rm dis}, P_{12}, P_{13}$, and P_2, integrated over neutrino energy spectrum, versus baseline for $\sin^2 2\theta_{13} = 0.01$.

In the literature, a simplified expression for oscillation probability involving only two neutrino flavors is often used for describing reactor neutrino experiment at short distance:

$$P_2 = \sin^2 2\theta_{13} \sin^2 \Delta_{31} \,. \tag{14}$$

The difference between the two-flavor expression P_2 and the three-flavor expression $P_{\rm dis}$ could be large,

especially for small $\sin^2 2\theta_{13}$. However, when we are interested in extracting $\sin^2 2\theta_{13}$, we should take out the contribution of P_{12} before fitting $\sin^2 2\theta_{13}$. The magnitudes of these oscillation probabilities are shown in Fig. 1.11 for a smaller θ_{13}, $\sin^2 2\theta_{13} = 0.01$. Although $P_{\rm dis}$ is significantly larger than P_2 at short distance, P_{13} is almost the same as the two-flavor expression. Therefore, the two-flavor expression is valid for most physical purposes, e.g. baseline optimization, sensitivity estimation, etc.

Current determinations of θ_{12} and Δm^2_{21} carry large uncertainties. P_{13} itself is insensitive to Δm^2_{21} and $\sin^2 2\theta_{12}$. However, since we calculate it by $P_{\rm dis} - P_{12}$, the error of θ_{12} and Δm^2_{21} will propagate to P_{13}. For the analysis of experimental data, this systematic error must be taken into account, and the two-flavor expression is no longer adequate. It is easy to check that, given the best fit values in Eq. (3), when $\sin^2 2\theta_{13}$ varies from 0.01 to 0.10 the relative size of P_{12} to the value of P_{13} is about 25% to 2.6% at the first oscillation maximum. Yet the uncertainty in determining $\sin^2 2\theta_{13}$ due to the uncertainty of P_{12} is always less than 0.005.

Let us summarize with the following remarks:

- The disappearance probability directly related to θ_{13} is insensitive to θ_{12} and Δm^2_{21} at short distance. The mixing angle θ_{13} can be unambiguously determined by reactor neutrino experiment.

- It is interesting to note that the useful region of the reactor $\bar{\nu}_{\rm e}$ energy spectrum is sufficient to cover the 2σ allowed range of Δm^2_{32} which is the focus of our discussion. And we determine that the optimal choice of $L_{\rm far}$ to be between 1.5 km to 2.5 km.

- The disappearance probability is sensitive to Δm^2_{31}. On one hand it creates a challenge in the selection of baseline of the far detector. On the other hand, the wide neutrino energy spectrum will provide information of Δm^2_{31}.

- The simplified two-flavor oscillation expression is a very good approximation of the three-flavor expression, except that errors of θ_{12} and Δm^2_{21} cannot be taken into account in the former. These systematic errors may have a significant impact on the data analysis.

Finally, we conclude from this phenomenological investigation that the choice of $L_{\rm far}$ be made so that it can cover as large a range of Δm^2_{31} as possible.

1.3.5 Past Measurements of θ_{13}

In the nineties, two reactor-based neutrino experiments, Chooz [10] and Palo Verde [11], were carried out to investigate neutrino oscillation. Based on $\Delta m^2_{32} = 1.5\times10^{-2}$ eV^2 as reported by Kamiokande [30], the baselines of Chooz and Palo Verde were chosen to be about 1 km. This distance corresponded to the location of the first oscillation maximum of $\nu_e \to \nu_\mu$ when probed with low-energy reactor $\bar{\nu}_e$. Both Chooz and Palo Verde were looking for a deficit in the $\bar{\nu}_e$ rate at the location of the detector by comparing the observed rate with the calculated rate assuming no oscillation occurred. With only one detector, both experiments must rely on the operational information of the reactors, in particular, the composition of the nuclear fuel and the amount of thermal power generated as a function of time, for calculating the rate of $\bar{\nu}_e$ produced in the fission processes.

Chooz and Palo Verde utilized Gd-doped liquid scintillator to detect the reactor $\bar{\nu}_e$ via the inverse beta-decay $\bar{\nu}_e p \to n e^+$ reaction. The ionization loss and subsequent annihilation of the positron give rise to a fast signal obtained with photomultiplier tubes (PMT's). The energy associated with this signal is termed the prompt energy, E_p. As stated in Sec. 1.3.2, E_p is directly related to the energy of the incident $\bar{\nu}_e$. After a random walk of about 30 μs, the neutron is captured by a Gd nucleus,* emitting several gamma-ray photons with a total energy of about 8 MeV. This signal is called the delayed energy, E_d. The temporal correlation

*The cross section of neutron capture by a proton is 0.3 b and 50,000 b for Gd.

between the prompt energy and the delayed energy constitutes a powerful tool for identifying the $\bar{\nu}_e$ and for suppressing backgrounds.

The value of $\sin^2 2\theta_{13}$ was determined by comparing the observed antineutrino rate and energy spectrum at the detector with the predictions that assumed no oscillation. The number of detected antineutrinos N_{det} is given by

$$N_{\rm det} = \frac{N_p}{4\pi L^2} \int \epsilon \sigma P_{\rm sur} S dE \tag{15}$$

where N_p is the number of protons in the target, L is the distance of the detector from the reactor, ϵ is the efficiency of detecting an antineutrino, σ is the total cross section of the inverse beta-decay process, P_{sur} is the survival probability given in Eq. 8, and S is the differential energy distribution of the antineutrino at the reactor shown in Fig. 1.8.

Since the signal rate is low, it is common to carry out reactor-based neutrino experiments underground for reducing the dangerous cosmogenic background events, such as neutrons and radioactive isotope ^{9}Li. Gamma rays originated from the natural radioactivity in materials and the surrounding rock are also problematic. For Chooz, their background rate was 1.41 ± 0.24 events per day in the 1997 run, and 2.22 ± 0.14 events per day after the trigger was modified in 1998. The background events were subtracted from $N_{\rm det}$ before $\sin^2 2\theta_{13}$ was extracted.

The systematic errors and efficiencies of Chooz are summarized in Tables 1.1 and 1.2 respectively.

parameter	relative error (%)
reaction cross section	1.9
number of protons	0.8
detection efficiency	1.5
reactor power	0.7
energy released per fission	0.6
combined	2.7

Table 1.1. Contributions to the overall systematic uncertainty in the absolute normalization in Chooz [10].

selection	ϵ (%)	relative error (%)
positron energy	97.8	0.8
positron-geode distance	99.9	0.1
neutron capture	84.6	1.0
capture energy containment	94.6	0.4
neutron-geode distance	99.5	0.1
neutron delay	93.7	0.4
positron-neutron distance	98.4	0.3
neutron multiplicity	97.4	0.5
combined	69.8	1.5

Table 1.2. Summary of the anti-neutrino detection efficiency in Chooz [10].

Neither Chooz nor Palo Verde observed any rate deficit in $\bar{\nu}_e$. This null result is used to set a limit in the neutrino mixing angle θ_{13}, as shown in Fig. 1.12. Chooz obtained the best limit of 0.17 in $\sin^2 2\theta_{13}$ for $\Delta m^2_{31} = 2.5 \times 10^{-3}$ eV^2 at the 90% confidence level.

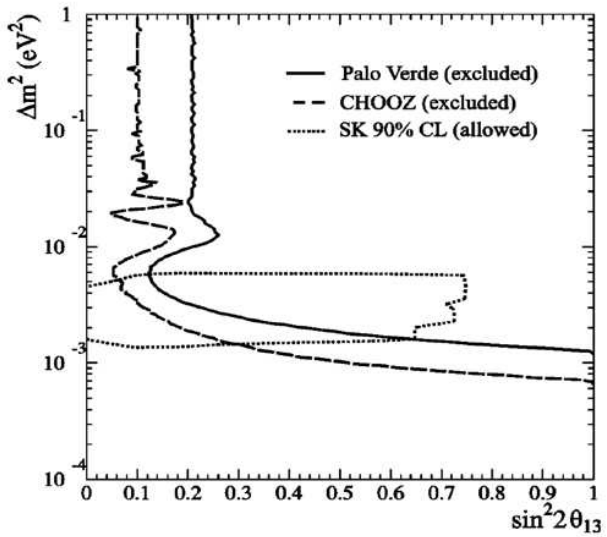

Fig. 1.12. Exclusion contours determined by Chooz, Palo Verde, and allowed region obtained by Kamiokande [10].

1.4 Synergy of accelerator and reactor experiments

The three parameters that are not determined by the solar, atmospheric, and KamLAND data are θ_{13}, the sign of Δm^2_{32}, which fixes the hierarchy of neutrino masses, and the Dirac CP phase δ_{CP}.

Long-baseline accelerator experiments, in addition to improving the measurements of $|\Delta m^2_{32}|$ and θ_{23} via ν_μ survival, will also be able to search for ν_e appearance in $\nu_\mu \rightarrow \nu_e$ oscillations, which is very sensitive to these unknown parameters. A measurement of both $\nu_\mu \rightarrow \nu_e$ and $\bar{\nu}_\mu \rightarrow \bar{\nu}_e$ oscillations allows one to measure θ_{13} and test for CP violation in the lepton sector, provided that θ_{13} is large enough. However, there are potentially three two-fold parameter degeneracies, for which the same parameter sets are consistent with the same data, which lead to ambiguities in the measured values of θ_{13} and δ_{CP} [1,31]:

1. the $(\delta_{CP}, \theta_{13})$ ambiguity,
2. the ambiguity due to our lack of knowledge of the mass hierarchy (the sign of Δm^2_{32} ambiguity), and
3. the θ_{23} ambiguity, which occurs because only $\sin^2 2\theta_{23}$, *not* θ_{23}, is measured in ν_μ survival in atmospheric neutrino experiments.

All three parameter degeneracies can lead to different inferred values for δ_{CP} and θ_{13}, and they can all be present simultaneously, leading to as much as an eight-fold ambiguity in the determination of θ_{13} and δ_{CP}. Another problem is that Earth-matter effects can induce fake CP violation, which must be taken into account in any determination of θ_{13} and δ_{CP}. One advantage of matter effects is that they may be able to distinguish between the two possible mass hierarchies,

There are experimental strategies that can overcome some of these problems. For example, by combining the results of two long-baseline experiments at different baselines, the sign of Δm^2_{32} could be determined if θ_{13} is large enough [32]. By sitting near the peak of the leading oscillation with a narrow-band beam, θ_{13} can be removed from the $(\delta_{CP}, \theta_{13})$ ambiguity [33]. However, neither of these approaches resolves the θ_{23} ambiguity, and θ_{13} may not be uniquely determined.

The $\bar{\nu}_e$ survival probability for reactor neutrinos depends primarily on only θ_{13} and Δm^2_{31}, and is independent of δ_{CP} and insensitive to θ_{12} and Δm^2_{21} at short distance. Furthermore, matter effects are

negligible due to the short baseline. Therefore, a short-baseline reactor neutrino experiment is an ideal method for measuring θ_{13} with no degeneracy problem. If θ_{13} can be unambiguously determined by a reactor neutrino experiment, then there is no $(\delta_{CP}, \theta_{13})$ ambiguity, and long-baseline accelerator experiments can more easily measure δ_{CP} and determine the sign of Δm^2_{32} [34]. Figure 1.13 is an illustration of how a reactor experiment can resolve the ambiguity of θ_{23} for a hypothetical case that $\sin^2 2\theta_{23}$ is known to be 0.95 ± 0.01 [35].

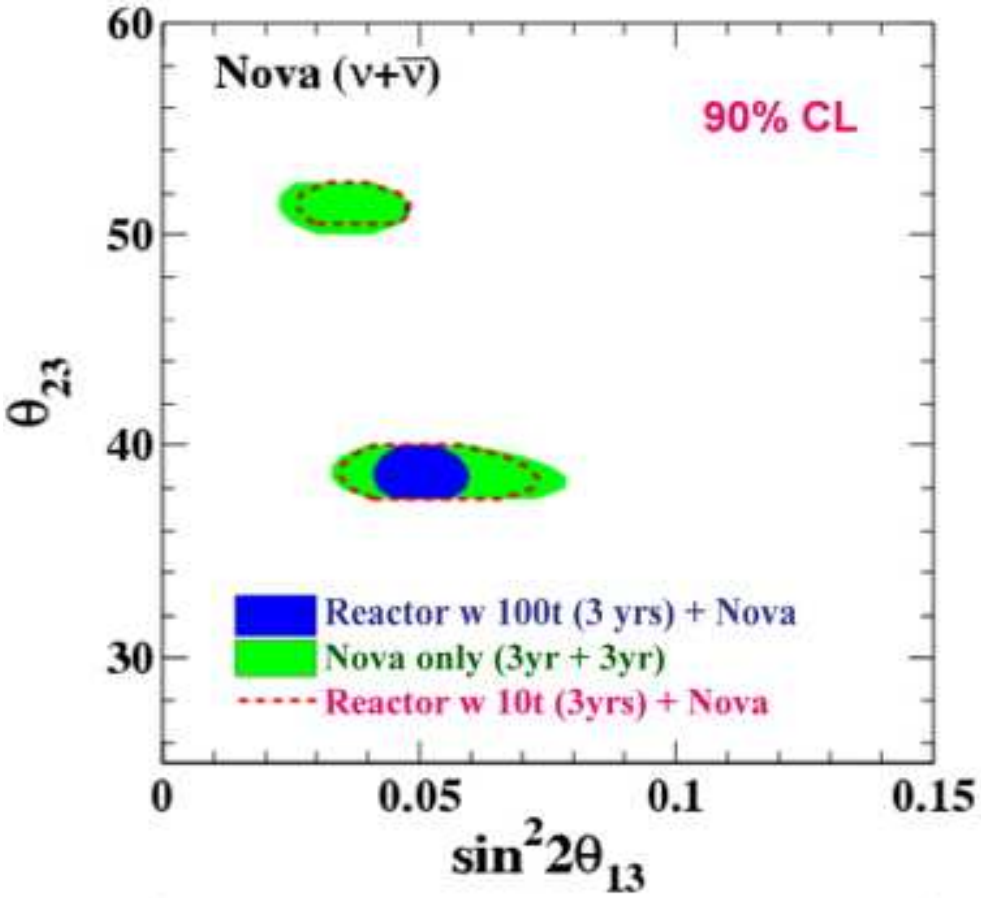

Fig. 1.13. Resolving the θ_{12} ambiguity with $\sin^2 2\theta_{13}$ determined by reactor experiments for $\sin^2 2\theta_{23} = 0.95 \pm 0.01$ [35].

1.5 The Daya Bay Reactor Neutrino Experiment

As discussed in Section 1.3.4, the mixing angle θ_{13} plays very important roles in further studies of the neutrino and a precise determination of its value is crucial to both experimental and theoretical programs. Experimentally, a precise value for θ_{13} will help resolve parameter degeneracies; theoretically, it would provide a strong constraint on model building. Probing $\sin^2 2\theta_{13}$ down to the 0.01 level will be an important milestone in the development of neutrino physics. There are proposals to determine $\sin^2 2\theta_{13}$ with sensitivities approaching the level of 0.01 [21]. The goal of the Daya Bay experiment is to determine $\sin^2 2\theta_{13}$ to 0.01 or better.

In order to reach the designed sensitivity in $\sin^2 2\theta_{13}$, it is important to reduce both the statistical error and systematic uncertainties as well as suppressing background in the Daya Bay neutrino oscillation

experiment.

1.5.1 The Daya Bay Site

This experiment will be located at the Daya Bay nuclear power facility in southern China. Its geographic location is shown in Fig. 1.14. The experimental site is about 55 km north-east from the Victoria Harbour

Fig. 1.14. Daya Bay and the vicinity. The nuclear power plants are located about 55 km from central Hong Kong.

of Hong Kong. Fig. 1.15 is a photograph of the facility. The complex consists of the Daya Bay Nuclear Power Station, the Ling Ao Nuclear Power Station, and the Ling Ao II Nuclear Power Station which is under construction and will be operational by 2010–2011. There are two identical reactors in each station. Each reactor can generate 2.9 GW_{th} during normal operation. The Ling Ao reactors are about 1.1 km east of the Daya Bay reactors. The Ling Ao II reactors are about 400 m east from the Ling Ao cluster. There are mountain ranges to the north of the nuclear power plants and can provide sufficient overburden to cut down cosmogenic background at the underground experimental halls. Within 2 km of the site the elevation is generally 185 m to 400 m.

The six reactors can be roughly grouped into two clusters. We plan to deploy identical detectors at a distance between 300 m and 500 m from the respective reactor cluster to monitor the characteristics of the anti-neutrinos and a group of identical detectors, called the far detectors, approximately 1.5 km north of the two near detectors. Since the overburden of the experimental sites increases with distance, the cosmogenic background decreases as the signal decreases, hence keeping the background-to-signal ratio roughly constant. This is beneficial to controlling systematic uncertainties. With such an experimental setup, the Daya Bay experiment will determine $\sin^2 2\theta_{13}$ to a sensitivity of 0.01 or better by comparing the antineutrino

Fig. 1.15. The Daya Bay nuclear power facility. The Daya Bay Nuclear Power Plant is in the foreground. The Ling Ao Nuclear Power Plant is in the background. The experimental halls of the proposed experiment will be underneath the hills to the left.

fluxes and energy spectra between the near and far detectors. Detailed baseline optimization accounting for statistical and systematic errors, backgrounds, and topographical information will be discussed in the following chapters.

It is possible to instrument a mid detector site between the near and far sites. The mid detectors along with the near and far detectors can be used to carry out measurements for systematic studies and for internal consistency checks. In combination with the near detectors close to the Daya Bay nuclear power plant, they could also be utilized to provide a quick determination of $\sin^2 2\theta_{13}$ in the early stage of the experiment.

1. For a recent review, see V. Barger, D. Marfatia, and K. Whisnant, Int. J. Mod. Phys. **E 12** (2003) 569 [arXiv:hep-ph/0308123].
2. SNO Collaboration: Q.R. Ahmad et at., Phys. Rev. Lett **87** 071301 [arXiv:nucl-ex/0106015]; **89** (2002) 011301 [arXiv:nucl-ex/0204008]; **89** (2002) 011302 [arXiv:nucl-ex/0204009]; **92** (2004) 181301 [arXiv:nucl-ex/0309004]; Phys. Rev. **C72** (2005) 055502 [arXiv:nucl-ex/0502021].
3. SuperK Collaboration: Y. Fukuda *et al.*, Phys. Rev. Lett., **81** (1998) 1158 [arXiv:hep-ex/9805021]; **82** (1999) 2430 [arXiv:hep-ex/9812011]; S. Fukuda *et al.*, Phys. Rev. Lett. **86** (2001) 5651 [arXiv:hep-ex/010302]; M. B. Smy *et al.*, Phys. Rev. **D69** (2004) 011104 [arXiv:hep-ex/0309011].
4. B. T. Cleveland *et al.*, Astrophys. J. **496** (1998) 505.
5. J. N. Abdurashitov *et al.*, [SAGE Collaboration], J. Exp. Theor. Phys. **95** (2002) 181 [arXiv:astro-ph/0204245]; W. Hampel *et al.* [GALLEX Collaboration], Phys. Lett. **B447** (1999) 127; M. Altman *et al.* [GNO Collaboration], Phys. Lett. **B490** (2000) 16 [arXiv:hep-ex/0006034].
6. KamLAND Collaboration: K. Eguchi *et al.*, Phys. Rev. Lett., **90** (2003) 021802 [arXiv:hep-ex/0212021]; **94** (2005) 081801 [arXiv:hep-ex/0406035].
7. SuperK Collaboration: Y. Fukuda et al., Phys. Lett. **B433** (1998) 9 [arXiv:hep-ex/9803006]; **B436** (1998) 33 [arXiv:hep-ex/9805006]; Phys. Rev. Lett., **81** (1998) 1562 [arXiv:hep-ex/9807003]; S. Fukuda *et al.*, Phys. Rev. Lett. **85** (2000) 3999 [arXiv:hep-ex/0009001]; Y. Ashie *et al.*, Phys. Rev. Lett. **93** (2004) 101801 [arXiv:hep-ex/0404034].
8. K2K Collaboration: E. ALiu *et al.*, Phys. Rev. Lett. **94** (2005) 081802.
9. MINOS Collaboration: D. Michael *et al.*, arXiv:hep-ex/0607088].
10. Chooz Collaboration: M. Apollonio *et al.*, Eur. Phys. J. C**27**, 331 (2003) [arXiv:hep-ex/0301017].
11. F. Boehm *et al.*, Phys. Rev. D**62**, 072002 (2000) [hep-ex/0003022].

12. LSND Collaboration: C. Athanassopoulos *et al.*, Phys. Rev. **C54** (1996) 2685 [arXiv:hep-ex/9605001]; Phys. Rev. Lett. **77** (1996) 3082 [arXiv:hep-ex/9605003]; A. Aguilar *et al*., Phys. Rev. **D64** (2001) 112007 [arXiv:hep-ex/0204049].
13. KARMEN Collaboration: K. Eitel *et al.*, Nucl. Phys. Proc. Suppl. **91** (2000) 191 [arXiv:hep-ex/0008002]; B. Armbruster *et al.*, Phys. Rev. **D66** (2002) 112001 [arXiv:hep-ex/0203021].
14. S. Doldelson, A. Melchiorri, and A. Slosar, [arXiv:astro-ph/0511500].
15. I. Stancu *et al., The MiniBooNE detector technical design report*, FERMILAB-TM-2207, May 2001.
16. Z. Maki, M. Nakagawa, and S. Sakata, Prog. Theor. Phys. **28** (1962) 870; B. Pontecorvo, Sov. Phys. JETP **26** (1968) 984; V.N. Gribov and B. Pontecorvo, Phys. Lett. **28B** (1969) 493.
17. G.L. Fogli, E. Lisi, A. Marrone, and A. Palazzo, and A.M. Rotunno, 40th Rencontres de Moriond on Electroweak Interacions and Unified Theories, La Thuile, Aosta Valley, Italy, 5-12 March 2005 [arXiv:hep-ph/0506307].
18. T. Schwetz, Talk given at 2nd Scandanavian Neutrino Workshop (SNOW 2006, Stockholm Sweden, 2-6 May 2006 [arXiv:hep-ph/0606060].
19. K. Anderson, *et al., White paper report on using nuclear reactors to search for a value of* θ_{13}, arXiv:hep-ex/0402041.
20. M. Lindner, Phys. Scripta **T121** (2005) 78 [arXiv:hep-ph/0503101]; G. Altarelli, *Proceedings of the 19th Rencontres de Physique de la Vallee D'Aoste: Results and Perspectives in Particle Physics*, :a Thuile, Aosta Valley, Italy 27 Feb - 5 Mar 2005 [arXiv:hep-ph/0508053].
21. R.N. Mohapatra *et al., Theory of Neutrinos: A White Paper*, arXiv:hep-ph/0510213.
22. R.N. Mohapatra, Talk at the 11th International Workshop on Neutrino Telescopes, Venice, Italy, 22-25 Feb. 2005, arXiv:hep-ph/0504138.
23. M.F. James, J. Nucl. Energy **23** 517 (1969).
24. L. Miller, Ph.D Thesis, Stanford University, 2000, unpublished.
25. V.I. Kopeikin, Phys. Atom. Nucl. **66** (2003) 472 [arXiv:hep-ph/0110030].
26. P. Vogel and J. Engel, Phys. Rev. **D39**, 3378 (1989).
27. P. Huber and T. Schwetz, Phys. Rev. **D70**, 053011 (2004) [arXiv:hep-ph/0407026].
28. K. Schreckenbach *et al.*, Phys. Lett. **B160**, 325 (1985); A. A. Hahn *et al.*, Phys. Lett. **B218**, 365 (1989).
29. P. Vogel and J. F. Beacom, Phys. Rev. **D60**, 053003 (1999) [hep-ph/9903554].
30. K. S. Hirata *et al.*, Phys. Lett. B**205**, 416 (1988); Y. Fukuda *et al.*, Phys. Lett. B**335**, 237 (1994).
31. V. Barger, D. Marfatia and K. Whisnant, Phys. Rev. **D65** (2002) 073023 [arXiv:hep-ph/0112119].
32. V. Barger, D. Marfatia and K. Whisnant, Phys. Lett. B **560** (2003) 75 [arXiv:hep-ph/0210428]; P. Huber, M. Lindner and W. Winter, Nucl. Phys. B **654** (2003) 3 [arXiv:hep-ph/0211300]; H. Minakata, H. Nunokawa and S. Parke, Phys. Rev. **D68** (2003) 013010 [arXiv:hep-ph/0301210].
33. V. D. Barger, D. Marfatia and K. Whisnant, "Neutrino Superbeam Scenarios At The Peak," in *Proc. of the APS/DPF/DPB Summer Study on the Future of Particle Physics (Snowmass 2001)* ed. N. Graf, eConf **C010630** (2001) E102 [arXiv:hep-ph/0108090].
34. H. Minakata *et al.*, Phys. Rev. **D68** (2003) 033017 [Erratum-ibid. **D70** (2004) 059901] [arXiv:hep-ph/0211111]; P. Huber, M. Lindner, M. Rolinec, T. Schwetz and W. Winter, Phys. Rev. D **70** (2004) 073014 [arXiv:hep-ph/0403068]; K. Hiraide *et al.*, Phys. Rev. **D73** (2006) 093008 [arXiv:hep-ph/0601258].
35. K. McConnel and M.H. Shaevitz, arXiv:hep-ex/0409028.

2 Experimental Design Overview

In order to establish the presence of reactor neutrino oscillations, and to determine $\sin^2 2\theta_{13}$ to a value of 0.01 or better, statistics of $>$50,000 events are needed in a far detector and systematic uncertainties in the ratios of near/far detector acceptance, expected flux and background have to be controlled at a level below 0.5%, an improvement of almost an order of magnitude over previous experiments. From recent reactor experiments such as Chooz, Palo Verde and KamLAND, there are three main sources of systematic uncertainty: 1) reactor-related uncertainty of (2–3)%, 2) background-related uncertainty of (1–3)%, and 3) detector-related uncertainty of (1–3)%. Each source of uncertainty can be further classified into the correlated and uncorrelated uncertainty. Hence a carefully designed experiment, including the detector design, configuration, and background control, are required. The primary considerations driving the improved performance are listed below:

- **identical near and far detectors** Use of identical detectors at the near and far sites to cancel reactor-related systematic uncertainties, a technique first proposed by Mikaelyan et al. for the Kr2Det experiment in 1999 [1]. The event rate in the near detector will be used to normalize the yield in the far detector. Even in the case of a multiple reactor complex, reactor related uncertainties can be controlled to negligible level by a careful choice of locations of the near and far sites.

- **multiple modules** Employ multiple, identical modules at the near and far sites to cross check between modules at each location and reduce detector-related uncorrelated uncertainties. The use of multiple modules in each site enables the measurement of systematic uncertainties at the limit of statistics. Multiple modules implies smaller modules which are easier to move from the near site to far site, or vice versa. In addition, small modules have less cosmic-ray flux, enabling simpler muon tagging resulting in less dead time, backgrounds and systematic uncertainties. A balance of cost, complication of calibration system, and risk results in a design with two modules for each near site and four modules for the far site.

- **three zone detector module** Employ a newly designed antineutrino detector with substantially reduced detector-related systematic uncertainties compared to past experiments: target volume and mass, position cut, positron energy threshold, scintillator aging, etc. The idea is to use a three zone detector module, in which the inner most layer is filled with Gd-loaded liquid scintillator as the neutrino target, the middle layer is filled with normal scintillator to fully contain the energy of neutrino events even at the target edge, and the outer most layer is filled with transparent, non-scintillating liquid to shield gamma backgrounds from PMT glass and other environmental backgrounds.

- **sufficient overburden and shielding** Ensure sufficient overburden and shielding at all detector sites to reduce backgrounds to the level that they can be measured with an acceptable uncertainty. For radioactive backgrounds from rocks and other environmental materials, sufficient passive shielding of the antineutrino detectors is needed. For cosmic-ray-induced fast neutron backgrounds, a cosmic-muon detector with sufficient internal passive shielding is needed. For cosmic-ray induced radioisotope backgrounds good muon tagging and sufficient overburden are essential.

- **multiple muon detectors** The muon detector has to be sufficiently efficient (with a small uncertainty in that efficiency) to control the cosmic-muon-induced neutron backgrounds to a negligible level. Monte Carlo study shows that the efficiency has to be better than 99.5% (with an uncertainty less than 0.25%). The muon detection system is designed to have two sub-detectors: one utilizes the water shield as a Cerenkov detector, and the other is a muon tracking detector with a good position resolution. Each muon detector can easily be constructed with an efficiency of (90–95)% and their combined efficiency (OR of both) will be better than 99.5%. They can be cross checked with each other to measure the uncertainty to better than 0.25%.

- **movable detectors** The detector modules are movable such that swapping of modules between the near and far sites will cancel all detector-related uncertainties that remain unchanged before and after swapping. The residual uncertainties, being secondary, are caused by the energy scale uncertainties, as well as other site dependent ones. The systematic uncertainties are small enough, such that swapping of the detectors is not necessary. However, it is quite likely that swapping will allow even further reduction in systematic uncertainties and sensitivity.

With these improvements, the total detector-related systematic uncertainty is expected to be $\sim$0.2% in the near/far ratio per detector site which is comparable to the statistical uncertainty of $\sim$0.2% at the far site. Using a global χ^2 analysis (see Section 3.5.1), incorporating all known systematic and statistical uncertainties, we find that $\sin^2 2\theta_{13}$ can be determined to better than 0.01 precision with 90% confidence as discussed in Sec. 3.

2.1 The experimental layout and site optimization

Taking currentthe best fit value of $\Delta m^2_{31} = 2.5 \times 10^{-3}$ eV^2 [**?**], the maximum of reactor neutrino oscillation occurs at $\sim$1800 m. The oscillation probability is the most important parameter in the baseline optimization. Considerations based on statistics alone will result in a shorter baseline, especially when the statistical uncertainty is larger or comparable to the systematic uncertainty. For the Daya Bay experiment, the overburden influences the optimization since it varies along the baseline. In addition, a shorter tunnel will decrease the civil construction cost.

The Daya Bay experiment will use identical detectors at the near and far sites to cancel reactor-related systematic uncertainties, as well as part of the detector-related systematic uncertainties. For a reactor with only one or two cores, all uncertainties from the reactor, correlated or uncorrelated, can be cancelled precisely by using one far detector and one near detector. The Daya Bay site currently has four cores in two groups: the Daya Bay nuclear power plant (NPP) and the Ling Ao NPP. Another two cores will be installed adjacent to Ling Ao, the Ling Ao II NPP, which will start to generate electricity in 2010–2011. Figure 2.1 shows the locations of the Daya Bay cores, Ling Ao cores, and the future Ling Ao II cores. The distance between the two cores in each NPP is about 88 m. The Daya Bay NPP is 1100 m from the Ling Ao NPP, and the maximum distance between cores will be 1600 m when Ling Ao II starts operation. The experiment will require detectors close to each reactor cluster to monitor the antineutrinos emitted from their cores as precisely as possible. At least two near sites are needed, one for the Daya Bay cores and another for the Ling Ao—Ling Ao II cores. The reactor-related systematic uncertainties can not be cancelled exactly, but can be reduced to a negligible revel, as low as 0.04% if the overburden is not taken into account. A global optimization taken all factors into account, especially balancing the overburden and reactor-related uncertainties, result in a residual reactor uncertainty of $<$0.1%

Three major factors are involved in the near site determination. The first one is overburden. The slope of the mountains near the cores is around 30 degrees. When we put the detector site closer to the cores, the overburden will be significantly reduced. The second concern is oscillation loss. The oscillation probability is appreciable even in the near sites. For example, for near detectors placed at approximately 500 m from the center of gravity of the cores, the integrated oscillation probability is $0.19 \times \sin^2 2\theta_{13}$, computed with $\Delta m^2_{31} = 2.5 \times 10^{-3}$ eV^2. The oscillation contribution of the other pair of cores, which is around 1100 m away, has been included. The third concern is the near-far cancellation of reactor uncertainties. As discussed above, the cancellation is not exact if detectors are too close to the cores.

After careful study of many different schemes, the best configuration of the experiment is shown in Fig. 2.1 together with the tunnelling scheme. A global χ^2 fit (see Eqn. 26) for the best sensitivity and baseline optimization is made, taking into account backgrounds, mountain profile, detector systematics and residual reactor related uncertainties, the result is shown in Fig. 2.2.

Each near detector should be positioned equidistant from the cores that it monitors to cancel uncorre-

Fig. 2.1. Layout of the Daya Bay experiment.

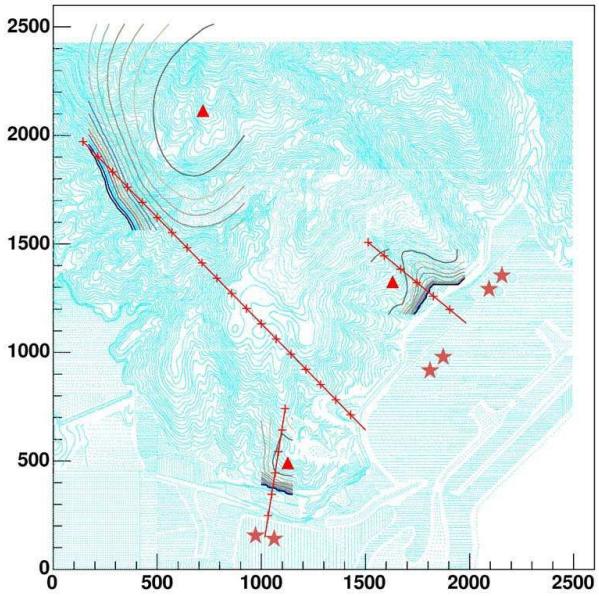

Fig. 2.2. Site optimization using the global χ^2 analysis. The optimal sites are labelled with red triangles. The stars show the reactors. The contours show the sensitivity when one site varies and the other two are fixed at optimal sites. The red line with ticks are the perpendicular bisectors of the reactor pairs. The mountain contours are also shown as background of the plot.

lated reactor uncertainties. Optimizing the experimental sensitivity, including overburden and statistics, the Daya Bay near detector site is best located 363 m from the center of the Daya Bay cores where the overburden is 98 m.* The Ling Ao near detector hall is optimized to be 481 m from the center of the Ling Ao cores, and 526 m from the center of the Ling Ao II cores† where the overburden is 112 m.

The far detector site is north of the two near sites. Ideally the far site should be equidistant between the Daya Bay and Ling Ao—Ling Ao II cores; however, the overburden would be only 200 m (520 m.w.e). At present, the distances from the far detector to the midpoint of the Daya Bay cores and to the mid point of the Ling Ao—Ling Ao II cores are 1985 m and 1615 m, respectively. The overburden is about 350 m (910 m.w.e).

It is possible to install a mid detector hall between the near and far sites such that it is 1156 m from the midpoint of the Daya Bay cores and 873 m from the center of the Ling Ao—Ling Ao II cores. The overburden at the mid hall is 208 m (540 m.w.e.). This mid hall could be used for a quick measurement of $\sin^2 2\theta_{13}$ and to carry out measurements to study systematics and for internal consistency checks.

There are three branches for the main tunnel extending from a junction near the mid hall to the near and far underground detector halls. There are also access and construction tunnels. The length of the access tunnel, from the portal to the Daya Bay near site, is 295 m. It has a grade between 8% and 12% [2]. A sloped access tunnel will allow the underground facilities to be located deeper with more overburden.

2.2 Detector

As discussed above, the antineutrino detector employed for the near (far) site has two (four) modules while the muon detector consists of a cosmic-ray tracking device and active water shielding. There are several possible configurations for the water shielding and the muon tracking detector as discussed in section 7. The baseline design is shown in Fig. 2.3.

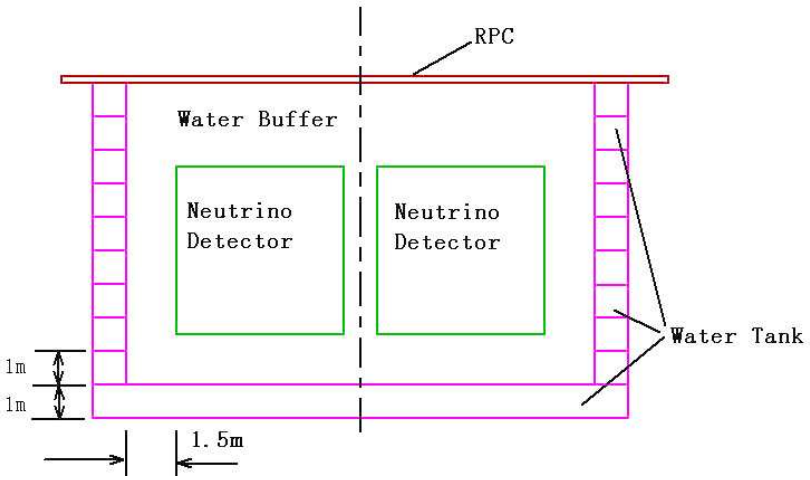

Fig. 2.3. Layout of the baseline design of the Daya Bay detector. Four antineutrino detector modules are shielded by 1.5 m-thick active water buffer. Outside of it are Water cerenkov tanks serving as muon tracker, together with RPC's at the top.

The water shielding in this case is a water pool, equipped with PMT's to serve as a Cerenkov detector

*The Daya Bay near detector site is about 40 m east from the perpendicular bisector of the Daya Bay two cores to gain more overburden.

†The Ling Ao near detector site is about 50 m west from the perpendicular bisector of the Ling Ao-Ling Ao II clusters to avoid installing it in a valley which is usually geologically weak, and to gain more overburden.

of cosmic muons. The outer region of the water pool is segmented into water tanks made of reflective PVC sheets with a cross section of 1 m$\times$1 m and a length of 16 m. Four PMT's at each end of the water tank are installed to collect Cerenkov photons produced by cosmic-muons in the water tank. The water tank scheme was first proposed by Y.F. Wang for very long baseline neutrino experiments as a segmented calorimeter [3], it is a reasonable choice for its cost and technical feasibility as a muon tracking detector in a large water pool. Above the pool the muon tracking detector is made of RPC, which is light weight, with good performance, excellent position resolution and low cost. The antineutrino detector modules are submerged in the water pool for background shielding.

Other possible water shielding configurations will be discussed in section 2.3.

2.2.1 Central detector

Antineutrinos are detected by an organic liquid scintillator (LS) with high hydrogen content (free protons) and large uniform volume, via the inverse beta decay reaction:

$$\bar{\nu}_e + p \longrightarrow e^+ + n$$

The prompt positron signal and delayed neutron capture signal constitute a neutrino event with timing and energy requirements on both signals. In pure LS, neutrons are captured by free protons in the scintillator emitting 2.2 MeV γ-rays with a capture time of 180 μs. On the other hand, Gadolinium (Gd), with its huge neutron-capture cross section, and high energy release of gamma-rays (total energy of about 8 MeV), is an attractive dopant for the LS. The much higher gamma energies separate the signal from natural radioactivity, which is mostly below 3.5 MeV. Both Chooz [4] and Palo Verde [5] used 0.1% Gd-doped LS that yielded a capture time of 28 μs, about a factor of seven shorter than in undoped liquid scintillator. Backgrounds from random coincidences will thus be reduced by a factor of seven.

Based on experience of past experiments such as Palo Verde, Chooz and KamLAND, the central detector has to follow the following guidelines:

- Employ three-zone detector modules partitioned with acrylic tanks as shown in fig 2.4. The target

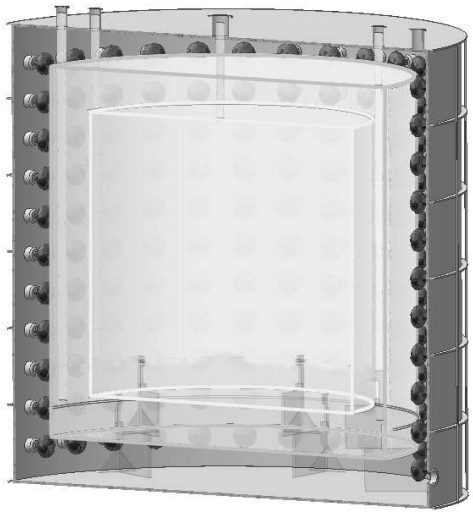

Fig. 2.4. Cross section of a 3-zone detector module showing the acrylic vessels holding the Gd-doped liquid scintillator at the center, and liquid scintillator between the acrylic containers. The PMT's are mounted inside the outer-most stainless steel tank.

volume is physically well defined by a central region of Gd-loaded scintillator, surrounded by an intermediate region filled with normal scintillator to catch the gammas leaking out of the central region, and further surrounded by mineral oil to separate the PMT's from the scintillator, reducing natural radioactivity background from the PMT's. In this design, the homogeneous target volume can be well determined without the position cut, since neutrino capture in normal scintillator will not satisfy the energy selection. The neutron spill-in and spill-out across the boundary between the two regions will be cancelled out by the use of identical detector modules at the near and far sites. With the shielding of normal mineral oil, the singles rate will be reduced substantially, and the threshold can thus be lowered to below 1.0 MeV, producing essentially 100% detection efficiency for the prompt positron.

- The Gd-loaded liquid scintillator, which is the target material, should have the same composition, and the fraction of hydrogen (free protons), for each pair of near/far detectors. Other detector components shall be measured in advance of assembly, and divided among detector modules to equalize the properties of the modules.

- The energy resolution should be better than 15% at 1 MeV. Good energy resolution is desirable for reducing the energy-related systematic uncertainty. Good energy resolution is also important for studying the spectral distortion as a signal of neutrino oscillation.

- The time resolution should be better than 1 ns for determining the event time and for studying backgrounds.

Detector modules of different shapes, including cubical, cylindrical, and spherical, have been considered. From the point of view of easy construction, cubical and cylindrical shapes are particularly attractive. Monte Carlo simulation shows that modules of cylindrical shape can provide better energy and position resolutions for the same number of PMT's. Figure 2.4 shows the structure of a cylindrical module. The PMT's are arranged along the circumference of the outer cylinder. The surfaces at the top and the bottom of the outer-most cylinder are coated with white reflective paint or other reflective materials to provide diffuse reflection. Such an arrangement is feasible since 1) the event vertex is determined only with the center of gravity of the charge, not relying on the time-of-flight information,[‡] 2) the fiducial volume is well defined with a three-layer structure, thus no accurate vertex information is required.

Details of the central detector will be discussed in Chapter 5.

2.2.2 Muon detector

Since most of the backgrounds come from the interactions of cosmic-ray muons with nearby materials, it is thus desirable to have a very efficient active muon detector coupled with a tracker for tagging the cosmic-ray muons. This will provide a means for studying and rejecting cosmogenic background events. The three types of detectors that are being considered are water Cherenkov counter, resistive plate chamber (RPC), and plastic scintillator strip. When the water Cherenkov counter is combined with a tracker, the muon detection efficiency can be close to 100%. Furthermore, these two independent detectors can cross check each other. Their inefficiencies and the associated uncertainties can be well determined by cross calibration during data taking. We expect the inefficiency will be lower than 0.5% and the uncertainty of the inefficiency will be lower than 0.25%.

Besides being a shield, the water buffer can also be utilized as a water Cherenkov counter of the muon system by installing PMT's in the water. The water Cherenkov detector is based on proven technology, and known to be very reliable. With proper PMT coverage and diffuse reflection on the inner wall of the

[‡]Although time information may not be used in reconstructing the event vertex, it will be used in background studies. A time resolution of 0.5 ns can be easily realized in the readout electronics.

water buffer, the efficiency of detecting muons should exceed 95%. The current baseline design of the water buffer is a water pool, similar to a swimming pool with a dimensions of 16 m (length) $\times$ 16 m (width) $\times$ 10 m (height) for the far hall containing four detector modules, as shown in Fig. 2.5. The PMT's of the water

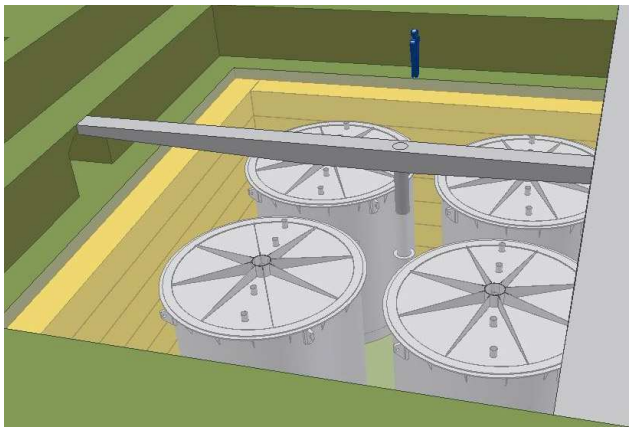

Fig. 2.5. The water pool with four center detector modules inside. 1m$\times$1m water tanks are used as outer muon tracker.

Cherenkov counters are mounted facing the inside of the Water Pool. This is a simple and proven technology with very limited safety concerns. This shield design will effectively shield the antineutrino detectors from radioactivity in the surrounding rocks and from Radon, while also being simple, cost-effective and with relatively short construction time.

The muon tracking detector consists of water tanks and RPCs. RPC's are very economical for instrumenting a large area, and simple to fabricate. The bakelite based RPC developed by IHEP for the BESIII detector has a typical efficiency of 95% and noise rate of 0.1 Hz/cm^2 per layer. [6]. A possible configuration is to build three layers of RPC, and require 2 out of 3 layers hits within a time window of 50 ns to define a muon event. Such a scheme has an efficiency of 99% and noise rate of 0.05 Hz/m^2. Although RPC's are an ideal large area muon detectors due to their light weight, good performance, excellent position precision, and low cost, it is hard to put them inside water to fully surround the water pool. The best choice seems to use them only at the top of the water pool.

Water tanks with a dimension of 1 m$\times$1 m and a length of 16 m as the outer muon tracking detector has a typical position resolution of about 30 cm. Although not as good as other choices, the resolution is reasonably good for our needs, in particular with the help of RPC's at the top in most cases. Actually the water tank are not really sealed tank, but reflective PVC sheets assembled on a stainless steel structure, so that water can flow freely among water pool and water tanks, and only one water purification system is need for each site. Water tanks can be easily installed at the side of the water pool, but to be cut into pieces at the bottom to leave space for the supporting structure of antineutrino detector modules. Each tank will be equipped with four PMT's at each end to collect Cerenkov photons produced by cosmic-muons. A few more PMT's are needed for bottom tanks to take into accounts the blocked optical path by the supporting structure of the central detector modules. A detailed Monte Carlo simulation and a 13 m long prototype has been built and tested [3]. Results show that the total light collected at each end is sufficient as will be discussed in detail in Chapter 7. The technology employed in this design is mature, and the detector is relatively easy and fast for construction.

2.3 Alternative Designs

We have chosen a water-pool as the baseline experimental design (see Figure 2.3). The two near detector sites have two central detector modules in a rectangular water pool, whereas the far site has four central detector modules in a square water pool. The distance from the outer surface of each CD is at least 2.5 m to the water surface, with 1 m of water between each CD.

Our primary alternative to the baseline design is the “aquarium” option. A conceptual design, showing the side view is provided in figure 2.6. The end view is shown in figure 2.7. The primary feature of this

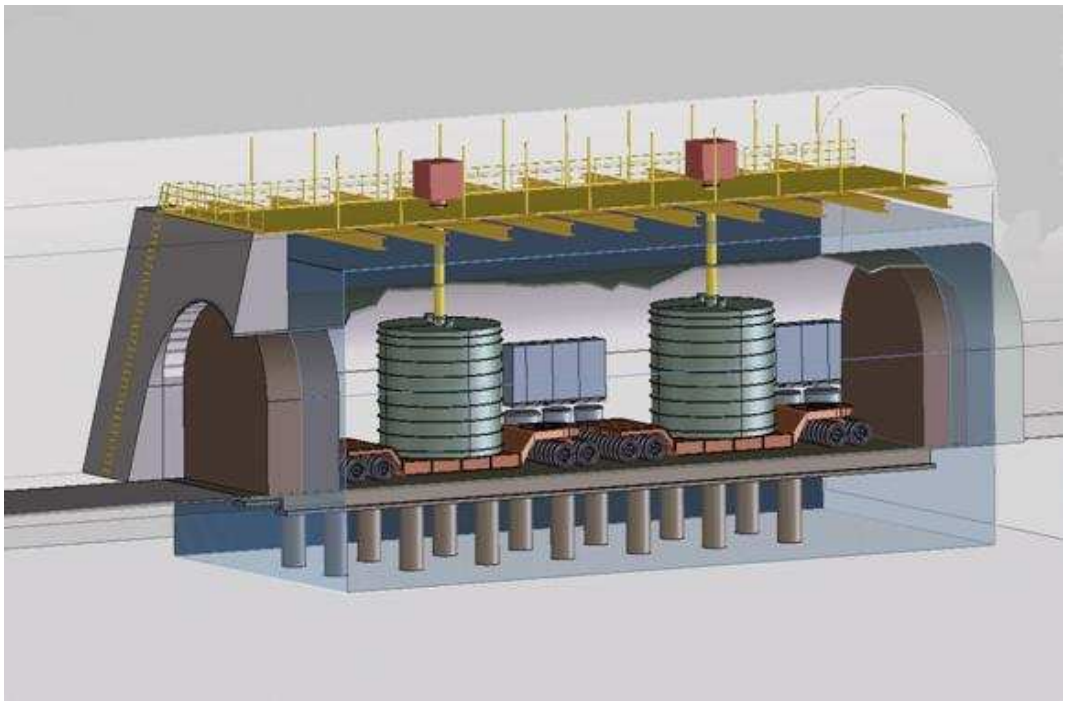

Fig. 2.6. Side view of the conceptual design of a near detector site aquarium with two detectors visible.

aquarium design is that the central detector modules do not sit in the water volume, but are rather in air. The advantages of this design are ease of access to the CD, ease of connections to the CD, simpler movement of the CD, more flexibility to calibrate the CD and a muon veto that does not need to be partially dissambled or moved when the CD’s are moved. The primary disadvantages of this design include the engineering difficulties of the central tube and the water dam, safety issues associated with the large volume of water above the floor level, cost, maintenance of the CD’s free of radon and radioactive debris. This is preserved as the primary option for a “dry detector” and serves as our secondary detector design option. Other designs that have been considered include: Ship-Lock, modified aqaurium, water pool with a steel tank, shipping containers, water pipes, ...

The cost drivers that we have identified for the optimization of the experimental configuration include:

- Civil construction
- Cranes for the CD
- Transporters for the CD
- Safety systems in the event of catastrophic failure

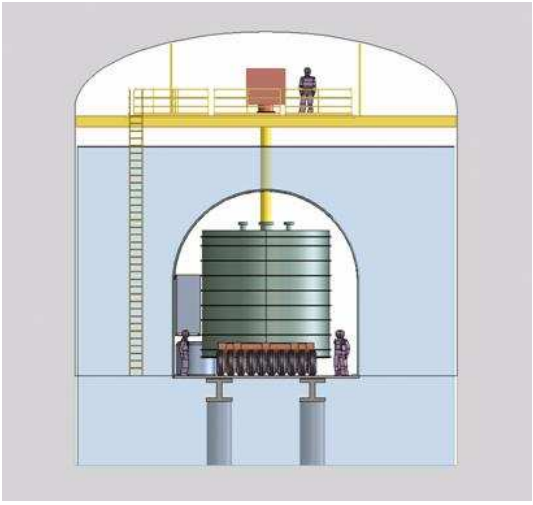

Fig. 2.7. End view of the conceptual design of a near detector site aquarium with one detector visible.

- Storage volume of purified water
- Complexity of seals in water environment

The physics performance drivers that we have identified include:

- Uniformity of shielding against γ's from the rock and cosmic muon induced neutrons
- Cost and complexity of purifying the buffer region of radioactive impurities
- Amount and activity of steel near the CD (walls and mechanical support structures)
- Efficiency of tagging muons and measurement of that inefficiency

The primary parameters that we have investigated in the optimization of the detector design are the thickness of the water buffer, the optical segmentation of this water Cherenkov detector, the PMT coverage of this water Cherenkov detector, the size and distribution of the muon tracker system, the number of PMT's in the central detector, the reflectors in the central detector. The study is ongoing, but existing work favors this water pool.

1. L. A. Mikaelyan and V. V. Sinev, Phys. Atom. Nucl. **63**, 1002 (2000); L. Mikaelyan, Nucl. Phys. Proc. Suppl. **91**, 120 (2001); L. A. Mikaelyan, Phys. Atom. Nucl. **65**, 1173 (2002).
2. *Report of Preliminary Feasibility Study of Site Selection for the Daya Bay Neutrino Experiment*, prepared by Beijing Institute of Nuclear Energy, September, 2004.
3. Y.F. Wang, Nucl. Instr. and Meth. A 503 (2003) 141; M.J. Chen *et al.*, Nucl. Instr. and Meth. A 562 (2006) 214
4. M. Apollonio *et al.* (Chooz Collaboration), Phys. Lett. B**420**, 397 (1998); Phys. Lett. B**466**, 415 (1999); Eur. Phys. J. C**27**, 331 (2003).
5. F. Boehm *et al.* (Palo Verde Collaboration), Phys. Rev. Lett. **84**, 3764 (2000) [arXiv:hep-ex/9912050]; Phys. Rev. D**62**, 072002 (2000) [arXiv:hep-ex/0003022]; Phys. Rev. D**64**, 112001 (2001) [arXiv:hep-ex/0107009]; A. Piepke et al., Nucl. Instr. and meth. A**432**, 392 (1999).
6. J.W. Zhang *et al.*, High Energy Phys. and Nucl. Phys., **27**, 615 (2003); Jia-Wen Zhang et al., Nucl. Instrum. Meth. A 540(2005)102.

3 Sensitivity & Systematic Errors

The control of systematic errors is critical to achieving the $\sin^2 2\theta_{13}$ sensitivity goal of this experiment. The most relevant previous experience is the Chooz experiment [7] which obtained $\sin^2 2\theta_{13} < 0.17$ for $\Delta m^2_{31} = 2.5 \times 10^{-3}\text{eV}^2$ at 90% C.L., the best limit to date, with a systematic uncertainty of 2.7% and statistical uncertainty of 2.8%. In order to achieve a $\sin^2 2\theta_{13}$ sensitivity below 0.01, both the statistical and systematic uncertainties need to be an order of magnitude smaller than CHOOZ. The projected statistical error of the Daya Bay far detectors is 0.2% with three years data taking. In this section we discuss our strategy for achieving the level of systematic error comparable to that of the statistical error. Achieving this very ambitious goal will require extreme care and substantial effort that can only be realized by incorporating rigid constraints in the design of the experiment.

There are three main sources of systematic uncertainties: reactor, background, and detector. Each source of error can be further classified into correlated and uncorrelated errors.

3.1 Reactor related errors

For a reactor plant with only one core, all errors from the reactor, correlated or uncorrelated, can be canceled precisely by using one far detector and one near detector (assuming the average distances are precisely known) [22]. In reality, the Daya Bay Power Plant has four cores in two groups, the Daya Bay Plant and the Ling Ao Plant. Another two cores will be installed adjacent to Ling Ao, called Ling Ao II, which will start to generate electricity in 2010. Fig. 2.1 shows the locations of the Daya Bay cores, Ling Ao cores, and the future Ling Ao II cores. Superimposed on the figure are the tunnelling scheme and the proposed detector sites. The distance between the two cores at each reactor site, called a pair here, is about 88 m. The Daya Bay pair is 1100 m from the Ling Ao pair, and will be 1600 m from the Ling Ao II pair. Reactor systematic errors are associated with uncertainties in the power levels of the different cores and the effective locations of the cores relative to the detectors.

3.1.1 Power fluctuations

Typically, the measured power level for each reactor core will have a correlated (common to all the reactors) error of the order of 2% and an uncorrelated error of similar size. Optimistically, we may be able to achieve uncorrelated errors of 1%, but we conservatively assume that each reactor has 2% uncorrelated error in the following. (We note that both CHOOZ and Palo Verde achieved total reactor power uncertainties of $0.6 - 0.7\%$. The appropriate value for the Daya Bay reactors will need to be studied in detail with the power plant personnel.) If the distances are precisely known, the correlated errors will cancel in the near/far ratio. In the multiple-reactor (> 2) case one cannot separately measure the event rate from each reactor. We will measure the following combination of ratios in the event rates of the far and near detectors:

$$\rho = \left[\alpha \sum_r \frac{\phi_r}{(L_r^{DB})^2} + \sum_r \frac{\phi_r}{(L_r^{LA})^2}\right] \Big/ \sum_r \frac{\phi_r}{(L_r^f)^2} \tag{16}$$

where ϕ_r is the antineutrino flux at unit distance from core r, L_r^f is the distance from reactor r to the far site, L_r^{DB} (L_r^{LA}) is the distance from reactor r to the near Daya Bay (Ling Ao) site, and α is a constant chosen to minimize the sensitivity of ρ to the relative reactor power levels. The optimal choice of the weighting factor α is determined by Monte Carlo simulations and will substantially reduce the systematic error associated with uncorrelated reactor power levels while introducing only a slight increase ($< 11\%$ fractional increase) in the statistical error. The correlated errors of the reactors are common to both the numerator and denominator of the ratio ρ, and therefore will cancel.

We assume a detector configuration shown in Fig. 2.1, with two near sites at ~ 500 m baselines to sample the reactor cores and the far site at an average baseline of ~ 1800 m. For an uncorrelated error of

2% for each core and optimal choice of α, Table 3.1 shows the estimated reactor power contribution to σ_ρ (i.e., the error in the ratio ρ) for the two cases of four reactor cores and six reactor cores.

3.1.2 Location uncertainties

The location of the reactor cores will be determined to a precision of about 30 cm. We assume that the location errors are uncorrelated, and so their combined effect will be reduced by $\sim \sqrt{N_r}$ where N_r is the number of reactor cores. The resulting error in the far/near event ratio is estimated to be 0.08% for the near baseline of ~ 500 m.

Number of cores	σ_ρ(power)	σ_ρ(location)	σ_ρ(total)
4	0.035%	0.08%	0.087%
6	0.097%	0.08%	0.126%

Table 3.1. Reactor-related systematic errors for different reactor configurations. The uncorrelated error of a single core is assumed to be 2%.

3.1.3 Spent fuel uncertainties

3.2 Detector related errors

For the detector-related errors, we consider the CHOOZ results as a reference, and then compute 2 values for the Daya Bay case: baseline and goal. The baseline value is what we expect to be achievable through essentially proven methods with straightforward improvement in technique and accounting for the fact that we need to consider only *relative* errors between near and far detectors. The goal value is that which we consider reachable through improved methods and extra care beyond the level of previous experiments of this type. The results are summarized in Table 3.2 and discussed in the rest of this section.

Source of error		CHOOZ	Daya Bay	
			Baseline	Goal
# protons	H/C ratio	0.8	0.2	0.1
	Mass	-	0.2	0.02
Detector Efficiency	Energy cuts	0.8	0.2	0.1
	Position cuts	0.32	0.0	0.0
	Time cuts	0.4	0.1	0.03
	H/Gd ratio	1.0	0.1	0.1
	n multiplicity	0.5	0.05	0.05
	Trigger	0	0.01	0.01
	Live time	0	< 0.01	< 0.01
Total detector-related uncertainty		1.7%	0.38%	0.18%

Table 3.2. Comparison of detector-related systematic uncertainties (all in percent, per detector module) of CHOOZ experiment and projections for Daya Bay. Baseline values for Daya Bay are achievable through essentially proven methods, whereas the goals should be attainable through additional efforts described in the text.

3.2.1 Target mass and H/C ratio

The antineutrino targets are the free protons in the detector, so the event rate in the detector is proportional to the total mass of free protons. The systematic error in this quantity is controlled by precise knowledge of the relative total mass of the central volumes of the detector modules as well as filling the modules from a common batch of scintillator liquid so that the H/C ratio is the same to high precision.

The mass of the central detector is accurately determined in several ways. First the detector modules will be built to specified tolerance so that the volume is known to $\sim 0.1\%$ (typically $<$1 mm dimension out of a radius of 1.6 meters). We will make measurements of these volumes after construction to characterize them to higher precision than 0.1%. We plan to fill each module from a common stainless steel tank at a controlled constant temperature. We will measure the fluid flow using premium grade precision flowmeters with a repeatability specification of 0.02%. Several flowmeters will be run in series for redundancy. Residual topping up of the detector module to a specified level (only about $\sim$ 20 kg since the volume is known and measured) is measured with the flowmeters as well. We aim for a goal of 0.02% relative precision on the central detector mass based on the specification of the flowmeters. We quote a baseline of 0.2%, which should be fairly straightforward even if we rely on the absolute calibration of flowmeters alone.

The absolute H/C ratio was determined by CHOOZ using scintillator combustion and analysis to 0.8% precision based on several laboratories. We will only require that the *relative* measurement on different samples be known, so an improved precision of 0.2% or better is expected.

We are presently engaged in a program of R&D with the goal of measuring the *relative* H/C ratio in different samples of liquid scintillator to $\sim 0.1\%$ precision. We are exploring two different methods the achieve this goal: precision NMR and neutron capture. The neutron capture method would need to be utilized before the introduction of Gd into the scintillator, but could be used to precisely characterize the organic liquids used in the liquid scintillator cocktail. In principle, the NMR method could be used on the final Gd-loaded scintillator.

In addition, we will need to determine the *relative* H/C ratio in the gamma catcher liquid scintillator to about 1%. This is to control the relative amount of "spill-in" events where a neutron generated in the gamma catcher is captured in the Gd-loaded scintillator after thermal diffusion. Differences in spill-in and spill-out fractions between different detector modules must be understood, and the H/C ratio in the gamma catcher must be determined to 1% to insure that we can achieve the baseline systematic error in Table 3.2.

As discussed in 3.3.1 below, we intend to deploy the detector modules in designated pairs. For each of the 4 pairs, one detector will be at a near site and one at a far site. We plan to fill the detector module pairs simultaneously from the same batch of scintillator (for Gd-loaded and gamma-catcher as well). Thus each pair should have identical H/C ratio, and the event ratio of this pair will have no contribution from this potential source of error.

3.2.2 Position cuts

Due to the design of the detector modules, the event rate is measured without resort to reconstruction of the event location. Therefore the error in the event rate is related to the physical parameters of the central volume. We do not anticipate employing cuts on reconstructed position to select events.

3.2.3 Positron energy cut

Due to the high background rates a low energy, CHOOZ employed a positron energy threshold of 1.3 MeV. This cut resulted in an estimated error of 0.8%. The improved shielding design of the Daya Bay detectors makes it possible to lower this threshold to below 1 MeV while keeping uncorrelated backgrounds as low as 0.1%. The threshold of visible energy of neutrino events is 1.022 MeV. Due to the finite energy resolution of $\sim 12\%$ at 1 MeV, the reconstructed energy will have a tail below 1 MeV. The systematic error associated with this cut efficiency is studied by Monte Carlo simulation. The tail of the simulated energy

spectrum is shown in Fig. 3.1 with the full spectrum shown in the inset. For this simulation, 200 PMTs are used to measure the energy deposited in a 20-ton module. The energy resolution is $\sim$ 15% at 1 MeV. The inefficiencies are 0.32%, 0.37%, and 0.43% for cuts at 0.98 MeV, 1.0 MeV, and 1.02 MeV, respectively. Assuming the energy scale error is 2% at 1 MeV, this inefficiency variation will produce a 0.05% error in the detected antineutrino rate. The upper energy cut for the positron signal will be $E > 8$ MeV and will also contribute a negligible error to the positron detection efficiency.

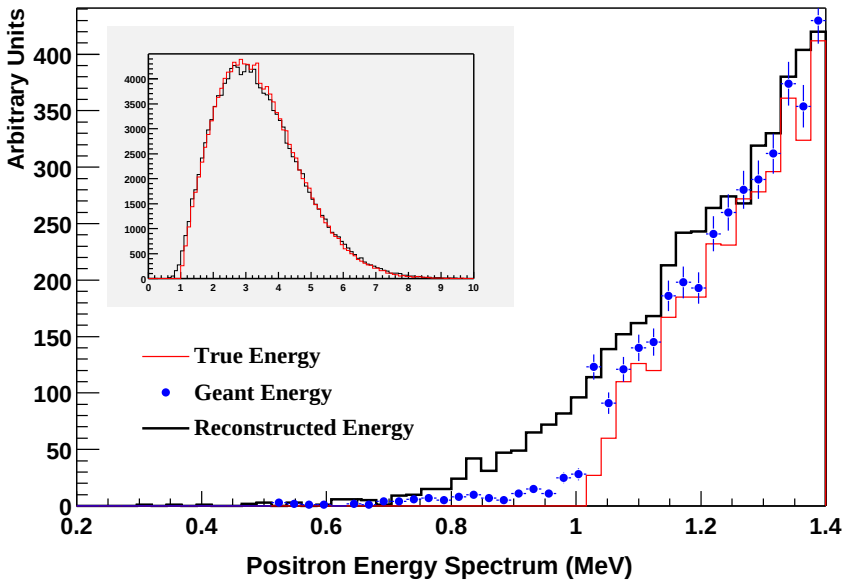

Fig. 3.1. Spectra of prompt energy for true energy, simulated energy (Geant Energy), and reconstructed energy at around 1 MeV. The full spectrum is shown in the inset, where the red line corresponds to the true energy and the black one corresponds to the reconstructed energy.

3.2.4 Neutron Detection Efficiency

The delayed neutron from the inverse beta decay reaction is produced with $\sim$ 10 keV of kinetic energy. The neutron loses energy in the first few interactions with H and C in the scintillator, and reaches thermal energy in a few microseconds. The neutrons can capture on either H or Gd during or after the thermalization process. We will detect the neutrons that capture on Gd, yielding at least 6 MeV of visible energy from the resulting capture gamma rays, during the time period $0.3 < T < 200$ μsec.

The efficiency for detecting the neutron is given by

$$\epsilon_n = P_{Gd}\epsilon_E\epsilon_T \tag{17}$$

in which P_{Gd} is the probability to capture on Gd (as opposed to H), ϵ_E is the efficiency of the $E > 6$ MeV energy cut for Gd capture, and ϵ_T is the efficiency of the delayed time period cut. In order to measure the rates for two detectors (near and far) with a precision to reach $\sin^2 2\theta_{13} = 0.01$ we require that the *relative* neutron detection efficiencies be known to better than 0.25%. The ϵ_n for neutrons at the center of a detector module can be determined directly by using a tagged neutron source (either ^{252}Cf or AmBe, or both can be used) and counting the number of neutrons using the time and energy cuts after neutron producing event. (Corrections associated with uniformly distributed neutrons are studied with spallation neutrons, as discussed in Chapter 6.) This will require measurement of order 1 million neutron captures, and would

likely require several hours of measurement. In addition, the individual components P_{Gd}, ϵ_E, and ϵ_T can be monitored separately as an additional check on the measurement of ϵ_n.

H/Gd ratio

Neutrons are thermalized during their first 10μs of existence in the detector central volume. Thus for times longer than 10μs the delayed neutron capture events will exhibit an exponential time constant, τ, related to the average concentration of Gd in the detector module. The rate of capture, $\Gamma \equiv 1/\tau$, is given by:

$$\Gamma = \Gamma_{Gd} + \Gamma_H = [n_{Gd}\sigma_{Gd} + n_H\sigma_H]v \; . \tag{18}$$

The fraction of neutrons that capture on Gd rather than H is then

$$P_{Gd} = \frac{1}{1 + \Gamma_H/\Gamma_{Gd}} \tag{19}$$

and we would like to know this *relative* fraction between different detector modules to $\sim 0.1\%$. Thus we must measure the time constants τ for different detector modules to a *relative* precision of 0.2 μsec. The value of τ is expected to be about 30 μsec , so we need to measure it to about 0.5% relative precision. Such a measurement requires measuring about 30,000 neutron captures, which can be done in a few minutes with a neutron source. The CHOOZ experiment measured the (*absolute*) $\sim 30\mu$sec capture time to $\pm 0.5\mu$sec precision.

Energy cut efficiency

Another issue is the neutron detection efficiency associated with the signal from capture of neutrons on Gd in the central detector volume. An energy threshold of about 6 MeV will be employed to select these delayed events, and the efficiency ($\sim 93\%$) of this criterion may vary between detector modules depending upon the detailed response of the module. However, this can be calibrated through the use of radioactive sources (see Chapter sec:cal) and spallation neutron captures. The KamLAND detector gain is routinely (every 2 weeks) monitored with sources, and a relative long-term gain drift of $\sim 1\%$ is readily monitored with a precision of 0.05%.

We have performed Monte Carlo simulations of the detector response to neutron sources and spallation neutrons. The results of these studies indicate that we can indeed establish the relative value of ϵ_E to 0.1%, even for reasonable variations of detector properties (such as scintillator attenuation length). As an example, Figure 3.2 shows how the source data can be used with uniform spallation neutrons to bootstrap a non-linear energy scale that corrects the spectrum, independent of attenuation length over the extreme range of 4.5 - 18 m.

Time cuts

The time correlation of the prompt (positron) event and the delayed (neutron) event is a critical aspect of the event signature. Matching the time delays of the start and end times of this time window between detector modules is crucial to reducing systematic errors associated with this aspect of the antineutrino signal. If the starting time ($\sim 0.3\mu$sec) and ending time ($\sim 200\mu$sec)of the delayed event window is determined to ~ 10 nsec precision, the resulting error associated with the lost event fraction is $\sim 0.03\%$. We will insure that this timing is equivalent for different detector modules by slaving all detector electronics to one master clock. We estimate that with due care, the relative neutron efficiency for different modules due to timing is known to $\sim 0.03\%$.

3.2.5 Neutron multiplicity

CHOOZ required a cut on the neutron multiplicity to eliminate events where it appeared that there were 2 neutron captures following the positron signal, resulting in a 2.6% inefficiency and associated 0.5% systematic error. These multiple neutron events are due to muon-induced spallation neutrons, and will be reduced to a much lower level by the increased overburden available at the Daya Bay site. For the near

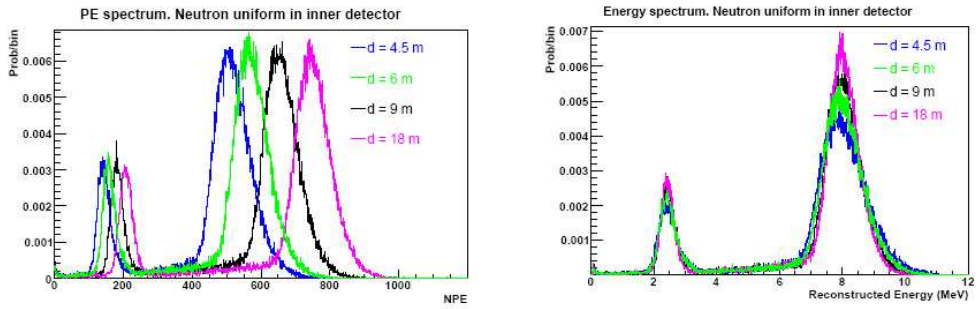

Fig. 3.2. Spallation neutron response for detector modules with scintillator optical attenuation lengths of $4.5 \leq d \leq 18$ m. The left panel shows the raw photoelectron spectra, whereas the right panel shows the spectra rescaled according to a non-linear rescaling procedure we have developed. The rescaled 6 MeV effective energy threshold produces a constant value of $\epsilon_E = 93\%$ to within 0.4% over this extreme range of attenuation length.

site at 500 m baseline, the muon rate relative to the signal rate will be more than a factor 9 lower than for the CHOOZ site. Therefore, events with multiple neutron signals will be reduced by this factor relative to CHOOZ, and should present a much smaller problem for the Daya Bay site.

3.2.6 Trigger

The trigger efficiency can be measured to high precision (0.01%) using studies with pulsed light sources in the detector. (We note that KamLAND has used this method to determine 99.8% absolute trigger efficiency [21].)

3.2.7 Live time

The detector live time can be measured accurately by counting a 100 MHz clock using the detector electronics, and normalizing to the number of clock ticks in a second (as defined by a GPS receiver signal). The uncertainty associated with this procedure should be extremely small, and certainly negligible relative to the other systematic errors. For example, SNO measured the relative live times for their day/night analysis with a relative fractional uncertainty of 5×10^{-7}.

3.3 Cross-calibration and Swapping of Detectors

3.3.1 Detector Swapping

The connection of the two near detector halls and the far hall by horizontal tunnels provides the Daya Bay experiment with the unique and important option of swapping the detectors between the locations. This will enable the further reduction of detector-related systematic errors in the measurement of the ratio of neutrino fluxes at the near and far locations.

The swapping concept is easy to demonstrate for a simple scenario with a single neutrino source and only 2 detectors deployed at 2 locations, near and far. The desired measurement is the ratio of event rates at the near and far locations: N/F. With detector #1 (efficiency ϵ_1) at the near location and detector #2 (efficiency ϵ_2)at the far location we would measure

$$\frac{N_1}{F_2} = \left(\frac{\epsilon_1}{\epsilon_2}\right) \frac{N}{F} \,. \tag{20}$$

By swapping the two detectors and making another measurement, we can measure

$$\frac{N_2}{F_1} = \left(\frac{\epsilon_2}{\epsilon_1}\right)\frac{N}{F}\,, \tag{21}$$

where we have assumed that the detector properties (e.g., efficiencies) do not change when the detector is relocated. We can now combine these two measurements to obtain a value of N/F that is, to first order, independent of the detector efficiencies:

$$\frac{1}{2}\left(\frac{N_1}{F_2} + \frac{N_2}{F_1}\right) = \frac{N}{F}\left(1 + \frac{\delta^2}{2}\right) \tag{22}$$

where we have defined

$$\delta \equiv \frac{\epsilon_2}{\epsilon_1} - 1\,. \tag{23}$$

Note that even if the detector efficiencies are different by as much as 1%, we can determine N/F to a fractional precision better than 10^{-4}.

The layout of the Daya Bay experiment involves 2 near sites with 2 detectors each, and a far site with 4 detectors. The simplest plan is to designate the eight detectors as 4 pairs: (1,2), (3,4), (5,6), (7,8). Using 4 running periods (designated I, II, III, IV, separated by three detector swapping events) we can arrange for each detector to be located at the far site half the time and a near site half the time by swapping 2 pairs between running periods, as shown in Table 3.3. Ratios of event rates can be combined in a fashion analogous to the above discussion to provide cancelation of detector-related systematic errors and also reactor power systematic errors. Careful calibration of the detectors following each swap will be necessary to insure that each detector's performance does not change significantly due to relocation. In particular, all the parameters in Table 3.2 need to be checked and, if necessary, corrections applied to restore the detection efficiency to the required precision through, e.g., changes in calibration constants.

Run Period	Near(DB)	Near(LA)	Far
I	1,3	5,7	2,4,6,8
II	2,3	6,7	1,4,5,8
III	2,4	6,8	1,3,5,7
IV	1,4	5,8	2,3,6,7

Table 3.3. Swapping scheme with 4 running periods. The detectors (labelled 1-8) are deployed at the Near(DB), Near(LA), and Far sites during each period as indicated in this table.

3.3.2 Detector Cross-calibration

Another important feature of the design of the Daya Bay experiment is the presence of two detector modules at each near site. During a single running period (I, II, III, or IV) each near detector module will measure the neutrino rate with 0.23% statistical precision. If the systematic errors are smaller than this, the two detectors at the near site should measure the same rate, giving a detector asymmetry of $0 \pm 0.34\%$ (statistical error only). Combining all the detector pairs in all 4 running periods will yield an asymmetry of $0 \pm 0.04\%$ (statistical error only). These asymmetries are an important check that the detector-related systematic errors are under control. In addition, this analysis can provide information on the the degree to which the detector-related systematic errors are correlated or uncorrelated so that we know how to handle them in the full analysis including the far site.

Finally, the near detector data can provide important information on the reactor power measurements. We will measure the ratio

$$R_{\rm near} = \frac{S_{DB}}{S_{LA}} \tag{24}$$

where S_{DB} (S_{LA}) is the detector signal (background subtracted, normalized to the reactor power) for the Daya Bay (Ling Ao) near site. If the reactor powers are correct (and the detector systematic errors are under control) then we expect $R_{\rm near} = 1.0 \pm 0.24\% \pm 0.51\%$, where the first error is statistical (only 1 of the 4 running periods) and the second error is the detector (baseline) systematic error. Note that these errors are small relative to the expected 2% uncorrelated reactor power uncertainty, so measurement of $R_{\rm near}$ will provide an important check (and even perhaps additional information) on the reactor powers. Furthermore, studies of the measured neutrino spectra in the different near detectors during different parts of the reactor fuel cycle can help provide constraints on the fuel cycle effects on the spectrum.

3.4 Backgrounds

In the Daya Bay experiment, the signal events (inverse beta decay reactions) have a distinct signature of two time-ordered signals: a prompt positron signal followed by a delayed neutron-capture signal. Backgrounds can be classified into two categories: correlated and uncorrelated backgrounds. If a background event is triggered by two signals that come from the same source, such as those induced by the same cosmic muon, it is a correlated background event. On the other hand, if the two signals come from different sources but satisfy the trigger requirements by chance, the event is an uncorrelated background.

There are three important sources of backgrounds in the Daya Bay experiment: fast neutrons, ^{8}He/ ^{9}Li, and natural radioactivity. A fast neutron produced by cosmic muons in the surrounding rock or the detector can produce a signal mimicking the inverse beta decay reaction in the detector: the recoil proton generates the prompt signal and the capture of the thermalized neutron provides the delayed signal. The ^{8}He/ ^{9}Li isotopes produced by cosmic muons have substantial beta-neutron decay branching fractions, 16% for ^{8}He and 49.5% for ^{9}Li. The beta energy of the beta-neutron cascade overlaps the positron signal of neutrino events, simulating the prompt signal, and the neutron emission forms the delayed signal. Fast neutrons and ^{8}He/ ^{9}Li isotopes create correlated backgrounds since both the prompt and delayed signals are from the same single parent muon. Some neutrons produced by cosmic muons are captured in the detector without proton recoil energy. A single neutron capture signal has some probability to fall accidentally within the time window of a preceding signal due to natural radioactivity in the detector, producing an accidental background. In this case, the prompt and delayed signals are from different sources, forming an uncorrelated background.

All three major backgrounds are related to cosmic muons. Locating the detectors at sites with adequate overburden is the only way to reduce the muon flux and the associated background to a tolerable level. The overburden requirements for the near and far sites are quite different because the signal rates differ by more than a factor of 10. Supplemented with a good muon identifier outside the detector, we can tag the muons going through or near the detector modules and reject backgrounds efficiently.

In this section, we describe our background studies and our strategies for background management. We conclude that the background-to-signal ratio will be around 0.5% at the near sites and around 0.2% at the far site, and that the major sources of background can be quantitatively studied *in-situ*.

3.4.1 Cosmic muons at underground laboratories

The most effective and reliable approach to minimize the backgrounds in the Daya Bay experiment is to have sufficient amount of overburden over the detectors. The Daya Bay site is particularly attractive because it is located next to a 700-m high mountain. The overburden is a major factor in determining the optimal detector sites. The location of detector sites has been optimized by using a global χ^2 analysis described in section 3.5.1.

Detailed simulation of the cosmogenic background requires accurate information of the mountain profile and rock composition. Fig. 3.3 shows the mountain profile converted from a digitized 1:5000 topographic map. The horizontal tunnel and detector sites are designed to be about 10 m below sea level. Several rock samples at different locations of the Daya Bay site were analyzed by two independent groups. The measured rock density ranges from 2.58 to 2.68 g/cm^3. We assume an uniform rock density of 2.60 g/cm^3 in the present background simulation.

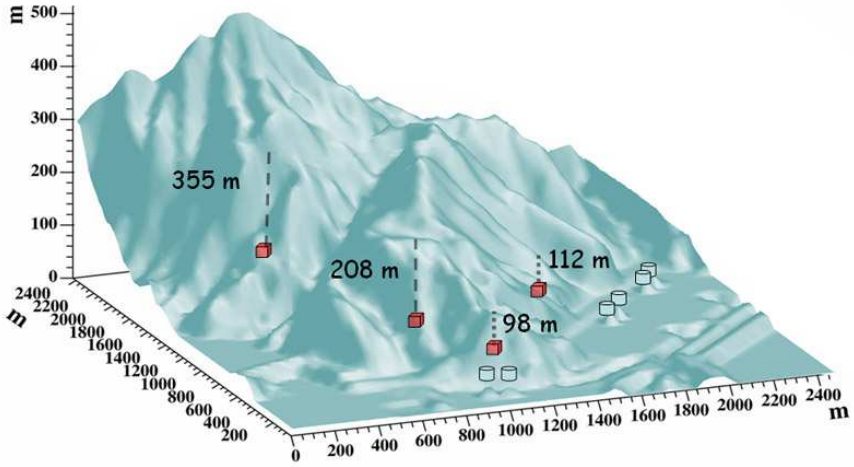

Fig. 3.3. Three dimensional profile of Pai Ya Mountain generated from a 1:5000 topographic map of the Daya Bay area.

The standard Gaisser formula is known to poorly describe the muon flux at large zenith angle and at low energies. This is relevant for the Daya Bay experiment since the overburden at the near sites is only $\sim$ 100 m. We modified the Gaisser formula [2] to describe the muon flux at the sea level. The comparison of the modified formula with data is shown in Fig. 3.4, where the calculations with the standard Gaisser formula are also shown. At muon energies of several tens of GeV, the standard Gaisser formula has large discrepancies with data while the modified formula agrees with data in the whole energy range.

Using the mountain profile data, the cosmic muons are transported from the atmosphere to the underground detector sites using the MUSIC package [1]. Simulation results are shown in Table 3.4 for the optimal detector sites. The muon energy spectra at the detector sites are shown in Fig. 3.5. The four curves from upper to lower corresponds to the Daya Bay near site, the Ling Ao near site, the mid site and the far site, respectively.

	DYB site	LA site	Mid site	Far site
Vertical overburden (m)	98	112	208	355
Muon Flux (Hz/m^2)	1.16	0.73	0.17	0.041
Muon Mean Energy (GeV)	55	60	97	138

Table 3.4. Vertical overburden of the detector sites and the corresponding muon flux and mean energy.

3.4.2 Simulation of neutron backgrounds

The neutron production rates will depend upon the cosmic muon flux and average energy at the detector. However, the neutron backgrounds in the detector also depend on the local detector shielding. The neutrino

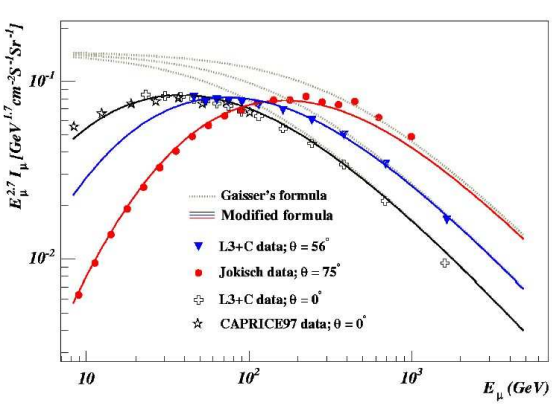

Fig. 3.4. Comparison of the modified formula (solid lines) with data. Calculations with the standard Gaisser's formula are shown in dashed lines. The data are taken from Ref. [4,5].

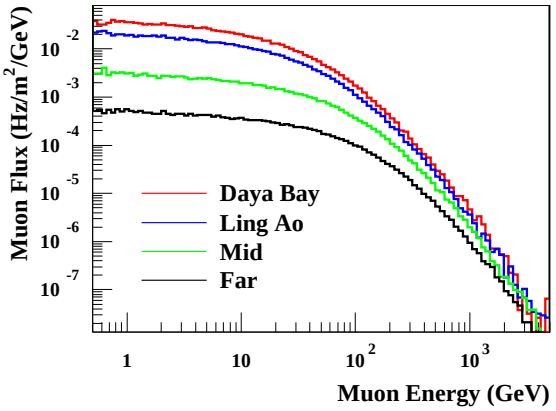

Fig. 3.5. Muon flux as a function of the energy of the surviving muons. The four curves from upper to lower corresponds to the Daya Bay near site, the Ling Ao near site, the mid site and the far site, respectively.

detectors will be shielded by at least 2 meters of water. The veto water will be used as a Cerenkov detector to detect muons. Thus neutrons produced by muons in the detector module or the water shield will be identified by the muon signal in the water veto detector. In addition, neutrons created by muons in the surrounding rock will be effectively attenuated by the 2 m water shield. Together with another muon tracker outside the veto water, the combined muon tag efficiency is designed to be 99.5%, with an uncertainty smaller than 0.25%.

With the detailed muon flux and mean energy at each detector site, the neutron yield, energy spectrum, and angular distribution can be estimated with an empirical formula [6] which has been tested against experimental data whenever available. A full Monte Carlo simulation has been carried out to propagate the primary neutrons produced by muons in the surrounding rocks and the water buffer to the detector. The primary neutrons are associated with their parent muons in the simulation so that we know if they can be tagged by the veto detector. All neutrons produced in the water buffer will be tagged with an efficiency of 99.5%, since their parent muons must pass through the muon systems. About 30% of the neutrons produced in the surrounding rocks arise from muons that miss the veto system ($\equiv$ "untagged"). Neutrons produced in the rocks, however, have to traverse at least 2.5 meters of water to reach a detector module. The neutron background after veto rejection is the sum of the untagged events and 0.5% of the tagged events.

Some energetic neutrons will produce tertiary particles, including neutrons. For those events that have energy deposited in the liquid scintillator, quite a lot of them have a complex time structure due to multiple neutron scattering and captures. These events are split into sub-events in 50 ns time bins. We are interested in two kinds of events. The first kind has two sub-events. The first sub-event has deposited energy in the range of 1 to 8 MeV, followed by a sub-event with deposited energy in the range of 6 to 12 MeV in a time window of 1 to 200μs. These events, called fast neutron events, can mimic the antineutrino signal as correlated backgrounds. The energy spectrum of the prompt signal of the fast neutron events, e.g. at the far site, is shown in Fig. 3.6 up to 50 MeV. The other kind of events has only one sub-event with deposited energy in range of 6 to 12 MeV. These events, when combined with the natural radioactivity events, can provide the delayed signal to form the uncorrelated backgrounds. We call them single neutron events. The neutron simulation results are listed in Table 3.5.

		DYB site	LA site	far site
fast neutron	vetoed	57.8	45.6	3.8
(/day/module)	not vetoed	0.83	0.64	0.08
single neutron	vetoed	1365	1070	94.7
(/day/module)	not vetoed	27.2	21.0	2.1

Table 3.5. Neutron rates in a 20-ton module at the Daya Bay sites. The rows labelled "vetoed" refer to the case where the parent muon track traversed the veto detectors, and thus it could be tagged. Rows labelled "not vetoed" refer to the case where the muon track did not traverse the veto detectors. (numbers to be updated.)

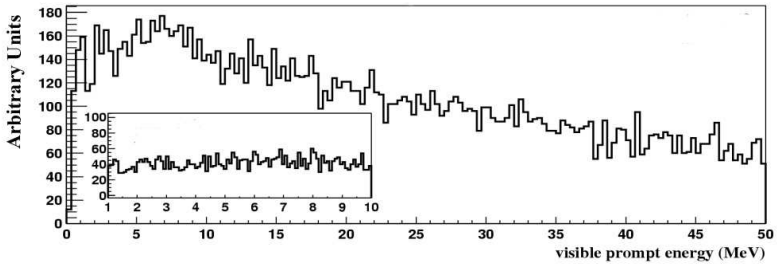

Fig. 3.6. The prompt energy spectrum of fast neutron backgrounds at the Daya Bay far detector. The inset is an expanded view of the spectrum from 1 to 10 MeV.

The rate and energy spectrum of the fast neutron backgrounds can be studied with the tagged sample, which is 200 times larger than the untagged one.

3.4.3 Cosmogenic isotopes

Cosmic muons, even if they are tagged by the muon identifier, can produce radioactive isotopes in the detector scintillator which decay by emitting both a beta and a neutron (β-neutron emission isotopes). Some of these so-called cosmogenic radioactive isotopes live long enough such that their decay cannot be reliably associated with the last vetoed muon. Among them, ^{8}He and ^{9}Li with half-lives of 0.12 s and 0.18 s, respectively, constitute the most serious correlated background sources. The production cross section of these two isotopes has been measured with muons at an energy of 190 GeV at CERN [10]. Their combined cross section is $\sigma(^9\mathrm{Li} + ^8\mathrm{He}) = (2.12 \pm 0.35)\mu\mathrm{barn}$. Since their lifetimes are so close, it is hard to get their individual cross sections. About 16% of ^{8}He and 49.5% of ^{9}Li will decay by β-neutron emission. Using the muon flux and mean energy given in last section at the detector sites and an energy dependence of the cross section, $\sigma_{\mathrm{tot}}(E_\mu) \propto E_\mu^\alpha$, with $\alpha = 0.74$, the ^{8}He+^{9}Li backgrounds are estimated to be

The KamLAND experiment measures this ^{9}Li/ ^{8}He background very well by fitting the time since last muon. The muon rate is 0.3 Hz in the active volume of KamLAND detector. The mean time interval of successive muons is 5 seconds, much longer than the lifetimes of ^{9}Li/ ^{8}He. For the Daya Bay experiment,

	DYB site	LA site	Far site
(^{8}He+^{9}Li)/day/module	3.7	2.5	0.26

Table 3.6. ^{8}He+^{9}Li rates in a 20-ton module at the Daya Bay sites.

the target volume of a 20 ton detector module has a cross section around 10 m^2, thus the muon rate is around 10 Hz at the near sites, resulting in a mean time interval of successive muons shorter than the lifetimes of ^{9}Li/^{8}He. With a modified fitting algorithm, we find that it is still feasible to measure the isotope background *in-situ*.

From the decay time and β-energy spectra fit, the contribution of ^{8}He relative to that of ^{9}Li was determined by KamLAND to be less than 15% at 90% confidence level [11]. Furthermore, the ^{8}He contribution can be identified by tagging the double cascade $^8\text{He} \rightarrow ^8\text{Li} \rightarrow ^8\text{Be}$. So we assume that all isotope backgrounds are ^{9}Li. They can be determined with a maximum likelihood fitting even at 10 Hz muon rate, by taking all contributions from the preceding muons into account. The resolution of the background-to-signal ratio can be determined to be [12]

$$\sigma_b = \frac{1}{\sqrt{N}} \cdot \sqrt{(1+\tau R_\mu)^2 - 1}\,, \tag{25}$$

where N is the total number of neutrino candidates, τ is the lifetime of ^{9}Li, and R_μ is the muon rate in the target volume of detector. The resolution is insensitive to the ^{9}Li level since the statistical fluctuation of neutrino events dominates the uncertainty. The background-to-signal ratio of ^{9}Li background can be measured to $\sim 0.3\%$ with two 20-ton modules at the near sites of the Daya Bay experiment and $\sim 0.1\%$ at the far site with four 20-ton modules, with the data sample of three years of running. The fitting uses time information only. Inclusion of energy and vertex information could further improve the precision.

A Monte Carlo has been carried out to check the fitting algorithm. The background-to-signal ratio is fixed at 1%. The total number of neutrino candidates is 2.5×10^5, corresponding to the far site statistical error, 0.2%. Fig. 3.7 shows the fitting results as a function of muon rate. The data sample generation and fitting were performed 400 times for each point to get the fitting precision. In Fig. 3.8 the fitting precision is compared to the analytic formula Eq. 25 with the same Monte Carlo samples. The Monte Carlo results for minimizing χ^2, the maximum likelihood fit, and the simple analytical estimation are in excellent agreement.

KamLAND also found that most (perhaps all) ^{8}He/ ^{9}Li background are produced by showering muons [11]. A 2-second veto of the whole detector is applied at KamLAND to reject these backgrounds. Roughly 3% of cosmic muons shower in the detector. It is not feasible for Daya Bay to apply a 2-second veto since the dead time of the near detector would be more than 50%. However, if the Daya Bay detector is vetoed for 0.5 s after a showering muon, about 85% isotope backgrounds caused by shower muons can be rejected. Approximately 30% of the ^{8}He/ ^{9}Li background will remain: $\sim 15\%$ from non-showering muons and $\sim 15\%$ from showering muons. Although additional errors may be introduced due to the uncertainties in the relative contributions from showering and non-showering muons and the uncertainties arising from the additional cuts (e.g., increased dead time), this rejection method can cross check the fitting method and firmly determine the background-to-signal ratio to 0.3% at the near sites and to 0.1% at the far site.

3.4.4 Radioactivity

Natural radioactivity and the single neutron events induced by cosmic muons may occur within a given time window accidentally to form an uncorrelated background. The coincidence rate is given by $R_\gamma R_n \tau$, where R_γ is the rate of natural radioactivity events, R_n is the rate of spallation neutron, and τ is the length of the time window. With the single neutron event rate given in previous section, the radioactivity should be controlled to 50 Hz to limit the accidental backgrounds $< 0.1\%$. The accidental backgrounds can be well determined *in-situ* by measurement of the individual single rates from radioactivity and the single neutrons. The energy spectrum can be also well determined.

Past experiments suppressed uncorrelated backgrounds with a combination of carefully selected construction materials, self-shielding, and absorbers with large neutron capture cross section. However, additional care is necessary to lower the detector energy threshold much below 1 MeV. A higher threshold will

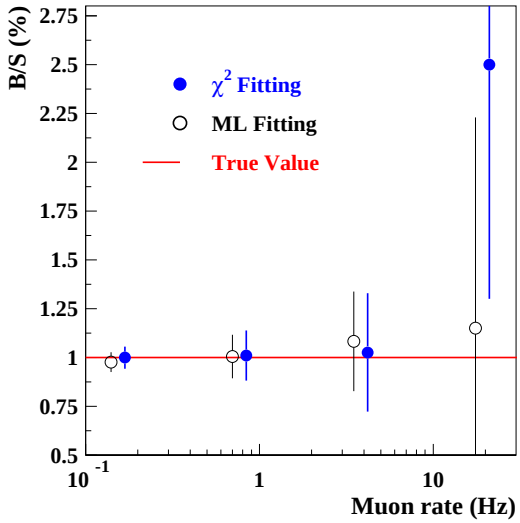

Fig. 3.7. Fitting results as a function of the muon rate. The error bars show the precision of the fitting. The χ^2 fitting uses the same muon rate as ML fitting but shown on the right of it.

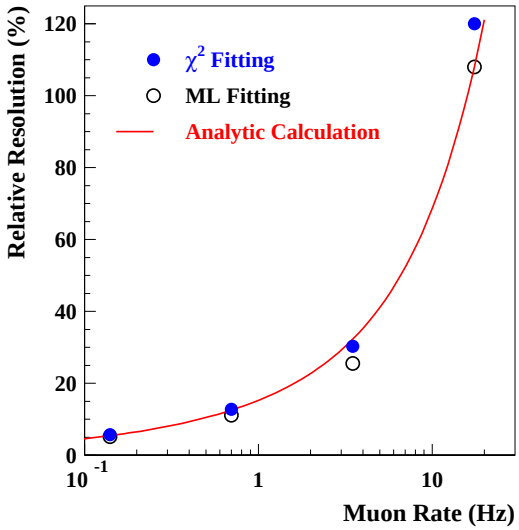

Fig. 3.8. The fitting precision as a function of the muon rate, comparing with the analytic estimation of Eq. 25. The y-axis shows the relative resolution of the background-to-signal ratio.

introduce a systematic error in the efficiency of detecting the positron. In the following, the singles rate is the radioactivity of > 1 MeV visible energy in detector.

Radioactive background can come from a variety of sources:

- U/Th/K in the rocks around the detector hall.
- U/Th/K in the veto water.
- ^{60}Co in the detector vessel and other supporting structures.
- U/Th/K in the PMT glass.
- U/Th/K in the scintillator.
- U/Th/K in materials used in the detector.
- Dust and other impurities
- Radon in air.
- Cosmic rays.

The radioactivity of the rock samples from the Daya Bay site have been measured by several independent groups. The concentration is ~ 10 ppm for ^{238}U, ~ 30 ppm for ^{232}Th, and ~ 5 ppm for ^{40}K. The rock radioactivity has been studied with Monte Carlo. With the shielding of 2-meter veto water and 45 cm oil buffer, there are 5 Hz, 20 Hz, and 2 Hz singles rate of visible energy greater than 1 MeV at each center detector module, for U/Th/K respectively. The total rate is ~ 27 Hz.

The geological environment and rock composition are very similar for Hong Kong and Daya Bay. The spectrum of the natural radioactivity of the rocks in the Aberdeen Tunnel in Hong Kong is shown in Fig. 3.9.

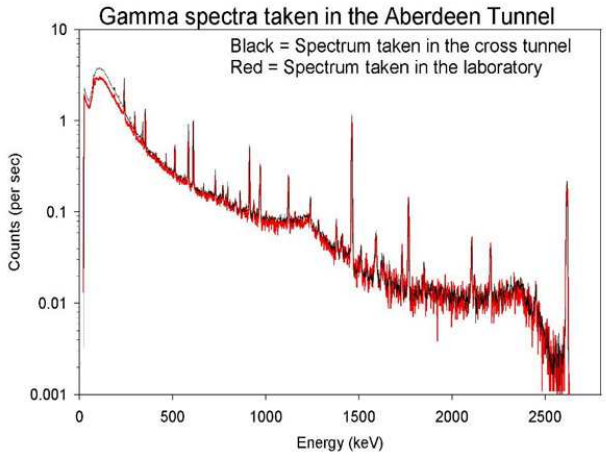

Fig. 3.9. Spectrum of natural radioactivity measured with a Ge crystal in the Hong Kong Aberdeen Tunnel.

The veto water will be circulated and purified to achieve enough attenuation length for water Cerenkov light as well as low radioactivity. KamLAND veto water has 1 ppb ^{238}U, 1 ppb ^{232}Th, and also 1 ppb ^{40}K. Assuming the same concentration, the veto water will contribute 1.8 Hz, 0.4 Hz, and 6.3 Hz single rates from U/Th/K, respectively.

The ^{60}Co in stainless steel varies from batch to batch and should be measured before use as detector material, such as the outer vessel. Conservatively, assuming 1 pCi/kg ^{60}Co in the outer vessel, the single rates will be $\sim$ 6 Hz.

A potential PMT candidate is the Hamamatsu R5912 with low radioactivity glass. The concentrations of ^{238}U and ^{232}Th are both less than 40 ppb in the glass, and that of ^{40}K is 25 ppb. The Monte Carlo study shows that the single rate is 2.2 Hz, 1 Hz, 4.5 Hz for U/Th/K, respectively, with 20 cm oil buffer from the PMT surface to the liquid scintillator. The total rate from the PMT glass is 7.7 Hz.

Following the design experience of Borexino and Chooz, backgrounds from impurities in the detector materials can be reduced to the required levels. The U/Th/K concentration of $10^{-12}g/g$ in liquid scintillator will contribute only 0.8 Hz of background in a 20 ton module.

Radon is one of the radioactive daughters of ^{238}U, which can increase the background rate of the experiment. The Radon concentration in the experimental halls can be kept to an acceptable level by ventilation with fresh air from outside. Since the neutrino detector modules are immersed in 2-meter thick water buffer, it is expected that the radon contribution can be safely ignored for the water pool design.

The β decay of long lived radioactive isotopes produced by cosmic muons in the scintillator will contribute a couple of Hz at the near detector, and less than 0.1 Hz at the far detector. The rate of accidental coincidence induced by muon decay or muon capture is less than the muon rate. So they can be ignored too.

3.4.5 Background subtraction error

There are other sources of backgrounds, such as cosmogenic nuclei, stopped-muon decay, and muon capture. While they are important for a shallow site, our study shows that they can be safely ignored at Daya Bay.

Assuming 99.5% muon veto efficiency, the three major backgrounds are summarized below while the other sources are negligible. In our sensitivity study, the errors were taken to be 100% for the accidental and fast neutron backgrounds. The ^{8}He/ ^{9}Li background can be measured to an uncertainty of 0.3% and 0.1% at the near and far sites, respectively.

	DYB site	LA site	far site
Antineutrino rate (/day/module)	930	760	90
Natural radiation (Hz)	$<$50	$<$50	$<$50
Single neutron (/day/module)	34	26	2.6
Accidental/Signal	$<$0.05%	$<$0.05%	$<$0.05%
Fast neutron/Signal	0.14%	0.1%	0.1%
^{8}He^{9}Li/Signal	0.3%	0.2%	0.2%

Table 3.7. Summary of backgrounds. A neutron detection efficiency of 78% has been applied to the antineutrino and single-neutron rates.

The rates and energy spectra of all three major backgrounds can be measured *in-situ*. Thus the backgrounds at the Daya Bay experiment are well controlled. The simulated energy spectra of backgrounds are shown in Fig. 3.4.5. The background-to-signal ratios are taken at the far site. The oscillation signal is the difference of the expected neutrino signal without oscillation and the "observed" signal with oscillation if $\sin^2 2\theta_{13} = 0.01$.

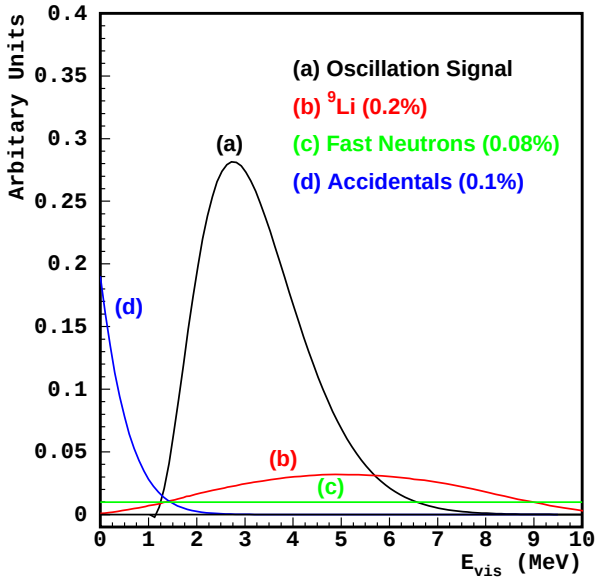

Fig. 3.10. Spectra of three major backgrounds for the Daya Bay experiment and their size relative to the oscillation signal.

3.5 Sensitivity

3.5.1 Global χ^2 analysis

If θ_{13} is non-zero, a rate deficit will be present at the far detector due to oscillation. At the same time, the energy spectra of neutrino events at the near and far detectors will be different because neutrinos of different energies oscillate at different frequencies. Both rate deficit and spectral distortion of neutrino signal will be explored in the final analysis to obtain maximum sensitivity. When the neutrino event statistics is low, say $<$ 400 ton·GW·y, the sensitivity is dominated by the rate deficit. For luminosities higher than 8000 ton·GW·y, the sensitivity is dominated by the spectral distortion [30]. The Daya Bay experiment will have $\sim$ 3000 ton·GW·y exposure in three years, where both rate deficit and shape distortion will be important to the analysis.

Many systematic errors will contribute to the final sensitivity of the Daya Bay experiment, and many of the errors are correlated, which must be taken into account. A rigorous analysis of systematic errors can be done by constructing a χ^2 function with pull terms, where the error correlations can be introduced naturally [28–31]:

$$\begin{aligned}\chi^2 &= \min_{\gamma} \sum_{A=1}^{3} \sum_{i=1}^{N_{bins}} \frac{\left[M_i^A - T_i^A\left(1+\alpha_c+\sum_r \omega_r^A \alpha_r + \beta_i + \varepsilon_D + \varepsilon_d^A\right) - \eta_f^A F_i^A - \eta_n^A N_i^A - \eta_s^A S_i^A\right]^2}{T_i^A + \sigma_{b2b}^2} \\ &+ \frac{\alpha_c^2}{\sigma_c^2} + \sum_r \frac{\alpha_r^2}{\sigma_r^2} + \sum_{i=1}^{N_{bins}} \frac{\beta_i^2}{\sigma_{\rm shp}^2} + \frac{\varepsilon_D^2}{\sigma_D^2} + \sum_{A=1}^{3}\left[\left(\frac{\varepsilon_d^A}{\sigma_d}\right)^2 + \left(\frac{\eta_f^A}{\sigma_f^A}\right)^2 + \left(\frac{\eta_n^A}{\sigma_n^A}\right)^2 + \left(\frac{\eta_s^A}{\sigma_s^A}\right)^2\right], \qquad (26)\end{aligned}$$

where A sums over detectors, i sums over energy bins, and γ denotes the set of minimization parameters, $\gamma = \{\alpha_c, \alpha_r, \beta_i, \varepsilon_D, \varepsilon_d^A, \eta_f^A, \eta_n^A, \eta_s^A\}$. The γ_s are used to introduce different sources of systematic errors. The standard deviations of the corresponding parameters are $\{\sigma_c, \sigma_r, \sigma_{\rm shp}, \sigma_D, \sigma_d, \sigma_f^A, \sigma_n^A, \sigma_s^A\}$. For each energy bin, there is a statistical error T_i^A and a bin-to-bin systematic error σ_{b2b}. For each point in the oscillation space, the χ^2 function has to be minimized with respect to the parameter γ_s.

Assuming each error can be approximated by a Gaussian, this form of χ^2 can be proven to be strictly equivalent to the more familiar covariance matrix form $\chi^2 = (M-T)^T V^{-1}(M-T)$, where V is the covariance matrix of $(M-T)$ with systematic errors included properly [28]. The systematic errors are described one by one in the following.

- Reactor-related correlated error $\sigma_c \approx 2\%$. This fully correlated error will be cancelled by the near-far relative measurement and has almost no impact on the sensitivity.

- Reactor-related uncorrelated error $\sigma_r \approx 2\%$. After minimization, it contributes $\sim$ 0.1% to the normalization of neutrino rate, as described in sec. 2.1.

- Shape error $\sigma_{\rm shp} \approx 2\%$: Shape error is the uncertainty on neutrino energy spectra calculated from reactor information. This error is uncorrelated between different energy bins but correlated between different detectors. Since we have enough statistics at near detector to measure neutrino energy spectrum to much better than 2%, in addition to this calculation, it has little impact for Daya Bay sensitivity.

- Detector-related correlated error $\sigma_D \approx 2\%$. Some detection errors are common to all detectors, such as H/Gd ratio, H/C ratio, neutron capture time on Gd, and edge effect, assuming we use the same batch of liquid scintillator and identical detectors. Based on Chooz's experience, σ_D is (1 - 2)%. Like other fully correlated errors, it has almost no impact on sensitivity.

- Detector-related uncorrelated error $\sigma_d \approx 0.2\%$. Detector-related uncorrelated errors include the mass of active volume, live time, etc., which do not cancel out with near-far measurement. It is estimated

to be 0.36% for a single detector module. However, with detector swapping between the near and far sites, most will cancel too. Those can not cancel are mainly related with the energy scale uncertainties, such as positron and neutron detection efficiency. They are estimated to be $\sim 0.2\%$.

- Background rate error σ_f^A, σ_n^A, and σ_s^A, labelling the rate error of fast neutron, accidental backgrounds, and isotopes. They are listed in table 3.7.

- Bin-to-bin error σ_{b2b}: Bin-to-bin error is systematic error that is uncorrelated between energy bins and uncorrelated between different detector modules. The bin-to-bin errors normally arise from the different energy scale at different energies and uncertainties of background energy spectra during background subtraction. Up to now, the only reactor neutrino experiment that performed spectral analysis with large statistics is Bugey, which has bin-to-bin error of order of 0.5% [25,26]. With better designed detectors and much less background, we should have much smaller bin-to-bin errors than Bugey. The bin-to-bin error can be studied by comparing the spectra of two detector modules at the same site. We will use 0.5% in the sensitivity analysis.

There are other errors not included in the χ^2 function. 1) Due to the energy resolution, the spectra are distorted. However, the energy bins used for sensitivity analysis (~ 30 bins) is $2 \sim 6$ times larger than the energy resolution, and the distortion happens at all detectors in the same way. It has almost no impact on the final sensitivity. 2) Detector energy scale error has significant impact on detection errors (neutron efficiency and positron efficiency). It is taken into account in σ_d. At the same time, an energy scale error will shift the whole spectrum, thus directly impacting the analysis, especially on the best fit values. However, this shift is not a distortion, and cannot mimic oscillation. It has very little impact on sensitivity computations. 3) Current knowledge on θ_{12} and Δm_{21} has around 10% errors. Although the net oscillation effect at Daya Bay baseline is related to θ_{13} only, the subtraction of θ_{12} oscillation effects might bring errors.

We have studied the above three error sources and found none of them having a significant impact on the sensitivity of the Daya Bay experiment. For simplicity, they are ignored in our χ^2 analysis of sensitivity.

3.5.2 θ_{13} sensitivity

Fig. 3.11 shows the sensitivity contours in the $\sin^2 2\theta_{13}$ versus Δm^2_{31} plane for three years of data, using the global χ^2 analysis. The green area covers the 90% confidence region of Δm^2_{31} determined by solar neutrino experiments. Taking a design with four 20-ton modules at the far site and two 20-ton modules at each near site, the statistical error is around 0.2%. The sensitivity of the Daya Bay experiment with this design can achieve the challenging goal of 0.01 with 90% confidence level in almost the whole range of Δm^2_{31}.

Fig. 3.12 shows the sensitivity versus time of data taking. After one year of data taking, $\sin^2 2\theta_{13}$ sensitivity will reach 0.014 (1.4%) at 90% confidence level.

The tunnel of the Daya Bay experiment will have a total length around 3 km. The tunnelling will take ~ 2 years. To accelerate the experiment, the first completed experimental hall, the Daya Bay near hall, can be used for detector commissioning. Furthermore, it is possible to conduct a fast experiment with only two detector sites, the Daya Bay near site and the mid site. For this fast experiment, the "far detector", which is located at the mid hall, is not at the optimal baseline. At the same time, the reactor-related error would be 0.7%, very large compared with that of the full experiment. However, the sensitivity is still much better than the current best limit of $\sin^2 2\theta_{13}$. It is noteworthy that the improvement comes from better background shielding and improved experiment design. The sensitivity of the fast experiment for one year data taking is shown in Fig. 3.11 in dashed line. With one year's data, the sensitivity is around 0.03 for $\Delta m^2 = 2.5 \times 10^{-3}$ eV^2, compared with the current best limit of 0.17 from the Chooz experiment.

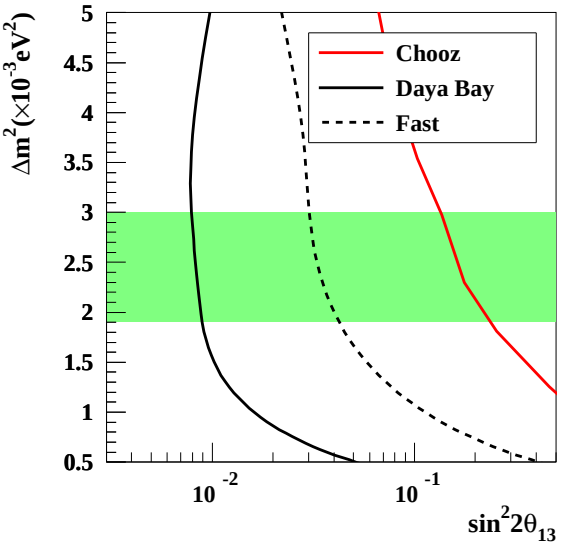

Fig. 3.11. Expected $\sin^2 2\theta_{13}$ sensitivity at 90% C.L. with 3 years of data, as shown in solid black line. The dashed line shows the sensitivity of the fast measurement with the DYB near site and the mid site only. The red line shows current upper limit measured by Chooz.

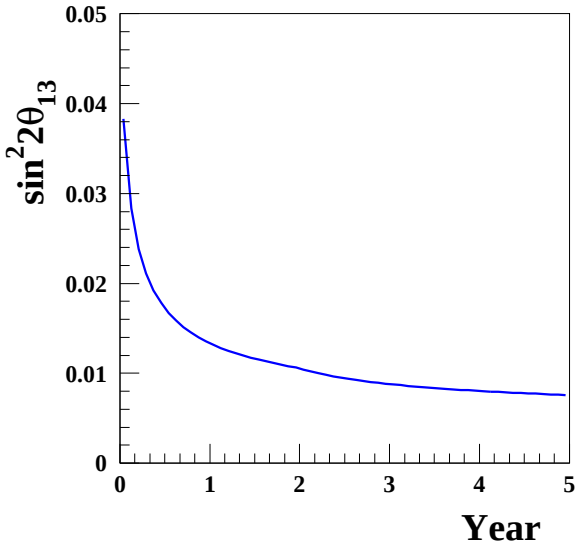

Fig. 3.12. Expected $\sin^2 2\theta_{13}$ sensitivity at 90% C.L. versus year of data taking of the full measurement, with two near sites and one far site. The Δm^2 is taken to be 2.5×10^{-3} eV^2.

3.5.3 Direct measurement of Δm^2_{31}

1. P. Antonioli *et al.*, Astro. Phys. **7**, 357 (1997).
2. T. Gaisser, *Cosmic Rays and Particle Physics*, Cambridge University Press, 1991.
3. Y. Muraki *et al.*, Phys. Rev. D **28**, 40 (1983).
4. J. Kremer *et al.*, Phys. Rev. Lett. **83**, 4241 (1999)
5. H. Jokisch *et al.*, Phys. Rev. D **19**, 1368 (1979).
6. Y. F. Wang *et al.*, Phys. Rev. D **64**, 013012 (2001).
7. M. Apollonio *et al.*, Phys. Lett. **420B**, 397 (1998); Phys. Lett. **466B**, 415 (1999); Euro. Phys. J. C **27**, 331 (2003).
8. M. Ambrosio *et al.*, (The MACRO Collaboration) Phys. Rev. D **52**, 3793 (1995); M. Aglietta *et al.*, (LVD Collaboration) Phys. Rev. D **60**, 112001 (1999); Ch. Berger *et al.*, (Frejus Collaboration) Phys. Rev. D **40**, 2163 (1989).
9. *Atomic Data and Nuclear Data Tables*, Vol. **78**, No. 2 (July, 2001).
10. T. Hagner *et al.*, Astro. Phys. **14**, 33 (2000).
11. T. Araki *et al.*, (KamLAND Collaboration) Phys. Rev. Lett. **94**, 081801 (2005).
12. Liangjian Wen *et al.*, Nucl. Instr. and Meth. A 564 (2006) 471C474.
13. K. S. McKinny, *A Search for Astrophysical Electron Anti-neutrinos at KamLAND*. Ph. D thesis, University of Alabama.
14. Double Chooz LOI: hep-ex/0405032.
15. John A. Rice, *Mathematical Statistics and Data Analysis*, second edition, Wadsworth Publishing Co., Inc., 1993.
16. F. Ashton, H. J. Edwards, and G. N. Kelly, J. Phys. A **4**, 352 (1971).

17. K. Anderson, *et al., White paper report on using nuclear reactors to search for a value of* θ_{13}, hep-ex/0402041.
18. Y. F. Wang *et al.*, Phys. Rev. D **62**, 013012.
19. A. Piepke *et al.*, Nucl. Instr. and Meth. **432A**, 392 (1999); F. Boehm *et al.*, Phys. Rev. D **62**, 072002 (2000).
20. F. Boehm *et al.*, Phys. Rev. D **64**, 112001 (2001); Phys. Rev. D **62**, 072002 (2000); Phys. Rev. D **62**, 092005 (2000).
21. K. Eguchi *et al.*, Phys. Rev. Lett. **90**, 021802 (2003).
22. L. A. Mikaelyan and V. V. Sinev, Phys. Atom. Nucl. **63**, 1002 (2000); L. Mikaelyan, Nucl. Phys. Proc. Suppl. **91**, 120 (2001); L. A. Mikaelyan, Phys. Atom. Nucl. **65**, 1173 (2002).
23. F. Suekane, *The systematic error induced from the baseline differences in Kashiwazaki-Kariwa* $\sin^2 2\theta_{13}$ *experiment: A conceptual description* (unpublished).
24. H. Kwon *et al.,*, Phys. Rev. D **24**, 1097 (1981).
25. Y. Declais *et al.*, Phys. Lett.**B338**, 383 (1994). B. Ackar *et al.*, Nucl. Phys. **B434**, 503 (1995); B. Ackar *et al.*, Phys. Lett. **B374**, 243 (1996).
26. H. Sugiyama and O. Yasuda, hep-ph/0508090.
27. K. Schreckenbach *et al.*, Phys. Lett. **B160**, 325 (1985); A. A. Hahn *et al.*, Phys. Lett. **B218**, 365 (1989).
28. D. Stump *et al.*, Phys. Rev. D **65**, 014012 (2001).
29. Y. Fukuda *et al.*, Phys. Rev. Lett. **81**, 1562 (1998); Y. Ashie *et al.*, hep-ex/0501064.
30. P. Huber, M Lindner, T. Schwetz, and W. Winter, Nucl. Phys. **B665**, 487 (2003); Nucl. Phys. **B645**, 3 (2002).
31. H. Minakata, H. Sugiyama, O. Yasuda, K. Inoue, and F. Suekane, Phys. Rev. D **68**, 033017 (2003); H. Minakata and H. Sugiyama, Phys. Lett. **B580**, 216 (2004).

4 Experimental Site and Laboratory Designs

The Daya Bay site is an ideal place for a reactor θ_{13} experiment. The close-by mountain range provides sufficient overburden to reduce cosmogenic background at the underground experimental halls. Since the Daya Bay nuclear power facility consists of multiple reactor cores, there will be two near detectors to monitor the yield of anti-neutrinos from these cores and one far detector to look for disappearance of anti-neutrinos. It is possible to install another detector about half way between the near and far detectors to provide independent consistency checks.

The proposed experimental site is located at the east side of the Dapeng peninsula, on the west coast of Daya Bay, where the coastline goes from southwest to northeast, see Fig. 1.14. It is in the Dapeng township of the Longgang Administrative District, Shenzhen Municipality, Guangdong Province. Two mega cities, Hong Kong and Shenzhen are nearby. Shenzhen City* is 45 km to the west and Hong Kong is 55 km to the southwest (all measured in a straight line). The geographic location is east longitude 114°33'00" and north latitude 22°36'00". Daya Bay is semi-tropical and the climate is dominated by the south Asia tropical monsoon. It is warm and rainy with frequent rainstorms during the typhoon season in one half of the year, while relatively dry in the other half. Frost is rare.

The Daya Bay Nuclear Power Plant (NPP) is situated to the southwest and the Ling Ao NPP to the northeast along the coastline. Each NPP has two cores that are separated by 88 m. The distance between the centers of the two NPPs is about 1100 m. The thermal power, $W_{\rm th}$, of each core is 2.9 GW. Hence the total thermal power available is $W_{\rm th} = 11.6$ GW. A third NPP, Ling Ao II, is under construction and scheduled to come online by 2010–2011. This new NNP is built roughly along the line extended from Daya Bay to Ling Ao, about 400 m northeast of Ling Ao. The core type is the same as that of the Ling Ao NPP but with slightly higher thermal power. When the Daya Bay—Ling Ao—Ling Ao II NPP are all in operation, the complex can provide a total thermal power of 17.4 GW.

The site is surrounded to the north by a group of hills which slope upward from southwest to northeast. The slopes of the hills vary from 10° to 45°. The ridges roll up and down with smooth round hill tops. Within 2 km of the site the elevation of the hills are generally vary from 185 m to 400 m. The summit, called Pai Ya Shan, is 707 m PRD†. Due to the construction of the Daya Bay and Ling Ao NPPs, the foothills along the coast from the southwest to the northeast have been levelled to a height of 6.6 m to 20 m PRD. Daya Bay experiment laboratories are located inside the mountain north of the Daya Bay and Ling Ao nuclear power station.

There is no railway within a radius of 15 km of the site. The highway from Daya Bay NPP to Dapeng Township (Wang Mu) is of second-class grade and 12 m wide. Dapeng Town is connected to Shenzhen, Hong Kong, and the provincial capital Guangzhou by highways which are either of first-class grade or expressways.

There are two maritime shipping lines near the site in Daya Bay, one on the east side and the other on the west side. Oil tankers to and from Nanhai Petrochemical use the east side. Huizhou Harbor, which is located in Daya Bay is 13 km to the north. Two general-purpose 10,000-ton docks were constructed in 1989. Their functions include transporting passengers, dry goods, construction materials, and petroleum products. The ships using these two docks take the west line. The minimum distance from the west line to the power plant site is about 6 km. Two restricted docks of 3000-ton and 5000-ton capacity, respectively, have been constructed on the power plant site during the construction of the Daya Bay NPP [1].

*Shenzhen is the first Special Economic Zone in China. With a total population of about 7 million, many international corporations have their Asian headquarters there. It is both a key commercial and tourist site in South China.

†PRD is the height measured relative to the mouth of the Zhu Jiang River (Pearl River), the major river in South China.

4.1 General Laboratory Facilities

The laboratory facilities include access tunnels connected to the entrance portal, a construction tunnel for waste rock transfer, a main tunnel connecting all the four underground detector halls, a LS mixing hall (MH), counting rooms, water and electricity supplies, air ventilation, and communication. There is an assembly hall and control room near the entrance portal on surface. The approximate location of the experiment halls and the layout of the tunnels are shown in Fig. 4.1. All experimental halls are located at similar elevations, approximately −20 m PRD.

Fig. 4.1. Layout of the Daya Bay—Ling Ao cores, the future Ling Ao II cores (also known as Ling Dong), and possible experiment halls. The entrance portal is shown on the left-bottom. 5 experiment halls marked as #1 (Daya Bay near hall), #2 (Ling Ao near hall), #3 (far hall), #4 (mid hall), #5 (LS mixing hall). The green line represents the access tunnel, the blue lines represent the main tunnels and the pink line represents the construction tunnel. The total tunnel length is about 2700 m

4.1.1 Tunnels

A sketch of the layout of the tunnels is shown in Fig. 4.2. There are three branches, which are represented by line{3-7-4-5}, line{4-8-Ling Ao near} and line{5-far site}, form the horizontal main tunnel extending from a junction near the mid hall to the near and far underground detector halls. The lines marked as A, B, C, D and E are for the geophysical survey. Line E, which is a dashed line on the top of figure across the far site, is the geophysical survey line investigated if the far site needs to be pushed further from the cores as a result of future optimizations. Line{1-2-3} is the access tunnel with a length of 292 m. Lines B and C are from the survey for the design of the construction tunnel (which may have different options for

cost optimization).

Figure 4.1 shows the entrance portal of the access tunnel behind the on-site hospital and to the west of the Daya Bay near site. From the portal to the Daya Bay near site is a downward slope with a grade of less than 10%. A sloped access tunnel will allow the underground facilities to be located deeper with more overburden.

The access and main tunnels will be able to accommodate vehicles transporting equipment of different size and weight. The grade of the main tunnel will be 0.3% upward from the Daya Bay near hall to the mid hall, and from the mid hall to both the Ling Ao hall and the far hall. The sloped tunnel has two important functions: to ensure a level surface for the movement of the heavy detectors filled with liquid scintillator inside the main tunnel and to channel any water seeping into the tunnel to a collection pool which is located at the lowest point near the Daya Bay near site. The collected water will be pumped to the surface.

The entrance portal of the construction tunnel is near the lower level of the Daya Bay Quarry. The length of this tunnel is 228 m from the entrance to the junction point with the main tunnel if the shortest construction tunnel option is chosen (see Fig. 4.1). During most of the tunnel construction, all the waste rock and dirt is transferred through this tunnel to the outside in order to minimize the interference with the operation of the hospital and speed up the tunnel construction. We expect the access tunnel and the Daya Bay near hall to be finished earlier than the far and Ling Ao halls since it requires much less tunnelling. After the work on this section of tunnel is finished, the Daya Bay near hall will be available for detector installation. Since the construction tunnel is far from the access tunnel and the Daya Bay near hall, we can therefore avoid interference with the rest of the excavation activities and the assembly of detectors in the Daya Bay near site can proceed in parallel. The cross section of the construction tunnel can be smaller than the other tunnels; it is only required to be large enough for rock and dirt transportation. The grade and the length of this construction tunnel will be determined later to optimize the construction cost and schedule.

Excavation will begin from the construction portal. Once it reaches the intersection of the main tunnel, the excavation will proceed in parallel in the directions of the Daya Bay near hall and the mid hall. Once the tunnelling reaches the the mid hall, it will proceed parallel in the direction of the far hall and the Ling Ao hall.

The total length of the tunnel is about 2700 m. The amount of waste to be removed will be about 200000 m^3. About half of the waste will be dumped in the Daya Bay Quarry to provide additional overburden to the Daya near site which is not far away from the Quarry. This requires additional protection slopes and retaining walls. The rest of the waste could be disposed of along with the waste from the construction of the Ling Ao II NPP. Our tunnel waste is about one tenth of the Ling Ao II NPP waste.

4.2 Site Survey

The geological integrity of the Daya Bay site was studied in order to determine its suitability for the construction of the underground experimental halls and the tunnels connecting them. The survey consisted of a set of detailed geological surveys and studies: (1) topographic survey, (2) engineering geological mapping, (3) geophysical exploration, (4) engineering drilling, (5) On-site tests at boreholes and (6) laboratory tests. The site survey has been conducted by the Institute of Geology and Geophysics (IGG) of Chinese Academy of Sciences (CAS). The work started in May 2005 and was completed in June 2006.

4.2.1 Topographic Survey

The topographic survey is essential for determining the position of the tunnels and experimental halls. From the topographic survey the location of the cores relative to the experimental halls is determined, as is the overburden above each of the experimental halls. This measurement of the overburden was input to the optimization of the experimental sensitivity. It is also needed for the portal design and construction. Appropriate maps are constructed out of this measurement. The area surveyed lies to the north of the Nuclear Power Plants (NPPs). The area of the survey extends 2.5 km in the north-south direction and varies from

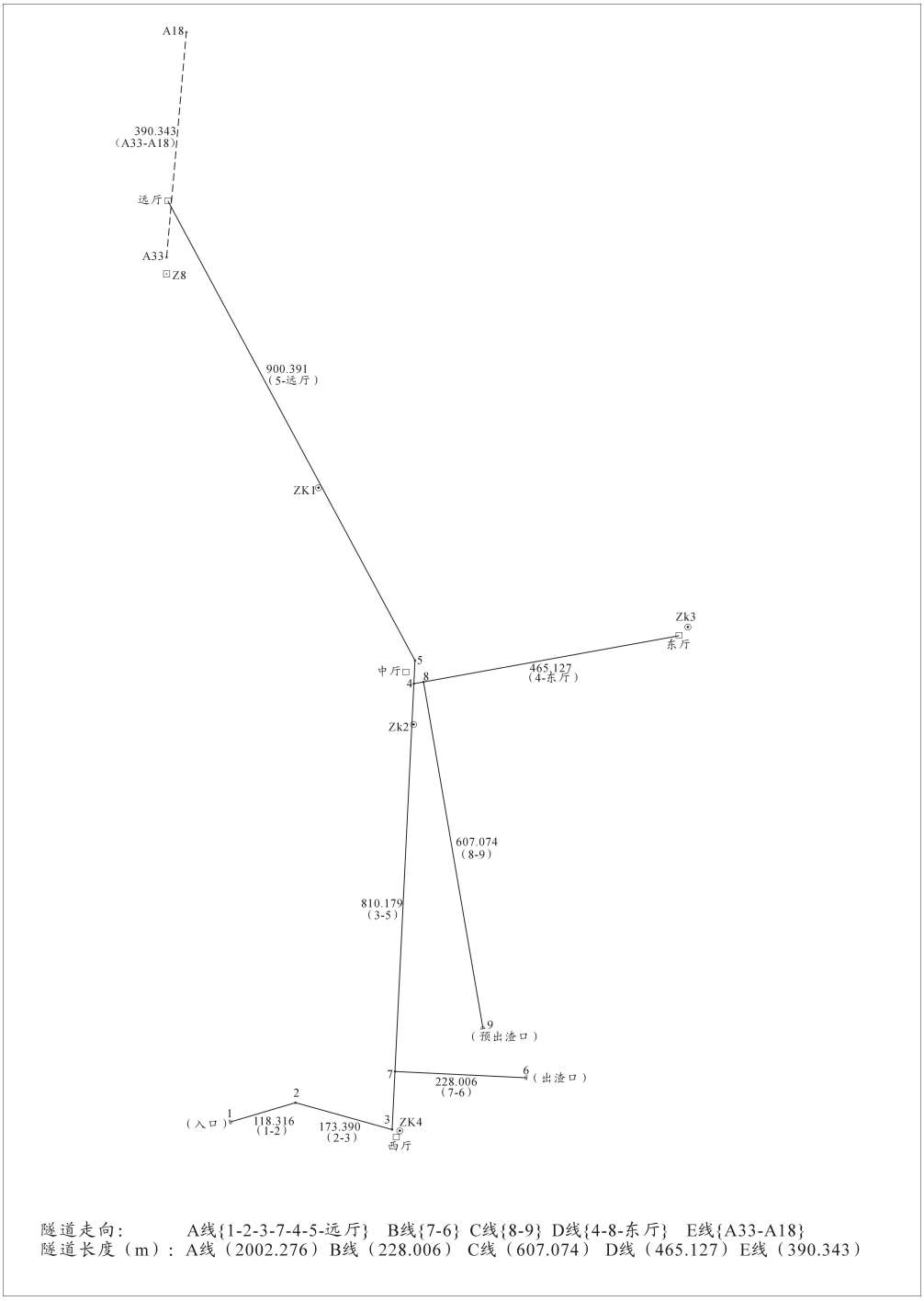

Fig. 4.2. Plan view of the experimental halls and the tunnels, Line A{1-2-3-7-4-5-far site} has a total length of 2002 m; Line B{7-6} has a total length of 228 m; Line C{8-9} has a total length of 607 m; Line D{4-8-Ling Ao near} has a total length of 465 m. Line E is the dashed line on the top across far site. Four bore holes are marked as ZK1, ZK2, ZK3, ZK4 from north to south.

450 m to 1.3 km in the east-west direction as determined by the location of the experimental halls and

tunnels. The total area measured is 1.839 km^2. The results of the survey are plotted at a scale of 1:2000.

The instrument used for the topographic measurement is a LEICA TCA2003 Total Station, with a precision of ± 0.5" in angle and ± 1 mm in distance. Based on four very high standard control points that exist in the area, twenty-six high grade control points and forty-five map baseline points are selected. In total, 7000 points are used to obtain the topographic map. As an example, Fig. 4.3 shows the topographic map around the far site. The altitude difference between adjacent contour lines is one meter. The area around the

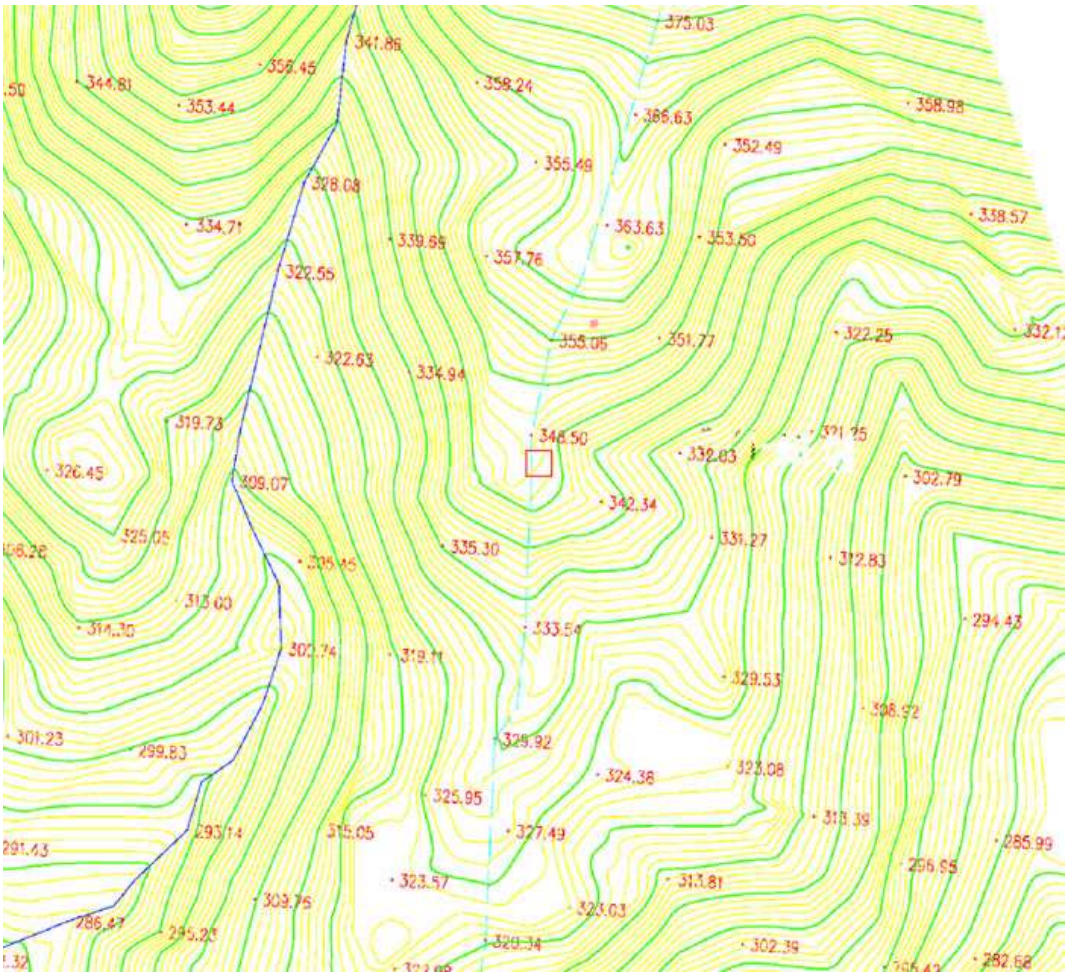

Fig. 4.3. The topography map around the far site. The location of the far detector hall is marked by a red square in the middle of the map.

entrance portal, which is behind the local hospital, and the two possible construction portals are measured at the higher resolution of 1:500. The cross sections along the tunnel line for the access and construction portals are measured at an even higher resolution of 1:200. The positions of the experimental halls, the entrance portal, and the construction portal are marked on the topographic map.

4.2.2 Engineering Geological Mapping

Geological mapping has been conducted in an area extending about 2.5 km in the north-south direction and about 3 km in the east-west direction. From an on-the-spot survey to fill in the geological map of the area, a listing of the geological faults, underground water distribution and contact interphase between different rocks and weathering zones could be deduced. The statistical information on the orientation of

joints is used to deduce the general property of the underground rock, and the determination of the optimal tunnel axes. The survey includes all the areas through which the tunnels will pass and those occupied by the experimental halls. Reconnaissance has been performed along 28 geological routes, of 18.5 km total length. Statistics of 2000 joints and rock mine skeletons are made at 78 spots. Rock mine appraisals are done with 36 sliced samples.

Surface exploration and trenching exposure show that the landforms and terrain are in good condition. There are no karsts, landslides, collapses, mud slides, empty pockets, ground sinking asymmetry, or hot springs that would affect the stability of the site. There are only a few pieces of weathered granite scattered around the region.

The mountain slopes in the experimental area, which vary from 10° to 30°, are stable and the surface consists mostly of lightly effloresced granite. The rock body is comparatively integrated. Although there is copious rainfall which can cause erosion in this coastal area, there is no evidence of large-scale landslide or collapse in the area under survey. However, there are small-scale isolated collapses due to efflorescence of the granite, rolling and displacement of effloresced spheroid rocks.

The engineering geological survey found mainly four types of rocks in this area: (1) hard nubby and eroded but hard nubby mid-fine grained biotite granite, (2) gray white thick bedding conglomerate and gravel-bearing sandstone, (3) siltstone, (4) sandy conglomerate sandstone. Most of the areas are of hard nubby granite, extended close to the far detector site in the north and reaching to the south, east, and west boundaries of the investigated area. There exists a sub-area, measured about 150 m (north-south) by 100 m (east-west), which contains eroded but still hard nubby granites north of a conspicuous valley existing in this region.[‡] Mildly weathered and weathered granites lie on top of the granite layer. Devonian sandstones are located in the north close to the far detector site. There are also scattered sandstones distributed on the top of the granites. The granites are generally very stable, and there exist only three small areas of landslide found around the middle of the above mentioned valley. The total area of the slide is about 20 m^2 and the thickness is about 1 m. Four faults (F2, F6, F7, F8) and two weathering bags have been identified, as shown in Fig. 4.4

The accumulation and distribution of underground water depends generally on the local climate, hydrology, landform, lithology of stratum, and detailed geological structure. In the investigated area of the Daya Bay site, the amount of underground water flux depends, in a complicated way, on the atmospheric precipitation and the underground water seeping that occurs. The sandstone area is rich in underground water seeping in, mainly through joints caused by weathering of crannies that formed in the structure. No circulation is found between the underground water and outside boundary water in this area. Underground water mainly comes from the atmospheric precipitation, and emerges in the low land and is fed into the ocean.

Table 4.1 gives the values of various aspects of the meteorology of the Daya Bay area. A direct comparison shows that the weather elements in Daya Bay are similar to those in the Hong Kong—Shenzhen area.

According to the historical record up to December 31, 1994, there have been 63 earthquakes above magnitude 4.7 on the Richter scale (RS), including aftershocks, within a radius of 320 km of the site.[§] Among the stronger ones, there was one 7.3 RS, one 7.0 RS, and ten 6.0–6.75 RS. There were 51 medium quakes between 4.7 and 5.9 RS. The strongest, 7.3 RS, took place in Nan Ao in 1918 [how far away is this?]. The most recent one in 1969 in Yang Jiang at 6.4 RS. In addition, there have been earthquakes in the southeast [foreland] and one 7.3 RS quake occurred in the Taiwan Strait on Sept. 16, 1994. The epicenters of the quakes were at a depth of roughly 5 to 25 km. These statistics show that the seismic activities in

[‡]The valley extends in the north-east direction from the north-east edge of the reservoir. The valley can be seen in Fig. 4.1, as a dark strip crossing midway along the planned tunnel connecting the mid hall and the far hall.

[§]The seismic activity quoted here is taken from a Ling Ao NPP report [2].

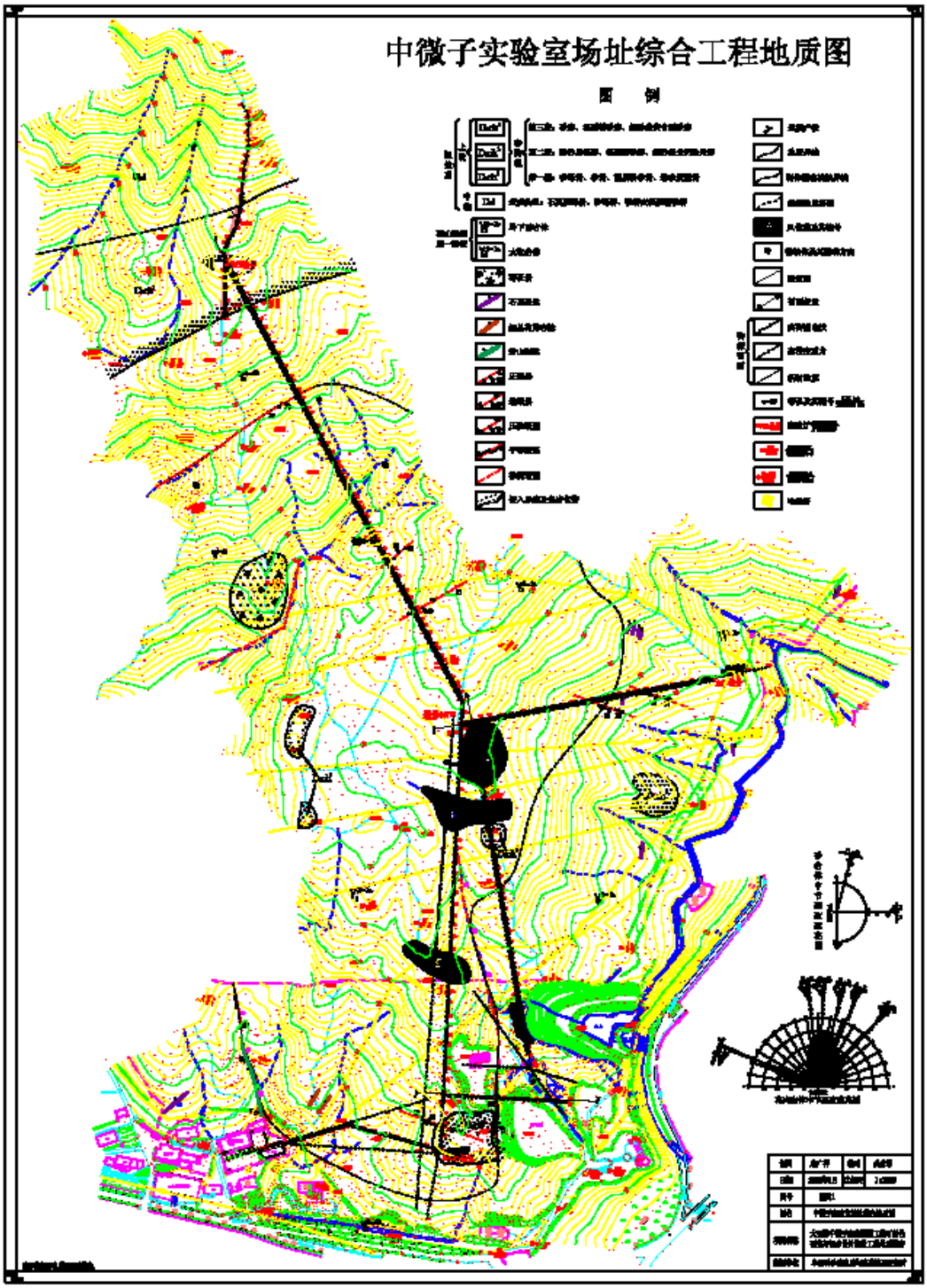

Fig. 4.4. Geological map of the experimental site.

this region originate from shallow sources which lie in the earth crust. The strength of the quakes generally decreases from the ocean shelf to inland.

Within a radius of 25 km of the experimental site, there is no record of earth quakes of $M_s \geq 3.0$ ($M_L \geq$

Meteorological Data	Units	Magnitude
Average air speed	m/s	3.29
Yearly dominant wind direction		E
Average temperature	°C	22.3
Highest temperature	°C	36.9
Lowest temperature	°C	3.7
Average relative humidity	%	79
Average pressure	hPa	1012.0
Average rainfall	mm	1990.8

Table 4.1. Average values from Da Ken station in 1985.

$3.5)$[¶], and there is no record of even weak quakes within 5 km of the site. The distribution of the weak quakes is isolated in time and separated in space from one another, and without any obvious pattern of regularity.

According to the Ling Ao NPP site selection report [3], activity in the seismic belt of the southeast sea has shown a decreasing trend. In the next one hundred years, this region will be in a residual energy-releasing period to be followed by a calm period. It is expected that no earthquake greater than 7 RS will likely occur within a radius of 300 km around the site; the strongest seismic activity will be no more than 6 RS. In conclusion, the experimental site is in a good region above the lithosphere, as was argued when the NPP site was selected.

4.2.3 Geophysical Exploration

Three methods are commonly used in geophysical prospecting: high density electrical resistivity method, high resolution gravity method, and seismic refraction image method using mechanical hammer. The first two methods together with the third as supplement have been used for the Daya Bay geophysical study[‖]. The combination of these three methods reveal the underground structure, including: faults, type of granite, rock mine contact interphase, weathering zone interphase and underground water distribution.

Geophysical exploration revealed another four faults (F1, F3, F4, F5 shown in Fig. 4.4) along the tunnel lines. Figure 4.5 shows the regions of the geophysical survey, including the experimental halls and tunnel sections from the Daya Bay near hall to the mid hall and the far hall. The experimental halls, tunnel sections, faults and weathering bags are marked explicitly in the figure. The electrical resistivity measurements are shown in the middle of the figure, the high resolution density measurements on the bottom, and two sections of seismic refraction measurement in the corresponding part on the top. Because of the complexity and variety of underground structures, the electrical resistivity was measured in boreholes ZK1 and ZK2. The resistivity and density of the rock samples from the boreholes were used for calibration of the resistivity map. Depending on the characteristics of the granite and its geological structure, the electrical resistivity of this area can vary from tens of ohm-m to more than 10k ohm-m. The non-weathered granite has the highest electrical resistivity, whereas the sandstone has medium resistivity due to trapped moisture. The weathered zone, consisting of weathered bursa and faults, has relatively low resistivity.

[¶] M_s is the magnitude of the seismic surface wave and M_L the seismic local magnitude. M_s provides the information of the normal characteristics of an earthquake. There is a complicated location-dependent relationship between M_s and M_L. In Daya Bay $\mathrm{M_s} \geq 3.0$ is equivalent to $\mathrm{M_L} \geq 3.5$.

[‖] In order not to affect the construction work of Ling Ao II, a heavy blaster cannot be used as a source of the seismic refraction measurement, as required for deep underground measurement. Therefore seismic refraction cannot be used as a major tool for the Daya Bay prospecting.

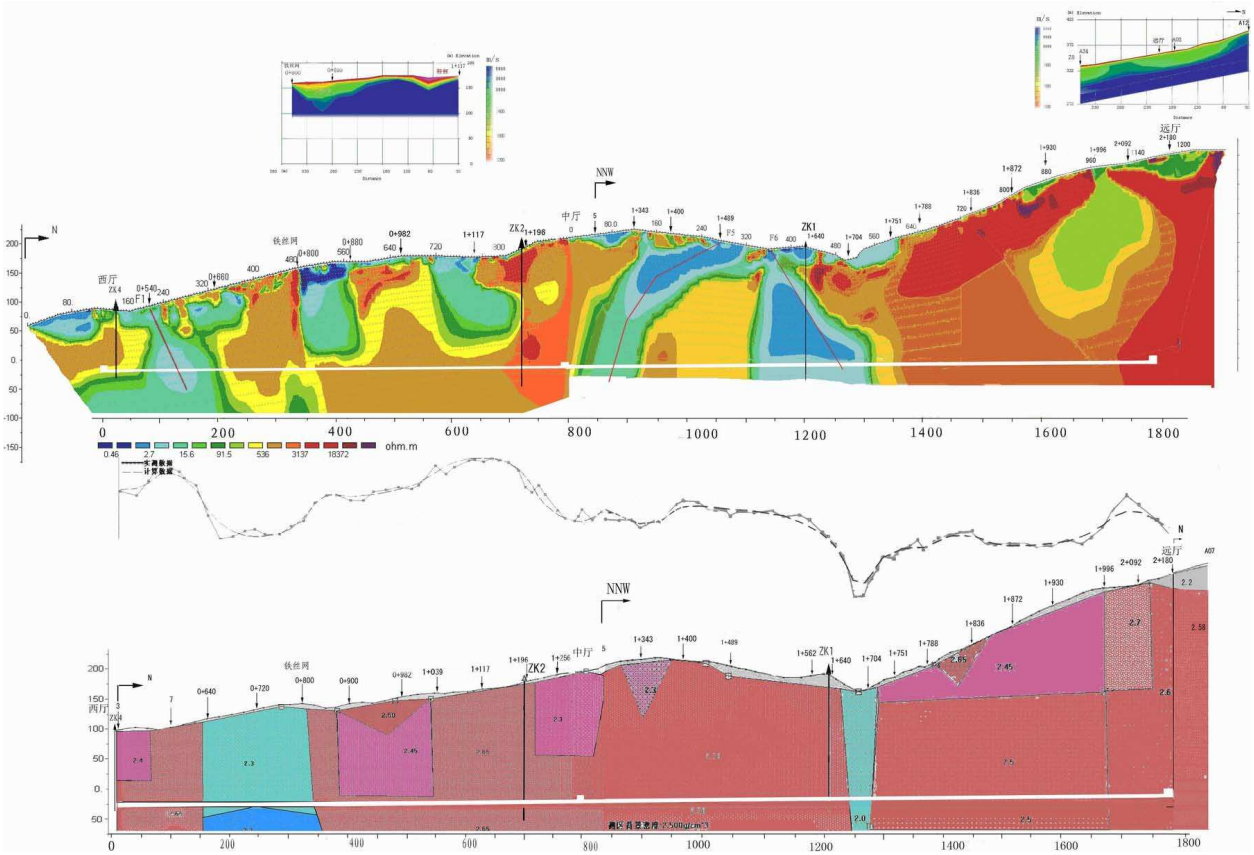

Fig. 4.5. Seismic refraction, electrical resistivity and high resolution density along the cross section from the Daya Bay experimental hall(left end) to the far hall(right end).

4.2.4 Engineering Drilling

Based on the information about faults, zones with relative high density of joints, weathering bags, low resistivity areas revealed from previous geological survey, four borehole positions were determined. The purpose of the boreholes was essentially to prove or exclude the inferences from the previous survey approaches above ground. These four boreholes are labelled as ZK1, ZK2, ZK3, Zk4 from north to south in Fig. 4.2. The depth of the four boreholes are 213.1 m, 210.6 m, 130.3 m, 133.0 m respectively (all to at least the tunnel depth). Figure 4.6 shows sections of rock samples obtained from borehole ZK1. Similar samples are obtained in the other three boreholes. The samples are used for various laboratory tests.

4.2.5 On-site Test at Boreholes

There are many on-site tests performed at the boreholes: (1) High density electrical resistivity measurement in boreholes ZK1 and ZK2. (2) Permeability tests at different time and depth are made in the boreholes during borehole drilling and at completion. The test shows that all measured values of the permeability parameter K are less than $0.0009\ \mathrm{m/d}$. The K values in ZK2, Zk3 are smaller than that in ZK1 and ZK4. Figure. 4.7 shows the water level variation vs time from pouring tests in the four boreholes. (3) Acoustic logging, which is tested at different segments separated by 0.5 m. There are 66, 26, 34, 23 segments tested in ZK1, ZK2, ZK3, ZK4 respectively. The combined results give the velocity of longitudinal wavelength $V_{\mathrm{p}} = 5500\ \mathrm{m/s}$ in the fresh granite. (4) Geo-stress test. (5) Digital video. (6) The radon emanation rate inside the borehole ZK4 was measured up to a depth of 27 m with an electronic radon dosimeter inserted

Fig. 4.6. Rock samples from borehole ZK1.

into the borehole. A rate of (0.16–0.68) $\times 10^{-3}$ Bq m^{-2} s^{-1} was determined at depths of 14–27 m after correction for back diffusion. These values generally agree with the rates (0.13–2.56)) $\times 10^{-3}$ Bq m^{-2} s^{-1} measured directly from the rock samples extracted from the borehole. (7) Measurements of the rock chemical composition. The chemical elements of the rock were measured, among these elements, the amount of radioactive U awas measured to be 10.7, 16.6, 14.5 and 14.2 ppm from the samples in each of the four boreholes, respectively. The Th concentrations were measured to be 25.2, 49.6, 29.4 and 41.9 ppm in each of the borehole respectively. (8) Water chemical analysis. Water samples from the four boreholes and a surface stream have a pH slightly smaller thaqn 7.5, considered neutral. The water hardness is smaller than 42 mg/l which is considered to be very soft. The underground water is thus very weakly corrosive to the structure of steel, but is not corrosive to reinforced concrete.

4.2.6 Laboratory Tests

Laboratory tests performed includes: rock chemical properties, mineral elements, physical and mechanical property tests. The following data are some of the physical properties of slightly weathered or fresh rock

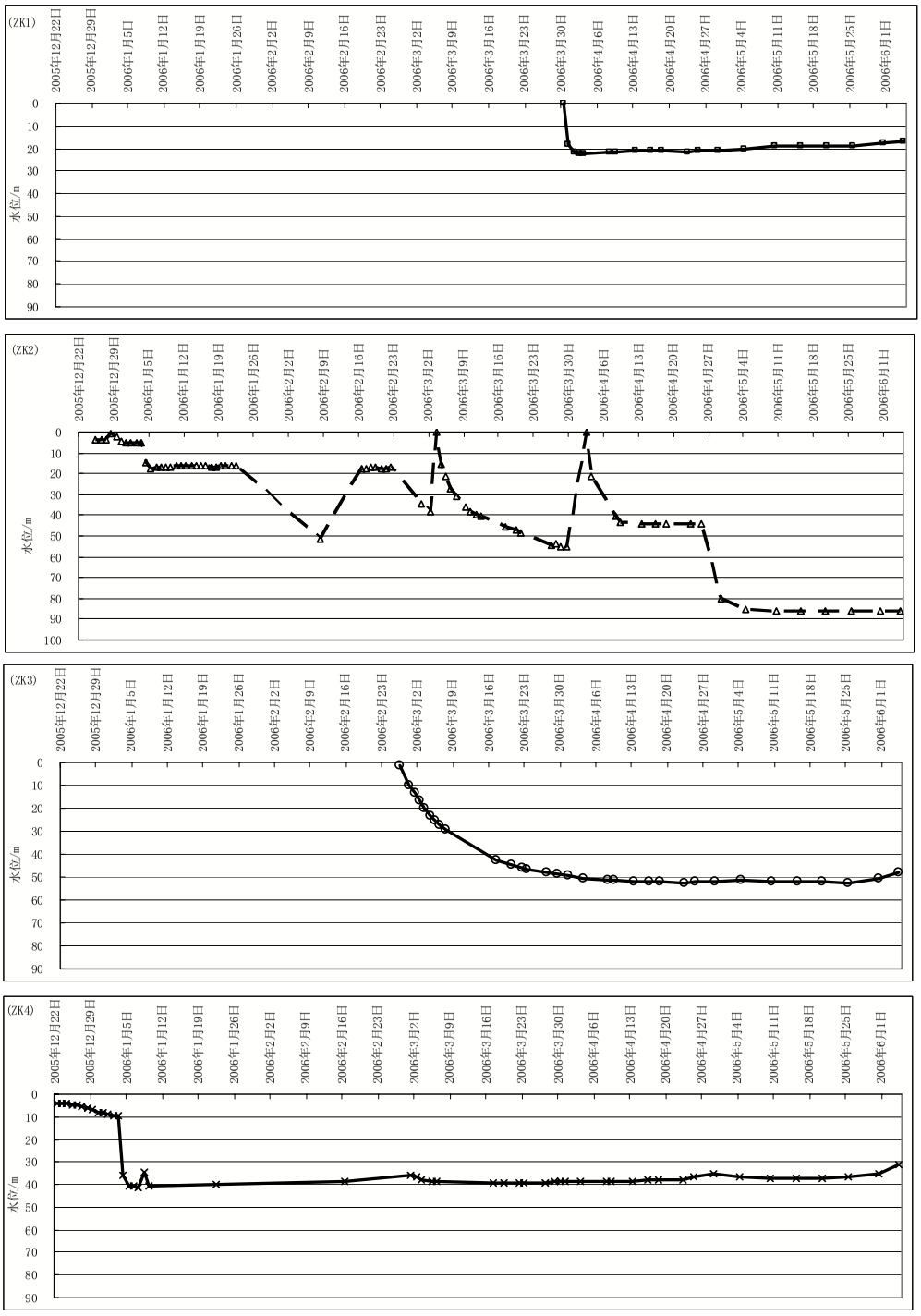

Fig. 4.7. Water level variation vs time period in four boreholes. There is no measurement during holiday in ZK2 in Jan. 2006 and a sudden unknown drop of the water level in April 2006. The unit of the x coordinate is 7 days, the date reads as year/month/day. The unit of y coordinate is the water level in meters down the starting position of borehole.

which are the most comment type of rocks in the tunnel construction:

- Density of milled rock: $2.609 \sim 2.620\ g/cm^3$
- Density of bulk rock: $2.59 \sim 2.60\ g/cm^3$
- Percentage of interstice: $0.765\% \sim 1.495\%$
- Speed of longitudinal wave (V_p) : $4800 \sim 5500\ m/s$
- Pressure resistance strength of a saturated single stalk: $85.92 \sim 131.48\ MPa$
- Pressure resistance strength of a dry single stalk: $87.88 \sim 125.79\ MPa$
- Softening coefficient: $0.924 \sim 1.000$
- Elastic modulus: $32.78 \sim 48.97\ GPa$
- Poisson ratio: $0.163 \sim 0.233$

4.2.7 Survey Summary

Based on the combined analyses of the survey and tests described above, IGG concludes that the geological structure of the proposed experimental site is rather simple, consisting mainly of massive, slightly weathered or fresh blocky granite. There are only few small faults with widths varying from 0.5 m to 2 m, and the affected zone width varies from 10 m to 80 m. There are a total of four weathering bags along the tunnel from the Daya Bay near site to the mid site and on the longer construction tunnel option from the Daya Bay quarry to the mid site. The weathering depth and width are 50–100 m. Just below the surface the granite is mild to mid weathered. This affected zones are well above the tunnel, more than three times tunnel diameter away, so it is not expected that the tunnel will be affected by the weathering bags. Nevertheless, there are joints around this region and some sections of the tunnel will need extra support.

The far hall, at a depth of 350 m is thought to consist of lightly effloresced or fresh granites; the far hall is most likely surrounded by hard granite. The distance to the interphase with devonian sandstone is about 100 m (to the North) from the present analysis estimate.

The rock along the tunnel is lightly effloresced or fresh granite, and mechanical tests found that it is actually hard rock. No circulation is found between the underground water and the outside boundary water in this area, underground water mainly comes from the atmospheric precipitation. Water borehole permeability tests show that underground water circulation is poor and no uniform underground water level at the tunnel depth. At the tunnel depth the stress is 10 MPa, which lies in the normal stress regime. The quality of most of the rock mass varies from grade II to grade III (RQD around 70% which indicates good and excellent rock quality). From the ZK1 and ZK2 stress measurements and structure analysis, the orientation of the main compressive stress is NWW. For the east-west oriented excavation tunnel, this is a favorable condition for tunnel stability. However, for the 810 m segment of the main tunnel from the Daya Bay near hall (#1) to the mid hall (#4) with orientation nearly perpendicular to the maximum stress, the rock stability is not under a favorable condition. However, since the rock quality is good the higher stress is not thought to be a significant problem. There are some tunnel sections, including the access tunnel, where the rock mass quality belongs to grade IV, and some belongs to grade V. Figure 4.8 shows the details of the engineering geological section along Line A. Detailed results from the site survey by IGG can be found in referenes [4]–[12].

4.3 Conceptual Design

We have organized a bid for the conceptual design of the civil construction. The major items of the conceptual design include: (1) the underground experimental halls, the connecting tunnel, access tunnel, and construction tunnel; (2) the infrastructure buildings above ground; (3) the electric power, communication, monitor, ventilation system, water supply, and drainage, safety, blast control, and environmental protection. Two design firms were selected: the Fourth Survey and Design Institute of China Railways (TSY) and the Yellow River Engineering Consulting Co. Ltd. (YREC). TSY has expertise in the design of railway tunnels,

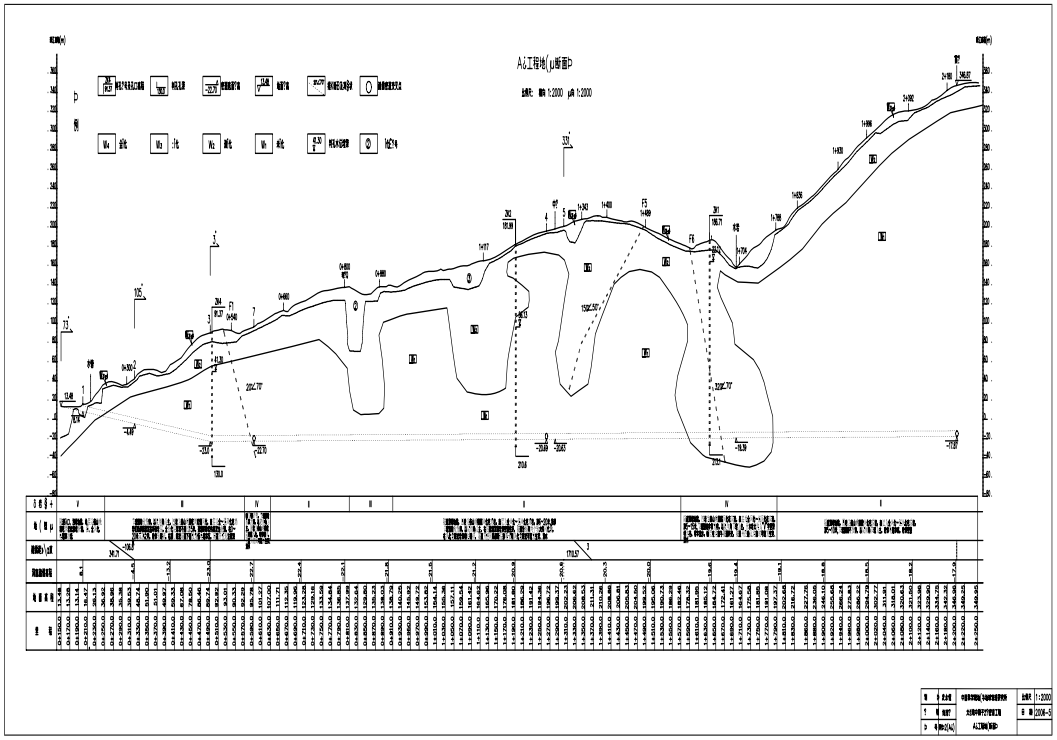

Fig. 4.8. Engineering geological section in line A, the faults, weathering bags and tunnel are shown on the figure. The first curve down from the surface shows the boundary of the weathered granite and the second curve down shows the boundary of the slightly weathered granite. The tunnel passes through one region of slightly weathered granite.

and YREC has a great deal of experience in underground hydroelectric engineering projects. They submitted their designs in the end of July and beginning of August 2006.

4.3.1 Transportation Vehicle and Lifting System for Central Detector

The biggest item to transport in the tunnel is the central detector (CD) module. The CD is a cylinder of 100 T with an outer diameter 5 m and a height of 5 m, with ports extending above. The transportation of the CD determines the cross section of the tunnel and directly affects the total tunnelling construction plan.

The space in the tunnel is limited, so the transportation vehicle for the heavy CD should be easy to operate and steady to move. TSY has investigated two kinds of transportation vehicles: (1) heavy-truck with a lowboy trailer, and (2) truck with a platform on top. The bed of the lowboy trailer is 40 cm off the ground and the loading height is 80 cm. The total length of the truck plus the trailer is more than 20 m long, the turnaround radius is 50 m. This turnaround radius makes it impossible to turn the vehicle around without significantly increase the total length of the tunnel. So TSY recommends the use of a truck with a platform on top and the specifications of this platform vehicle available in two manufacturing companies in Chain are listed in Table 4.2.

An example of the platform truck is shown in Fig. 4.9. It has an easy rotating system with the wheels rotatable in any directions. It has two driving cabs, one in the front and one in the back which makes turning around in the tunnel unnecessary. Its movement is more steady than the lowboy trailer which is very important for transporting the delicate CD modules.

YREC also investigated the above mentioned transporting vehicles with similar specifications. In ad-

Manufacturer	QinHuangDao Heavy Engineering Union Co. Ltd.	WuHan TianJie special transportation Co. Ltd.
Model	TLC100A	TJ100
Full loading(t)	100	100
Out dimension L x W (m)	11.0 x 5.0	11.0 x 5.5
Height of loading (mm)	1700(±300)	1750(±300)
Self weight(t)	28	28
Axes and Wheels/axis	4/8	4/8
Speed	full loading (on falt): 6 km/h	full loading (on flat): 5 km/h
Slope	Vertical 6% Horizontal 4%	Vertical 8% Horizontal 2%
Power	168 kw	235 kw

Table 4.2. Technical parameters of platform trucks.

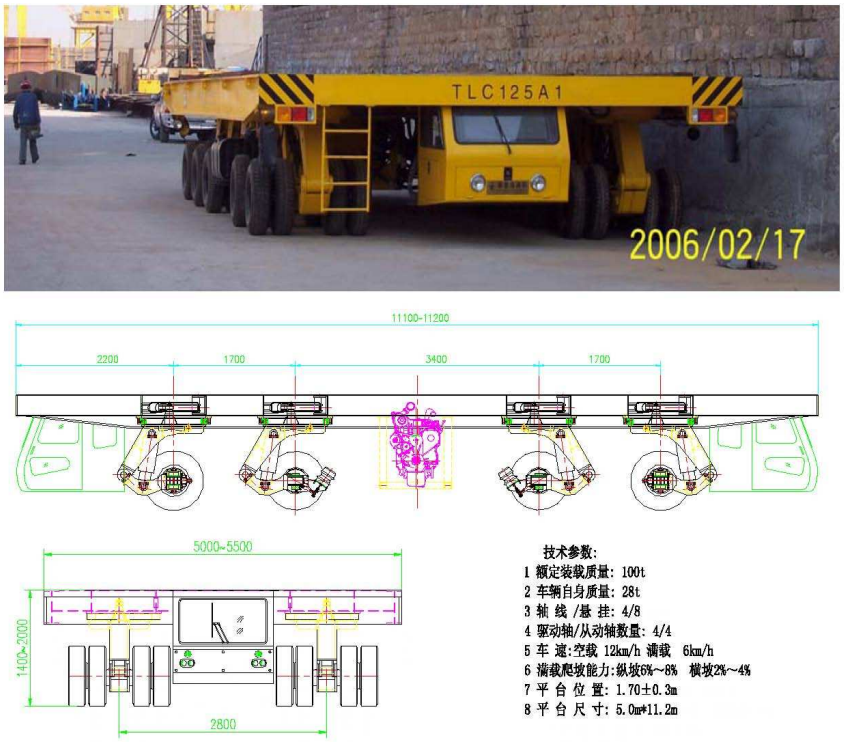

Fig. 4.9. Photo of a platform truck with schematic diagrams of wheel rotations. The specifications written in Chinese on the right-bottom are the same as in Table 4.2

dition, they have investigated an electric railway transportation system which consists of a transport framework, support frame, cable winding, and control desk. However, the loading height is 1 m, and laying the rail is expensive and time consuming. Finally, YREC recommend the use of a semi-trailer with a platform loading, as shown in Fig. 4.10. The total length is 15.8 m and the loading height is 95 cm. Since it is not very long, this semi-trailer will drive forward and backward in the tunnel without turning around. The ventilation speed in the tunnel has to be increased during the transportation of the detector modules to vent the exhaust discharged in the tunnel.

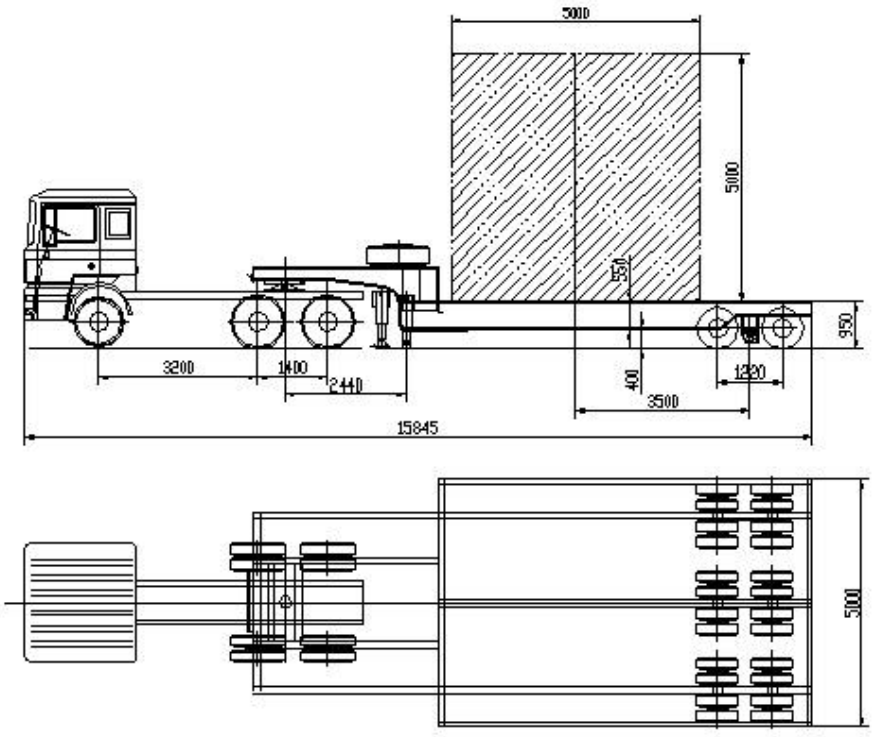

图 6.3-4　　载重 100t 牵引式半挂凹型低平板车

Fig. 4.10. Schematic diagram of a semi-trailer. The dimensions, length, width, and height are in mm.

Further investigation about the transportation vehicle with lower height of the loading platform is needed in order to lower the required height of the tunnel. It is also necessary to find a suitable electric powered vehicle instead of one powered by petroleum.

Lifting systems, mainly for handling the CDs, have been investigated. The lifting system should be low in order to minimize the height of the experimental hall and to gain overburden. Both gantry cranes (suggested by TSY) and bridge style cranes (suggested by YREC) satisfy our requirement. The heights of the experimental halls required to install and lift the CD with these two types of cranes are similar: about 12–13 m. Figures 4.11 and 4.12 show these two kind of cranes. Both cranes have two hooks working during the lifting which will greatly decrease the height of the hall and can be operated more steadily. The rails of the bridge crane are supported on the two side walls of the experiment hall. The finial choice of a crane system needs further studies.

4.3.2 Experimental Hall Layout

The experimental hall layout can not be fixed before we know how to install the CD, how to lay the veto detector on top, and what auxiliary facilities are needed. The two designers presented two sketches which include CD transportation, lifting space, and rooms for auxiliary facilities, see Fig. 4.13 (designed by TSY) and Figure 4.14 (designed by YREC). The auxiliary facilities rooms are at the side of the hall in Fig. 4.14 which may reduce the length of the electronics cables from the detector to the counting room, and other auxiliary facility rooms, which could be arranged parallel to the counting room, are more flexiblly arranged. A side tunnel links the main tunnel with the control room and the other possible rooms.

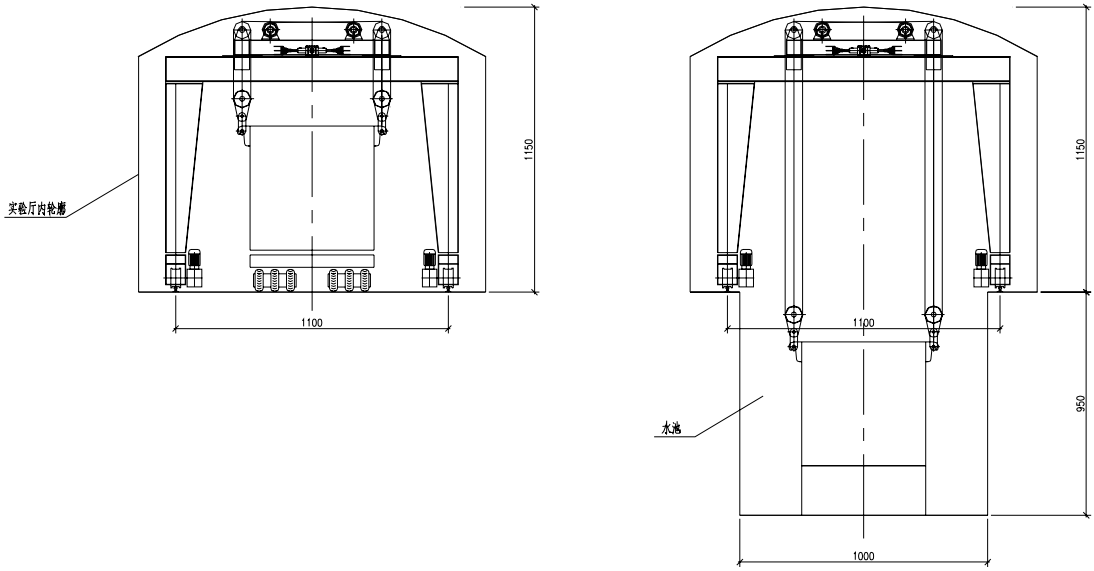

Fig. 4.11. Schematic diagrams of a gantry crane in the experimental hall to lift the central detector (left panel) and lower it into the water pool (right panel).

Fig. 4.12. A photo of a bridge style crane, the rail of the crane is fixed on the wall of the experimental hall.

The longitudinal direction of the Daya Bay (#1) and mid (#4) experimental halls is preferred to be

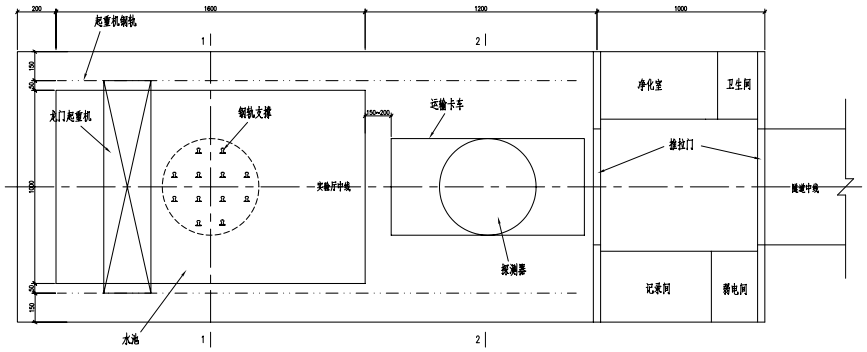

Fig. 4.13. Layout of the experimental hall where the counting room, etc., are laid out in series along the hall as proposed by TSY.

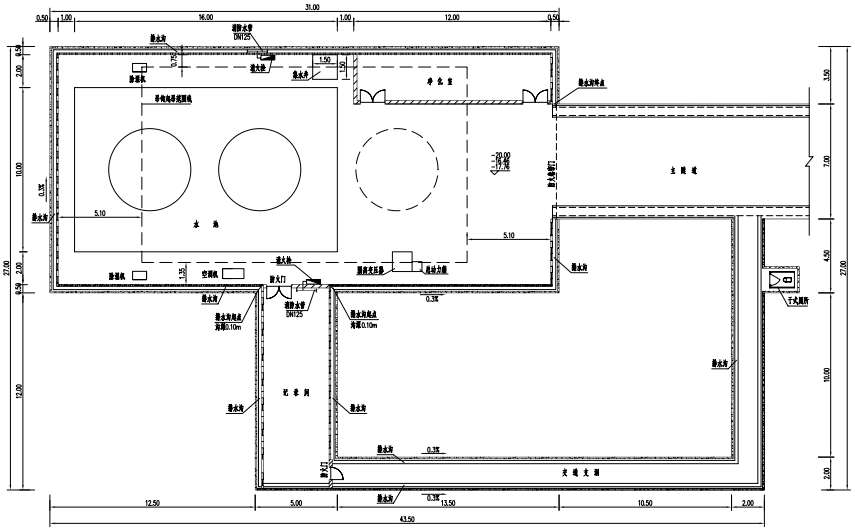

Fig. 4.14. Layout of the experimental hall where the counting room, etc., are along one side of the hall as proposed by YREC.

along the tunnel direction for construction convenience. The Ling Ao near hall (#2) is the only one with its longitudinal direction to be about 90° with the accessing tunnel in order to keep all the halls in the same orientation.

The LS mixing hall (#5) will be decided upon once we settle on the LS mixing and filling procedures. We expect no special questions about the design and construction of this hall. At this stage, we put it near the Daya Bay hall (#1).

4.3.3 Design of Tunnel

According to the size of the selected transportation vehicles, the cross section of the main tunnel will be relatively easy to define:

- Width of the roadway: 5.0 m.
- Width of safety distance to side wall: 1.0 m x 2.

- Width of drainage channel: 0.25 m x 2.
- The total width of the tunnel is: 7.5 m (YREC has 7.0 m because they have a narrower space for safety).
- Height of the transporting vehicle plus height of CD: 6.4 m.
- Duct diameter: 1.5 m.
- Safety distance between detector module to the duct: 0.5 m.
- Total height of the tunnel is: 8.4 m (YREC has 8.5 m)

Figures 4.15 and 4.16 describe the cross sections of the main tunnel. The lining of the tunnel depends

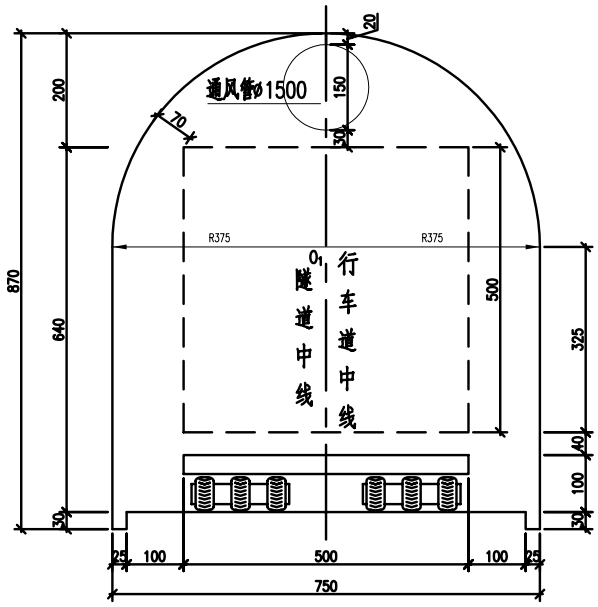

Fig. 4.15. An engineering schematic diagram of the tunnel layout proposed by TSY. The dimensions are in cm.

on the rock quality. Here in the Daya Bay site, rock quality varies from grades I to V, grade I being excellent and grade V poor. According to the site survey, more than 90% of the rock belongs to grade I, II or III which are stable rocks. Some very short section of the tunnel have grade IV rock and the only grade V rock is in the first tens of meters at the main portal. The lining for different quality of rocks are giving by two designers in their report [13] [14].

The access tunnel has the same cross section as the main tunnel to enable transportation of the CD. This tunnel section has a slope of up to 10%. The CD is not yet filled with LS when it is transported down the access tunnel. The length of the tunnel is less than 300 m and modern mining/industrial equipment will have no difficulties in moving on the 9.6% slope of the access tunnel (in the YREC design).

There are two possible design strategies for the construction tunnel. One is to transport the dirt by heavy truck, another one is by tram. In the truck option, the allowed slope is up to 13% (TSY), the width of this tunnel is 5.0 m and height 5.8 m. There will be a passing section in every 80 m along the tunnel for two trucks to cross into the opposite directions. The total length of such a tunnel is 528 m. If a tram is used for dirt transportation, the tunnel can tolerate a much steeper slope, up to 42% ($< 23^\circ$). The tunnel length can be as short as 200 m, the cross section in this case is 4.6 m wide, 4.08 m high. Construction with a tram will allow for a shorter tunnel, therefore saving both time and money. The dirt removal with a tram is

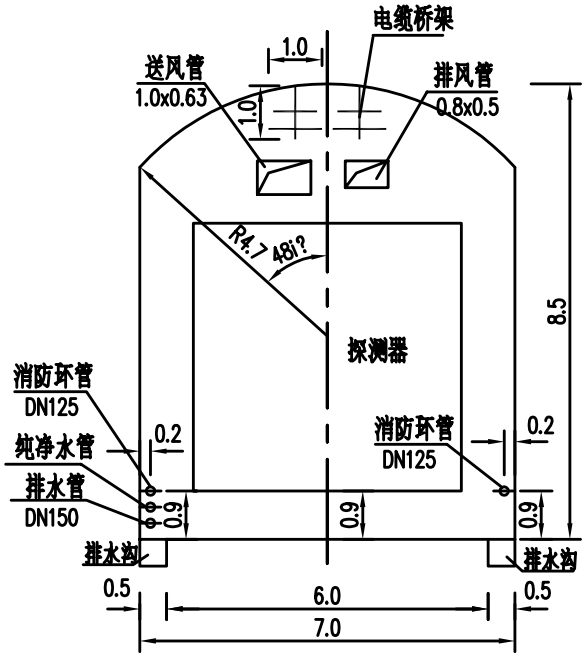

Fig. 4.16. The engineering schematic diagram of the tunnel layout Proposed by YREC.The dimensions are in meter.

more complicated than using heavy trucks, which will take more time and money. Let us note that in the case of a tram, since special tools are needed, the number of construction companies bidding on the tunnel construction contract may be more limited.

A possible layout of the main portal behind the local hospital is shown in Fig. 4.17 (YREC's design).

4.3.4 Other Facilities

Other facilities are also included in the conceptual design reports submitted by TSY [13] and YREC [14]. They include: (1) electricity, (2) ventilation system (3) water supply and drainage, (4) communication, (5) monitoring systems, (6) blast control, and (7) environmental effect evaluations.

4.4 Civil Construction Overview

The final tunnel design and civil construction contractors will be selected via a bidding process. Most likely the final designer and civil construction team will be separated. An oversight agency is needed for the construction. The time needed to complete the final design will be 4–5 months once all of the specifications are laid out. The civil construction will last 1.5–2 years as estimated by the conceptual designers.

The main civil construction work items are listed in Table 4.3.

1. *Report of Preliminary Feasibility Study of Site Selection for the Daya Bay Neutrino Experiment*, prepared by Beijing Institute of Nuclear Energy, September, 2004.
2. *Catalog of Chinese Earthquakes*, Quoted in the *Preliminary Safety Report on Ling Ao Nuclear Power Plant*.
3. *Report of Ling Ao Nuclear Power Plant*.
4. *Report on Geo-technical Survey(Feasibility Study and Conceptual Design)*, Institute of Geology and Geophysics, CAS, May, 2006.

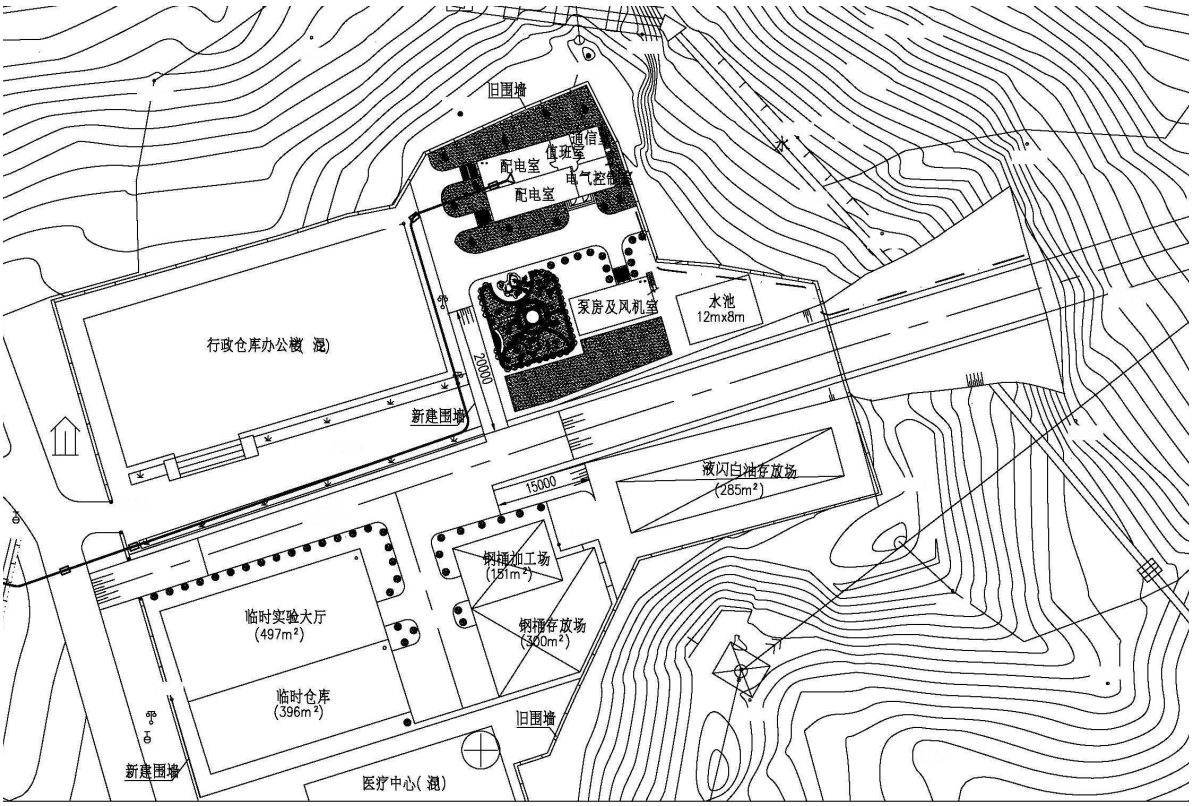

Fig. 4.17. A schematic diagram of the the main portal and the layout of auxiliary buildings.

Construction item	Volume (m^3)
Excavation dirt in open	17,068
Excavation dirt in tunnel	202,745
Concrete	8,740
Eject concrete	7,774

Table 4.3. Table of the main civil construction work items.

5. *Final Report on Topographic Survey of the Neutrino Experimental Site*, Institute of Geology and Geophysics, CAS, June, 2006;
6. *Map obtained from Topographic Survey of the Neutrino Experimental Site*, Institute of Geology and Geophysics, CAS, December, 2005;
7. *Report on Engineering Geology of the Neutrino Experimental Site*, Institute of Geology and Geophysics, CAS, May 6, 2006;
8. *Report on Geophysical Survey of the Neutrino Experimental Site*, Institute of Geology and Geophysics, CAS, May 6, 2006;
9. *Report on Bore Drilling and In-situ Sonic Investigation of the Neutrino Experimental Site*, Institute of Geology and Geophysics, CAS, May, 2006;
10. *Report on Stress-loading in Bore Holes at the neutrino Experimental Site*, Institute of Geology and Geophysics, CAS, April 18, 2006;

11. *Report on Ultra-sonic Imaging in Bore holes at the Neutrino Experimental Site*, Institute of Geology and Geophysics, CAS, May, 2006;
12. *Report on Laboratory Study of the Neutrino Experimental Site*, Institute of Geology and Geophysics, CAS, May 6, 2006.
13. *Feasibility study about Daya Bay neutrino experiment engineering work*, The Fourth Survey and Design Inst. of China Railway, July 2006
14. *Feasibility study about Daya Bay neutrino experiment engineering work*, Yellow River Engineering Consulting Co. Ltd., August 2006

5 Central detectors

5.1 Overview

It is an experimental challenge to determine the value of $\sin^2 2\theta_{13}$ to 0.01 or better, which yields only a tiny oscillation effect corresponding to a small difference in the number of antineutrino events observed at a proper distance with respect to the expectation. To observe such a small effect, the detector must be carefully designed beside the guildlines discussed in Chapter 2, and possible systematic uncertainties discussed in Chapter 3. Following requirements shall be satisfied for designing the detector module and related components:

1. The detector should be homogeneous to minimize edge effects that could lead to systematic uncertainties.

2. The energy threshold should be less than 1.0 MeV to have almost 100% efficiency for positrons.

3. The number of protons in the target liquid scintillator should be well defined and known, implying that the scintillator mass and the proton to carbon ratio should be precisely determined. The target scintillator should come from the same batch for each pair of near-far detectors, and the mixing procedure should be well controlled to ensures the composition of the target is the same.

4. The detector should not be too large; otherwise, it would be difficult to move from one detector site to another for cross check to reduce systematic effects. In addition, up to a certain size, the rate of cosmic-ray muons passing through the detector can be unacceptably high so as to compromise the performance of the detector.

5. The event time should be determined to be better than 25 ns for studying backgrounds.

6. The energy resolution should be better than 15% at 1 MeV in order to reduce systematic uncertainty, which is also important for the study of spectral distortion as a signal of neutrino oscillation.

5.1.1 Module geometry

Previous neutrino experiments usually design their detectors as a ball or an ellipsoid to assure uniform energy response in the entire volume. But this type of detector vessel is expensive and it requires many PMT's for the needed 4π coverage. Two types of alternative detector geometry have been investigated: cubic and cylindrical, as being attractive from the construction point of view. Monte Carlo simulation shows that cylindrical shape, as shown in Fig. 2.3, can deliver a better energy and position resolution while maintain a good uniformity of light response over the volume, similar to that of the ball or ellipsoid. This design is verified by our prototype tests, to be discussed in section 5.7. An optical reflector can be put at the top and bottom of the cylinder, so that PMTs are only arranged at the radial directions of the cylinder to trim the total number of PMT's down by a half.

This design, which allows a tremendous reduction of the detector cost including savings on the PMT readout, steel and acrylic vessels construction, is workable due the following considerations:

1. The event vertex is determined only by the center of gravity of the charge, not relying on the time-of-flight approach, hence reflected light from the top and bottom of the cylinder will not worsen the performance of the detector module. Hit time is measured to a resolution of 0.5 ns for the background study only.

2. The fiducial volume is well defined with a three-layers-structure as to be discussed below, no accurate vertex information is needed.

5.1.2 Target mass

The total target mass at the far site is determined by the requirement for the sensitivity which is shown in Fig. 5.1 as a function of the far detector tonnage. To measure $\sin^2 2\theta_{13}$ to better than 0.01, a total target

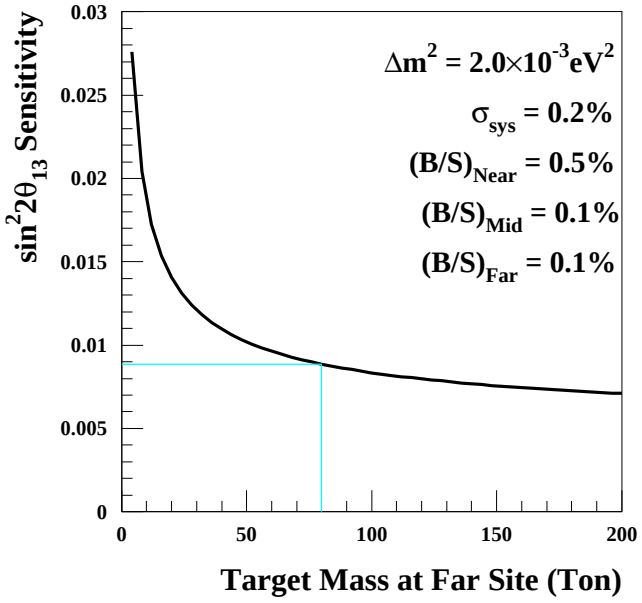

Fig. 5.1. Sensitivity of $\sin^2 2\theta_{13}$ at the90% C.L. as a function of the target mass at the far site.

mass of 80–100 tons is needed, which corresponds to a statistical error of $\sim$0.2% after three years data taking. A larger target mass is not attractive since the sensitivity improves rather slowly when the target mass goes beyond 100 tons. By adopting a multiple-module-scheme as discussed in Chapter 2, two modules are chosen for the near site in order to have a cross check of the module behaviors besides the statistical consideration. For the far detector, at least four modules are needed in order to have sufficient statistics to reach the designed sensitivity while maintaining the number of modules at a manageable level. A detector scheme of 8 identical modules, each with a target mass of 20 tons, is chosen. About 600 to 1200 events per day per module can be obtained at the Daya Bay near site (300–500 m) while about 80 events can be obtained at the far site ($>$1800 m).

5.1.3 Three-zone central detector

A Chooz-type detector with suitable upgrades can in principle fulfill the requirements although completely new concepts are not excluded. The energy threshold of a Chooz-type scintillator detector can be reduced by a three-layer structure as shown in Fig. 5.2. The inner-most layer (region I) is the Gd-loaded liquid scintillator as the antineutrino target. The second layer (region II) is filled with normal liquid scintillator which can contain the energy of all gammas from neutron capture or positron annihilation, while not acting as an antineutrino target since the neutron-capture time is about a factor of ten longer than that in the Gd-loaded scintillator. The outer-most layer (region III) contains mineral oil that shields radiation from the PMT glass from entering the fiducial volume. This buffer will substantially reduce the singles rate and the threshold can thus be lowered to below 1.0 MeV. The three regions are partitioned with transparent acrylic

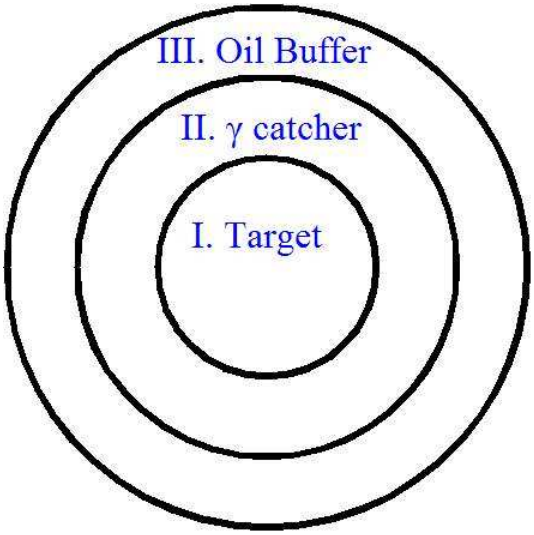

Fig. 5.2. Cross section of a simple detector module showing the three-zone central detector.

tanks so that the target mass contained in region I can be well determined without event vertex reconstruction and position cut.

5.1.4 Gamma catcher

The γ rays produced in the target region by positron annihilation or neutron capture will undergo many collisions with the LS molecules to transfer most of their energy to the liquid scintillator before converting to the visible scintillation light. However, the γ rays can also escape from this target region and cause energy loss from the region. To capture escaped γ rays a layer of regular liquid scintillator surrounding the target zone can be added, thus the energy loss is greatly suppressed. The energy spectrum of the delayed neutron capture signal is shown in Fig. 5.3. It can be clearly seen that there is a long tail on the low energy side, signifying the escaped events. The structure around 8 MeV is due to the coexistence of two major isotopes of gadolinium, ^{155}Gd and ^{157}Gd, which emits several gamma-rays with a total energy of 7.93 and 8.53 MeV, respectively.

To be clearly separated from the natural radiation background, the neutron capture signal has to be above 6 MeV. Therefore, part of the neutron events will be lost, and this causes degradation of the detection efficiency. The detector simulation gives the correlation between the thickness of the middle layer and the neutron detection efficiency, as shown in Fig. 5.4.

The figure shows that with a middle layer thickness of 45 cm and hence the neutron detection efficiency of 92%, a meaningful comparison with the Chooz detector can be made. Chooz has a smaller detector, its γ-catcher thickness is 70 cm, and its neutron source test shows a (94.6$\pm$0.4)% detection efficiency [4]. The error term includes the vertex selection error. According to Chooz, Palo Verde, and KamLAND the error in the energy scale at 6 MeV is better than 1%. Our detector simulation shows that 1% error in energy calibration can cause a 0.2% error in efficiency. After subtracting the error owing to the vertex selection, the results of the efficiency test are consistent with those of the simulation. The Daya Bay experiment will not use the vertex criteria, and in addition, the discrepancy between the data and simulation can be removed by the relative measurement of the near and far detectors, 0.2% will be the final neutron detection efficiency error. After a comprehensive consideration including detector size, detection efficiency, and possible experimental errors, we choose 45 cm as the middle layer thickness.

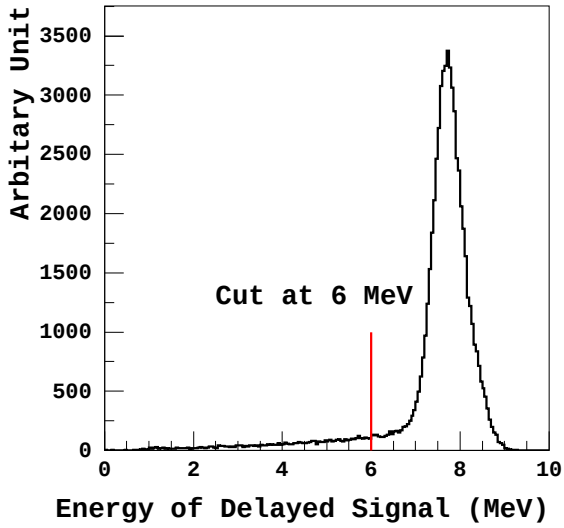

Fig. 5.3. The neutron capture energy spectrum in gadolinium as obtained from the GEANT3 simulation. The long tail at low energies corresponds to the escaped events.

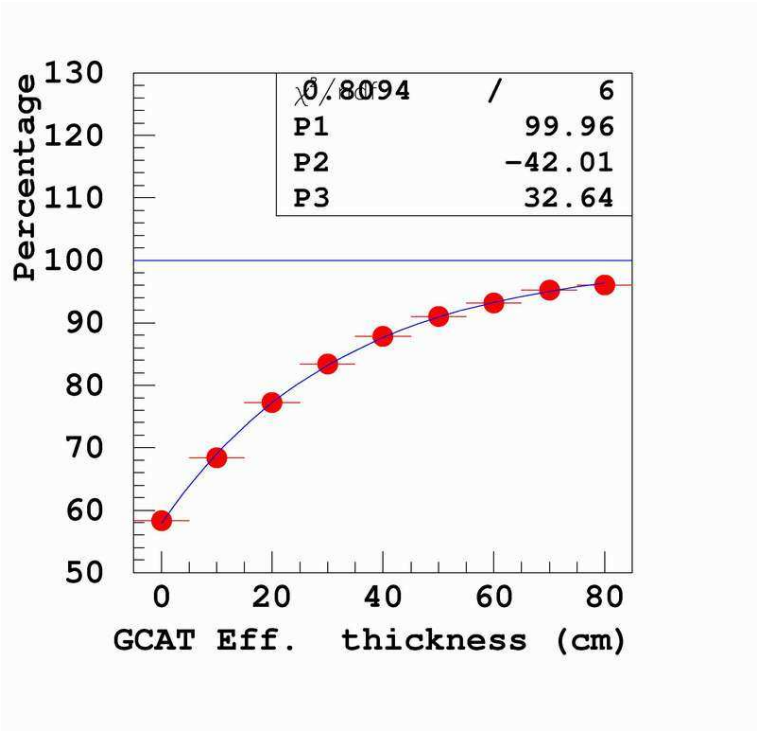

Fig. 5.4. The thickness of the middle layer vs. neutron detection efficiency. The neutron energy cut is set at 6 MeV. The thickness of the middle layer of the Daya Bay experiment will be 45 cm.

Neutron spill-in and spill-out across the boundary between regions I and II during thermalization has a very similar probability, as shown in Fig. 5.5. The effects hence largely cancelled for a three-zone detector and the residual effect can be corrected for by a suitable calibration process in combination with a Monte Carlo simulation.

Fig. 5.5. The neutron spill-in and spill-out probbaility as a function of distance to the acrylic vessel for a two-zone and three-zone detector module.

5.1.5 Oil buffer

The outmost layer of the detector is the mineral oil. The PMT's will be directly mounted on the container wall, facing toward the center, and immersed in the mineral oil to catch the scintillation light produced by the positron and neutron reacting in the liquid scintillator. This mineral oil layer is optically transparent, but emits very little scintillation light. The main role of this layer is two fold: 1) to eliminate the natural radiation from the PMT glass, steel tank and the other materials near the detector module; 2) to assure that PMT's are located at a distance reasonably away from the liquid scintillator, so as to eliminate events with lights emitted too close to a PMT. Through simulation and event reconstruction, it has been found that the light emitting point in the liquid scintillator has to be at least 15 cm away from a PMT surface, as indicated in Fig. 5.6.

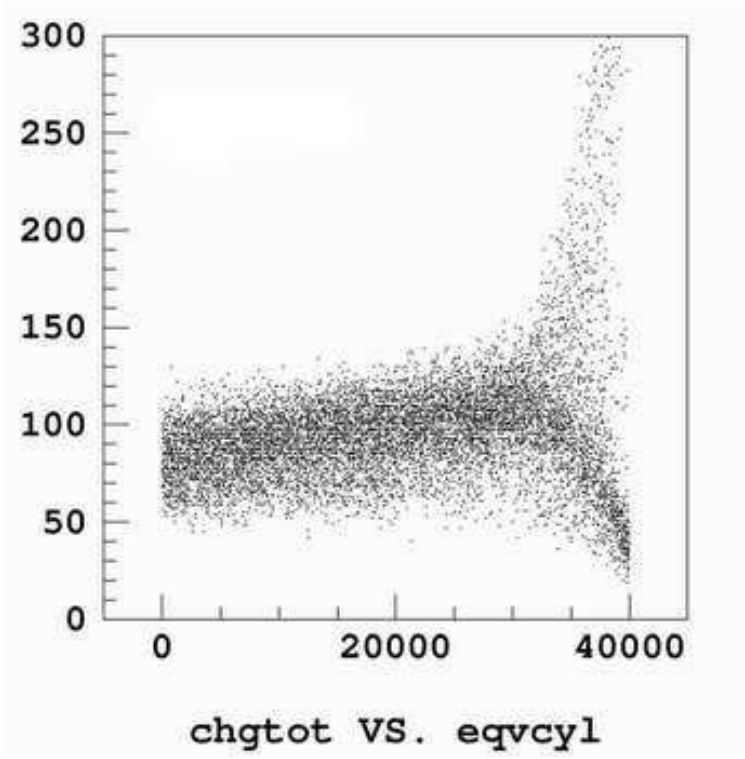

Fig. 5.6. The correlation between the event energy and the vertex location. The horizontal axis represents the equal volume bin, the red line is 15 cm from a PMT's photocathode. To the right of this line the event energy varies significantly.

The oil buffer is also used to prevent the natural radiation from the PMT glass from entering the fiducial

volume. Simulation shows that with a 20 cm oil buffer, the radiation from the PMT glass detected in the liquid scintillator is 7.7 Hz, as summarized in Table 5.1.

Isotope	Concentration	Buffer Oil Thickness			
		20 cm (Hz)	25 cm (Hz)	30 cm (Hz)	40 cm (Hz)
^{238}U	40 ppb	2.2	1.6	1.1	0.6
^{232}Th	40 ppb	1.0	0.7	0.6	0.3
^{40}K	25 ppb	4.5	3.2	2.2	1.3
Total		7.7	5.5	3.9	2.2

Table 5.1. Radiation of the PMT glass detected in the Gd-scintillator (in Hz) as a function of the oil-buffer thickness in cm.

The natural radioactivity of a rock sample collected at a potential detector site has been measured to be typically 560 ppm for ^{238}U, 1000 ppm for ^{232}Th, and 2.3 ppm for ^{40}K. Such γ rays can penetrate the 2 m water shield through the 45 cm of oil buffer to deposit more than 1 MeV of energy in the liquid scintillator, yield a background rate of 5.4 Hz for ^{238}U, 20.4 Hz for ^{232}Th, and 1.8 Hz for ^{40}K.

Summing up the PMT and rock radiation background gives a total background rate of of 33 Hz. Radon radioactivity can be controlled by ventilation, which will be discussed in detail later. Other materials near the central detector, such as steel vessel and supporting structure, welding rods, water, mineral oil, dust and Krypton in air plays a minor role.

Since the PMT's are placed in the mineral oil, and the length of PMT plus its base is about 25–30 cm, a 45-cm thick oil buffer will be sufficient to suppress the uncorrelated backgrounds to an acceptable level. The propose dimensions of the central detector is then shown in Table 5.2.

Region	IR(m)	OR(m)	inner height(m)	thickness(mm)	outer height(m)	material
target	0.00	1.60	0.00	10.0	3.20	Gd-LS
catcher	1.60	2.05	3.20	15.0	4.10	LS
buffer	2.05	2.50	4.10	8.0–10.0	5.00	Mineral oil

Table 5.2. Dimensions of the mechanical structure and materials of the central detector.

For a cylindrical module, the neutrino target is about 3.2 m high with a radius of 1.6 m. The middle section and the outer most oil buffer are both 0.45 m thick. For the whole module, the diameter will be 5.0 m and the height 5.0 m and the total weight will be 100 tons.

5.1.6 2-layer versus 3-layer detector

The possibility of adopting a detector with a 2-layer structure, by removing the γ-catcher of the current 3-layer one, has been carefully studied. A 2-layer detector of the same dimension of our 3-layer structure has a target mass of 40 ton when keeping the same oil buffer layer of the latter. The efficiency of the neutron energy cut at 6 MeV will be $\sim$70%, compared to $\sim$90% with the γ-catcher, although the 2-layer 40 ton detector will have $\sim$60% more events than the 3-layer 20 ton detector. This reduction of efficiency in the neutron energy cut will introduce an error due to the energy scale uncertainty. This error is irreducible, not removable by the near/far relative measurement, as the different detector modules may have different energy scales.

The energy scale is possibly site-dependent due to the site variation of calibration conditions. According to the experience gained from KamLAND, we could achieve easily a 1% energy scale stability at 8 MeV and 2% at 1 MeV. The inefficiency caused uncertainties have been studied by Monte Carlo for the 2-layer 40-ton detector, which is 0.4% at 6 MeV as compared with 0.22% for the 3-layer 20-ton detector. Similar uncertainties at 4 MeV have also been studied, see Table 5.3. This error will be the dominant residual

Configuration	6 MeV	4 MeV
2-zone	0.40%	0.26%
3-zone	0.22%	0.07%

Table 5.3. Error of the neutron energy threshold efficiency caused by energy scale error for 2-layer and 3-layer detectors. The energy scale error is taken to be 1% and 1.2% at 6 MeV and 4 MeV, respectively.

detector error, while other errors could be cancelled out by detectors swapping, e.g., a doubling of this error will significantly worses the $\sin^2 2\theta_{13}$ sensitivity that can be achieved.

As shown in Table 5.3, lowering the energy cut to 4 MeV can reduce the neutron energy threshold efficiency error. However, the effect of ambient and intrinsic radioactivities have to be reconsidered. In fact, the intrinsic radioactivity from the Gd-doped liquid scintillator or the acrylic vessel will significantly increase the accidental backgrounds. Let us examine radioactivity in some detail. Only gammas of the external radioactivity, such as from PMT's and environmental rock, can enter the liquid scintillator. Thus the external radioactivity has an upper limit of energy deposit of $\sim$3.5 MeV. So the 4 MeV cut is not affected. For intrinsic radioactivity, all gamma, beta, and alpha particles contribute simultaneously. For example, ^{208}Tl has significant contribution in the 4–6 MeV region as found by KamLAND. Chooz has also observed a significant number of events of delayed energy of 4–6 MeV (see Fig. 5.7). Furthermore, normally gadolinium has contamination from ^{232}Th. Hence, as a consequence of all these unfavorable factors, lowering the cut to 4 MeV will increase the accidental background by a couple of orders of magnitude. So our neutron energy cut is set at 6 MeV.

5.1.7 Expected performance

With the reflection at the top and bottom, the effective coverage is 12% with 224 PMT's, the energy resolution is around 5.9% at 8 MeV when the total-charge method is used, or 5.5% when use a maximum likelihood fit approach. The vertex can also be reconstructed at a comparable resolution in comparison with the design that has a PMT's coverage of 12% on all surface including the top and bottom. The energy reconstruction resolution and vertex reconstruction resolution is $\sim$14 cm for a point-like 8 MeV event using the maximum likelihood fit, as shown in Fig. 5.8. The horizontal axis is the distance of the reconstructed vertex to the true vertex and the vertical axis is the event number. Such a vertex resolution is acceptable since the neutron capture vertex has $\sim$20 cm intrinsic smearing, as found by Chooz [4] and by our Monte Carlo simulation as well. The intrinsic smearing of the neutron capture vertex is caused by the energy deposition of the gammas released from neutron-capture on Gd.

5.2 Containers and calibration ports

5.2.1 Containers

The Buffer vessel is the outer tank of the central detector module, and surrounds the buffer oil region. It will be built with low radioacivity 304L stainless steel and will satisfy the following requirements:

a. to be leak-tight to mineral oil over a long period of time (10 years);

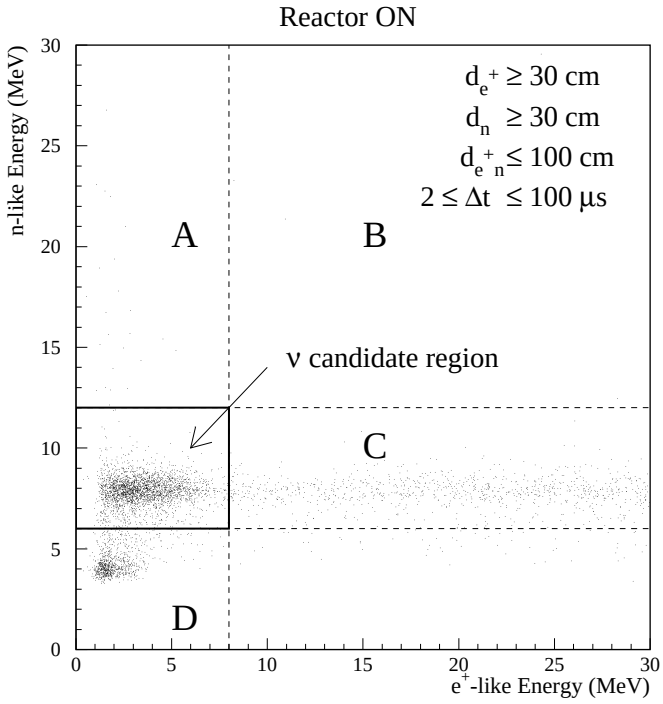

Fig. 5.7. The energy distribution observed by Chooz, horizontal axis is the prompt signal energy; the vertical axis is the delayed signal energy. In the region labelled D there are many background events with delayed signal falling into the 3–5 MeV energy range.

b. to be chemically compatible with the mineral oil of the Buffer region;

c. to have mechanical strength to support the 256 photomultiplier tubes (position precision is given at about 1 cm);

d. to use minimal material so as to reduce backgrounds.

The Buffer vessel is a cylinder of 5000 mm height, 5000 mm diameter (external dimensions), and 10 mm thick as depicted in Fig. 5.9. It weights about 10 tons and has a volume of $\sim$95 m^3 (without the chimney).

The Buffer vessel will be industrially machined in several pieces to be transported to the Daya Bay site for assembly. Each vessel consists of ten half-rings of stainless steel sheet and two half-bottom and -top lids. All pieces will be pickled and passivated at the contracted manufacturing company. Half-rings and lids will be initially welded. The Buffer vessel structure will be erected by welding 3 rings of stainless steel sheets. Tubes for the inner photomultipliers cable paths will be welded afterward. The work platform and necessary tools will be designed and manufactured to facilitate the assembly procedure and to guarantee good cylindricality of the vessel. Special care will be required in all these processes, especially during part of the welding process which is to be carried out after the installation of the phototubes. Leakage of welds will be systematically checked through the sweating method. The Buffer vessel will then be cleaned with de-ionized water and weak nitric acid. A reinforcing structure will be added at the top and bottom of the steel tank to increase its strength and to prevent distortion.

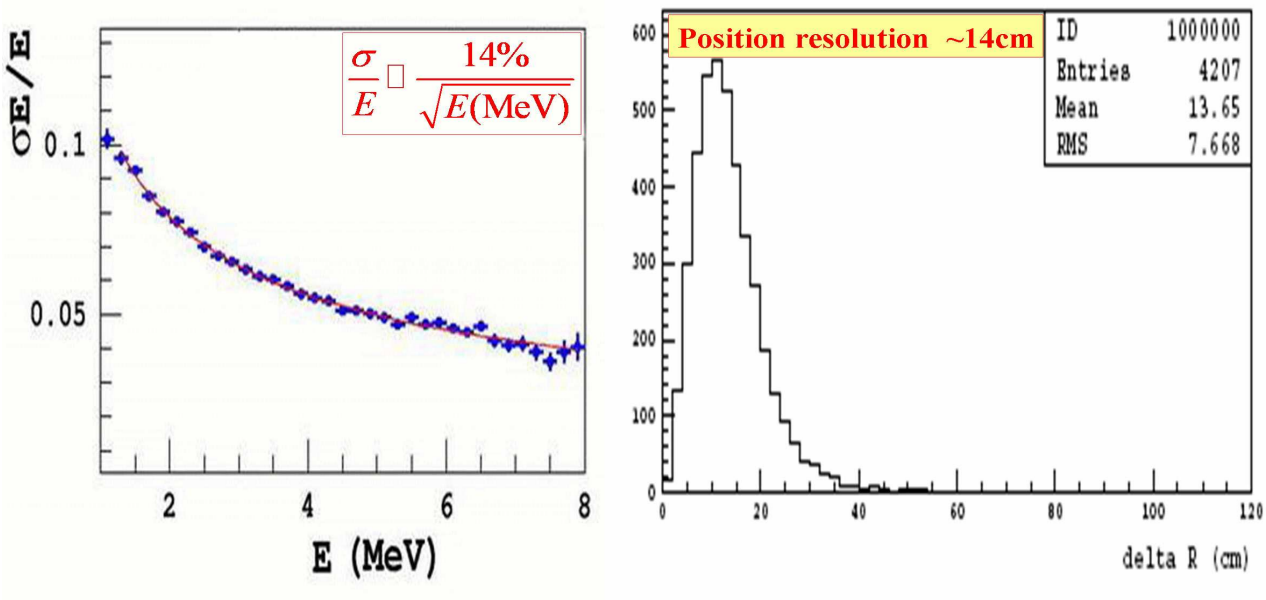

Fig. 5.8. The energy reconstruction resolution and vertex reconstruction resolution for a point-like 8 MeV event using maximum likelihood fitting. The x-axis is the distance of the reconstructed vertex to the true vertex and the y-axis is event number.

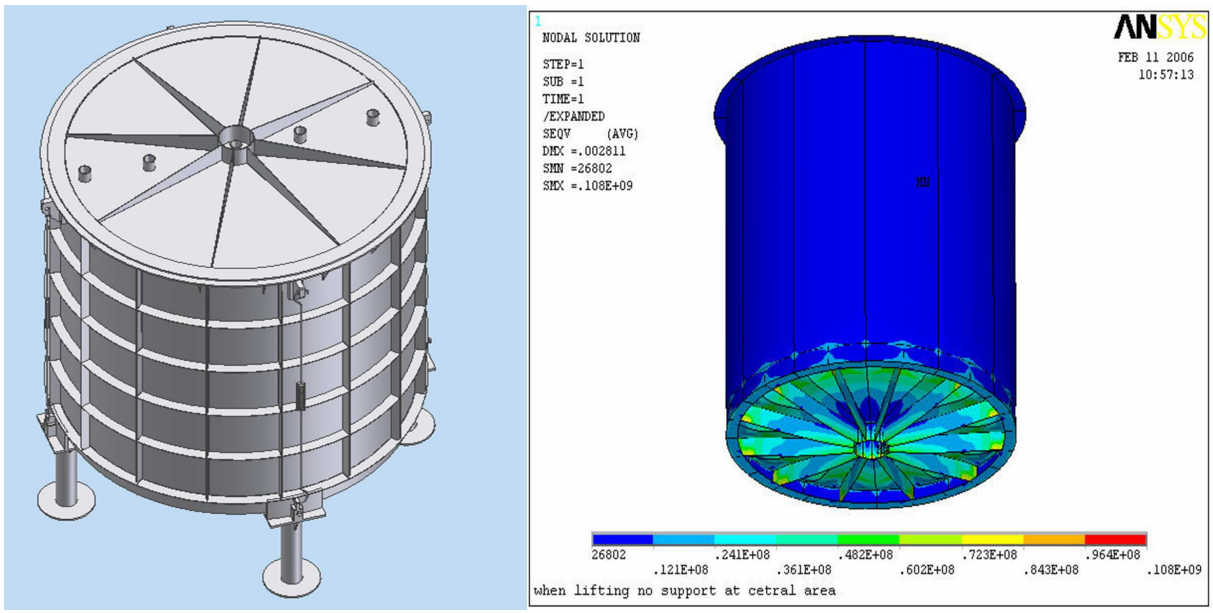

Fig. 5.9. 3D view of the stainless steel Buffer vessel.

5.2.2 Acrylic vessel

The target vessel is a cylinder of 3200 mm height, 3200 mm diameter (external dimensions), and 10 mm thickness wall. It weighs ∼580 kg, and contains a volume of ∼25 m^3 (without chimneys). The γ-catcher vessel surrounding the Target is a cylinder of 4100 mm height, 4100 mm diameter(external dimensions), and

15 mm thickness wall . It weighs 1420 kg, and contains a volume of $\sim$53-25=28 m^3 (without the chimneys). At the top of the target vessel, there are 2 or 3 chimneys for injecting the LS and for passage of radioactive calibration sources. There will be 1 or 2 chimneys for the γ-catcher as well. The chimneys diameter will be $\sim$50–100 mm. Drawings of the target and the γ-catcher are shown in Figure 5.10.

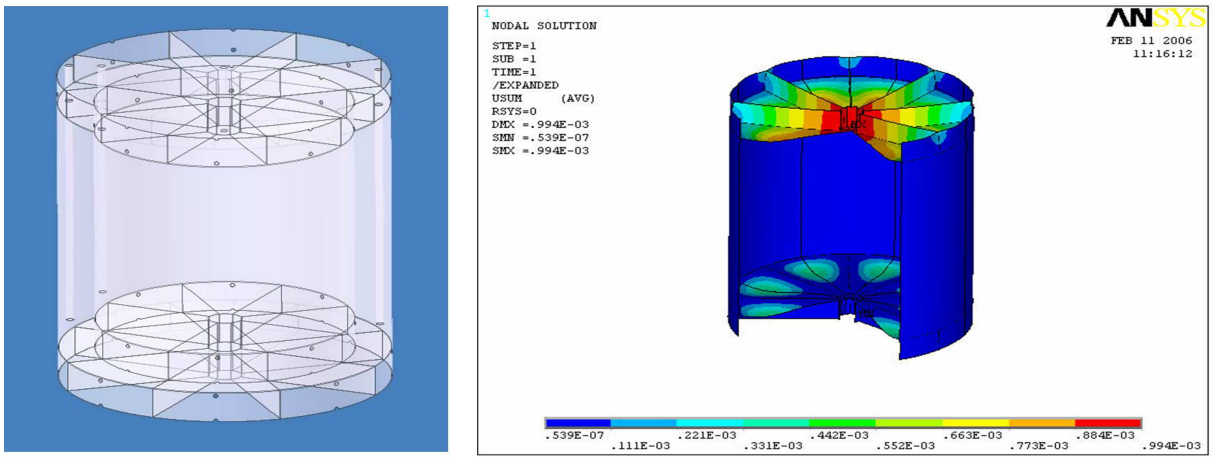

Fig. 5.10. The design of the double vessel.

The target and γ-catcher vessels will be built with acrylic plastic material which is transparent to photons with wavelength above 430 nm. Both vessels are designed to contain aromatic liquids with a long term tightness (free from leakage for 10 years) and stability. The critical constraint is the chemical compatibility between the vessel and the scintillating liquids, for at least 5 years. There must be no degradation of the liquid properties (scintillation efficiency, absorption length) nor any significant degradation of the acrylic material (breaking or crazing of more than a few percent of the acrylic surface area). The γ-catcher vessel will also be chemically compatible with the mineral oil in the buffer region.

Acrylic is normally PMMA plus additional ingredients to prevent aging and UV light absorption. Different manufacturing companies have different formulas and trade secrets for the additional ingredients, resulting in different appearance, chemical compatibility, and aging effects. For the material choice, we have surveyed many kinds of organic plastic. We have identified two possible sources for fabrication of the acrylic vessels: the Jiang Chuan Organic Plastic Ltd. Corp, located in city of Lang Fang, Hebei Province, China, and the Gold Aqua System Technical Co. in Kaoshiung, Taiwan (subsidiary of the Nakano company).

The Jiang Chuan Corp. uses the centrifugal casting method for their construction of the vessel. The approach of Nakano's subsidiary company uses bent plate sheets to be glued together by the polymerization method. It appears at this time that this method will be preferable as it should provide a higher quality vessel than casting.

In the polymerization gluing method, they add the same raw materials as the acrylic (PMMA + ingredients) into the gap between the plates. Thus the joints consist of exactly the same acrylic material as the joined plates, and there is no difference in their mechanical, chemical and optical properties. During polymerization, UV light is used instead of heating, in order to prevent the bent sheets from rebounding. The speed of polymerization is controlled to minimize the remaining stress. Once the tank is fabricated in shape, it will be put in a thermally insulated enclosure for up to a month ($\sim$1 week in our case) to be heated for releasing the stresses. The temperature will be controlled within $\pm 1^\circ$ C. Different acrylic types, shapes, thicknesses, etc., need different temperature curves for bending and curing. Hence experience is very important. The geometric precision can be controlled to $\pm$2 mm for a 2 m-diameter tank. The tank can have reinforcement structures at both the top and bottom; therefore the mechanical strength is not a problem for a

very thin tank ($\sim$1 cm). However, a thin sheet tends to have more residual stress which may be problematic for chemical compatibility. The minimum thickness of our tank is to be discussed after the compatibility test of acrylic sheets with LAB is completed. Figure 5.11 shows a example of the acrylic plastic vessel. Mechanically, the double vessels must be strong and stable enough to ensure identical shapes between near

Fig. 5.11. A sample production of the acrylic plastic vessel. The picture shows that it's an organic glass cylinder. The diameter and the height are both 2 m, with high precision.

and far target vessels. We will require that structural deformations of no more than 1 mm are allowed after the vessels are filled with liquids. Following fabrication, the vessels can be tested by gas pressurization and the deformation measured to insure that they will meet this specification.

The manufacture and transportation of the detector vessels can cause complications to the experiment and they need to be studied in great detail. Simulation has shown that the transportation phase is hazardous for a double acrylic vessel which has been completely assembled. Vibrations generated by the suspension system during ground transportation could be significant if the full double vessel construction were completed at the manufacturer's plant. This problem could also be solved, without changing the baseline design, by transporting the target and γ-catcher vessels separately, and integrate and glue the γ-catcher top lid and the chimney in the integration hall. There will be no annealing after the vessels are made, since the oven is far from Daya Bay and the transportation would induce intolerable stress.

As a result of these studies, our present plan is that the integration of the double acrylic vessel will be done in several steps:

a) the target vessel will be entirely built, annealed and checked for tightness at the manufacturers;

b) The chimney will be glued in the Daya Bay asssembly hall;

c) the γ-catcher vessel will be built without the top lid. It will be glued later in the Daya Bay assembly hall.

For the final step, air conditions in the integration hall have to be well controlled. During the 24 hours of the polymerization of the glue, the temperature has to be kept stable. In the Daya Bay assembly hall, the assembly will be handled with the ceiling crane and specifically developed tools. The γ-catcher vessel will arrive mounted on a supporting structure used to minimize the deformations and then rotated. The target vessel then will be inserted into γ-catcher. After the on site cleaning of the vessels, the top lid of the γ-catcher and the chimney will be glued by technicians from the manufacturer. Then, the γ-catcher will undergo final insertion in the buffer vessel (the phototubes will already be partially mounted).

In Daya Bay all regions within the Buffer vessel have to be filled simultaneously. The filling phase generates constraints related to the differences in height of the liquid. According to mechanical simulations, if we neglect density variations, the difference in acceptable height is 30 cm.

5.2.3 Calibration ports

In addition to the central chimney port, the buffer vessel lid will have several (3-6) ports, each 100–200 mm diameter, to facilitate the deployment of radioactive calibration sources and light sources. These ports will have gate valves to isolate the calibration devices when they are not in use and facilitate their removal. Around the side wall of the Buffer vessel there will be 32 ports of 5–10 cm diameter for high voltage, signal, and instrumentation cables.

The cables will be routed down to the bottom of the water pool and up the side so as to minimize interference with the water veto system. The cables may either be contained in pipes, or we will design a fail-safe isolation connector to allow the cables to be in the water.

5.3 Liquid Scintillator

5.3.1 Introduction

Organic liquid scintillator is rich in hydrogen (free protons), which is about 10% by weight. Gd is known to have a very large neutron-capture cross section in two of its stable isotopes : $\sigma(^{155}\mathrm{Gd}) = 61,400$ barns and $\sigma(^{157}\mathrm{Gd}) = 255000$ barns. The σ of natural abundance Gd is 49,000 barns so that isotopic enrichment of the Gd is not required. Furthermore, neutron-capture on Gd will lead to emission of γ rays with a total energy of about 8 MeV, that is much higher than the energies of the γ rays from natural radioactivity which are normally below 3.5 MeV. Hence, organic liquid scintillator doped with a small amount of Gd is an ideal antineutrino target and detector. Both Chooz [4] and Palo Verde [5] used 0.1% Gd-doping that yielded a capture time of $\tau \sim$28 μs, about a factor of seven shorter than that on protons in undoped liquid scintillator ($\tau \sim$180 μs). Backgrounds from random coincidence will thus be reduced by a factor of seven.

Extreme precaution must be exercised in preparing and using Gd-loaded liquid scintillator. For instance, the radio-purity of the Gd compound and the aging of the scintillator has to be taken into account at the beginning of an experiment. Fortunately, experience indicates that these issues can be resolved if proper methods for synthesizing the Gd-loaded liquid scintillator are applied.

In order to keep the random coincidence rate per module below 50 Hz, the scintillator should have contamination levels for ^{238}U, ^{232}Th, and ^{40}K below $10^{-13}\%$ in weight . Although this is achievable routinely for normal liquid scintillator made of pseudocumene and mineral oil [6], special care is required for the Gd compound since it usually contains ^{232}Th at a level of about 0.1 ppm. For a loading level of 0.1% by weight, the Gd compound has to be purified to a level of better than 10^{-10} g/g.

For a reactor neutrino experiment, Gd-LS must have a long light attenuation length, good light yield, and be table for several years. One of the major challenges is how to put Gd into the detector material. Since a liquid scintillator detector is made of aromatic solvent, it is difficult to add inorganic salts of Gd into

the organic liquid scintillator. The only solution to this problem is to form complexes of Gd with organic ligands. The solubility of the Gd compounds can be dramatically changed.

In the periodic table, Gd belongs to a series of elements called lanthanides (Ln) or rare earth elements (REE). Lanthanides are typically hard-acid element, which may form stable complexes with those ligands that possess hard donor atoms, such as oxygen and nitrogen. It has been found that Gd complexes, with some organophosphorus compounds and carboxylic acids. Several recipes of Ln-LS have been developed based on the above three kinds of organic ligands. For example, Gd-triethylphosphate (Univ. Sheffield), Yb-triisoamylphosphine oxide, Yb-dibutyl-butylphosphonate (LENS), Gd-ethylhexanoic acid (Palo Verde, Univ. Sheffield, Bicron), Gd-methylvaleric acid (BNL), and Gd-acetylacetone (Double-ChooZ, LENS).

Chooz and Palo Verde used different methods to produce their Gd-doped liquid scintillator. The Chooz experiment, dissolved $Gd(NO_3)_3$ in the scintillator, resulting in a scintillator which aged at a rate of 0.4% per day, where the aging rate is measured by the decrease of the attenuation length with time. The Palo Verde experiment, on the other hand, used $Gd(CH_3(CH_2)_3CH(C_2H_5)CO_2)_3$, yielding a scintillator which aged at 0.03% per day.

Based on the experience of the Palo Verde experiment, the concentrated liquid scintillator must be mixed with the mineral oil and pseudocumene at the experimental site to avoid additional aging effects, possibly caused by temperature and motion during transportation. The mixing equipment, consisting of a tank and stainless steel pipes, needs to be cleaned very carefully. A delicate mixing procedure must be followed to avoid local build-up of the Gd compound. The mixed liquid scintillator will be filtered to remove extraneous particles which, if left behind, will scatter light and shorten the attenuation length. The Palo Verde experiment has shown that the Gd compound will not be removed by the filter, and its exact amount in the doped liquid scintillator can be measured by weighing during the synthesis process or by a X-ray scattering measurement [7].

Major R&D efforts on liquid scintillator are being carried out for this Conceptual Design Report at BNL in the U.S. and IHEP in the PRC. It should be noted that while their general approach is the same, to prepare organo-Gd complexes that are soluble and stable in the LS organic solvent, the chemical details of the two efforts at BNL and at IHEP do differ in significant respects at present, such as purification procedures, reliance on solvent-extraction procedures, and the related control of pH. These differences do not affect the general goals of this CDR and are acceptable at this CD-1 stage of development of the Daya Bay $\sin^2 2\theta_{13}$project. It is expected that further cooperative R&D by these groups will resolve these issues.

5.3.2 Research with Gd-LS at IHEP

In the Daya Bay Project, Gd concentration of 1 g/L is needed in the LS to serve as the target for antineutrino capture. We began our research and development on Gd-LS in 2004 and the results so far are promising.

5.3.2.1 Purification of Gadolinium

As already mentioned above, in order to keep the random coincidence below 50 Hz, the total level of contaminations in the scintillator has to be extremely low. The most serious contamination is the ^{232}Th at a level of about 0.1 ppm — see Table 5.4. To eliminate Th, Gd_2O_3 powder is dissolved in hydrochloric acid and passed through a positive ion exchange resin column. This ion exchange procedure is an extremely effective method for removing thorium from Gd powder.

5.3.2.2 Preparation of Gadolinium Complexes

In our study, fourteen organic ligands including 4 organophosphorous compounds, 5 carboxylic acids, and 4 β-diketones have been tested. Carboxylic acids seem to be the most suitable organic ligands and three of them are used for further study. Gd carboxylate can be synthesized by the following methods:

Sample	^{238}U (ppb)	^{232}Th (ppb)	^{40}K (ppb)
glass fiber	250 ± 50	760 ± 220	56 ± 13
paper fiber	110 ± 30	< 136	11.4 ± 6.7
Gd_2O_3	< 13	440 ± 32	< 2.3
$GdCl_3$	< 28	< 95	< 5.1

Table 5.4. Radioactive impurities in Gd_2O_3 and fiber samples.

a. Carboxylic acids are neutralized by ammonium hydroxide and reacted with $GdCl_3$ in an appropriate ratio. The precipitation is collected by filtration, then washed with distilled water, and dried.

b. Carboxylic acids are dissolved in scintillator solvent and mixed with a $GdCl_3$ water solution. Then the pH of the solution is then adjusted with ammonium hydroxide or sodium oxide. The Gd-carboxylate is formed and can be extracted into scintillator solvent.

Both methods have been successfully applied.

5.3.2.3 Selection of Solvents

Pseudocumene (PC) and mesitylene are the most commonly used solvents for Gd-LS, but they have two drawbacks: low flash point (48° C) and corrosiveness to the acrylic tank. To solve these problems, a mixture of PC with dodecane or mineral oil has been a starting material for detergent, i.e., linear alkyl benzene (LAB), is a better choice as a Gd-LS solvent. LAB has higher light yield, high flash point (130° C), much lower price, and is compatible with acrylic. An unpurified LAB sample obtained from Fushun Petroleum Chemical, Inc. has an attenuation length longer than 30 m, and it can be used directly as the required solvent.

5.3.2.4 Preparation of Gd-LS

The Gd content in Gd-Carboxylate is determined by the colorimetric method and dissolved in a scintillator base which contains a primary fluorescent additive and a spectrum shifter. The final concentration of the solutes includes Gd 1 g/L, PPO 5 g/L, and bis-MSB 10 mg/L. The liquid is then pumped through a 0.22 μm filter and bubbled with nitrogen for the removal of oxygen.

5.3.2.5 Characterization of Gd-LS

The two main considerations for the quality of Gd-LS are attenuation length and light yield. Table 5.5 lists the light yield relative to anthracene crystal for several LS samples. We can see that the gadolinium loading has very little effect on the light yield.

The long-term stability of the scintillators developed for Daya Bay has been investigated by means of spectrophotometric techniques. The transmission of a collimated light beam through 10 cm of material is routinely measured with a Pgeneral TU1901 UV-Vis spectrophotometer. We pay great attention to the chemical evolution of the scintillator leading to an increase in the absorbency, i.e., the optical degradation.

Spectrophotometric measurements can be used not only to monitor the relative changes of the transmission of a sample (glass cell), but also to determine the absolute wavelength-dependent attenuation length (quartz cell). For the latter case, the effect of the light losses due to reflections at the air-quartz-liquid and liquid-quartz-air interfaces must be corrected, and the tiny absorption from the quartz windows must also be corrected in order to improve the accuracy of this absolute measurement. So, we zero the instrument with the response of the cell filled with cyclohexane, because cyclohexane has a similar refractive index as liquid scintillator.

Gd(g/L)	Scintillator	Complex	Solvent	Light Yield
—	PPO bis-MSB	—	PC:dodecane	0.459
—	PPO bis-MSB	—	LAB	0.542
1.5	PPO bis-MSB	Gd-ethylhexanoic acid	2:8 PC:LAB	0.538
2.0	PPO bis-MSB	Gd-ethylhexanoic acid	2:8 PC:LAB	0.528
1.5	PPO bis-MSB	Gd-isononanoic acid	LAB	0.492
2.0	PPO bis-MSB	Gd-isononanoic acid	LAB	0.478

Table 5.5. Light yield relative to anthracene crystal for several Gd-LS samples. M: Mesitylene, D: dodecane, LAB: linear alkyl benzene

Figure 5.12 shows the long term stability of absorptions at 430 nm of four Gd-LS samples. In all samples

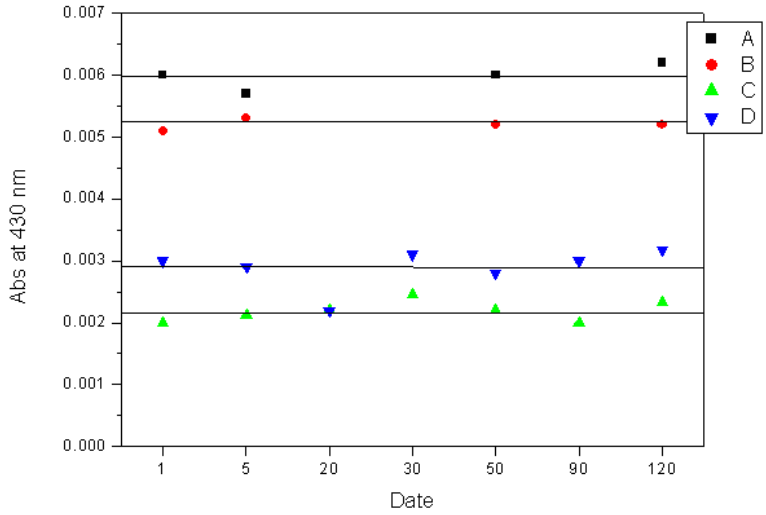

Fig. 5.12. Long-term Stability Test: 2 g/L Gd-LS as a Function of Time.

we used the same amount of fluors, 5 g/L PPO and 10 mg/L bis-MSB. The concentration of Gd, ligand and solvent used in four samples are as follows:

A. 2 g/L Gd, isononanoic acid as ligand, 4: 6 Mesitylene/dodecane;

B. 2 g/L Gd, ethylhexanoic acid as ligand, 2: 8 Mesitylene/dodecane;

C. 2 g/L Gd, isononanoic acid as ligand, LAB;

D. 2 g/L Gd, 2:8 ethylhexanoic acid as ligand, 2: 8 Mesitylene/LAB;

The results show that the variation of the absorption within four months for all four samples are very small. The attenuation lengths of samples C and D are longer than 10 m. We will continue our quality control program of long-term stability for more than 1 year. Long-term stability testing of Gd-LS samples will be continued for at least 1 year. We will synthesize 650 L of 1 g/L Gd-LS and conduct tests in a prototype detector which has been built at IHEP.

5.3.3 Research with Metal-Loaded LS, M-LS, at BNL

The Solar-Neutrino/Nuclear-Chemistry Group in the BNL Chemistry Department has been involved, since 2000, in R&D of chemical techniques for synthesizing and characterizing organic liquid scintillators loaded with metallic elements, M-LS. Much of that early work was done in collaboration with R. S. Raghavan at Bell Labs (now at Virginia Tech University), with the goal of developing a proposed new low-energy solar-neutrino detector, LENS/Sol [8]. In that experiment, concentrations of M $\sim$10% by weight are needed in the LS to serve as targets for neutrino capture. We had excellent results in synthesizing M-LS with the chemical elements that we focused on for LENS, ytterbium (Yb^{3+} ion) and especially indium (In^{3+} ion). It was immediately clear to us that it should be relatively straightforward to extend these chemical results to the new reactor antineutrino experiments, with the goal of preparing Gd-LS with ionic Gd^{3+} at the much lower concentrations required for neutron detection, $\sim$0.1%, a factor $\sim$1/100 of the In-LS concentrations. Because of the relevance of this earlier R&D to the present CDR, we discuss some of our results here for M^{3+}, where M primarily is In.

Key characteristics of the M-LS that are required for neutrino detection are (a) high optical transparency, (b) high photon production by the scintillator, (c) ultra-low impurity content, mainly of the natural radioactive contaminants, such as U, Th, Ra, K, and Rn, and (d) long-term chemical stability. It is necessary to avoid any chemical decomposition, hydrolysis, formation of colloids, or polymerization, which can lead over time in the LS to development of color, cloudy suspensions, or formation of gels or precipitates, all of which can degrade the optical properties of the LS.

5.3.3.1 Results for M-LS

Loading M into an organic LS solvent requires a complexing ligand to form an organometallic complex that is soluble in the organic solvent. Based on our experience, several organic complexing agents are appropriate, for example (i) carboxylic acids (R-COOH) that can be neutralized with inorganic bases such as NH_4OH to form carboxylate anions that can then complex the M^{3+} ion, (ii) organic phosphorus-oxygen compounds, "R-P-O", such as tributyl phosphate (TBP), or trioctyl phosphine oxide (TOPO), that can form complexes with neutral inorganic species such as MCl_3, and (iii) organic diketones, such as acetyl acetonate. At BNL, compounds from groups (i) and (ii) were candidates for testing proposed chemical procedures [12].

We began by working with the R-P-O compounds. The extraction of M is effective, but the attenuation length is only $\sim$few meters and the final M-LS was not stable for more than a few months. On the other hand, the carboxylic acids form organo-metal carboxylate complexes that can be loaded into the LS with more than 95% efficiency using solvent-solvent extraction. Moreover the carboxylic acids are preferable because they are produced in large quantity for industrial applications, less expensive, and easier to dispose of as chemical waste, compared to the phosphorus-containing compounds. In principle, the chemical reactions are (a) neutralization, $RCOOH + NH_4OH \rightarrow RCOO^- + NH_4^+ + H_2O$ in the aqueous phase, followed by (b) complex formation, $M^{3+} + 3RCOO^- \rightarrow M(RCOO)_3$, which is soluble in the organic LS. These reactions are very sensitive to pH: the neutralization step to form the $RCOO^-$ depends on the acidity of the aqueous solution, and hydrolysis of the M^{3+} can compete with formation of the $M(RCOO)_3$ complex, producing $M(OH)^{2+}$, $M(OH)_2{}^+$, $M(OH)_3$, and more complicated species .

We studied a range of liquid carboxylic acids with alkyl chains containing from 2 to 8 carbons. Carboxylic acids are normally present as dimers in the liquid. Their chemical complexation of the metal depends on the length of carbon chains; the longer the carbon chain, the more organic-like the carboxylic acid. Thus it's no surprise to find that acetic acid (C2) and propionic acid (C3) have very low efficiencies for extraction of M into the organic phase. Isobutyl acid (C4) and isovaleric acid (C5) both have unpleasant odors and require chelating ligands, such as TBPO or TOPO, to achieve high extraction efficiencies for M. On the other hand, carboxylic acids containing more than 7 carbons are difficult to handle because of their high viscosity; also as the number of carbon atoms increases in the carboxylate complex, the relative concen-

tration by weight of M decreases. The best complexant that we have found to date is the C6 compound, 2-methylvaleric acid, $C_5H_{11}COOH$ or "HMVA".

Several instrumental and chemical analytical techniques have been used at BNL to guide us in optimizing the synthesis procedures for M-LS. Among these, besides the measurements of light yield and optical attenuation length to be described below, are measurements in the LS of the concentrations of: (1) M^{3+} by spectrophotometry, (2) the total carboxylic acid, R-COOH, by acid-base titrations, (3) the uncomplexed R-COOH by IR spectroscopy, (4) the different organo-M complexes in the organic liquid by IR spectroscopy, (5) the H_2O by Karl-Fischer titration, and (6) the NH_4^+ and Cl^- by electrochemistry with specific ion-sensitive electrodes. These measurements produced very interesting results that indicated that the chemistry of the M-LS is more varied and complicated than what is expected from the simple chemical reactions (a) and (b) listed above. For example, with HMVA and MVA^-, we determined that in the M-LS: (A) For pH$\leq$6.7, the concentration ratio $MVA^-/M^{3+} \neq 3.0$ as expected, but = 2.56 ± 0.10. (B) Hydrolysis occurs, even at low pH values between 3.7–6.7, where the ratio $OH^-/M^{3+} = 0.5$. We also found that the OH^- content increases further as the pH is increased. Thus, the conclusions from our experiments, obtained mainly with In, are that the M molecular complex in the LS is not simply $M(MVA)_3$, but contains some OH as well, and that the form of this complex changes with changing pH. So, even though our long-term studies consistently show that the M-LS is chemically stable for periods $\geq$1 year, there is the lingering concern that hydrolysis reactions might occur over long times in the LS and possibly lead to insoluble hydroxides or organic polymers.

5.3.3.2 Extension of the BNL Procedures to Gd-LS

It is not obvious if these same concerns apply to our preparations of Gd-LS, since the Gd concentration in the LS is much less than the In concentration, and the hydrolysis constants for In^{3+} and Gd^{3+} are different. While we continue to study chemical speciation of the Gd-organo complexes as part of our R&D program, the results for the BNL Gd-LS, discussed below, indicate that it is stable over acceptably long time periods. However, the message for Gd-LS synthesis is clear: careful attention to chemical details, especially pH control, is crucial, as is long-term monitoring of the Gd-LS.

Our extensive laboratory R&D with M-LS has led to well-defined procedures for the synthesis of high-quality Gd-LS by solvent-solvent extraction in a simplified, consistent and reproducible way. Careful pH control is a key aspect of this approach, as is purification of all of the starting chemicals prior to the synthesis steps. Liters of metal-loaded scintillator can be synthesized in a few steps within a few hours. Note that we use high purity reagents in all of the synthesis steps, e.g., 18-Meg-Ohm H_2O, NH_4OH, and HCl.

5.3.3.3 Selection of LS Solvents

Several aromatic (organic compounds based on benzene) scintillation liquids were studied to test their applicability for M-LS. (1) Pseudocumene (PC), or 1,2,4-trimethylbenzene has been used in previous neutrino experiments. Its drawbacks are its low flash point and high chemical reactivity, which impose extra safety concerns. (2) Phenylcyclohexane (PCH) has a lower reactivity compared to PC, but only half of the light yield. (3) Both di-isopropylnaphthalene (DIN) and 1-phenyl-1-xylyl ethane (PXE) have absorption bands in the UV region below 450-nm that cannot be removed by our purification processes. (4) Linear alkylbenzene, LAB [9] is composed of a linear alkyl chain of 10–13 carbons attached to a benzene ring, and has a light yield comparable to PC. It is claimed by the manufacturers to be biodegradable. LAB has a high flash point, which significantly reduces the safety concerns. (5) Mineral oil (MO) and dodecane (DD) both have very good light transmission in the UV-visible region between 350 and 550 nm, so that no further purification is required. They produce little or no scintillating light. It has been reported that mixtures of PC + mineral oil will not attack acrylic. At BNL we have selected PC and LAB, as well as mixtures of PC with dodecane and of LAB with PC, as the scintillation liquids for loading Gd.

The chemical properties and physical performance of these scintillation solvents, plus mineral oil and dodecane, are summarized in the Table 5.6.

LS	Gd Load into LS	Density (g/cm^3)	abs_{430}	Purification Method	Relative Light Yield	Flash Point
PC	Yes	0.889	0.002	Distillation	1	48^oC
PCH	Yes	0.95	0.001	Column	0.46	99^oC
DIN	Yes	0.96	0.023	Column	0.87	$\geq 140^oC$
PXE	Yes, but is not stable	0.985	0.022	Column	0.87	167^oC
LAB	Yes	0.86	0.000	Column	0.98	130^oC
MO	No	0.85	0.001	Not needed	NA	215^oC
DD	No	0.75	0.000	Not needed	NA	71^oC

Table 5.6. Properties of Selected Liquid Scintillators

5.3.3.4 Purification of Individual Components for Gd-LS

Most of the purification steps that we have developed are applied before and during the synthesis of the Gd-LS [13]. Chemical separation schemes that would be used after the Gd-LS has been synthesized are unsuitable because they would likely remove some of the Gd as well as other inorganic impurities. Purging with nitrogen gas to remove radon from the Gd-LS could also cause problems by changing the concentrations of the volatile organic components in the LS.

The removal of non-radioactive chemical impurities can increase the transmission of the light in the LS, and enhance the long-term stability of the Gd-LS. Our investigations found that some impurities could induce slow chemical reactions that gradually reduce the transparency of the Gd-LS. We have developed chemical purification steps to use prior to or during the synthesis phase: (1) The purification of chemical ingredients in the aqueous phase, such as ammonium hydroxide and ammonium carboxylate, is done by solvent extraction with toluene mixed with TBPO. (2) The low-volatility solvent, LAB, is purified by absorption on a column of activated Al_2O_3. (3) The high-volatility liquids, such as the carboxylic acids and PC, are purified by temperature-dependent vacuum distillation at ≤ 0.04 bar. For the organic solvents, it is expected that vacuum distillation will also remove any radioisotopic impurities, including radon. Figure 5.13 and Figure 5.14

compare the optical spectra before and after the purification steps. Fig. 5.13 shows the effects of the activated Al_2O_3 column on the optical spectra of LAB. Fig. 5.14 shows the results of vacuum distillation for PC, and shows as well the spectrum of the yellowish high-boiling impurity that remains at the end of the distillation process.

Two methods, cation exchange and solvent extraction, are being considered for the purification of radioactive impurities, mainly U and Th chains, associated with Gd^{3+}. The contents of the radioactive impurities in the 99% and 99.999% $GdCl_3.6H_2O$ solids that we used as starting materials were measured by low-level counting at BNL and at the New York State Department of Health and found to be less than the detectable limits (10^{-8} g/g). More sophisticated radioactivity measurement steps will have to be developed to quantify these radioactive species at concentrations of 10^{-12} g/g in the 0.1% Gd-LS (implying impurity levels in the original inorganic Gd material of 10^{-9} g/g).

Another important issue we are beginning to study is the chemical compatibility with the material of the detector vessel of the organic Gd-LS and of the unloaded LS that will be used in the buffer region. Acrylic is known from SNO R&D to be attacked by many chemical liquids. Nylon, as used in transparent thin-walled balloons in Borexino [10] and in KamLAND [11], is known to be resistant to PC and mineral

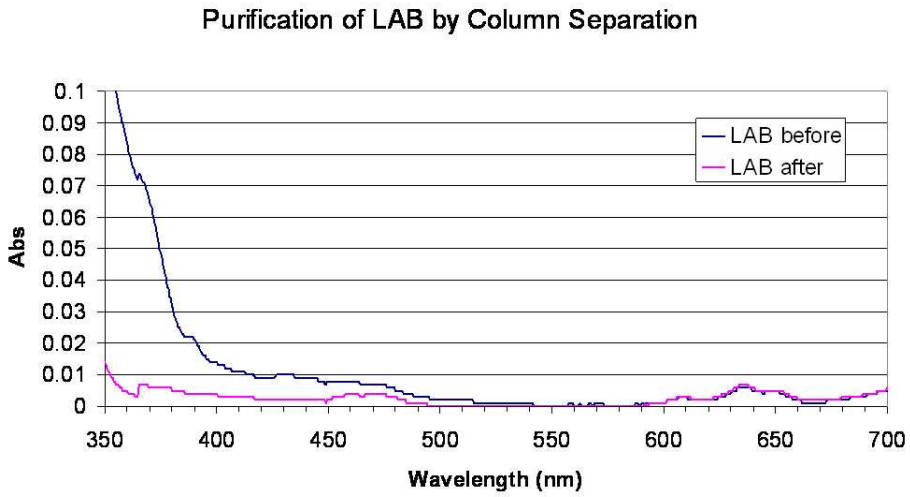

Fig. 5.13. UV-visible spectra of LAB before and after purification

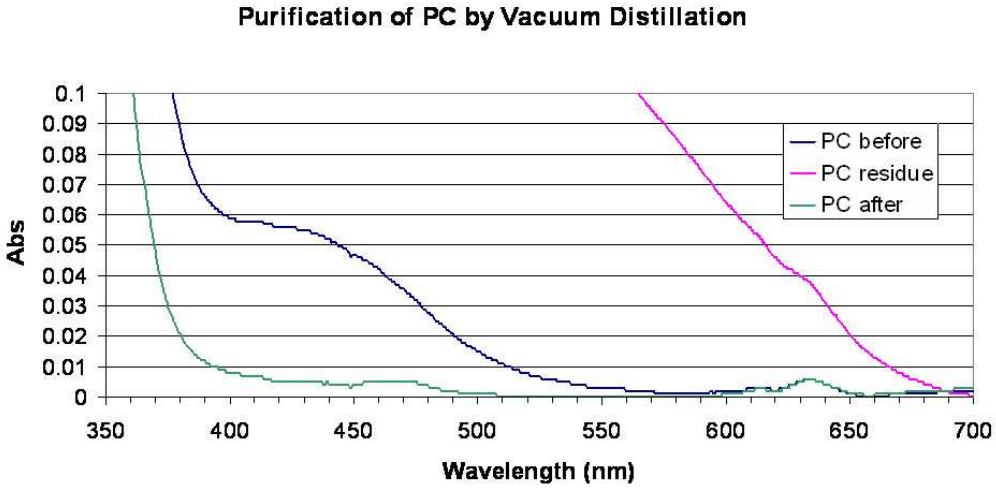

Fig. 5.14. UV-visible spectra of PC before and after purification plus residue fraction

oil, but thick-walled nylon is opaque to light. Another aspect of this problem that should be realized is that chemical attack of the vessel by the LS will introduce unwanted impurities, organic as well as inorganic, from the vessel into the liquid and may adversely affect the LS properties.

5.3.3.5 Long-Term Stability, Attenuation Length and Light Yield of Gd-LS

In 2004, we began R&D to apply our procedures for M-LS to the preparation of Gd-LS. We were successful in showing that it is rather straightforward to use our methods to obtain excellent Gd-LS in the range of 0.1–0.2% Gd. To date, we have prepared many hundreds of M-LS samples. There are two approaches for preparing batches of the Gd-LS: (i) synthesizing each batch at the desired final Gd concentration, 0.1–0.2%, or (ii) synthesizing more concentrated batches, $\geq$ 1–2% Gd, and then diluting with the organic LS

by a factor $\geq$10 to the desired concentration. The two approaches are not identical, with regard to possible long-term effects such as hydrolysis, polymerization, and effects on the properties of the final Gd-LS. We prefer approach (ii), because it simplifies the logistics of preparing and transporting very large volumes of Gd-LS.

We periodically monitor the long-term stability of our Gd-LS preparations in a "QC", quality control, program, by measuring the light absorbance and the light yield. Samples from the same synthesis batch are sealed respectively in 10-cm cylindrical optical glass cells (that are stored in the dark) for UV absorption measurements, and in scintillation vials for light yield measurements. Monitoring the UV absorption spectrum as a function of time gives a more direct indication of chemical stability than does the light yield. In Figure 5.15,

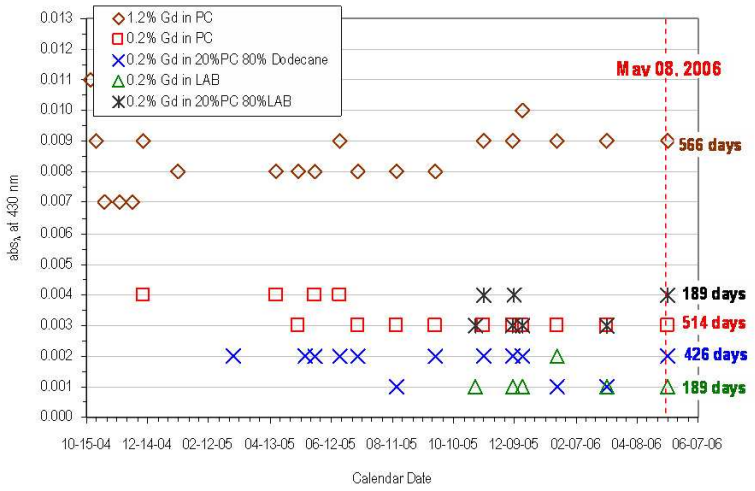

Fig. 5.15. the UV absorption values at 430 nm as a function of time

the UV absorption values for wavelength = 430 nm (in the UV spectrometer) are plotted as a function of time, until May 2006, for different concentrations of Gd from 0.2% to 1.2% by weight in a variety of solvent systems — pure PC, mixtures of PC and dodecane at different weight percents, and pure LAB. The figure shows that, since synthesis, samples of: (a) the 1.2% and 0.2% of Gd in pure PC have so far been stable for more than 1.5 and 1 years, respectively; (b) the 0.2% of Gd in the mixture of 20% PC and 80% dodecane has so far been stable for more than a year; and (c) the recently developed 0.2% of Gd in pure LAB has been stable so far for approximately 6 months.

The optical attenuation length, L is extrapolated from our UV absorption data. It is defined as the distance at which the light transmitted through the sample has its intensity reduced to $1/e$ of the initial value: L = 0.434 d/a, where a is the absorbance of light at wavelength measured in an optical cell of length d. Note that for d = 10 cm, a value of a = 0.004 translates into an attenuation length $L\sim$11 m. We have developed two techniques to obtain L of Gd-LS: (1) The optical transmission spectrum is scanned by our UV- Visible Spectrophotometer from 350–700 nm, using the 10-cm optical cell that contains 35 mL of solution. The equivalent attenuation length is calculated with the above equation from the measured absorbance at 430 nm. (2) It is difficult to extract accurate optical attenuation lengths from these short pathlength measurements because the a values are close to zero. Measurements over much longer pathlengths are needed. We have constructed a system with 1-meter-pathlength, horizontally aligned quartz tube that holds $\sim$350 mL of Gd-LS. The source of light is a He-Cd, blue laser with λ = 442 nm. The detectors are two photodiodes. The light beam is split into two beams. 80% of the light is passed through the 1-m tube containing the Gd-LS

and arrives at one photodiode. 20% of the light passes through an air-filled 10-cm cell and reaches the other photodiode to measure the fluctuations of the laser intensity, without any interactions in liquid. Both diode outputs are recorded in a Lock-In Amplifier. Use of this dual-beam laser system with 1-m pathlength confirmed the values of the attenuation length extrapolated from the measurements with the 10-cm cell in the UV Spectrometer. For 0.2% Gd in a 20% PC + 80% dodecane mixture without fluors, the 1-m measurement gave 99.54% transmission, corresponding to attenuation length $\sim$22 m. This agreed with the value $\sim$21.7 m that was extrapolated from the measured a= 0.002 in the 10-cm cell.

The light production (S%) of the Gd-LS is also measured at BNL. A scintillation vial containing ten mL of Gd-LS plus the wavelength-shifting fluors, butyl-PBD (3 g/L) and Bis-MSB (15 mg/L), is used for measurement of the photon production. The counting system including the PMT is enclosed in a brass container with 3.8-cm thick walls to block out the surrounding radioactive background. We determine the light yield from the Compton-scattering spectrum produced by an external ^{137}Cs γ-ray source that irradiates the sample, and express its value as S%, relative to a value of 100% for pure PC with no Gd loading. Measured light yields, relative to PC, are respectively 55% for 0.1% Gd in 20% PC + 80% dodecane, and 95% for 95% LAB + 5% PC. LAB has a photon efficiency that is very similar to PC.

5.3.3.6 Comparisons of BNL Gd-LS with Commercial Gd-LS

We have compared a sample of commercially available Gd-LS, purchased from Bicron, BC-521, containing 1% Gd in pure PC, with a BNL Gd-LS sample containing 1.2% Gd. We note that BC-521 is the concentrated Gd-doped scintillator with organic complexing agent in PC that was used in the Palo Verde reactor experiment after it was diluted to 40% PC + 60% mineral oil. The light yields of the respective BNL and Bicron samples were found to be comparable, 82% vs. 85%, when measured at BNL relative to 100% PC, and, as quoted by Bicron, 57% relative to anthracene. However, the attenuation length for the BNL-prepared Gd-LS was $\sim$2.5 times longer than the value for the Bicron BC-521 sample, 6.2 m vs. 2.6 m as measured at BNL; Bicron quoted a value ¿4.0 m for its sample. This significant difference in attenuation may reflect the care put into the BNL pre-synthesis purification steps.

The chemical stability of these BNL and Bicron BC-521 samples are being followed in our QC program. No perceptible worsening of the optical properties of these samples has been observed over periods of 1.5 and 1 years, respectively. Note that Bicron simply characterizes the stability of its BC-521 as being ”long term”. Our results support the claim of the Palo Verde collaboration that their Gd-LS showed some degradation during its initial period of use and then stabilized.

5.3.3.7 Future R&D at BNL, in Preparation for Scale-Up to Full-Scale Production of Gd-LS

Tasks that we have begun or will undertake in the next several months are as follows: (1) to continue our QC program of long-term stability of different Gd-LS preparations; (2) to determine the quality, quantity, and types of fluors required to add to the Gd-LS to optimize photon production and light attenuation; (3) to develop an optical system with variable vertical pathlengths up to $\sim$2 m to measure optical attenuation and scattering lengths over a range of wavelengths; (4) to build a closed synthesis system that eliminates exposure of the Gd-LS to air; (5) to scale our chemical procedures for Gd-LS synthesis up from the current lab-bench scale to volumes of several hundred liters, for prototype detector module studies, and as a prelude to industrial-scale production on the level of 160 tons; (6) to automate many of these chemical procedures, which are currently done by hand; (7) to use standardized ASTM-type tests to study the chemical compatibility of the LS with the materials that will be used to construct the detector vessel, e.g., acrylic; (8) to find methods to measure accurately, with high precision, the concentration ratios, C/H and Gd/H, and the H and C concentrations.

When we scale up to production of $\sim$200 tons of Gd-LS for the full-size experiment, it is conceivable that industrial cooperation may well be required in China and in the US. At that juncture, it will be very

important to have written acceptance specifications and a quality control program fully developed and in place, including analyses and measurements, to apply to materials that will be supplied by vendors, e.g., pure solvents, the starting materials for the Gd-LS syntheses, or even commercially manufactured Gd-LS.

We are also starting to explore the methods of transportation and storage for large quantities of LS. The 20-ft. x 8-ft. ISO tank, as proposed by the NOvA project, is a shipping container approved for international shipments, which conforms to the standards set by the International Standards Organization. The tank has a shell made of stainless steel, holds 6,341 gallons of liquid, and has interior temperature control. Each tank can be leased at a few $thousands$ dollars per year. This option represents an ideal solution for delivering (and storing) hundreds of tons of liquid if transported from the US to the Daya Bay reactor site.

5.3.3.8 A Planned Prototype Study of BNL Gd-LS

We are preparing ,with colleagues from Hong Kong and LBNL, to do a prototype study of 0.1% Gd-LS in the underground laboratory at the Aberdeen Tunnel in Hong Kong, as a satellite project for the Daya Bay 13 experiment. Concentrated, 1%, Gd-LS will be synthesized at BNL and subsequently diluted to 0.1% with unloaded LS at the University of Hong Kong (HKU). Both the Gd-LS and the unloaded liquid scintillator will be shipped from BNL to HKU, where they will be mixed to produce the final 0.1% Gd-LS prior to transport to the Aberdeen Tunnel. To dilute the 1% Gd-LS in batches of $\sim$50 L, we will either construct a stainless steel tank with inner liner and requisite plumbing, or purchase a commercial Jacketed Reactor System (from Chemglass Co.). The total volume for this prototype study will be 0.5 tons of 0.1% Gd-LS.

To determine if the properties of the Gd-loaded LS will be affected by transportation overseas from the US to the PRC, a series of tests, with the same samples of Gd-LS and unloaded LS, each $\sim$100g, will be performed at BNL before, and at HKU after, shipping. The optical properties and light yields of the Gd-loaded and unloaded LS will be measured both at BNL and HKU and compared to search for evidence of sample degradation.

5.3.3.9 Summary of R&D at BNL

After extensive syntheses and testing of many hundreds of samples, a very consistent procedure has been established at BNL for preparing 0.1–0.2% Gd-loaded liquid scintillator to be used in reactor neutrino experiments [14]. The distinguishing characteristics for 0.2% Gd-LS are $>$95% Gd chemical extraction efficiency, $>$15m attenuation length, $\sim$95% light yield relative to 100% PC, and long-term chemical stability, $\geq$1.5 years to date. The QC monitoring of chemical stability will continue to be an integral part of our program.

5.3.4 Mass production of the liquid scintillator

5.3.4.1 Material and compatibility

All eight inner volumes, one in each detector module which include target, γ-catcher and buffer, are in contact with acrylic vessels, therefore the material compatibility of the respective liquids with the acrylic used in the experiment is crucial. The compatibility of several PXE/dodecane mixtures and of LAB Gd-carboxylate-scintillator versions with acrylic has been tested. That the LAB Gd-carboxylate-scintillator seems to be the best sufficient material compatibility and scintillator light yield has been confirmed.

There are also other materials in contact with the scintillator during the measurement (the calibration system), handling and purification. Steel surfaces should be avoided for the target scintillator, which is expected to be reactive in contact with steel and the stability of the scintillator can be compromised. In the production and synthesis of the Gd-scintillator for the prototype, only PFA, PTFE, PP, PE and glass was used. Only such materials should be used for the final Daya Bay systems as well.

The central detector will need 200 tons of 1–2 g/L Gd loaded liquid scintillator, which is essentially an industrial production scale. We have found a high quality LAB supplier and their product can be used

without further purification. Production of enough quantity of Gd-carboxylate and making the solution at the required concentration are critical. We plan to cooperate with a chemical plant to carry out the job, including the purification of the carboxylic acid.

5.3.4.2 Mixing

A 150 L liquid scintillator mixing container has been finished and will be used for preparation of LS. This mixing container inner face was coated by PTFE to avoid affecting the aging of the Gd-loaded liquid scintillator; it is shown in Fig. 5.16.

Fig. 5.16. Liquid scintillator mixing container prototype.

When we begin mass production, we plan to synthesize solid Gd-carboxylate in Beijing and transport it to Daya Bay. Gd-LS will be blended in Shenzhen, about 30 km away from Daya Bay.

We will prepare two large mixing containers ($\sim$8 m^3 each), one is for the Gd-loaded liquid scintillator, the other for the non-Gd liquid scintillator. It is planned to purify and mix the scintillator at a hall near the port of the tunnel. At that time these two mixing containers will work at the same time. When mixing the liquid scintillator, the liquid is flushed with N_2 for 4 hours in order to purge oxygen, which is a potential danger in regard to the chemical stability of the scintillator.

5.3.4.3 Fluid handling and Purification

There will be scintillator fluid systems on-site in the reactor area. All mixing and purification of the needed liquids will be done on-site. It is expected that a sufficient storage area is available for all detector liquids. All eight inner volumes have to be filled simultaneously.

Since the antineutrino targets are free protons in the Gd-loaded scintillator, the event rate is proportional to the total mass of free protons in the target volume. The systematic error of the event rate is controlled by

the accuracy of the information on the relative total masses of the central volumes of all detector modules, as well as by the ability in filling the modules from a common batch of scintillator liquid so that the H/C ratio is the same for all modules. Satisfying the second criterion above allows the uncertainty in the H/C ratio to be cancelled out between the near and far detectors. We plan to fill each module from a common stainless steel tank maintained at a constant temperature. We will measure the fluid volume using premium grade precision flowmeters with a repeatability of 0.02%. Several flowmeters will be connected in series for redundancy. Residual topping off of the detector module to a specified level is measured with the flowmeters as well. This involves only about 20 kg since the volume is known by design and measured for verification. We conservatively assign an error of 0.2% on the target mass based on the absolute calibration of the flowmeters.

The liquid handling system for the target scintillator has to be made exclusively out of "Teflon-like" material. It can be used for loading, unloading, altering, mixing, storage, and nitrogen purging of liquids. After its preparation, the Gd-scintillator will be transported in dedicated tanks to the far and near detector sites. The procedure for handling the γ-catcher will be similar. The volume of the γ-catcher fits into one typical ISO-container.

5.4 PMT's and Support structure

5.4.1 Central Detector PMT Requirements

According the goal and design of the Daya Bay experiment, light produced in the liquid scintillator of far and near targets will be detected by 8 identical photomultiplier (PMT) systems. The number of phototubes (256 per detector) and geometrical arrangements of the 8 detectors should be the same .

The requirements for the central detector PMT's are being developed with computer simulations of the Daya Bay apparatus, and experience gained from past neutrino experiments, from test-stand studies, and with prototypes of the Daya Bay detector. The specifications will quantify the minimum quantum efficiency (as a function of wavelength) and gain, as well as maximum probability for pre- and after-pulsing, insensitivity to external magnetic fields, mechanical strength, single photon response, photocathode uniformity, pulse linearity, dark pulse rate, and anode efficiency. The maximum amount of thorium, uranium, and potassium within the phototube will also be specified.

However, the previously mentioned criteria are very crude, and we have to have detailed specifications. We discuss below the parameters of the PMT system that are used in the design.

These parameters are either from the baseline configuration or specified by the PMT manufacturers, or from the measurement we have made with the samples of phototubes provided by the manufacturers.

The 8 inch diameter PMT represents an optimal ratio of glass weight to photocathode area (active photo cathode diameter 190 mm and mass of the phototube $\sim$1000g). The total number of PMT's is 256 per detector module. On each cylindrical surface there are 8 rings of 32 PMT's each. The PMT's will be installed in the detector with their axis tilted to the center of the target. For non-tilted PMTs in the central plane, the distance from the PMT apex to the back of the supporting wall is 300 mm. From the experience of earlier experiments, we expect that the possible losses of PMT in the detector will be less than 1%. The key to low PMT mortality rate is to have a comprehensive testing program during the PMT installation. The total number of PMT's should be large enough so as to maintain a constant uniformity within a $< 1\%$ accuracy throughout the detector. The total number of PMT's to be acquired is 8×280, including 10% spares. For the mechanical support of the PMT's we plan to use the light-weight mounting developed by IHEP. During the installation PMT's will be mounted one-by-one on the walls of the stainless steel buffer vessel. Construction materials for the supporting structure (stainless steel and acrylic) will have been radioassayed to assure that they produce a negligible contribution to the detector single counting rate.

Positive supply voltage at the PMT anode can minimize the dark current and the discharge rate. Double cable will be used to supply the high voltage and signal readout. This minimizes the ground loop noise from the high voltage cable. Low-current PMT voltage dividers (0.1 mA at the nominal voltage) minimize power

dissipation in the detector. 20–30 m long oil-resistant HV cables and 50-ohm signal cables sealed in the PMT base with HV and signal connector at the outer end will be used. PMT glass resistance to the buffer oil (dodecane) has been tested for Hamamatsu and ETL tubes, with no effect for an equivalent $>$10 years of operation.

The dark rate can be higher for tubes immersed in the mineral oil to look at a large scintillator volume. Assuming that the dark rate does not scale with the detector volume and the coverage, but only with the PMT photocathode area, we can conservatively estimate the average dark rate per phototube at the level of $\sim$10,000–12,000 Hz.

5.4.2 PMT Candidates

For the PMT acquisition we will contact the major PMT manufacturers, including Hamamatsu in Japan, Electron Tubes Limited in England, Photonis in France and other companies. There are currently two candidate photomultiplier tubes for use in the central detector, the Hamamatsu R5912 and the Electron Tubes 9354KB. Both are 2π PMT's with a 190 mm wide photocathode and peak wavelength sensitivity near 400 nm. They are similar in design and construction. However, the R5912 has 10 dynodes while the 9354KB has 12. The Hamamatsu R5912 is an improved version over the R1408, which was used by SNO. The R5912 is used by MILAGRO and AMANDA, while ICECUBE, KamLAND and Super-K use either 10" or 20" Hamamatsu tubes. The Electron Tubes 9354KB has been selected by Double Chooz. Both PMT's will be extensively tested.

The manufacturers will be asked to integrate potted bases and oil-resistant cables into the construction of the deliverable products. We would enlist their help in the R&D effort, saving on construction time, and guaranteeing more robust operation of the tubes. Also we plan to specify the type of the voltage divider optimized by us for Daya Bay operation, which the manufacturer will build from high radiopurity components and seal in the PMT/base assembly. The final decision on the selection of a specific manufacturer will be made after verifying the compliance with the required level of radiopurity, detailed performance comparisons, and price.

5.4.3 PMT's arrangements

The 228 PMT's in a central detector module will be arranged to 8 rings, and each ring consists of 32 PMT's. Two adjacent 16-HV cables can be exported by one cable port, and two adjacent 16-signal cables are exported by another cable port. This exportation method is easy to bend, lift and readout by electric system for each port consist of fewer cables.

5.4.4 Support structure

The PMT's mechanical support system adopts a tripod structure which is directly fixed on the stainless vessel wall. A tripod is stable and convenient for adjusting the orientations of the PMT's. Figure 5.17 shows the PMT's mechanical support structure.

The structure that supports the PMT's is at the top of the legs. The orientation of the PMT can be adjusted by varying the lengths of the three legs. This structure is light and can be made with radio-pure materials. The PMT circular grip can be firmly adjusted during the assembly of the support structure. It can provide reliable suopport of the phototube in all possible positions relative to the direction of the buoyant force. The assembly of PMT's and mechanical structures will be carried out in a clean room next to the characterization/acceptance tests at the Daya Bay site, not far from the respective detectors. The PMT's, cables, and all mechanical parts will be cleaned with alcohol prior and after the assembly. The PMT grip ring will also tightened with a torque controlled tools and the whole assembly sealed in a hermetic plastic bag. Sealed assemblies will be stored and later transported to the detector site for installation. Sealing bags will be removed inside the clean area of the detector. Assembly production will go in parallel and somewhat in advance, with the PMT installation in the detector.

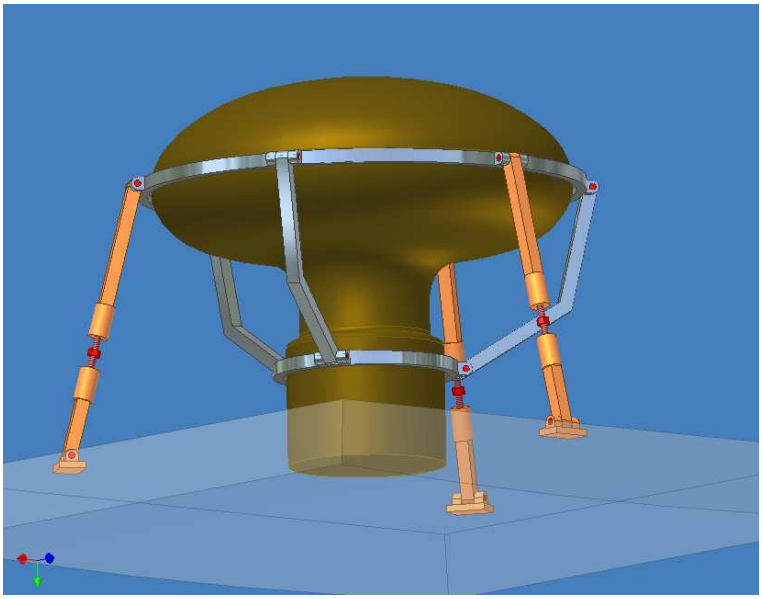

Fig. 5.17. The PMT's mechanical support structure.

5.4.5 Testing and Validation

We believe that the key to reliable and lasting operation of the large PMT array system is in the comprehensive tests conducted prior to installation and commissioning of the phototubes. Several levels of tests are planed to be performed at different locations and times.

First, we will ask manufacturers to provide us with certificates of acceptance measurements made at the factory. The measurements typically include: cathode and anode luminous sensitivity, cathode blue sensitivity, anode dark current and dark counting rate, supply voltage with a gain of 10^7, peak-to-valley ratio for single photoelectron and transit time spread. Furthermore, tests will be made on burning-in time of at least 24 hours for each phototube, at a voltage which can provide a gain of $\sim 10^7$.

This will be followed by measurements of major performance parameters of each phototube. The performance parameters will include: single photoelectron peak vs. high-voltage, dark rate vs. high-voltage, photocathode quantum efficiency relative to the reference, s.p.e. spectrum at the nominal gain of 10^7, and peak-to-valley ratio, measurement of linearity at nominal gain of 10^7, measurement of transition time spread at the nominal gain of 10^7, pedestal noise RMS when viewing the PMT signals with an oscilloscope.

The purpose of the characterization/acceptance test is to obtain a set of individual parameters for each tube, such as operating voltage at the nominal gain, the slope of gain vs. high-voltage, s.p.e. spectrum dark rate, transition time spread, and linearity, which will be included to the data base to characterize the detector performance. This data can be later used in the analysis and/or in detector simulation. Furthermore, in a first stage of the experiment, we will need to put PMT's into groups, each group with similar sets of high-voltage parameters, since four or eight tubes in a group will share a common power supply channel.

Selective acceptance radiopurity tests will be made: 1–2 randomly selected tubes from each monthly delivery batch will be assayed for radiopurity, in non-destructive tests. If the K, Th, or U content exceeds the specified level of contaminations, 10 other randomly selected tubes from the same batch will be radioassayed. If more than 3 out of 10 PMT's exceed the specified contamination level, the whole batch will be returned to the manufacturer.

The newly installed PMT's will be tested daily one-by-one for functionality and correct cable numbering to the position assignment. The final test with an LED in the central position of the detector, at the

normal PMT voltages, will be performed upon the installation of all PMT's in the detector and before the installation of the central acrylic vessels. For this test all PMT's will be connected to the HV distribution system and tested one-by-one with a dedicated DAQ station to verify the functionality of each channel and the correspondence between the HV channel number and the signal output. Daily functionalilty tests during the installation will be performed by the members of installation crew.

Testing and validation of the PMT's will be conducted using a custom test-stand. An LED will be pulsed to simulate scintillation light. The light will be collected within optical fibers and transported to the PMT. This setup allows us to adjust the intensity and position (on the photocathode) of the light reaching the phototube. Central detector electronics and a DAQ code will be used to readout the test-stand. Both the front-end module and the trigger card are 9U VME boards that are 340 mm deep. The VME crate is a VME 9U crate with a VIPA (VME64xP) back plane supporting CBLT (Chained Block Transfer). The crate controller is a Motorola MVME 5100 series. PMT validation will consist of the following tests:

- Quantum Efficiency (QE) is to be measured using a calibrated light source with optical bandpass filters with values between 300 and 500 nm. The relative QE of the PMT photocathode will be measured by looking at the mean pulse height of the PMT anode signals taken from various points, normalized to the signals taken from the central part of the photocathode, using a pulsed green LED system coupled to the PMT with a 1 mm clear optical fiber.
- The gain will be measured using either single photoelectrons, or a photostatistics method in combination with a flashing LED (300–500 nm) and a variable neutral density filter.
- A dual pulsed green LED system utilizing a variable neutral density filter will be used to check PMT linearity by using the "two LED pulse height" method. This setup can also be used to determine the single photoelectron response (SPR) and dark pulse rate.
- Pre- and after-pulsing will be studied using a pulsed LED source to look at the time correlation of signals (pre-trigger pulses for pre-pulsing and delayed signals for after-pulsing).
- A sampling digital oscilloscope with 500 MHz bandwidth and 2 Giga-samples/second will be used to measure the rise and fall times of the PMT dark pulses at +2000 volts.
- The transit time spread will be measured using a fast pulsed LED (100 spe equivalent signal) and a TDC.
- HPGe detectors will be used to obtain the count rate and spectra of the radioactive elements in the PMT's.
- The mechanical strength can be tested using a magnetically shielded dark box set on a vibrating table. This could be repeated for the PMT axis aligned in three perpendicular directions.

5.5 High Voltage and its Control System

The high voltage and its control system is designed around an Analog Devices' variant of the 8052 microcontroller. It functions for both HV control and monitoring. The system is capable of 0.5 volts resolution up to 2048 volts. An EMCO DC-to-DC HV generator will be mounted near the phototube and will act as our voltage source. The EMCO chips have low ripple, good regulation, and are economical. The base will be a simple tapered divider design mounted directly to the phototube, having a footprint smaller than the standard socket provided by each manufacturer.

Control software is currently written using LabView. The design of this unit is a modified version of the STAR EMC (4800 towers) code, which allowed for 4096 units to be controlled from a single serial port

(plus a RS485 converter) in a multi-drop, master-slave network using an RS485 bus. RS485 repeaters will be used to connect various branches of the HV control network to the main control bus. The firmware on the microcontroller and the LabView based control program are both available.

5.6 Readout electronics

The Center Detector Readout Electronic System is designed to process the photomultiplier tube (PMT) output signals. The essential functions are as follows:

- Determine the charge of each PMT signal to measure the energy deposit in the liquid scintillator. This will enable us to select neutrino events, reject backgrounds and deduce the neutrino energy spectrum.
- Determine the event time by measuring arrival time of the signals to the PMT's in order to build the time correlation between prompt and delayed sub-event. The timing information can also help us to reconstruct the location of the antineutrino interaction in the detector, and to study and reject potential background events.
- Provide fast information to the trigger system.

5.6.1 Readout system and specifications

When a reactor antineutrino interacts in the target, its energy is converted into ultraviolet or visible light, some of which will ultimately be transformed into photoelectrons (p.e.) at the photocathodes of the PMT's. For a given PMT, the minimal number of p.e.'s is one and, based on Monte Carlo simulation, the maximum number is 50 when an antineutrino interaction occurs in the vicinity of the interface between the Gd-doped liquid scintillator and the γ-catcher. Since typically 500 p.e.'s will be recorded by PMT's for a cosmic-ray muon passing through the detector, the dynamic range of the PMT's is required to be up to about 500 p.e.'s. The intrinsic energy resolution for a single p.e. is typically about 40% with some variation from PMT to PMT, while the energy threshold of a PMT is constrained by the dark noise, typically at the level of about 1/3–1/4 of a p.e. The peak-to-peak noise and the charge resolution of the PMT readout electronics is thus required to be less than 1/10 of a p.e. in both cases. The total charge measurement determined by the center-of-gravity method will produce the total energy deposited by an antineutrino signal or a background event.

The arrival time of the signal from the PMT will be measured relative to a common stop signal, for example, the trigger signal. The time jitter of a PMT for a single p.e. is about 1–2 ns, caused by the PMT transit time jitter, the PMT rise time, and the time walk effect of the signal, etc. The design goal for the time resolution of the readout electronics is thus determined to be less than 0.5 ns.

Since an antineutrino event is a coincidence of the prompt and delayed sub-event, their time interval is a crucial parameter for physics analysis. The precision of this interval is dominated by the trigger signal which is synchronized to the 100 MHz system clock. Hence a 10 ns precision is expected, which is sufficient given the fact that the coincident window of sub-events is 200 μs and the resulted uncertainties to efficiecy is less than 0.03is employed at the trigger board to measure the actual trigger arrival time with respect to the system clock, a better precision can be achieved.

The dynamic range of the time measurement depends on the uncertainty of the trigger latency and the maximum time difference between the earliest and the latest arrival time of light to PMTs. The range is chosen to be from 0 to 500 ns.

The time measurement of the individual PMT time can also be used to determine the event vertex. Although such a method is particularly suitable for large detectors similar to KamLAND, it provides an independent measurement which complements the charge-gravity method for small detectors with diameters of several meters. Hence it offers a cross-check of systematic errors and an additional handle for studying backgrounds. The Readout Electronics Specifications are summarized in Table 5.7.

Quantity	Specification
Dynamic range	0–500 p.e.
Charge resolution	¡ 10% @1 p.e. 0.025% @400 p.e.
noise	¡ 10% @1 p.e.
Digitization resolution	14 bits
Time range	0–500 ns
Time resolution	¡ 500 ps
Sampling rate	40 MHz
Channels/module	16
VME standard	VME64xp-340mm

Table 5.7. Readout Electronics Specifications.

5.6.2 Readout Modules

Each detector module is designed to have a readout electronic system without any relationship with that of other modules except receiving a common clock signal and GPS information. The positron and neutron sub-events are both recorded with time stamps and the their matching in time will be done offline by software. The readout electronics for each detector module is housed in a 9U VME crate, each can handle up to 16 readout modules, one trigger module, and one or two fan-out modules. In such an arrangement, moveable modules can be easily realized, and correlations among modules can be minimized.

Each readout module receives 16 channels of PMT signals and completes the time and charge measurement. The sum of hit numbers and the total energy of this module is fed into the trigger system for a fast decision. After collecting information from all readout modules, a trigger signal may send to all readout modules for data readout upon a positive decision.

A simplified circuit diagram of the electronic readout system, showing its main functions, is given in Fig. 5.18.

The analog signal from a PMT is amplified with a fast, low noise (FET input stage) amplifier. The output of the amplifier is split into two branches, one for time measurement, and the other for charge measurement.

The signal for time measurement is first sent to a fast discriminator with a programmable threshold to generate a timing pulse, whose leading edge defines the arrival time of the signal. A stable threshold set by a 14-bit DAC (AD7247) via the VME controller is needed for the discrimination in order to achieve the required time resolution.

The timing pulse is sent to a TDC as the start signal, while the trigger signal is used as the common stop. The TDC is realized by using internal resources of a high-performance FPGA with key components of two ultra high speed Gray-code counters. The first counter changes at the rising edge of the 320 MHz clock, while the second one changes at the falling edge. Thus, the time bin is 1.5625 ns and the RMS of the time resolution is less than 0.5 ns.

To measure the charge of a PMT signal, an ultra low-noise FET input amplifier (AD8066) is selected for the charge integrator. A passive RC differentiator is used after the integrator to narrow the signal. Since the signal rate of a typical PMT is about 5 kHz including noise, a 300 ns shaping time is chosen, corresponding to an output signal width of less than 1 μs. The analog signal is accurately digitized by a 14-bit Flash ADC with 40 MHz sampling rate after a baseline recovering. The digitized result goes directly into FPGA, in which all data-processing like data pipelining, pedestal subtraction, nonlinearity correction, and data buffering are implemented.

The readout module has a standard VME A24:D32 interface. Both ADC and TDC data of the triggered

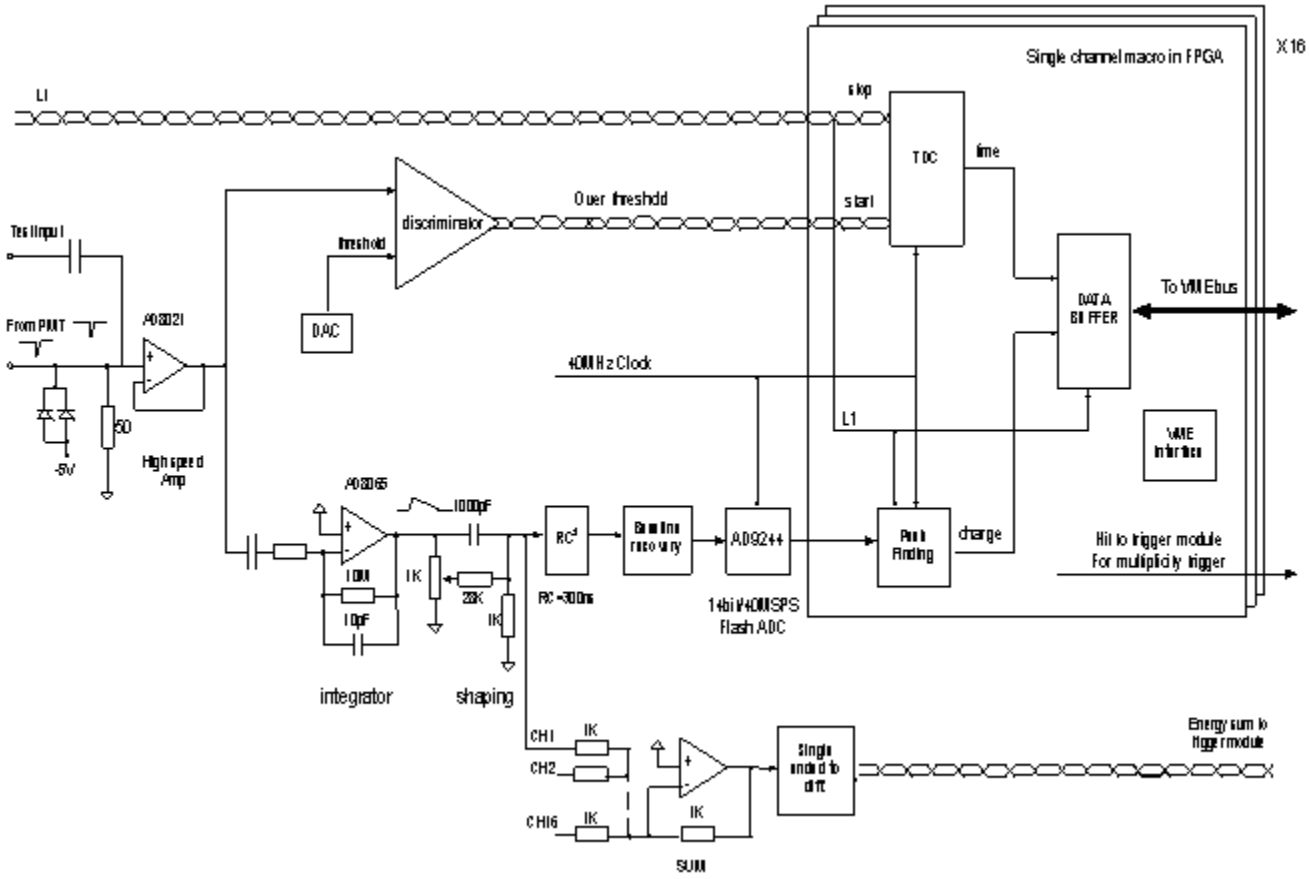

Fig. 5.18. Block diagram of a readout module for processing PMT signals.

event are sent to a buffer, which can store a maximum of 256 events. The data will be readout through the VME backplane by the DAQ system within a reasonable time span.

5.7 Prototype and test result

The critical step towards the successful construction of the central detector is R&D on a scaled down prototype, which is built at the Institute of High Energy Physics, Beijing, China. The goal of this R&D work is multifold: 1) to verify the detector design principles such as reflectors at the top and the bottom, uniformity of the response in a cylinder, energy and position resolution of the detector, etc.; 2) to study the structure of the central detector; 3) to investigate the long term stability of the liquid scintillator; 4) to practice detector calibration; 5) to provide necessary information for the Monte Carlo simulation.

5.7.1 Configuration of the prototype

As shown in Fig. 5.19, the prototype consists of two cylinders: the inner cylinder is a transparent acrylic vessel with the dimension of 0.9 m in diameter, 1 m in height, and 1 cm in wall thickness. The outer cylinder is a 2 m diameter, 2 m height stainless steel barrel. Currently, the acrylic vessel is filled with normal liquid scintillator, while Gd-loaded liquid scintillator is planed for the near future. The liquid scintillator consists of 30% mesitylene, 70% mineral oil with 5g/l PPO and 10mg/l bis-MSB. The space between the inner and outer vessel is filled with 4.8 tons of mineral oil. A total 45 8” Hamamatsu R5912 PMT’s, arranged in three layers and mounted in a circular supporting structure are immersed in mineral oil.

An optical reflector made of Al fiim is placed at the top and bottom of the cylinder to increase the effective coverage area from 10% to 14%. The scintillator light yield is about 10000 photons/MeV, and the expected detector energy response is about 200 p.e./MeV.

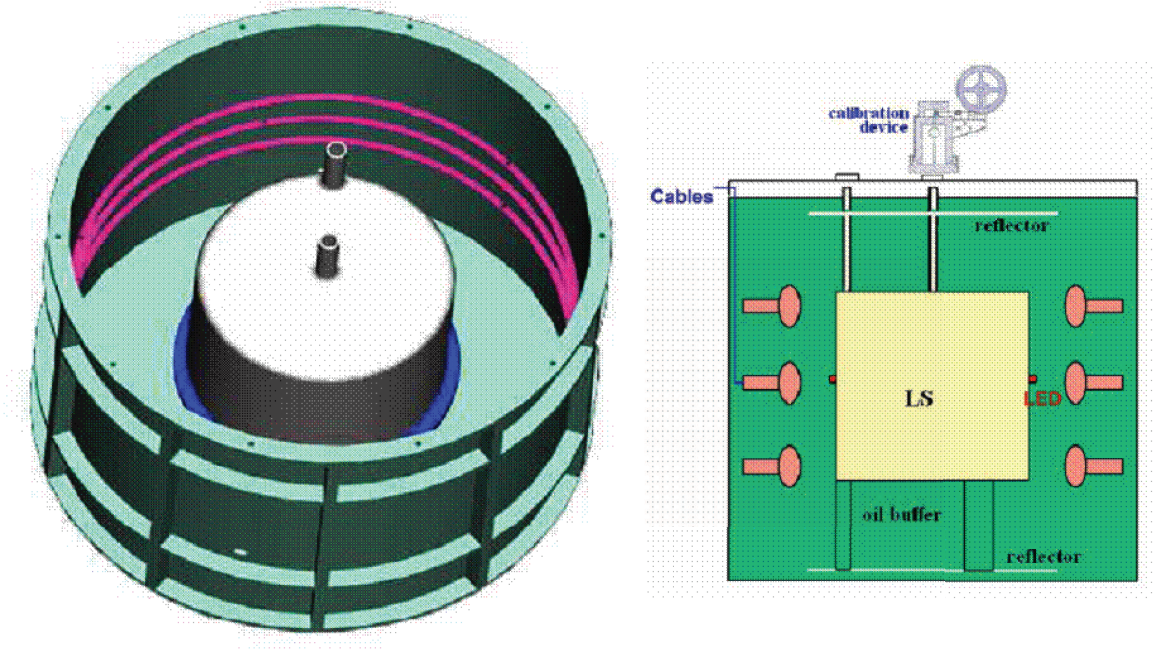

Fig. 5.19. Sketch of the prototype (Left) Top view, (Right) Side view.

The prototype is placed inside a cosmic ray anti-coincident detection frame, which has a dimension 3 m×3 m×3 m. It covers fully the five sides except the bottom. The top side is covered by 20 TOF counters (used earlier by the BES TOF system), each 15 cm wide × 3 m long. The four side walls are covered by 36 1.2 m×1.2 m square-shaped scintillation counters, which were used by the L3C experiment. Figure 5.20 shows a photograph of the prototype test setup, before and after the anti-coincident counters are mounted.

The readout electronics is designed according to the requirement discussed in previous section as a prototype. The trigger system, DAQ system and online software are all assemble that to be used in the experiment as a prototype.

5.7.2 Test result

Several radioactive sources including ^{133}Ba (0.356 MeV), ^{137}Cs (0.662 MeV), ^{60}Co (1.17 MeV, 1.33 MeV, 1.17+1.33 MeV) and ^{22}Na (1.022+1.275 MeV) are placed at different locations through a central calibration tube inside the liquid scintillator to study the energy response of the prototype. The gain of all PMTs are calibrated by using LED light sources, and the trigger threshold is set at 30 p.e., corresponding to about 110 KeV.

Fig. 5.21 shows the energy spectrum after summing up all PMT response for the ^{137}Cs source located at the center of the detector. A total of about 160 p.e. is observed, corresponding to an energy response of 240 p.e./MeV, higher than naive expectations. The Energy resolution can be obtained from a fit to spectra, resulting a value of about 10A detailed Monte Carlo simulation is performed to compare the experimental results with the expectation, as shown in Fig. 5.21. Very good agreement is achived, showing that the detector behaviour is well understood.

Sources with different energies as listed above are all tested at the center of the detector, resulting an

Fig. 5.20. The prototype test set up, before (left) and after (right) the anti-coincident detectors being mounted.

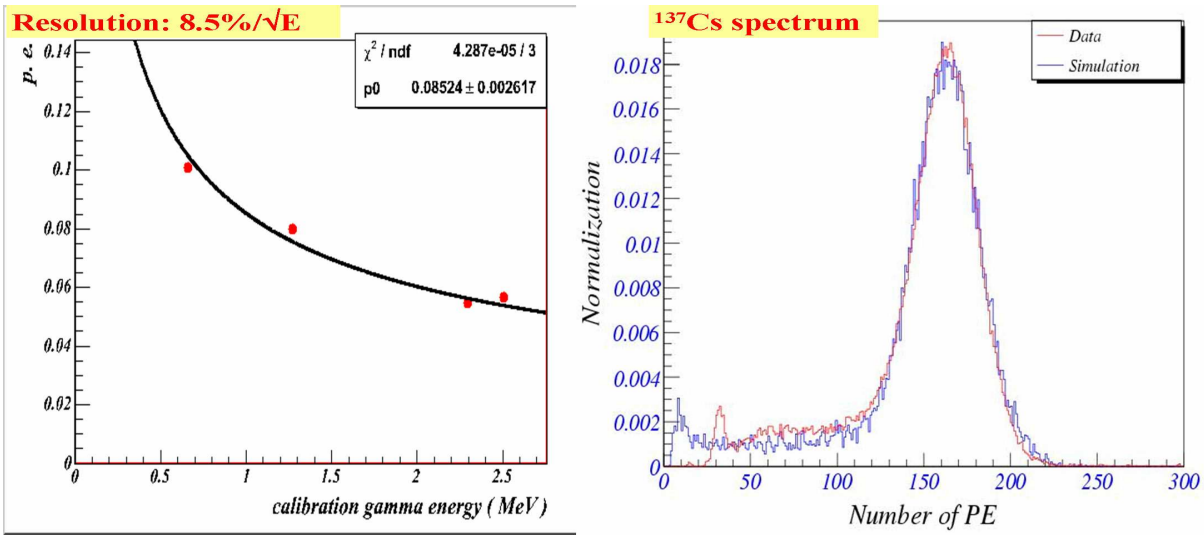

Fig. 5.21. Energy response of the prototype to ^{137}Cs source at the center of the detector with a comparision to Monte Carlo simulation.

energy response to different energies as shown in Fig. 5.22(left). Good linearity is observed although at low energies, non-linear effects possibly due to light quenching and Cherenkov lights are observed. The energy resolution at different energies is also shown in Fig. 5.22(right), following a simple expression of $9\%\sqrt{E}$, in good agreement with Monte Carlo simulation as shown in Fig. 5.21.

The energy response as a function of vertical depth along the Z axis is shown in Fig. 5.23. Very good uniformity (better than 10shows that the transparency of the liquid is good, and the light reflector at the top

Fig. 5.22. Energy response of the prototype to various sources at the center of the detector(left), and their energy resolution(right).

and the bottom of the cylinder works well as expected. The fact that the data and Monte Carlo expectation are in good agreemnt, as shown in Fig. 5.23, demonstrates that the prototype, including its light yield, light trasnport, liquid scintillator, PMT response, and the readout electronics is largely understood.

Fig. 5.23. Energy response of the prototype to ^{137}Cs sources as a function of z-coordinate, in comparison with Monte Carlo simulation.

1. R. Brun, F. Carminati, GEANT Detector Description and Simulation Tool, CERN Program Library Long Writeup W5013, September 1993.
2. C. Zeitnitz and T. A. Gabriel, The GEANT-Calor interface user's guide. September, 2001.
3. L. H. Miller, Ph.D thesis (unpublished), Stanford University (2000).
4. M. Apollonio *et al.* (Chooz Collaboration), Phys. Lett. B420, 397 (1998); Phys. Lett. B466, 415 (1999); Eur. Phys. J. C27, 331 (2003).
5. Boehm *et al.* (Palo Verde Collaboration), Phys. Rev. Lett. 84, 3764 (2000) [arXiv:hep ex/9912050]; Phys. Rev. D62, 072002 (2000) [arXiv:hep-ex/0003022]; Phys. Rev. D64, 112001 (2001) [arXiv:hep-ex/0107009]; A. Piepke *et al.*, Nucl. Instr. and meth. A432, 392 (1999).
6. K. Eguchi *et al.* (KamLAND collaboration), Phys. Rev. Lett. 90, 021802 (2003).
7. V. M. Novikov, Nucl. Instr. and Meth. A366, 413 (1995).
8. H. Back, I. R. Barabanov, J. Benziger, L. B. Bezrukov, A. Champagne, Z. Chang, V. Gavrin, A. Garnov, V. I. Gurentsov, R. L. Hahn, Y. Kamishkov, V. N. Kornoukhov, C. Musikas, M. Pitt, R. S. Raghavan, R. B. Vogelaar, E. A. Yanovitch, and M. Yeh, Proceedings of the 5th International Workshop B!B0Neutrino Oscillations and Their Origin (NOON 2004)B!B1, World Scientific Publishing Co., Eds. Y. Suzuki, M. Nakahata, S. Moriyama, Y. Koshio (University of Tokyo, Japan), June 2005.
9. C. Kraus, *et al.* (SNO+ Collaboration), Prog. Part. Nucl. Phys. **5 7** (2006) 150–152.
10. C. Galbiati, Borexino collaboration, Nucl. Phys. B (Proc. Suppl.) **143** (2005) 21–24.
11. KamLAND Collaboration: K. Eguchi *et al.*, Phys. Rev. Lett., **90** (2003) 021802 [arXiv:hep-ex/0212021]; **94** (2005) 081801 [arXiv:hep-ex/0406035].
12. M. Yeh, R. L. Hahn, A. Garnov, and Z. Chang, AIP Conf. Proc. **785** (2005) 209.
13. R. L. Hahn, Progress in Particle and Nuclear Physics, **57** (2006) 134–143.
14. M.Yeh, A. Garnov and R. L. Hahn, B!B0Gadolinium-Loaded Liquid Scintillator for High-Precision Measurements of Antineutrino Oscillations and the Mixing Angle, θ_{13}B!B1, submitted to Nucl. Instr. and Meth. **A** (2006)

6 Calibration and Monitoring Systems

The measurement of $\sin^2 2\theta_{13}$ to a precision of 0.01 in the Daya Bay experiment will require extreme care in the characterization of the detector properties as well as frequent monitoring of the detector performance and condition. The physics measurement requires that the neutrino flux be measured with *relative* precision that is substantially better than 1%. This is accomplished by taking ratios of observed event rates in the detectors at near and far sites to separate the oscillation effect. This will require that differences between detector modules be studied and understood at the level of $\sim$0.1% and that changes in a particular detector module (over time or after relocation at another site) be studied and understood at $\sim$0.1%. Achieving these goals will be accomplished through a comprehensive program of detector calibration and monitoring.

We anticipate a program with three different classes of procedures:

1.) "complete" characterization of a detector module,
2.) "partial' characterization, and
3.) routine monitoring.

We envision that the complete characterization (procedure 1.) will generally be performed once during initial commissioning of a detector module before taking physics data. Procedure 2.) would be employed after relocation of a detector module or after some other change that requires a careful investigation of the detector properties and will involve a subset of the activities in procedure 1.). If substantial changes are detected during procedure 2.), then we would likely opt for reverting to procedure 1.). Finally, procedure 3.) will involve both continuous monitoring of some detector parameters as well as frequent (i.e., daily or weekly) automated procedures to acquire data from LED light sources and radioactive sources deployed into the detector volume.

Requirement	Description	Proposed Solution(s)
Optical Integrity	Spatial uniformity of response, light attentuation	LED, gamma sources
PMT gains	Match gains of all PMT's	LED - single PE matching
PMT timing	$\sim$ 1 ns timing calibration for each PMT	Pulsed LED
Energy scale	Set scale of energy deposition	Gamma sources
H/Gd ratio	Measure relative Gd fraction	^{252}Cf neutron source

Table 6.1. Requirements for procedure 1.

The requirements and proposed solutions for procedure 1.) are listed in Table 6.1. These will be manually operated procedures using equipment and systems to be described below, and will likely entail several weeks activity.

Requirement	Description	Proposed Solution(s)
Mechanical/thermal	Verify these properties are stable	Load sensors, thermometers, etc.
Optical stability	Track variations in light yield	Gamma sources, spallation products
Uniformity, light attenuation	Monitor spatial distribution of light	Gamma sources, spallation products
Detection efficiency	Monitor ϵ for neutrons and positrons	Gamma sources, neutron sources
PMT gains	Monitor 1pe peaks	LED source

Table 6.2. Requirements for procedure 3.

Procedure 2.) will be a subset (to be determined) of the activities in procedure 1.) These will be also be manually operated procedures using equipment and systems to be described below, and will likely entail several days activity.

The requirements and proposed solutions for procedure 3.) are listed in Table 6.2. Procedure 3.) will entail continuous in-situ monitoring (Sec. 6.3), monitoring of continuously produced spallation-induced activity (Sec. 6.4), and regularly scheduled automated deployment of sources (Sec. 6.5).

6.1 Sources

The main goal of the source calibration is to reach the maximum sensitivity to neutrino oscillations by comparing the energy spectra measured by near and far detectors. The response of the detectors for far and near site may have small differences, these minute differences can lead to slight distortion in the measured energy spectra of the antineutrinos. Therefore, it is necessary to characterize the detector properties carefully before data taking and monitor the stability of the detectors during the whole experiment. The calibration sources must be deployed regularly throughout the active volume of the detectors to simulate and monitor the detector response to positrons, neutron capture gammas and gammas from the environment.

The sources will be used in the calibration are listed in Table 6.3. These sources cover the energy range

Sources	**Calibrations**
Neutron sources:	Neutron response, relative and
Am-Be and ^{252}Cf	absolute efficiency, capture time
Positron sources:	Positron response, energy scale
^{22}Na, ^{68}Ge	trigger threshold
Gamma sources:	Energy linearity, stability, resolution
	spatial and temporal variations, quenching effect
^{137}Cs	0.662 MeV
^{54}Mn	0.835 MeV
^{65}Zn	1.351 MeV
^{40}K	1.461 MeV
H neutron capture	2.223 MeV
^{22}Na	annih + 1.275 MeV
^{60}Co	1.173 + 1.333 MeV
^{208}Tl	2.615 MeV
Am-Be	4.43 MeV
^{238}Pu-^{13}C	6.13 MeV
Gd neutron capture	$\sim$ 8 MeV

Table 6.3. Radioactive sources to be used for the calibration

from about 0.5 MeV to 10 MeV, thus they can be used as energy calibration.

The Am-Be source can be used to calibrate the neutron capture detection efficiency by detecting the 4.43 MeV gamma in coincidence with the neutron. The absolute neutron detection efficiency can be determined with a ^{252}Cf source, because the neutron multiplicity is known with an accuracy of about 0.3%. In order to absolutely determine the neutron detection efficiency, a small fission chamber will be used to tag neutron events by detecting the fission products. In addition, neutron sources allow us to determine the appropriate thresholds of neutron detection and to measure the neutron capture time for the detectors.

The positron detection can be simulated by ^{22}Na source. When a ^{22}Na source emits a 1.275 MeV gamma, a low energy positron will emitted along with the gamma and then annihilate. The primary gamma

and the following annihilation gammas mimic the the antineutrino event inside the detector.

The sources must be encapsulated in a small container to prevent any possible contamination of the ultra-pure liquid scintillator. They can be regularly deployed to the whole active volume of the detectors and the gamma catcher.

6.2 LED Calibration System

LEDs have proven to be reliable and stable light sources that can generate fast pulses down to ns width. They are therefore ideal light sources for checking the optical properties of the liquid scintillator, the performance of the PMTs and the timing characteristics of the data acquisition systems. A schematic diagram of the LED calibration system is shown in Fig. 6.1.

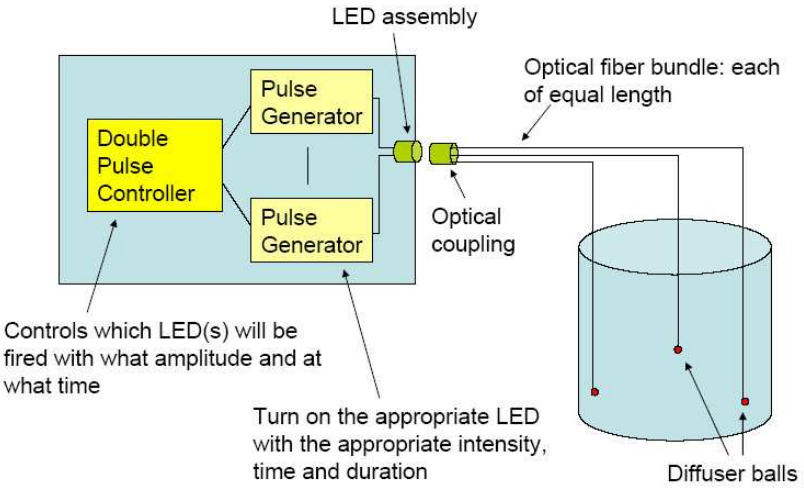

Fig. 6.1. Schematic diagram of the LED calibration system.

The LED controller box controls the pulsing of the individual LEDs which are coupled through optical fibers to diffuser balls installed inside the detector module. To ensure consistency among detector modules, a single controller box will be used and it can be coupled to the optical fiber bundle of each detector module when needed. Some of the features of the controller box are as follows:

- The pulse heights of each of the double pulses and their separation are fully programmable to simulate the scintillation light produced in an inverse beta-decay interaction. The first pulse will simulate the annihilation photons and direct energy deposition from the positron and the second pulse will simulate the gamma burst resulting from neutron capture on Gd.
- The pulse separation can be generated randomly or stepped gradually.
- The gamma burst can be simulated by simultaneously flashing a number of diffuser balls at various locations inside the detector.
- The controller can be triggered by the muon veto system to test the detector response following muon events.

The performance of the LEDs will be checked regularly against scintillation produced by a gamma source in a solid scintillator viewed by a PMT. This could be done by coupling the controller box to an optical fiber

bundle that is viewed by the same PMT. The number of diffuser balls and their locations inside the central acrylic vessel and the gamma catcher will be determined through computer simulation. Most of the diffuser balls will be fixed while a few can be moved in the vertical direction by using the same deployment system for radioactive source calibration. The diffuser balls and optical fibers will have to be fully compatible with liquid scintillator.

6.3 In-situ Detector Monitoring

Each detector module will be equipped with a suite of devices to monitor in-situ some of the critical detector properties during all phases of the experiment The in-situ monitoring includes load and liquid sensors for the detector mass, attenuation length measurements of the Gd-loaded LS target and the LS gamma catcher, a laser-based monitoring system for the position of the acrylic vessel, accelerometers, temperature sensors, and pressure sensors for the cover gas system. A sampler for routine extraction of a LS sample complements this multi-purpose suite of monitoring tools.

The purpose of these tools is to provide close monitoring of the experiment during three critical phases of the experiment:

1. detector filling
2. data taking
3. detector transport and swapping

During filling of the modules the changing loads and buoyancy forces on the acrylic vessels and the detector support structure are carefully monitored with load and level sensors to ensure that this dynamic process does not exceed any of the specifications for the acrylic vessels.

Most of the time during the duration of the experiment the detectors will be stationary and taking data. Experience from past experiments has shown that the optical properties of detectors will change over time due to changes in the attenuation lengths of the liquid scintillator or changes in the optical properties of the acrylic vessel. It is important to track these characteristics to be able to explain any possibly changes in the overall detector response as determined in the regular, automated calibration. In-situ monitoring of the LS attenuation length and regular extractions of LS samples from the detector modules will help monitor some of the basic detector properties.

The transport of the filled detectors to their location and the swapping of detectors over a distance of up to 1.5km is a complex and risky task that will require close monitoring of the structural health of the detectors modules during the move. The proposed swapping scheme of the detectors is a novel method without proof-of-principle yet. While conceptually very powerful, extreme care has to be taken in the calibration and characterization of the detectors before and after the move to be able to correct for all changes in the detector response or efficiencies. The accelerometers, pressure sensors, and the monitoring of the AV positions will provide critical real-time information during this procedure to ensure that the detectors – and in particular the acrylic vessels and PMTs – are not put at risk. Recording any changes in the detector modules will also help us understand possible differences in the detector response before and after the move. The AV position monitoring system will use a laser beam and reflective target on the AV surfaces. By measuring the angular deflection of the laser beam over the length of the detector transverse displacements of the AV can be monitored quite precisely.

6.4 Detector monitoring with data

Cosmic muons passing through the detector modules will produce useful short-lived radioactive isotopes and spallation neutrons. These events will follow the muon signal (detected in the veto as well as the detector) and will be uniformly distributed throughout the detector volume. Therefore, these provide

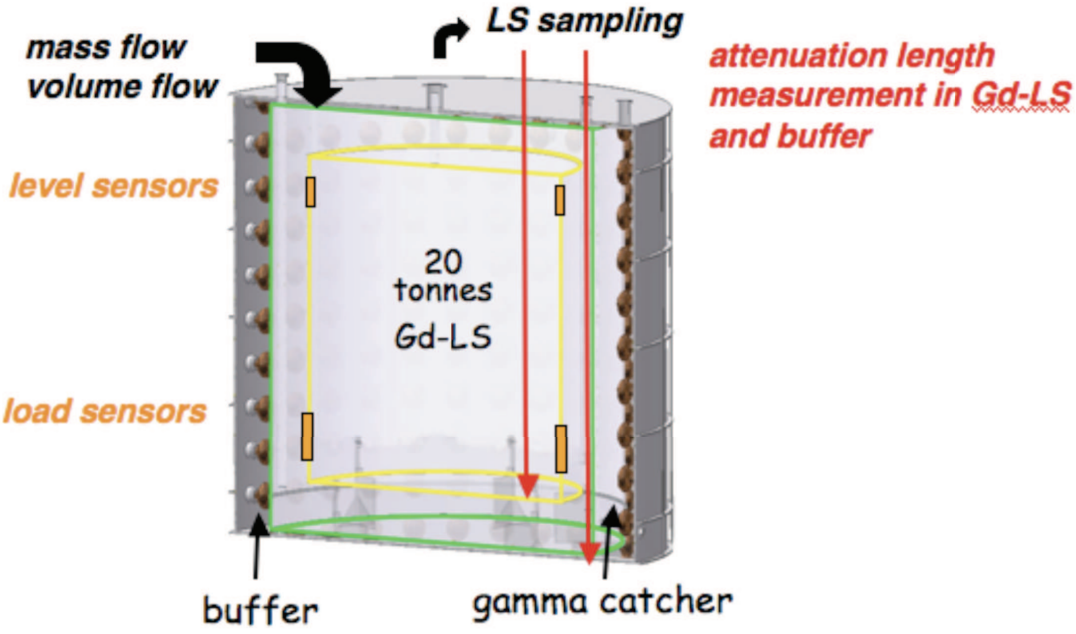

Fig. 6.2. Diagram illustrating the variety of monitoring tools we will integrate into the design of the detector modules.

very useful information on the full detector volume which is complementary to the information obtained by deploying point sources (Sec. 8.5 and 8.6). For example, such events are used by KamLAND to study the energy and position reconstruction as well as to determine the fiducial volume. As for KamLAND, the Daya Bay experiment will use primarily spallation neutron capture and ^{12}B decay ($\tau = 29.1$ ms and $Q = 13.4$ MeV). The rates of these events for Daya Bay are given in Table 6.4.

Event type	Near Site Rate	Far Site Rate
Neutrons	9000/day	400/day
^{12}B	180/day	8/day

Table 6.4. Estimated production rates (per 20 T detector module) for spallation neutron and ^{12}B events in the Daya Bay experiment.

Regular monitoring of the full-volume response for these events, compared with the regular automated source deployments, will provide precise information on the stability (particularly of optical properties of the detector, but also general spatial uniformity of response) of the detector modules. With the addition of Monte Carlo simulations, this comparison can be used to accurately assess the relative efficiency of different detector modules as well as the stability of the efficiency of each module.

6.5 Automated deployment

Automated deployment systems will be used to monitor all detector modules on a routine (perhaps daily) basis. Each detector module will be instrumented with three (or possibly four) identical automated deployment systems. Each system will be located above a single port on the top of the detector module,

and will be capable of deploying four different sources into the detector volume (see Fig. 6.3). This will be

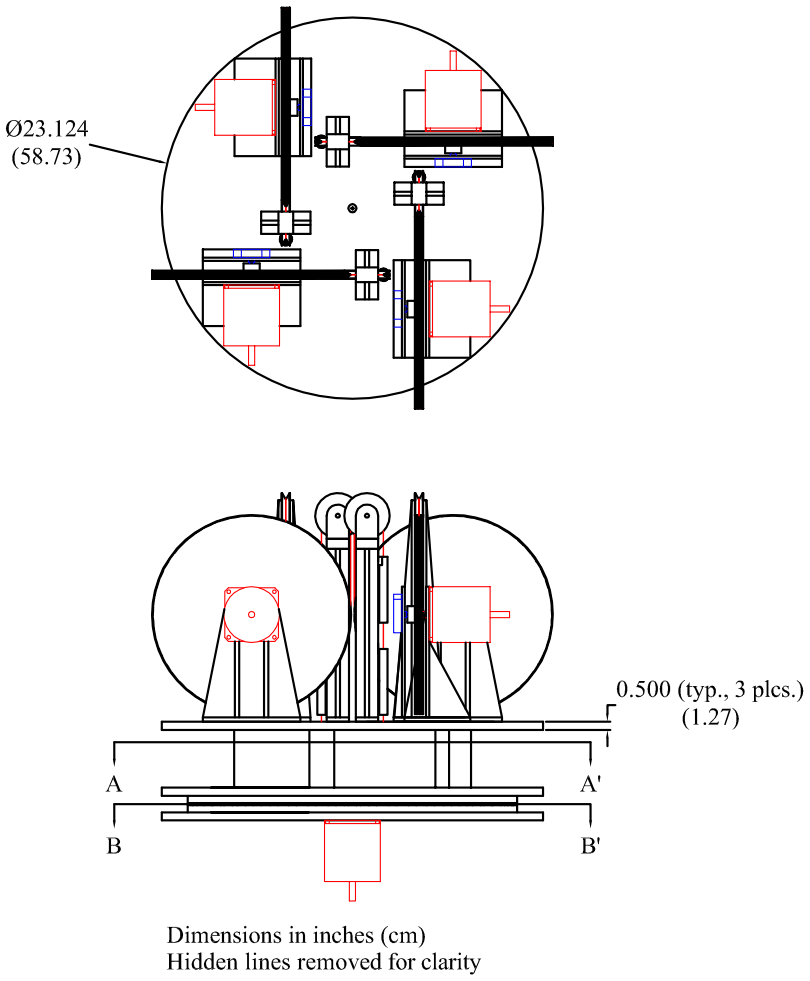

Fig. 6.3. Schematic diagram of the automated deployment system concept.

facilitated by four independent stepping-motor driven source deployment units all mounted on a common turntable. The turntable and deployment units will all be enclosed in a sealed stainless steel vessel to maintain the isolated detector module environment from the outside. All internal components must be certified to be compatible with liquid scintillator. The deployment systems will be operated under computer-automated control in coordination with the data acquisition system (to facilitate separation of source monitoring data from physics data). Each source can be withdrawn into a shielded enclosure on the turntable for storage. The deployed source position will be known to about 2 mm.

At present, we anticipate including three radioactive sources on each deployment system:

- ^{68}Ge source providing two coincident 0.511 MeV γ's to simulate the threshold positron signal,
- ^{60}Co source providing a γ signal at 2.506 MeV

- ^{252}Cf fission source to provide neutrons that simulate the neutron capture signal.

These sources can be deployed in sequence by each of the systems on each detector module. During automated calibration/monitoring periods, only one source would be deployed in each detector module at a time. Simulation studies are in progress to determine the minimal number of locations necessary to sufficiently characterize the detector (in combination with spallation product data as discussed in section 6.4). At present we anticipate that three or four radial locations will be sufficient with at least three as follows:

- Central axis
- A radial location in the central Gd-loaded volume near (just inside) the inner cylindrical acrylic vessel wall
- A radial location in the gamma-catcher region.

An additional radial location may be instrumented if it is demonstrated to be necessary by the ongoing simulation studies.

Simulation studies indicate that we can use these regular automated source deployments to track and compensate for changes in:

- average gain of the detector (photoelectron yield per MeV)
- number of PMT's operational
- scintillation light attenuation length

as well as other optical properties of the detector system.

As an example of how the system can be utilized to monitor the attenuation length of the scintillator, Figure 6.4 shows simulations of neutron captures and ^{60}Co source deployments. Both methods can clearly be used to measure the attenuation length of the Gd-loaded liquid scintillator. Thus these methods will provide frequent monitoring of the condition of the scintillator, and will allow us to track changes and differences between detector modules.

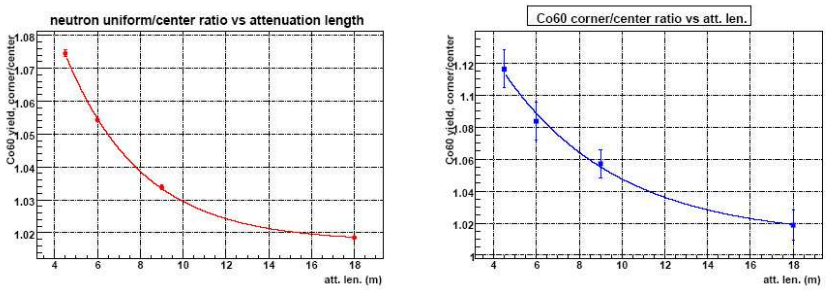

Fig. 6.4. The left panel shows how the scintillator attenuation length can be determined from the ratio of the neutron capture peak from spallation neutrons (uniform distribution) to that from a source at the center of the detector. The right panel shows a similar measurement using the ratio of the ^{60}Co peak for a source at the center to one at the corner ($r = 1.4$ m, $z = 1.4$ m) of the central volume (1000 events each).

6.6 Manual deployment system

A mechanical system will be designed to deploy sources throughout the active volume of the detectors. The source inside the detector can be well controlled and the position can be repeated at a level less than 5 cm. The whole deployment system must be treated carefully to prevent any contamination to the liquid scintillator. The system must be easy to setup and operate, tolerate frequent use and must have a reliable method to put sources into the detectors and to take the sources out as well. The space for operation should not be too large.

Figure 6.5 shows the schematic view of the manual source deployment system. The philosophy of such

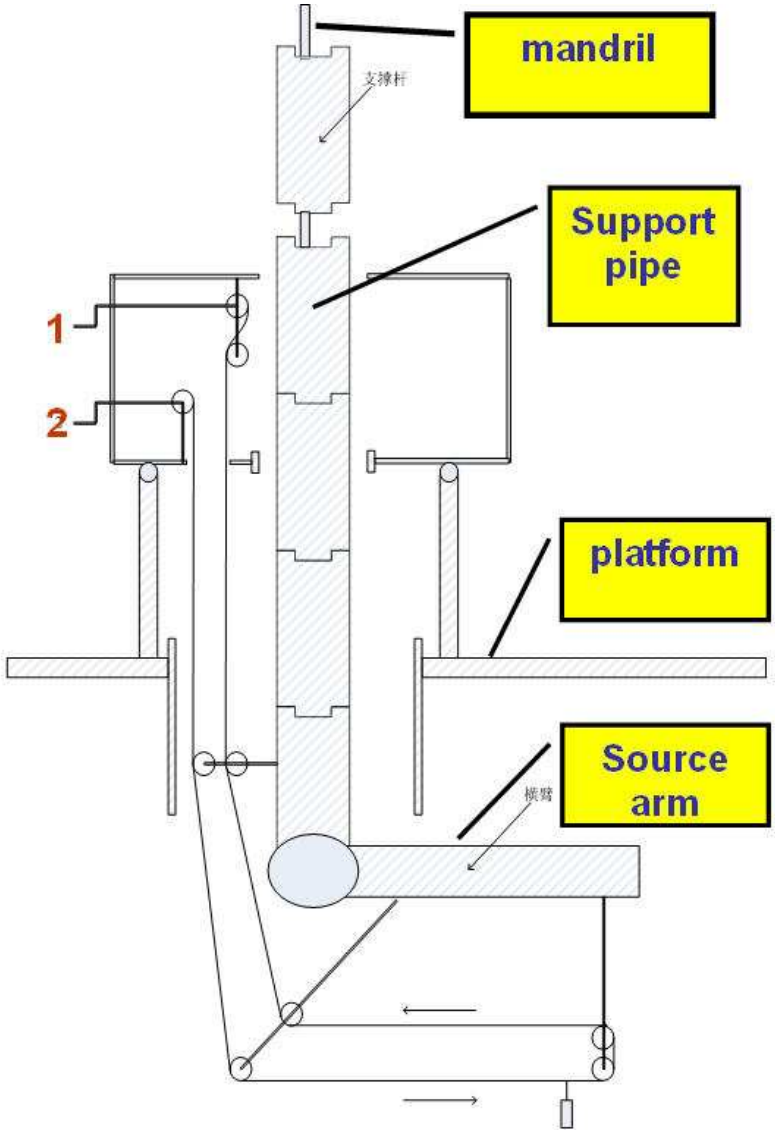

Fig. 6.5. Schematic diagram of the manual source deployment system.

a system is taken from the oil drilling system. The support pipe is separated into several segments. They can be connected one by one to get a long support pipe. This design would reduce the requirement for larege space for operations.

The operation procedure will be the following: first, the support pipe and the source arm will be installed

in line (vertical). Then, it will be put into the desired position inside the detector, by adjusting the number of segments. When it reach the measurement position, turn the source arm to horizontal. After this, the source position can be adjusted by the rope system. The rope system must be designed to insert and remove the sources easily and the position of the source must be accurately controlled. The whole system can be rotated around the axis of the pipe on the platform, thus it can deploy the sources to any position inside the detector.

6.7 Manufacturing plan

The radioactive sources and the manual deployment system will be fabricated at the Chinese Institute for Atomic Energy (CIAE) in Beijing. The LED calibration system will be fabricated at Hong Kong University. The automated deployment system will be fabricated at the California Institute of Technology. Continuous monitoring of detector module mechanical and thermal properties will be implemented by the group at the University of Wisconsin.

6.8 Integration/installation

All of these calibration/monitoring systems are to be coupled to the detector module. Entry ports in the stainless steel and acrylic vessels, guide tubes, clearance for mounting hardware, etc. must be accounted for in the mutual design efforts of the detector module and calibration/monitoring systems. Therefore, it is essential that the designs of the detector modules and calibration/monitoring hardware be closely coordinated. The calibration/monitoring systems will be installed during the assembly of the detector module at the Daya Bay site.

6.9 Quality assurance, risk, ES&H, Environment, management

Introduction of materials (particularly radioactive sources) into the detector volume requires strict adherence to certification procedures and administrative controls to prevent contamination or degradation of the detector. All materials must be certified to be compatible with the liquid scintillator, thoroughly cleaned, and radioassayed to prevent contamination of the detector by radioactive substances. Radioactive sources must be carefully tested to certify that they can not leak radioactive material into the detector. The deployment systems must operate in a closed common atmosphere, free of Rn, through gate valves.

7 Muon System

7.1 Introduction

The main backgrounds to the Daya Bay Experiment are induced by cosmic-ray muons. These backgrounds are minimized by locating the detectors underground with maximum possible overburden. Background due to muon spallation products at the depths of the experimental halls as well as ambient gamma background due to the radioactivity of the rock surrounding the experimental halls is minimized by shielding the antineutrino detectors with 2.5 meters of water. The ten-folding length of water for 1–2 MeV gammas is about 50 cm [1]. Thus the 2.5 meters of water provides a five order of magnitude reduction in the rock gamma flux. This "water buffer" also attenuates the flux of neutrons produced outside the water pool.

Events associated with fast neutrons produced in the water itself remain a major potential background. A system of tracking detectors will be deployed to tag muons that traverse the water buffer. Events with a muon that pass through the water less than 200μs before the prompt signal, which have a small but finite probability of creating a fake signal event, can be removed from the data sample without incurring excessive deadtime. By measuring the spectrum of the tagged background events and having precise knowledge of the the tagging efficiency of the tracking system, the background from untagged events (due to tagging inefficiency) can be estimated and subtracted statistically with small uncertainty. Our goal is to keep the uncertainty of this background below 0.1%.

The tracking system will also tag events that have high propensity for producing other cosmogenic backgrounds, ^{9}Li being the most important one. While tagging muon showering events may help to suppress the ^{9}Li background, the working assumption is that no extra requirements are imposed on the tracker in order to reduce the ^{9}Li background.

The current baseline configuration for meeting these challenges is shown schematically in Fig. 7.1. The anti-neutrino detectors are separated by 1 m from each other and immersed in a large pool of highly-purified water. The pool is rectangular in the case of the near halls and square in the case of the far hall. The minimum distance between the detectors and the walls of the pool is 2.5 m. The water shield constitutes the inner section of the pool and is instrumented with phototubes to detect Čerenkov photons from muons impinging on the water. The sides and bottom of the pool are lined with 1 m $\times$ 1 m cross-section water tanks read out by phototubes at either end. The muon tracker is completed by layers of Resistive Plate Chambers (RPC's) above the pool. The top veto extends 1 m beyond the edge of the pool in all directions, both to minimize the gaps in veto coverage and to allow studies of background caused by muon interactions in the rocks surrounding the pool.

Note that it is not envisioned that this system will act as an online veto. This will allow ample opportunity for careful studies to optimize the performance of the system.

Requirements of the muon system are summarized in more detail in the following subsections.

7.1.1 Muon Detection Efficiency

The combined efficiency of the muon tracker and the water shield has to exceed 99.5%, with an uncertainty $< 0.25\%$. This is driven by the need to reject the fast neutron background from muon interactions in the water and to measure its residual level. As can be seen in Table 3.5, without suppression, this background would otherwise be $\geq$30 times that of the fast neutron background from muon interactions in the surrounding rock, *i.e.* at a level roughly 5% of that of the signal. A factor 200 reduction in this rate brings the fast neutron background from the water safely below that from the rock, and the total residual fast neutron background down to the 0.1% level. The requirement on the uncertainty in the efficiency brings the systematic due to the uncertainty on the fast neutron background from the water to a level where it is small compared with other systematics.

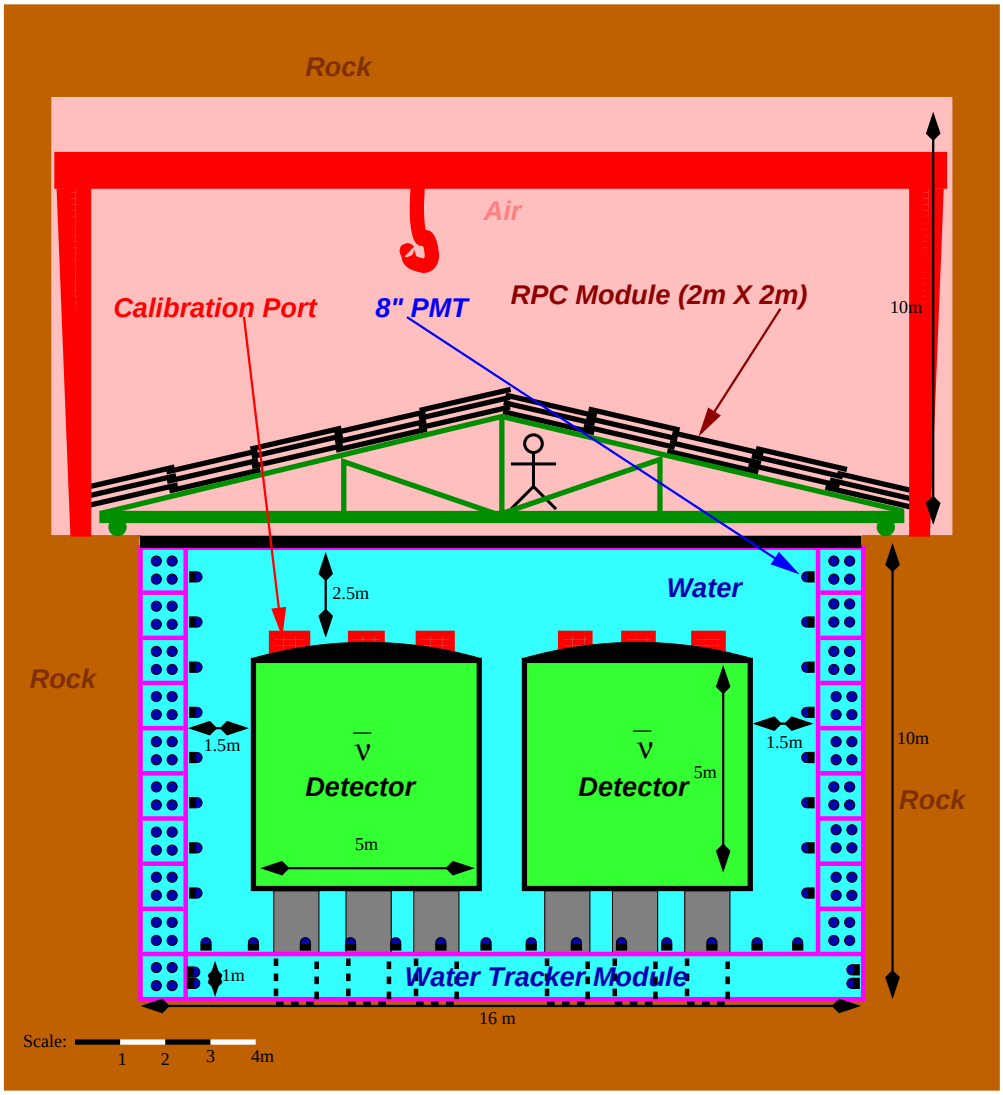

Fig. 7.1. Elevation view of experimental hall.

7.1.2 Redundancy of the Tracker

It is difficult to achieve the requisite efficiency with only one tracking system. Moreover it is necessary to have a method of measuring the residual level of background after the imposition of the muon rejection cuts. Therefore it is desirable to have two complementary tracking systems to cross check the efficiency of each system.

As discussed below, the current baseline design is to instrument the water shield as a Čerenkov tracker by deploying large PMT's in the water with 1.6% coverage. Such systems are expected to have >95% efficiency. A second tracking system, in our baseline a combination of RPC's [2] [3] above and water Čerenkov modules [4] at the sides and bottom of the water shield, can give an independent efficiency of >90%. The two systems compliment each other, with the probability of a muon being missed by both systems below 0.5%.

7.1.3 Spatial Resolution

The fast neutron background due to muons interacting in the water shield falls rapidly with distance from the muon track. The spatial resolution of the muon tracker should be sufficient to measure this falloff. Measurements from previous experiments show that the falloff is about 1 meter [5]. A spatial resolution of 50–100 cm in the projected position in the region of the central detectors is necessary in order to study this radial dependence. All the technologies we are considering are capable of achieving sufficient resolution in each coordinate.

7.1.4 Timing Resolution

There are several constraints on the timing resolution. The least restrictive is on the time registration of the muon signal with respect to that of the candidate event. To avoid compromising the veto rejection to a significant extent, this resolution need only be in the range of fractions of a microsecond. More stringent requirements are imposed by other, technology-dependent, considerations. The water shield pmts need $\sim$2 ns resolution to minimize the effect of accidentals and assure event integrity. The water Cerenkov modules require $\sim$3 ns resolution to match the position resolution given in the transverse direction by the 1 m granularity of the system (see Sect. 7.3.6). If scintillator strips are used, 1ns time resolution will allow the random veto deadtime from false coincidences in that system to be held to the order of 1%. RPCs will need $\sim$ 10 ns resolution to limit random veto deadtime from false coincidences in that system a similar level.

7.1.5 Thickness

As mentioned above the shield must attenuate γ's and neutrons from the rock walls of the cavern by large factors to reduce the accidental background in the antineutrino detectors. A minimum thickness of 2 m of water is required; 2.5 m gives an extra margin of safety.

7.1.6 Summary of Requirements

The requirements discussed above are summarized in Table 7.1

Product of inefficiencies for the μ tracker & water shield for cosmic rays should be $\leq$0.5%.
The uncertainty on this quantity should be no greater than $\pm$0.25%.
The uncertainty on the random veto deadtime should be no greater than $\pm 0.05\%$
The position of the muon in the region of the antineutrino detectors should be determinable to $\leq$ 1m
Timing resolution of $\pm$ 1, 2, 3 10 ns for scintillator, water shield, water Č modules, and RPCs respectively
Thickness of the water buffer of at least 2 m

Table 7.1. Muon veto system requirements

7.2 Water Buffer

The neutrino detectors will be surrounded by a buffer of water with a thickness of at least 2.5 meters in all directions. Several important purposes are served by the water. First, fast-neutron background originating from the cosmic muons interacting with the surrounding rocks will be significantly reduced by the water. Simulation shows that the fast-neutron background rate is reduced by a factor of 2 for every 50-cm of water. Second, the water will insulate the neutrino detectors from the air, reducing background from the radon in the air as well as gamma rays from surrounding rocks and dust in the air. With the low-energy gamma ray flux reduced by a factor of 10 per 50-cm of water, the water can very effectively reduce the accidental background rate associated with the gamma rays. Third, the inner portion of the water buffer, the "water shield" can be instrumented with PMT's for observing the passage of cosmic muons via the detection of the Ĉerenkov light.

Table 7.2. Number of PMT's for the water shield.

Site	bottom	sides	total
DB Near	60	192	252
LA Near	60	192	252
Far	100	240	340
All three	220	624	844

The active water shield, together with the RPC and the Ĉerenkov water module detectors, form an efficient muon tagging system with an expected overall efficiency greater than 99.5%. The ability to tag muons with high efficiency is crucial for vetoing the bulk of the fast-neutron background, and for determining the amount of cosmogenic ^{8}He/^{9}Li background. Finally, the large mass of water can readily provide a constant operating temperature for the anti-neutrino detectors at the near and far sites, eliminating one potential source of systematic uncertainty

7.2.1 Water shield configuration

The schematics of the water shield is illustrated in Fig. 7.1 for the water pool configuration. The cylindrical neutrino detector modules are placed inside a rectangular cavity filled with purified water, *i.e.* a water pool configuration. The dimensions of the water pool are 16 m$\times$16 m$\times$10 m (high) for the far site, and 16 m$\times$10 m$\times$10 m (high) for the near sites. The four detector modules in the far site will be immersed in the water pool forming a 2 by 2 array. As shown in Fig. 7.1, the adjacent detector modules are separated by 1 meter and each module is shielded by at least 2.5 meters of water in all directions. For the near sites, the two neutrino detector modules are separated by 1 meter. Again, any neutrons or gamma rays from the rock must penetrate at least 2.5 m of water in order to reach the neutrino detector modules. The weight of water is 2170 tons and 1400 tons, respectively, for the far site and for each of the two near site detectors.

As discussed in Sect. 7.3.6, Ĉerenkov water module detectors of 1 m$\times$1 m cross sectional area and lengths of up to 16 m will be laid against the four sides and the bottom of the water pool, shown in Fig. 7.1. Therefore, the water buffer is effectively divided into two independent sections, each capable of cross-checking the performance of the other.

7.2.2 PMT layout of the water shield

The water shield will be instrumented with arrays of 8" PMT as shown in Fig. 7.1. Inward-viewing PMT arrays will be mounted on frames placed at the sides and on the bottom of the pool, abutting the inner surfaces of the Ĉerenkov water modules. The PMT's will be evenly distributed forming a rectangular grid with a density of 1 PMT per 2 m^2. This corresponds to a 1.6% areal coverage. The total number of PMT's for the far site and the two near sites is 844,as detailed in Table 7.2.

A total of 800 8" PMT's (EMI D-642) from the MACRO experiment were made available for the Daya Bay experiment. Additional 8" Hamamatsu PMT's will be acquired for the balance of the water shield detectors. The HV system will be very similar to that described in Sect. 5.5 for the central detector pmts.

7.2.3 Readout electronics of the water shield PMT

The readout electronics for the water shield PMT will be identical to that for the neutrino detector as described in Sect. 5.6. This readout electronics will have a dynamic range of 1 to 500 photoelectrons. The total number of photoelectrons for typical bialkali photo-cathodes with full geometric coverage for a fast muon passing through one meter of water is approximately 4000. Given the current water shield configuration, most muons would traverse at least 5 meters of water. Taking into account the 1.6% PMT

geometric coverage, these muons would produce at least 320 photoelectrons in the PMT's. Depending on the trajectories of these muons, these photoelectrons will be distributed over at least 16 PMT's. Therefore, the dynamic range of 1 to 500 photoelectrons for the readout is entirely adequate. In addition to the pulse height information, timing information will also be provided by the readout electronics. A timing resolution of 2 nsis easily achievable for a single PMT channel. The energy sum of the PMT's as well as the multiplicity of the struck PMT's will be used for defining the muon trigger (see Sect. 8.1.2.2.

7.2.4 Calibration of the water shield PMT

The gain stability and the timing of the PMT's will be monitored by a LED/Laser system identical to that for the neutrino detectors. No radioactive sources will be required.

7.2.5 Purification scheme of the water shield

We must purify the water to maintain constant water transparency and prevent microbial growth.

We must also recirculate to the water to maintain a constant relatively low temperature (15°C) to inhibit microbial growth and maintain the scintillator at constant temperature. Also, we must remove impurities that have leached into the water from the detector materials and wall during recirculation.

The level of purity needed to prevent growth will reduce radioactive backgrounds to well below the level where they would make detectable background in the central detectors.

7.2.6 Expected performance

Optimized efficiency, position resolution, energy resolution, timing resolution, etc. are to be determined from Monte-Carlo simulations now in progress.

7.3 Muon Tracker

The muon tracker has the job of tagging the entering muons and determining their path through the region of the central detectors. In addition, it must measure the efficiency of the water shield for muons.

Three technologies are being considered for the muon tracker. RPC's can be used on top of the water shield, but to use them in the water would require a large program of R&D on techniques of encapsulation. Water Čerenkov modules are cheap and practical to operate in the water, but would be difficult to remove from the top of the water shield when the central detectors need maintenance or have to be moved. Plastic strip scintillators can be operated either on top of the water or in it, although the latter requires developing an encapsulation scheme.

7.3.1 Resistive Plate Chambers

The RPC is an attractive candidate tracking detector since it is economical for instrumenting large areas. Furthermore, RPC's are simple to fabricate. The manufacturing technique for both Bakelite (developed by IHEP for the BESIII detector [2]) and glass RPC's (developed for Belle [3]) are well established.

An RPC is composed of two resistive plates with gas flowing between them. High voltage is applied on the plates to produce a strong electric field in the gas. When a charged particle passes through the gas, an avalanche or a streamer is produced. The electrical signal is then registered by a pickup strip and sent to the data acquisition system. In our case, the RPC's will operate in the streamer mode.

The RPC's for the BESIII spectrometer were constructed using a new type of phenolic paper laminates developed at IHEP. The surface quality of these plates is markedly improved compared to the Bakelite plates previously used to construct RPC's. IHEP has developed a technique to control the resistivity of the laminates to any value within a range of $10^9 - 10^{13}$ Ω. About 1000 bare chambers ($\sim$1500 m^2) have been produced for BESIII. Tests show that the performance of this type of RPC without a linseed oil coating is comparable to RPC's made with linseed oil-treated Bakelite and resistive glass RPC's operated in streamer mode.

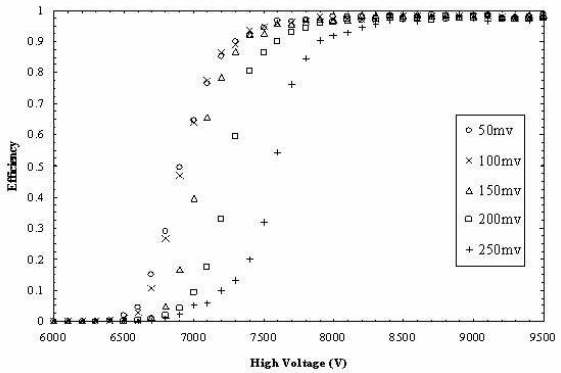

Fig. 7.2. Efficiency of the BESIII RPC versus high voltage for different thresholds.

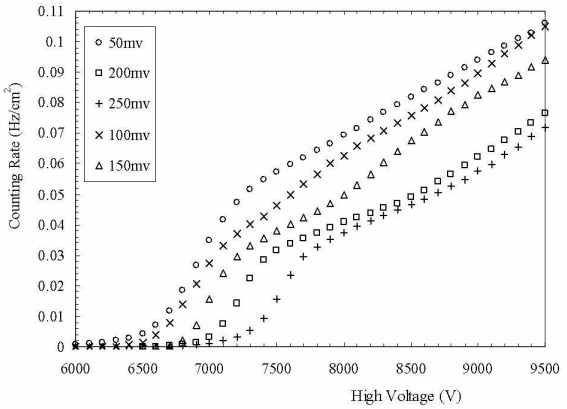

Fig. 7.3. Noise rate of the BESIII RPC versus high voltage for different thresholds.

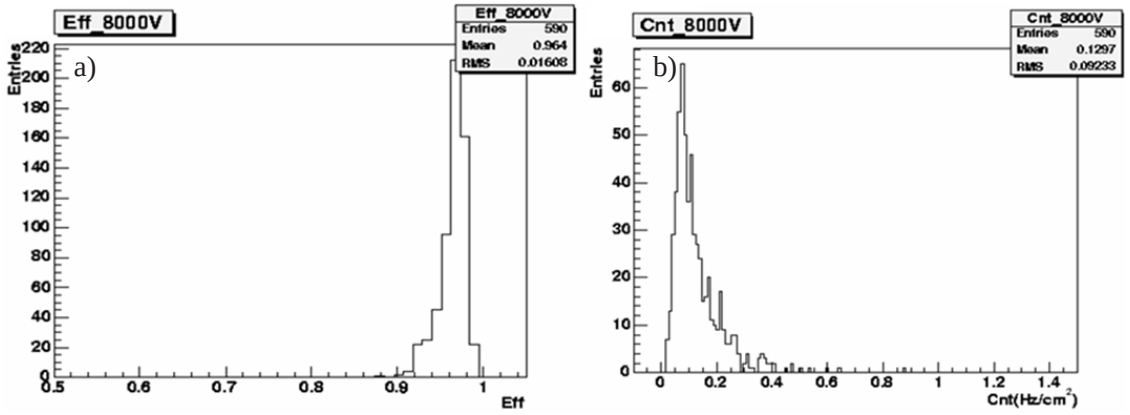

Fig. 7.4. Distribution of tested RPC a) efficiencies and b) singles rates.

The efficiency and noise rate of the BESIII RPC's have been measured. In Fig. 7.2, the efficiencies versus high voltage are shown for threshold settings between 50 and 250 mV. The efficiency as plotted does not include the dead area along the edge of the detector, but does include the dead region caused by the insulation gasket. This kind of dead area covers 1.25% of the total detection area. The efficiency of the RPC reaches plateau at 6.8 kV and rises slightly to 98% at 7.2 kV. There is no obvious difference in efficiency above 7.0 kV for thresholds below 250 mV. The singles rate of the RPC shortly after production is shown in Fig. 7.3.

When the threshold is 150 mV or higher, the singles rate is less than 0.16 Hz/cm^2.After training it typically falls to $<$0.1 Hz/cm^2.The noise rate increases significantly when the high voltage is higher than 8 kV.

In cosmic ray tests of a large sample of BES chambers, the average efficiency was 97%, and only 2 had efficiency less than 92%. Fig. 7.4a shows the efficiency distribution. This efficiency was obtained with no corresponding excessive chamber noise. Fig. 7.4b shows the RPC's singles rate. The most probable value was $\sim$0.08 Hz/cm^2 and the average was 0.13 Hz, with only 1.5% higher than 0.3 Hz/cm^2.

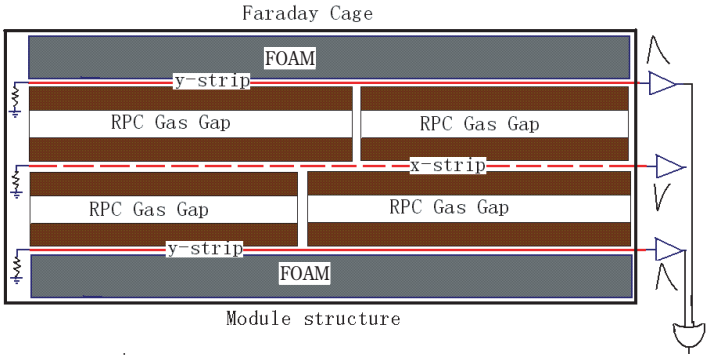

Fig. 7.5. Structure for a single gap RPC module.

7.3.2 Design for Daya Bay

The above measurements were made with one dimensional readout RPC's. For the Daya Bay experiment, we may use RPC's with readout in two dimensions in order to get both x and y-coordinates of the cosmic muons (similar in design to the BELLE RPC's [3]). Three double gap layers would be combined to form a module. A shield is inserted between the layers to avoid cross talk. The structure of a single such module is shown in Fig. 7.5.

Plastic spacers will be used periodically to precisely maintain the gap width. These spacers are potentially a source of dead space. Therefore, within each module, spacers in different layers will be offset, resulting in no net dead space. Also, modules will overlap at the edges, so there will be no inter-module dead space.

Bakelite modules as large as 1×2 m are straightforward to manufacture. Two of these will be bonded together to make a single 2 m×2 m unit. The chambers will be read out by strips of 10cm dimension. Thus each unit will have 40 readout channels. With adequate module overlap and the peaked roof shown in Fig. 7.1 extending an extra 1m on all sides of the pool, it will be necessary to cover an area of 20 m×18 m at the Far Hall and 20 m×12 m at each of the near halls. This will require a total of 630 units for three layers, and a total of 25,200 readout strips.

Alternatively glass modules as large as 1.5×1.5 meter are easy to make and convenient to handle. These would require a total of 1092 units and 32,760 readout strips.

7.3.3 Mounting of RPC's

Fig. 7.6 shows a candidate scheme for mounting the RPC's on a peaked roof over the water pool. The roof will be divided into two sections of different heights and the RPC's mounted in a way that allows one section to slide over or under the other.

7.3.4 Expected Performance of RPC's

Taking into account inefficiencies due to dead-spaces, we expect the overall efficiency of a single layer to be at least ε ∼96%. If we adopt the definition of a track as hits in at least 2 out of 3 layers then the coincidence efficiency is $\varepsilon^3 + C_3^2\varepsilon^2(1-\varepsilon) = 0.96^3 + 3 \times 0.96^2 \times (1-0.96) = 99.5\%$, where $C_3^2 = 3$ is the binomial coefficient. Assuming a bare chamber noise rate, r, of 800 Hz/m^2 is achieved (consistent with BES chamber measurements), a signal overlap width τ, of 50 ns, and a coincidence area, A, of 0.25 m^2, the module noise rate would be $C_3^2 A^2 r^2 \tau (4\ \mathrm{m}^2/A^2) = 3 \times 800^2 \times 0.5 \cdot 10^{-7} \times 4 = 0.384$ Hz. For the Far Hall, this gives a total accidental rate of 60 Hz and a corresponding contribution to the deadtime of 1.2% in the case that a muon signal is defined by a hit in the RPC's alone. A test of the 3 layer scenario with prototypes

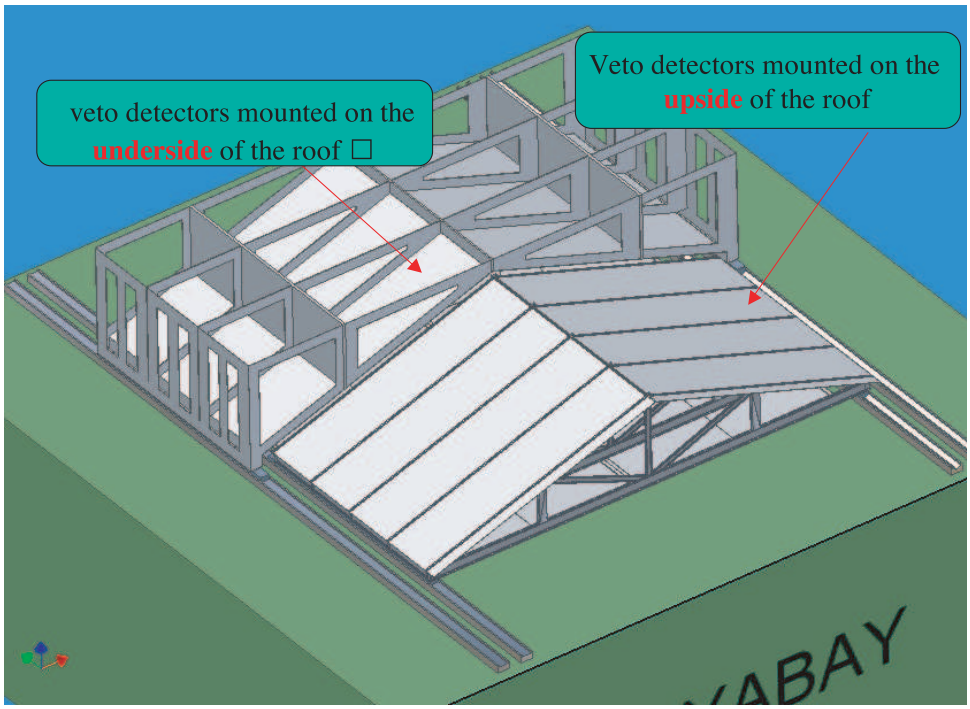

Fig. 7.6. Sliding roof mount for muon tracker modules above the water pool.

of the Daya Bay chambers, using a track definition of 2 out of 3 hits, found a coincidence efficiency of 99.5±0.25%, which is consistent with the calculated efficiency. The efficiency curves are shown in Fig. 7.7.

7.3.5 Electronics and Readout of RPC's

The readout system consists of a readout subsystem, a threshold control subsystem, and a test subsystem. The readout system, shown in Fig. 7.8, contains a 9U VME crate located above the detector, which holds a system control module, a readout module, an I/O modules, and a JTAG control modules.

1) Control Module

The control module receives the trigger signals (L1, Clock, Check, and Reset) from the trigger system and transmits them to the Front End Card (FECs) through the I/O modules. It also receives commands (such as setting thresholds, testing, etc.) and transmits them to the FECs. The control module is also a transceiver which transfers the FULL signal between the readout module and FECs.

2) I/O Module

The VME crate contains several I/O modules, each of which consists of 12 I/O sockets connected by a data chain. The I/O module drives and transmits the signals of the clock and trigger to all the FEC's, and transmits control signals between the readout module and the FECs.

3) VME Readout Module

The readout module is responsible for all the operations relative to data readout. It not only reads and sparcifies the data from all the data chains (it can read 40 of them in parallel), constructs the sub-event data to save into the buffer, and requests the interrupt to the DAQ system to process the sub-event data, but also communicates the Full signals to the FEC's to control the data transmission. The readout module checks and resets signals control signals to the trigger system. It also controls the reading and sparcifying of the FEC data, the requesting of a DAQ interrupt, and the counting and resetting of the trigger number.

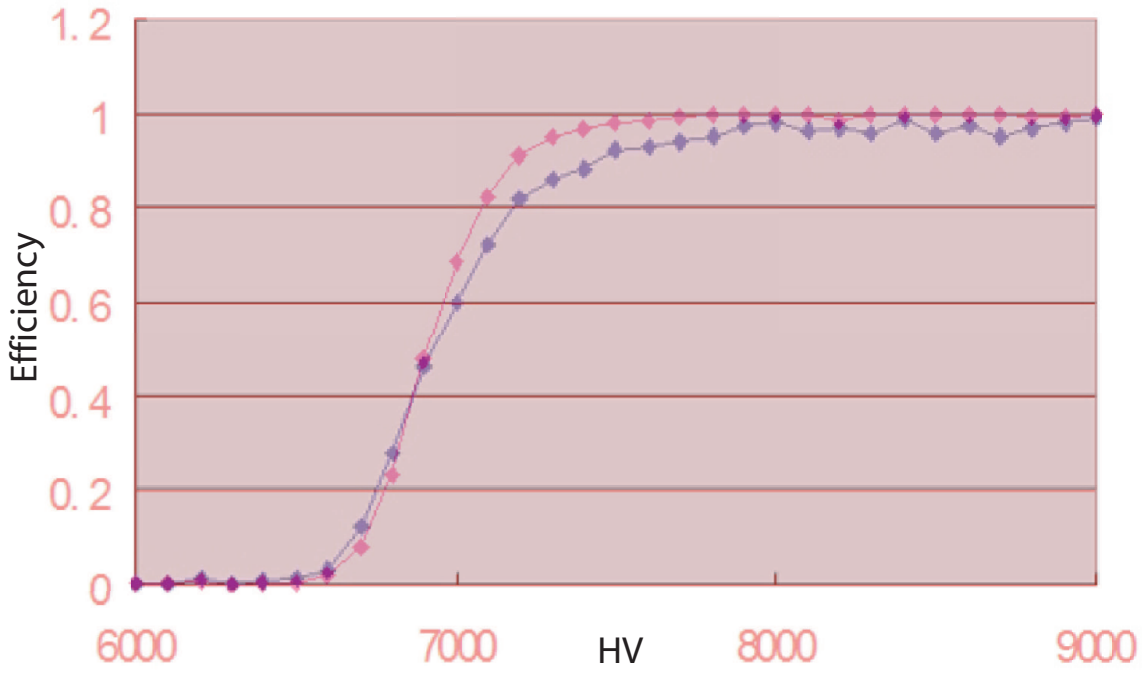

Fig. 7.7. Efficiency as a function of gap voltage for the individual modules of the Daya Bay prototype RPCs (blue) and for the system when 2 out of three hit modules are required (red).

4) Front-End Card

The FECs are located on the RPC detector. Their task is to transform signals from the strips into a bit map, encode the time of the first hit, store the data in a buffer and wait for a trigger signal. Events with a trigger will be transmitted in a chain event buffer in the VME readout modules. Events without a trigger are cleared. Analog signals from groups of 16 strips are discriminated and the output read and stored in parallel into a 16-bit shift register, which is connected to a 16-shift daisy chain. A total of 16 FECs compose one FEC Daisy-Chain, which covers 256 strips. The data from each chain, as position information, are transferred bit-by-bit to the readout module in the VME crate through the I/O modules using differential LVDS signals. Each datum of the chain will be stored temporarily in the relative data chain buffer of the readout module. After the data sparcification, the whole data chain will be stored into the sub-event data buffer awaiting DAQ processing.

In each FEC there is also a DAC chip, which is used to generate test signals. When a test command goes to the test signal generator which resides in the system control module in the VME crate, the generator sends timing pulses to the FEC's DAC chip through an I/O module. This chip then delivers a test signal to each channel's comparator.

The principle of the threshold setting circuit is the same as the test circuit. The timing pulses are gener-

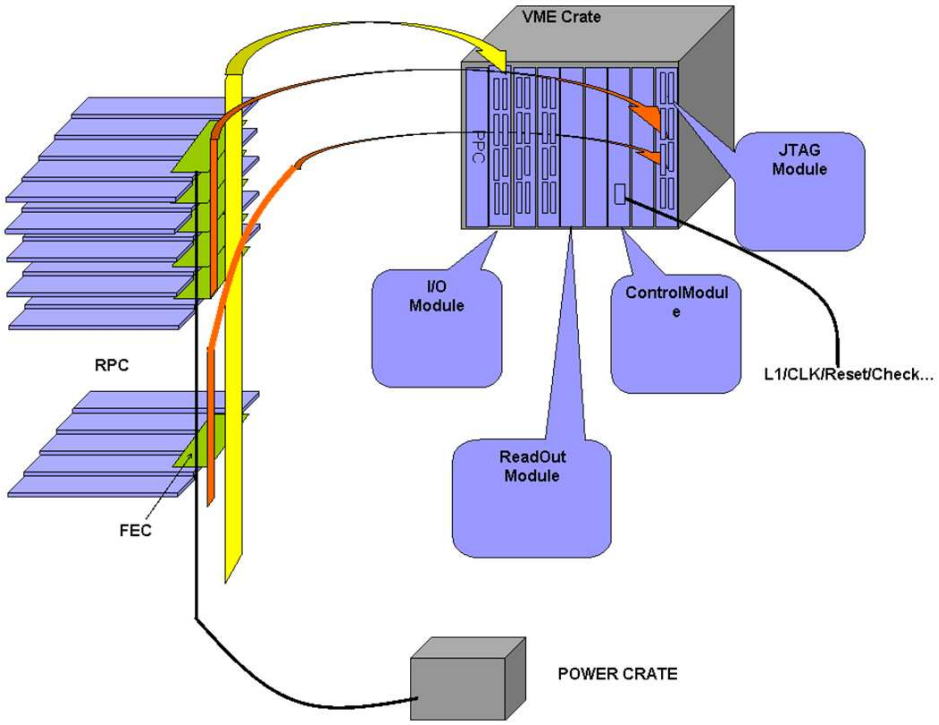

Fig. 7.8. Configuration of electronics & readout system.

ated by the threshold controller in the system control module, and sent to the DAC to generate the threshold level at each of the input ports of the discriminators in the FEC.

5) JTAG Module

The JTAG module gets the FPGA setting command from the VME BUS, transforms the command into the JTAG control timing, and sends it to the FECs. Each of the JTAG modules has 12 slots on the panel of the module, enough to satisfy the requirements of the whole readout system.

6) Test System

The test system for the readout system consists of the test control module in the VME crate, and a test function generator in the FEC.

7) Threshold-Setting System

The threshold-setting system for the readout system consists of the threshold-setting control module in the VME crate, and a threshold-setting generator in the FEC.

7.3.6 Water Čerenkov Modules

As a part of the preliminary R&D for a long baseline neutrino oscillation experiment, the novel idea of a water Čerenkov calorimeter made of water tanks was investigated [4]. A water tank prototype made of PVC with dimensions $1\times1\times13$ m^3 was built, as shown in Fig. 7.1. The inner wall of the tank is covered by Tyvek film 1070D from DuPont. At each end of the tank is a Winston cone that can collect parallel light at its focal point, where an 8-in photomultiplier is installed. The Winston cone is again made of PVC, covered by aluminum film with a protective coating. Čerenkov light produced by through-going charged particles is reflected by the Tyvek and the Al film and collected by the photomultiplier.

The light collected due to cosmic-muons is a function of the distance from the point of incidence of the muon to the phototube. Such a position dependent response of the tank is critical to its energy resolution and pattern recognition capability. Typically it is characterized by an exponential behavior of $e^{-x/\lambda}$, where x is

the distance of the muon event to the phototube and λ is the characteristic parameter, often called "effective attenuation length". The characteristic parameter λ depends on the water transparency, the reflectivity of the Tyvek film, and the geometry of the tank. Using trigger scintillation counters to define the muon incident location, keeping the y coordinate constant as indicated in Fig. 7.9, the total light collected as a function of x at several locations was obtained as shown in Fig. 7.9. It can also be seen from Fig. 7.9 that, for a through-going muon entering the center of the tank, $\sim$20 photoelectrons are collected by each PMT, corresponding to a statistical determination of about $7\%/\sqrt{E}$.

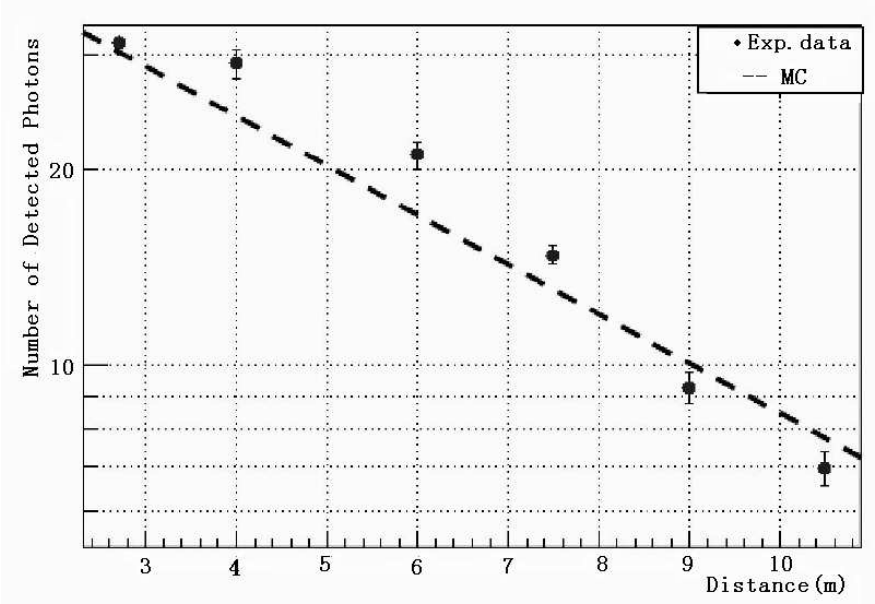

Fig. 7.9. Position dependent response of the water tank to cosmic-muons. X is the distance from trigger counters to the PMT at right. The line represent the Monte Carlo prediction with an effective attenuation length of 5.79 m. The measured effective attenuation length of the water tank is (5.74$\pm$0.29) m.

As discussed in Section 7.2 the Daya Bay antineutrino detector modules are to be shielded from external radiation (such as gamma-ray and cosmic-ray induced neutrons) by a $\sim$2.5-m thick water buffer. One could use modules similar to the above-mentioned Čerenkov units as the muon tracker (Fig. 7.1). Such modules have many advantages: (1) very good cosmic-ray detection efficiency (theoretically, the efficiency is close to 100%); (2) insensitivity to the the natural radioactivity of Daya Bay's rock; (3) very modest requirements on the support system because the whole detector is immersed in the water; (4) low cost because water is used as the medium.

The geometry of the water Čerenkov units located at the four sides of water pool is shown in Fig 7.10. We use four PMT's at each end to decrease the risk of failure of a unit if one PMT dies. The unique geometry of two ends reduces the optically dead region. Similar modules would be placed at the bottom of the pool. A modified version of the LED system discussed in Sec. 8.2 would be used for gain calibration.

7.3.6.1 Expected Performance for Water Čerenkov Modules

A GEANT4 simulation tuned to match the performance of the prototype described above was adapted to the longer modules proposed for Daya Bay. To study the detection efficiency for the Čerenkov photons of

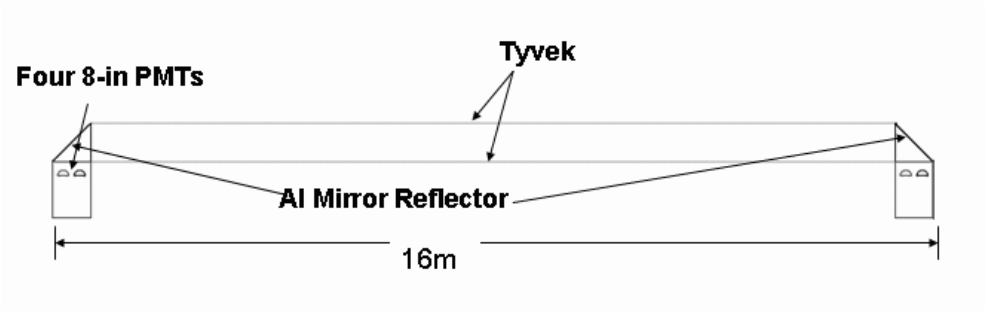

Fig. 7.10. The geometry of a water Čerenkov unit. Four 8-in PMT's are installed in each of ends, and the Al mirror reflector is used.

this unit, we have been developing a full GEANT4 simulation. The optical parameters come from the our previous MC simulation program of the prototype. Preliminary MC results are shown in Table 7.3. These show that adequate signal can be obtained from both ends of these modules for muons at any point along them.

Table 7.3. Number of photoelectrons detected in the water Čerenkov module with different incident positions of (vertical) muons from Monte Carlo simulation.

	-7m	-5m	-2m	0	2m	5m	7m
Left	9.8	23.1.	52.8	86.1	149.5	343.8	1044.9
Right	985.3	340.8	152,7	88.6	51.3	23.0	10.0

Position resolution in the direction transverse to the axis of the module will be given by its size: $\sigma_x = 100\mathrm{cm}/\sqrt{12} = 29$ cm. In the other dimension, 2ns resolution on the end-to-end timing will contribute $\sim$32 cm to the position uncertainty. We can also use the comparison of pulse height from the two ends for determining the position. Including both methods we expect a resolution comparable or better than that in the other orthogonal coordinate. For muons that traverse the water pool and hit modules on either side, these resolutions yield uncertainties of $\sim$21 cm on the position at the center of the trajectory.

Accidental rates in this system, which is blind to rock radioactivity, are expected to be negligibly small.

From Table 7.3, we see it is desirable to measure signals that are $\sim$ 1 photoelectron to those that are several hundred photoelectrons. Thus the same electronics discussed in Sect. 7.2.3 can be used here.

7.3.7 Plastic Scintillator Strips

Plastic scintillator strips serve as a backup option for both the top and in-water veto systems. For both purposes we propose to use the extruded plastic scintillator strip technology developed by MINOS, OPERA and other previous experiments. The parameters of this system are shown in Table 7.4.

If the scintillators are used for the entire muon tracker system they will be set back from the walls and floor of the pool by 50cm to allow attenuation of the gammas from rock radioactivity. For a similar reason they will be mounted 50 cm below the top of the pool. There will be two orthogonal layers on each wall, the floor and the top. In the case where only the top is to be covered by scintillator strips, they would be arrayed in the manner described above for the RPC's, *i.e.* there would be three layers mounted on the sliding roof.

Name	value	unit
strips	5304	
length of strip	5.25	m
width of strip	0.2	m
thickness of strip	1	cm
fibers/strip	5	
length of fiber	7.25	m
diameter of fiber	1	mm
strips/module	6	
modules (full/top only)	884/295	
phototubes (full/top only)	1768/530	

Table 7.4. Parameters of strip scintillators

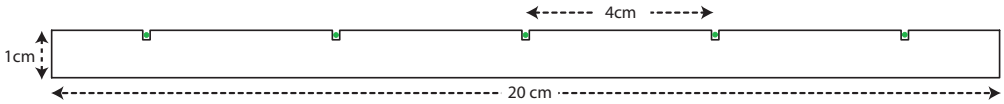

Fig. 7.11. Cross-section of single strip scintillator.

In this case a triple coincidence could be demanded if made necessary by the random rates.

7.3.7.1 Plastic Scintillator Strips

Almost all the scintillators will be of the same type: 5.25 m$\times$0.2 m$\times$0.01 m extruded polystyrene, co-extruded with a coating of TiO2-doped PVC. Five 1 mm Kuraray Y-11(200) S-type wavelength-shifting fibers will be glued into 2 mm deep $\times$ 1.6 mm wide grooves in the plastic using optical glue [6]. Six such scintillators will be placed in a single frame and read out as one 1.2 m-wide unit. Fig. 7.11 shows the cross section of one scintillator.

7.3.7.2 Photoreadout

A $1\frac{1}{8}$-inch photomultiplier tube such as a Hamamatsu R6095 or Electron Tubes 9128B will be used to read out 30 fibers on each end of the six-scintillator module. The PMT's will be run at positive HV, via a system similar to that discussed in Sect. 5.5. Calibration will be via thin-film ^{241}Am sources placed near the ends of the scintillators. The sources provide $\sim$400 Hz of $\sim$0.5 MeV signals.

7.3.7.3 Counter Housing and Support

Above the water, the counters will be mounted on a simple system of strongbacks supported by the sliding roof. In the water, the requirements for deployment are much more demanding. The six scintillator strips will be housed in an RPVC extruded box, shown in Fig. 7.12. The box ends are closed by custom manifolds that contain the fiber ends which are dressed to have an equal length of $\sim$90 cm. The fibers will be routed through a molded cookie, gathered into single bundle and conducted in a PVC pipe through the water into a separate small enclosure containing the PMT/base assembly. Fig. 7.13 shows the module end, routing cookie and pmt containment.

The scintillator housings will be supported by a steel frame in a manner similar to the H-clip technique used by MINOS [7], although our version, shown in Fig. 7.14, will be made of RPVC. It will be glued onto the module housing and fixed to the frame with two hole-drilling screws or blind rivets. Fig. 7.15 shows the support scheme for the side walls of the veto system.

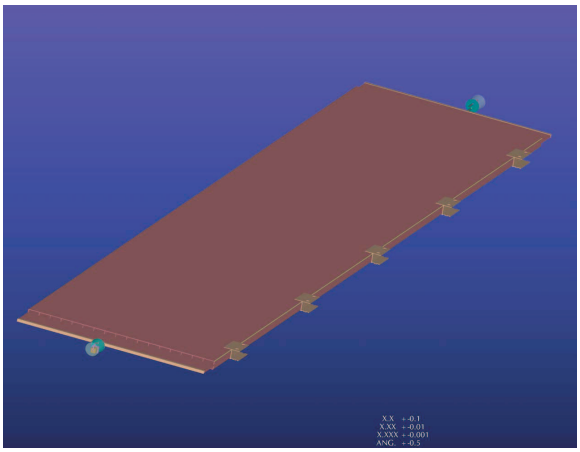

Fig. 7.12. Extruded container for six-scintillator module

.

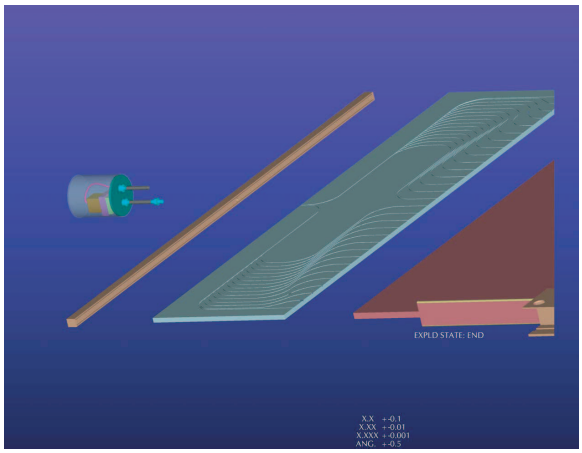

Fig. 7.13. Exploded view of end of scintillator housing module showing routing of fibers, pmt containment, and other details.

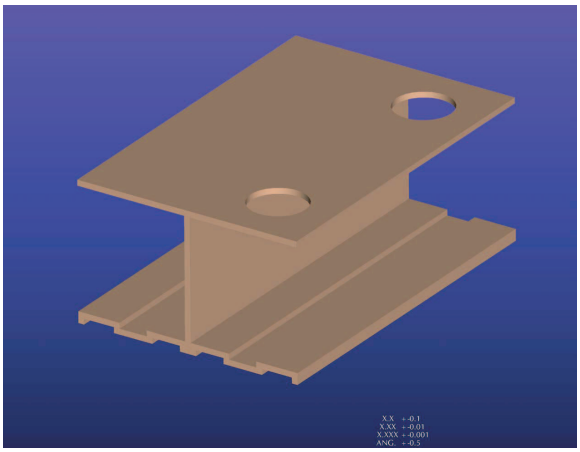

Fig. 7.14. H-clip.

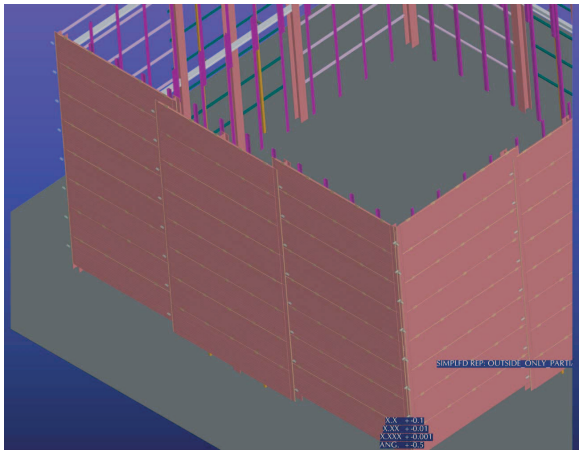

Fig. 7.15. Side walls of the strip scintillator veto system partially assembled.

7.3.8 Expected Performance for Plastic Scintillator Strips

We base our expectation of performance on that of the prototype OPERA target tracker scintillators [9]. Fig. 7.16 shows the yield of photoelectrons versus distance to the photomultiplier tubes. Note that our

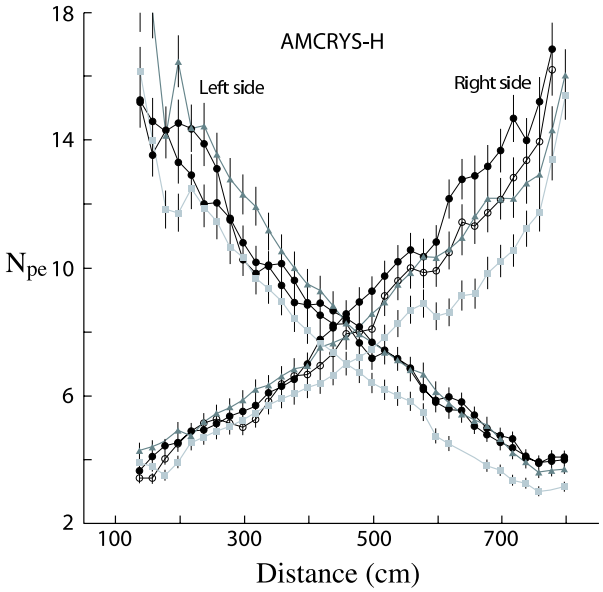

Fig. 7.16. Number of photoelectrons detected on each side of several AMCRYS-H plastic scintillator strips versus the distance to the photomultipliers (from Dracos *et al.*).

counters are only a little longer than 5 m, a point at which the OPERA strips yield about 6 p.e.

The OPERA strips are 26 mm wide by 10.6 mm thick. Our strips are 200 mm wide by 10 mm thick. The MINOS GEANT3 Monte Carlo was adapted to compare the two cases. For collection into the wavelength-shifting fibers, the fraction of OPERA performance for 4, 5, and 6 fibers per 20 cm is 0.74, 0.89, and 1.02 respectively. OPERA uses Hamamatsu H7546-M64 PMT's, which have a photocathode efficiency about 80% as high as either of the single-anode tube we are planning to use. Thus any of the 4–6 fiber cases should achieve performance similar to that of OPERA. For estimation purposes we choose 5 fibers, which nominally should give 1.15 times OPERA performance in our system. The single photoelectron pulse height distribution will reduce the effective number of photoelectrons by a factor of (1 + the variance of the distribution). With pmts of the type discussed, this will result in an inefficiency of $\sim$0.6% in the worst case (hit at one end of the counter). An upper limit on the position resolution is given by the granularity of the counters: $\sigma_x = 120\mathrm{cm}/\sqrt{12} \approx 35\,\mathrm{cm}$. For a muon that hits two sides of the pool, the resolution on the position at the center of its trajectory through the pool will be $\sim$ 25 cm. End-to-end timing and pulse height are expected to improve this. A timing resolution of 1 ns will contribute $\sim$15 cm to the resolution along the counter and $\sim$11 cm to the resolution at the center of the trajectory for through-going muons.

Plastic scintillators are sensitive to the ambient radioactivity from rock. Tests of these rates were carried out with a scintillator telescope in the Aberdeen Tunnel in Hong Kong [8], which has similar granite to that of Daya Bay. These indicate that the true coincidence rate of two 1cm layers at a threshold of 0.5 MeV would be $\sim$7 Hz/m^2. For the relevant active area of the top of the Far Hall water pool, this gives an overall rate of $\sim$1800 Hz. If the top scintillator array alone were used as a 200 μs veto, it would give an unacceptable random veto deadtime. However for through-going muons that could be required to register as well on the side or bottom of the pool, the random veto rate would be reduced to a negligible level (with the shielding

from 50 cm of water, the coincidence rate in scintillators in the pool would be expected to be only 0.7 Hz/m^2, so 180 Hz on the bottom which is the worst case). Since the background from stopping muons is extremely small, scintillators seem acceptable in either or both roles.

7.3.9 Electronics/Readout for Plastic Scintillator Strips

Once again, the electronics and readout discussed in Sect. 7.2.3 would be adequate for this system. However since it is not necessary to measure energies above a few MeV, a smaller dynamic range would be acceptable. Whether it is worth it to develop separate electronics for this case is under study. In any case the readout would be similar to that discussed in Sect. 5.6.

1. Hubbell, J.H. and Seltzer, S.M. (2004), "Tables of X-Ray Mass Attenuation Coefficients and Mass Energy-Absorption Coefficients" (version 1.4). [Online] Available: http://physics.nist.gov/xaamdi [2006, August 2]. National Institute of Standards and Technology, Gaithersburg, MD.
2. Need to get citation from Jiawen.
3. A. Abashian *et al.*, Nucl. Instrum. Meth. **A449**, 112 (2000).
4. M.-J Chen *et al.* Nucl. Instru. & Meth. A**562** (2006) 214-221
5. M. Aglietta *et al.* [LVD Collaboration], "Measurement of the neutron flux produced by cosmic-ray muons with LVD at arXiv:hep-ex/9905047.
6. SHELL EPON 815C with hardener TETA @ 13%.
7. C. James, private communication.
8. K. Luk et al., Daya Bay Internal Document, Nov 2005.
9. M. Dracos *et al.* Phys. At. Nucl bf 67 (2004) 1092-1096 (Yadernaya Fizika, **67** (2004) 1120-1124).

8 Trigger and Data Acquisition System

8.1 Trigger and Timing System

The trigger system of the Daya Bay experiment consists of both trigger and clock systems. The trigger system makes trigger decisions for the central and muon detectors to select neutrino-like events, muon-related events, periodic trigger events and calibration trigger events. The clock system provides a standard, consistent clock signal and time information to the trigger, front-end electronics and readout systems. The following sections will describe the requirements and technical baseline for the trigger and timing systems.

8.1.1 Requirements

The signature of a neutrino interaction in the Daya Bay central detectors is a prompt positron with a minimum energy of 1.022 MeV plus a delayed neutron. About 90% of the neutrons are captured on Gadolinium, giving rise to an 8 MeV gamma cascade with a capture time of 28 μs. The main backgrounds to the signal in the central detector are fast neutrons produced by cosmic muon interactions in the rock, ^{8}He/^{9}Li9 also produced by cosmic interactions and natural radioactivity. All three major backgrounds are related to cosmic muons. The following are the main trigger requirements imposed by the physics goals of the Daya Bay experiment:

1. **Energy threshold:** The trigger is required to independantly trigger on both the prompt positron signal of 1.022 MeV and the delayed neutron capture event with a photon cascade of ≈8 MeV with very high efficiency. The threshold level of the trigger is set at 0.7 MeV. This level corresponds to the minimum visible positron energy adjusted for a 3σ energy resolution effect. This low threshold requirement fulfils two trigger goals. For the neutrino signal, it allows the DAQ to record all prompt positron signals produced from the neutrino interactiona, enabling a complete energy spectrum analysis that increases the sensitivity to θ_{13}. For background, it allows the DAQ to register enough uncorrelated background events due to either PMT dark noise or low energy natural radioactivity to enable a detailed analysis of backgrounds offline.

2. **Trigger efficiency:** In the early stages of the experiment, the trigger efficiency is required to be as high as possible for signal and background, provided that the event rate is still acceptable and will not introduce any dead time. After an accurate characterization of all the backgrounds present has been achieved, the trigger system can then be modified to have more powerful background rejection without any efficiency loss for the signal. To measure the efficiency variation, the system should provide a random periodic trigger with no requirement on the energy threshold at trigger level. A precise spectrum analysis also requires an energy-independent trigger efficiency for the whole signal energy region.

3. **Time stamp:** Since neutrino events are constructed offline from the time correlation between the prompt positron signal and the neutron capture signal, the trigger system should provide a time stamp for each triggered event accurate to better than 1 μs. Therefore, the trigger system must be able to provide an independent local system clock to each detector site for trigger, electronics, and DAQ readout system. GPS time will be received at each site to synchronize the clocks in each central detector and muon veto DAQ board as well as provide a global absolute time. Events recorded by the central detectors, veto and muon trackers can thus be accurately associated in time offline using the timestamp.

4. **Flexibility:** The system must be able to easily implement various trigger algorithms using the same basic trigger board design for different purposes such as

(a) Using different energy thresholds to adapt to the possible aging effect of liquid scintillator, or for triggering on calibration source events which have lower energy signatures.

(b) Using different hit multiplicities to increase the rejection power due to the uncorrelated low energy background and for special calibration triggers.

(c) Implementing different pattern recognition for triggering on muon signals in the different muon veto systems.

(d) Using an OR of the trigger decision of different trigger algorithims to provide a cross-check and cross-calibration of the different algorithims as well as a redundancy to achieve a high trigger efficiency.

5. **Independency:** Separate trigger system modules should be used for each of the central detectors, and the muon veto systems. This is to to reduce the possibility of introducing correlations between triggers from different detector systems caused by a common hardware failure.

8.1.2 The Trigger System

8.1.2.1 The Central Detector Trigger System

Neutrino interactions inside a detector module deposit an energy signature that is converted to optical photons which are then detected by a number of the PMTs mounted on the inside of the detector module. Two different types of triggers can be devised to observe this interaction:

1) An energy sum trigger

2) A multiplicity trigger

In addition to neutrino interaction triggers, the central detector trigger system needs to implement several other types of triggers for calibration and monitoring:

3) Calibration triggers of which there are several types

3a) Triggers generated by the LED pulsing system that routinely monitors PMT gains and timing.

3b) Triggers generated by the light sources periodiclly lowered into the detector volume to monitor spatial uniformity of the detector response and the light attenuation.

3c) Speciality energy and multplicity triggers used to test detector response using radioactive sources

4) A periodic trigger to monitor detector random backgrounds.

5) An energy sum and/or multiplicity trigger (with looser threshold and multiplicity requirements) generated in individual central detector modules which is initiated by a delay trigger from the muon system. This trigger records events to study muon induced backgrounds. This trigger should be able to operate in both tag and veto modes.

A VME module with onboard Field Programmable Gate Arrays (FPGA)s is used to implement the central detector trigger scheme outlined in Figure 8.1 based on experiences gained at the Palo Verde [1] and KamLAND experiments. Figure 8.1 shows the schematic diagram of a possible trigger scheme. We use an OR of both an energy sum and a multiplicity trigger to signal the presence of neutrino interactions in the central detector. These two triggers provide a cross-check and cross-calibration of each other.

The multiplicity trigger is implemented with FPGAs which can perform complicated pattern recognition in a very short time. FPGAs are flexible and can be easily reprogrammed should trigger conditions

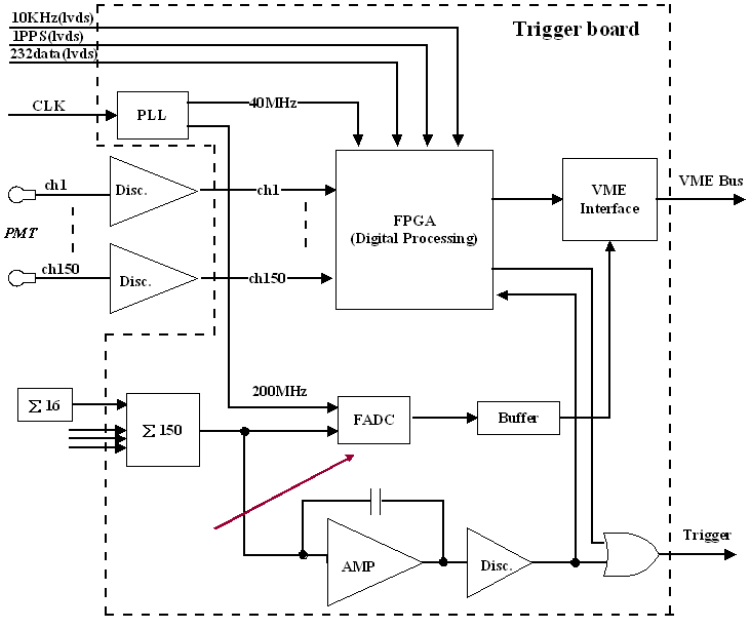

Fig. 8.1. A simplified trigger scheme

change. In addition, different pattern recognition software can be downloaded remotely during special calibration runs, such as might be needed for detector calibration with sources. The signal from different PMTs is compared with the threshold on onboard discriminators in the front-end readout cards as described in Section 5. The output of the PMT discriminators are input into the trigger module FPGA which performs clustering and pattern recognition and generates the multplicity trigger decision. The dark current rate of the PMT is typically around 5 kHz at 15° C. At a multiplicity of 16 PMTs, the total trigger rate would be less than 100 Hz with a 100 ns integration window at the PMT as shown from the simulation results in Figure 8.2.

The energy sum trigger is the sum of charges from all PMTs obtained from the front-end readout boards with a 100 ns integrator and discriminator. The threshold of the discriminator is generated with a programmable DAC which can be set via the VME backplane bus. The energy sum is digitized using a 200 MHz fast ADC (FADC) on the trigger module. We plan to have an energy trigger threshold of 0.7 MeV or less to be compatible with the positron energy of 1.022 MeV within 3σ of the energy resolution. At such low energy thresholds, the trigger will be dominated by two types of background: One is the natural radioactivity originating in the surrounding enviroment which is less than 50 Hz as shown in a Monte Carlo simulation in Section 5. At this threshold, the energy sum trigger rate from the PMT dark current with a 100 ns integration window is negligible.

Tagging antineutrino interactions in the detector requires measuring the time-correlation between different trigger events. The time-correlaton will be performed offline, therefore each triggered event needs to be individually timestamped with an accuracy of order of microseconds or better. It may become necessary to have a correlated event trigger in the case the background rate is too high.

A periodic trigger to monitor the PMT dark-current, the cosmic ray background, and detector stability will be included.

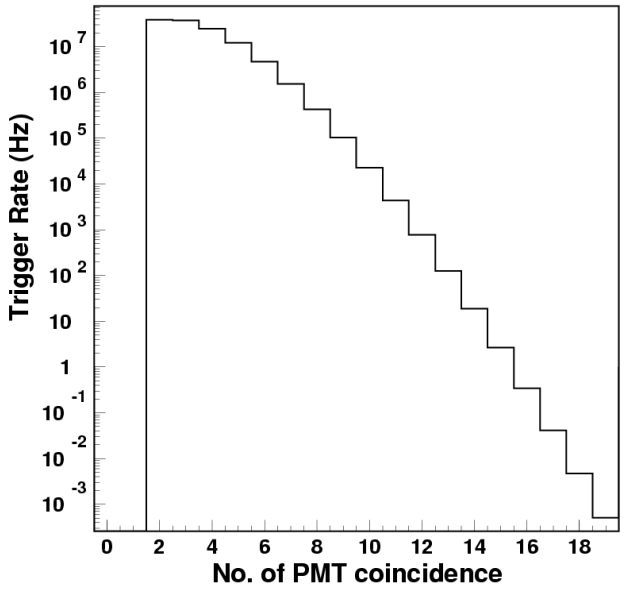

Fig. 8.2. Trigger rates caused by PMT dark current as a function of the multiplicity.

8.1.2.2 The Muon Veto Trigger System

The muon veto system will utilize three separate trigger and DAQ VME crates, one for each of the muon detector systems: The water Cerenkov detector, the RPC system and the muon tracker system (scintillators or water trackers).

The presence of a muon which goes through the water Cerenkov detector can be tagged with energy sum and multiplicity triggers using a similar scheme and hardware modules as used for the central detector. In addition, a more complicated pattern recognition scheme using localized energy and multiplicity information may be used. The trigger rate in the water Cerenkov detector is dominated by the cosmic muon rate which is $<$25 Hz in the far hall and $<$200 Hz in the near halls (see table 3.4). In addition to the water pool Cerenkov detector trigger, muons could be tagged by a system of double layers of scintillator strips or RPCs.

The FPGA logic used for the RPC and scintillator strip detectors forms muon ”stubs” from coincident hits in two overlapping layers of scintillator or two out of three layers of RPC. Although the readout electronics of RPC is very different from that of the PMT, the trigger board can still be similar to the other trigger boards. As we discussed before, each FEC of RPC readout electronics can provide a fast OR signal of 16 channels for the trigger. All the fast OR signals will be fed into the trigger board for further decision by FPGA chips. The principal logic is to choose those events with hits in two out of three layers within a time window of 25 ns in a localized region of typically 10 m^2. Since the noise rate of an RPC is typically about 500-1000 Hz/m^2, the false trigger rate can then be controlled to be less than 50 Hz in such a scheme. The co-incidence rate in the RPC system due to radioactivity is estimated to be 0.06/m^2 based on measurements in the Aberdeen tunnel. This corresponds to a radioactivity trigger rate of about 22 Hz in the far hall.

For the water tracker modules, we need two types of trigger:

1. an AND of the two ends with a threshold of approximately 3 p.e. on each end.

2. A prescaled single ended trigger with a lower threshold.

3. The energy sum of the two ends with a threshold of approx 20 p.e.

The central detector trigger board can be used to implement the trigger schemes for the water tracker. The fake trigger rates from radioactivity in the water tracker modules is expected to be negligible.

An alternative to the water tracker modules discussed above, two layers of scintillator strips in the water pool can be used as described in Section 7. The 0.5 m of water between the water pool walls and the scintillator strips provides some shielding from radioactivity in the rock which generates a rate of 180 Hz of background in the largest plane (bottom of the far detector). The scintillator PMT's noise rate is $<$2 kHz at 15° C. Requiring a co-incidence of two hits in overlapping layers with a 100 ns integration window reduces the fake trigger rate from the scintillator strip PMT noise to a negligable level. In principal, the same trigger module design can be used for both RPCs and scintillator strips with different FPGA software to handle the stub formation in the different geometries.

The global muon trigger decision is an OR of the three muon detector trigger systems: RPC, water Cerenkov and muon tracker. The muon trigger decision may be used to launch a higher level delay trigger looking for activity inside the central detector at lower thresholds and/or multiplicities for background studies.

8.1.3 Timing System

The design of the trigger and DAQ system is such that each central detector and muon veto system has independent DAQ and trigger modules. In this design it is necessary to synchronize the data from the individual DAQs and trigger systems. This is particularly critical for the muon veto systems, where a single muon candidate will be reconstructed offline from data originating in three independant systems: the water Cerenkov pool, muon tracker and RPC tracker. In addition cosmic muon candidates reconstructed in the muon veto systems have to be time correlated with activity in the central detector to study muon induced backgrounds. To this end, a single central clock generator (CCG) should be built to provide a global operation clock (GOC) for all VME crates to synchronize all DAQ and trigger modules and to broadcast a standard time reference. The CCG will preferably be located at the middle site to reduce synchronization errors due to time delays on different cable lengths to the far and two near sites. The main component of the CCG is a Global Positioning System (GPS) antennae, reciever board and server module which provides a precision clock synchronized to Co-ordinated Universal Time (UTC). A schematic of the CCG layout is shown in Fig. 8.3. Current GPS reciever modules have time resolutions of 50ns.

The GPS reciever generates a Pulse Per Second (PPS) signal and a time packet is transmitted from a serial port every second. The PPS, time packet and the Global Operation Clock are broadcast to a local clock system at each site via optical links as shown in Figure 8.4 which then fans out the signals to the trigger boards in each DAQ/Trigger crate. The trigger boards recieve the signals from the CCG, compensating for the cable delay and fan out the clock, PPS and time packet to each DAQ board.

8.1.3.1 T

imestamp and Event Information

Each trigger board recieves the PPS, GPS time packet and the GOC from the local clock fan-out system at each site. The internal operation clock on each board is used to drive an internal counter which then provides the time division inside one second. When the PPS pulse from the GPS arrives, this counter will be reset to the correct second. The absolute timestamp to the second will be decoded from the GPS time packet. For each trigger, the timestamp will be added together with the event data.

8.2 Data Acquisition System

The data acquisition (DAQ) system is used to read data from the electronics to on-line processors, to concatenate data fragments from all relevant electronics systems into complete a event, and to record event

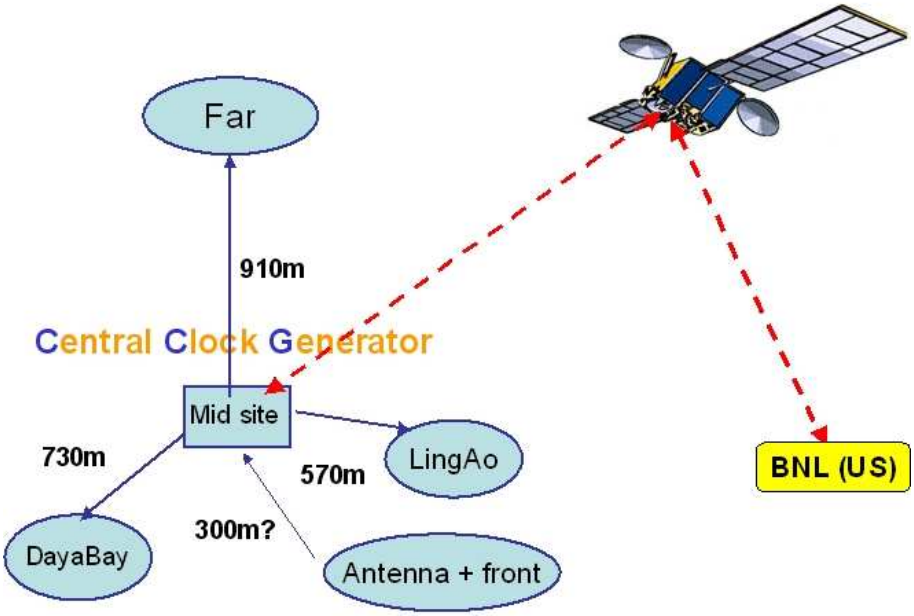

Fig. 8.3. Schematic layout of the global operation clock

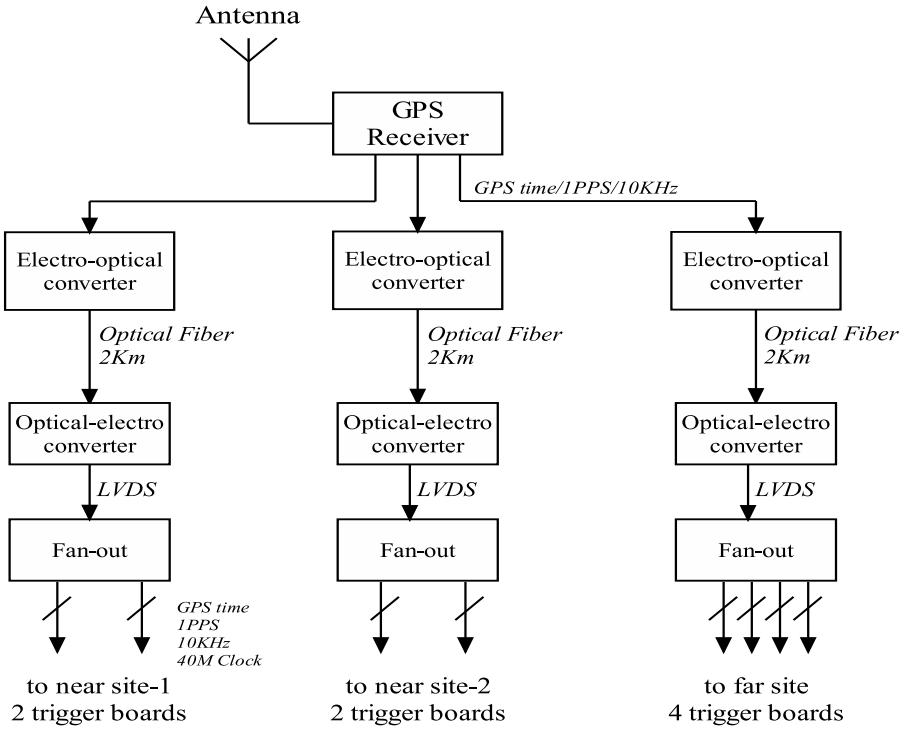

Fig. 8.4. Block diagram of the Daya Bay clock system.

data on archival storage.

A brief review of the DAQ design requirements is followed by discussion of the system architecture, DAQ software, and detector control and monitoring system.

8.2.1 Requirements

The Daya Bay DAQ system requirements are:

1. **Architecture requirements:** The architecture requires separate DAQ systems for the three detector sites. Each central detector module will have an independent VME readout crate that contains the trigger and DAQ modules. In addition, the water Cerenkov detector and muon tracking detectors will also have their own VME readout crates. The trigger and DAQ for the antineutrino and muon detector modules are kept separate to minimize correlations between them. The DAQ run-control is designed to be operated both locally in the detector hall during commisioning and remotely in the control room. In addition, run-control will enable independent operation of individual antineutrino and muon detector modules.

2. **Event rates** The trigger event rates discussed in the previous Section are summarized in Table 2

   Table 8.1. Trigger event rates by system (check numbers!)

System	Maximum event rates
Central Detector	150/200 Hz in far/near hall
RPC on top of water pool	100/300 Hz in far/near hall
Water Cerenkov detector	25/200 Hz in far/near hall
Muon tracker	25/200 Hz in near far/near hall

   While the trigger rate in the central detector is of order a few 100 Hz, an OR of the three muon trigger systems will produce a maximum trigger rate of $<$1 kHz. The Daya Bay event rate design requirement is therefore taken to be an average of 1 kHz. In addition, to trigger on the correlated neutrino and fast neutron signals in the central detector, the DAQ needs to be able to acquire events that occur 1 μs or more apart.

3. **Bandwidth**

   The maximum number of electronics channels for the Central Detectors, Water Cerenkov pool, and Muon Tracker PMTs at the far site is estimated to be at most 2000 channels as shown in Table 3. We assume that the largest data block needed for each PMT channel is 64 bits or less, provided waveform digitization is not used, the breakdown of the channel data block could be as follows:
   Address : 12 bits
   Timing(TDC+local time): 32 bits
   ADC : 14 bits

   For the RPC readout its 1bit/channel + header (12bits) + global timestamp (64bits) = 1.4 kBytes maximum.

   Assuming maximum occupancy numbers of 10% for the RPC system, 100% for 1 out of the 4 central detectors, 10% for the water tracker and 50% for the water Cerenkov, we estimate the maximum event size at the far site is $<$10 kBytes. With a maximum trigger rate of 1 kHz and some capacity for trigger decision words this corresponds to a maximum desired data throughput of $<$10 MBytes/second/site. If waveform digitization is used, this could increase the maximum desired data throughput by an order of magnitude to $<$100 MBytes/second/site.

Table 8.2. Estimated number of readout channels from various detector systems at the far site.

Detector Option	Geometry	No channels
RPC on top of water pool 2 mx2 m module	3 layers of double gap modules	10770
Scint tracker strip module 1.2 mx5.25 m	2 layers side/bottom water pool	524
OR		
Water tracker modules 1 mx16 m module	8 PMTs per module side/bottom	448
Water Cerenkov pool	1 PMT/2 m^2 4 sides/bottom	340
Central detector	4 modules	912

4. **Deadtime:** The DAQ is required to have negligible readout deadtime (¡0.5%).

8.2.2 The DAQ System

The task of the DAQ system is to record antineutrino candidate events observed in the central detector. In order to understand the background, other types of event are also collected, such as cosmic ray induced events, low energy radiative backgrounds, etc. Therefore, the DAQ must record data from the central detector, water Cherenkov and Tracker, with precise time information. Offline analysis can use time-correlation information between continuous events in the central detector or in both tracker and central detector to select antineutrino events or study the muon related background.

There should be three sets of DAQ systems: one for each of the three detector site. Each of them is built on the same architecture as shown in Fig. 8.5. The DAQ architecture design is multi-level using advanced commercial computer and network technology. The lowest level is the VME based readout system. Each VME crate is responsible for one detector system. Each module of the LS detector will have its own independent VME crate. Therefore, The lowest level VME readout system of the far detector hall will consist of the trigger, veto, tracker, and four VME readouts. The Near detector halls, Daya Bay and Ling Ao, have the same DAQ architecture but with different number of VME readout crates. Each VME crate holds a system controller and some FEE readout modules. The VME processor, an embedded single board computer, is used to collect, pre-process, and transfer data. The processor can read data from a FEE board via D8/D16/D32/MBLT 64 transfer mode, allowing a transfer rate up to 80 MB/s. All readout crates of the entire DAQ system at the given detector are connected to an online readout computer through a fast Ethernet. The readout computer is used for data collection from readout crates and for event building. The event will be sent remotely to the computer on the surface to be recorded in permenant storage through an optical fiber.

The data stream flow can work in two ways, depending on the requirement of offline analysis. One scheme is to send tracker event, veto event and LS event out into one data stream on the readout computer. Another scheme is that each type of sub-event, tracker event, veto event, or LS event, has a different data

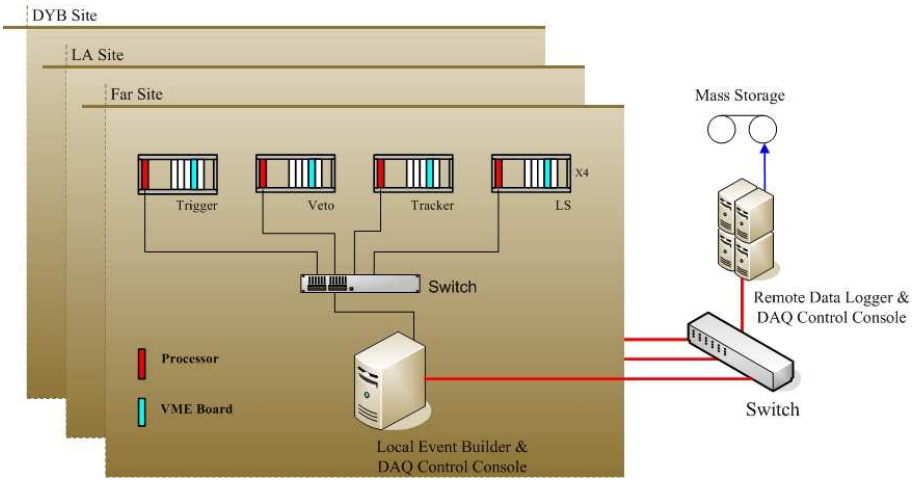

Fig. 8.5. Block diagram of data acquisition system

stream and will be recorded into different data file in the storage. The second scheme is simpler from viewpoint of DAQ and also comply with the principle of DAQ system design that each detector has independent DAQ system for both hardware and software design.

Since the DAQ system is required to be dead time free, each level should have a data buffer capability for the random data rate. In addition, both the VME bus and network should have enough margin of data bandwidth to deal with the data throughput of the experiment.

The DAQ control and monitoring systems can run either on the surface computer or the readout computer in the detector hall. The run control on the readout computer is for the debugging and commissioning of the detector. The software is configurable for different requirements.

8.2.2.1 Buffer and VME Interface

For each trigger, the event information (including the time stamp, trigger type, trigger counter) and the snapshot of the FADC values should be written into a buffer that will be read out via the VME bus for crosscheck.

It is possible to read out the overall event information from the trigger board while the channel data part is read out from all the DAQ boards. In this case the event synchronization between the DAQ boards and the trigger board is critical, and an independent event counter should be implemented in both the DAQ boards and the trigger board. These counters can be centrally cleared to make sure the whole detector module can start from a synchronized and clear status after a trigger event is recorded.

8.3 Detector Control and Monitoring

The detector control system (DCS) controls the various devices of the experiment (e.g., high voltage systems, calibration system, etc.), and monitors the environmental parameters and detector conditions (e.g., power supply voltages, temperature/humidity, gas mixtures, radiation, etc.). Some safety systems, such as rack protection and fast interlocks are also included in the DCS.

The DCS will be based on a commercial software package implementing the supervisory, control, and data acquisition (SCADA) standard in order to minimize development costs, and to maximize the maintenance ability. LabVIEW with Data logging and Supervisory control module (DSC) is a costs effective choice for the DCS.

The endpoint sensors and read modules should be intelligent, have digitalized output, and conform to industrial communication standard. We will select minimum number of necessary field bus technologies to be used for communication among the SCADA system and the readout modules.

1. G. Gratta *et al.*, Nucl. Instr. and Meth. A**400**, 54 (1997).
2. Trimble Navigation Ltd. http://www.trimble.com/acutime2000.html.

9 Installation and System Test

As detector subsystem elements arrive at the Daya Bay site, they will be delivered to the Storage Building (SB) or the Surface Assembly Bulding (SAB). Some elements, such as the mineral oil storage tanks, will arrive ready for installation on the surface or in the tunnel. Other elements, such as the muon tracker will require a brief retesting to ensure that no damage occurred during transport. However, elements such as the central detector tanks will require space for subsystem assembly and check out. The nested acrylic inner vessels will be lifted and placed into the steel vessel in the SAB. This building will be large enough to house many of the steel tanks and nested acrylic inner vessels. It will also have a crane of sufficient capacity to assemble the nested vessels and to lift the completed (but dry) central detectors onto their trailer or transporter. The SAB will require clean assembly space for working on the open vessels to maintain the appropriate surface cleanliness. Once subsystems are assembled and tested as required, they will be moved down into the tunnels on trailers or transporters at very low speed to their appropriate Experimental Halls (EH) for final assembly, alignment and system testing.

9.1 Central Detector Assembly Plans

We plan to purchase all of the LAB for the LS ($\sim$400 T) from one batch and ideally store this in a tank at the Daya Bay site (or at alternate sites such as the factory or other possible locations). The LS and Gd-LS will be mixed either in the SAB or the underground mixing hall (MH) near the Daya Bay near site and access tunnel. The three components: Gd-LS, LS and mineral oil will be filled simultaneously into two detectors in the MH. An alternate plan under consideration would be to fill the two detectors in their respective experimental halls.

9.2 Incoming Receiving and Storage

The elements of the detector — central detector tanks (stainless stell and acrylic), calibration systems, veto detectors, PMTs, liquid storage tanks, and so forth — will have to arrive on a well coordinated timeline. The space required just for storage of components would otherwise quickly overrun the available storage space. The large volume storage tanks for Gd loaded LS, pure LS and mineral oil will need to be in place prior to central detector elements arrival or completed central detectors will stack up down in the tunnel waiting to be filled. An incoming storage building will be required. The SB will be of sufficient size to hold the large elements of the central detector and veto system, but only for a few of these elements for short periods of time before they are moved into the Surface Assembly Building. For example, space for two steel outer vessels plus two sets of nested acrylic vessels as well as several large veto detector panels and boxes of PMTs, should be sufficient. But, even this, requires a building of roughly 200 m^2 area and a crane with two hooks (20 T and 5 T).

9.3 Surface Assembly Building

An assembly building of the scale of 15 m$\times$50 m (750 m^2) will be required to assemble, survey and test multiple central detectors at once. In parallel with central detector assembly, the muon detectors will be inspected and tested. A building of this size could allow us to set up several inspection and test stations and have a station for survey and alignment. It would be sized to handle assembly of two central detectors in parallel plus a short incoming veto RPC panel test station. If the building was arranged in a long (50 m), fairly narrow (15 m) orientation, a single 30 T bridge crane running the length of the building with a smaller 5–10 T crane utilizing the same rails would be sufficient. This would allow for the manipulation of partially or fully completed (dry) central detectors while moving veto panels or staging other structures in parallel.

9.4 Precision survey, fiducialization and placement of the detectors in the experimental halls

Precision survey at the $<$25 μm level will be required during assembly as well as after placement of the central detectors in the experimental halls. Precise knowledge of the as-assembled location of each of

the two nested acrylic vessels with respect to the outer wall of the steel outer tank is required, so that we can monitor any relative movement of these elements. (Note: the active monitoring system is discussed in Section 6.) This will be a radial as well as longitudinal measurement at a precision of 10–20 μm. This is well within the existing ability of modern survey instruments and techniques. Survey and fiducialization of the muon veto chambers, PMT support structures as well as the central detectors will be required in the SAB. Carrying internal geometries to these external fiducial points will ultimately allow a precise relative understanding of detector geometry to the experimental hall and the outside world.

9.5 Subsystem Test and Checkout in the Surface Assembly Building

Incoming inspection of each detector element for damage is an obvious task. However, system elements that are completely assembled and tested to meet specifications at far away sites (the US and Beijing for example) will require a limited retest to ensure no internal damage occurred during shipment. Testing for broken channels or shorts in RPC chambers, PMT function, calibration system function, etc., will all be required. To accomplish these tasks, appropriate test stations will be assembled and utilized in the SAB. The test stations will be manned by technicians, grad students, post-docs and physicists and will utilize a small set of simple electrical tests performed to a written test specification. It is not likely we will repeat all the original performance tests performed at the originating institutions. However, we may need the capability to provide appropriate gas mixes and high and low voltage power as well as a low-noise test environment.

9.6 Transport to experimental halls

Assembled and tested elements of the detectors will be transported to the experimental halls from the SAB using tractors and flat bed trailers or self-propelled transporters. There are several issues associated with this task that make it somewhat more difficult than simply using conventional transportation equipment.

1. The tunnel itself is not very large.
2. We are driving through long tunnels with relatively little ventilation (for cost and space considerations).
3. We enter through a steep grade (perhaps 10%).

Because of this, the transport mechanism should:

1. Have a low bed height ($\leq$1 m)
2. Be powered by an electric drive or by some very clean burning fuel such as LPG
3. If practical, be capable of ‘leveling’ the bed to maintain the vertical axis of the central detectors in a vertical orientation

During the transport down the access tunnel to the MH the Central Detectors are unfilled (and are therefore only about 20 T or 20% their final weight). During the transport to the experimental halls the central detectors are filled ($\sim$100 T). We are currently investigating several transportation systems. Custom made (short and wide) flatbed, ‘lowboy’ trailers pulled by an electric airport pushback tugs, is one option. A second option is to use self propelled, computer and remote controlled, small wheel diameter transporters which often have hydraulic lifting capability. A third option is an electric powered train-like transporter which runs on rails. All of these systems have the benefit of having a bed height of around 0.5 m. All of these can be powered by electric motors for clean, safe operation in confined spaces.

9.7 Final Assembly in the Eexperimental Halls

The veto detector elements (RPC chambers, structures and PMTs) will be delivered to the Experimental Halls after the test and check out phase on the surface. These elements will be installed in the pool (PMTs and PMT supports) and over the roof of the pool (RPCs).

After transportation through the access tunnel, the Central Detectors will be filled with mineral oil, LS and Gd-LS in the MH. Next, the assembled and filled Central Detectors will be slowly transported through the tunnels to the EH. Once there, they will have their calibration systems reinstalled so they can be calibrated and checked.

At this point, the Central Detectors will be lifted into the empty water pool and onto their stands. Long calibration tubes (to allow manual calibration after the pool is filled) will be installed and the readout cables will be dressed into the pool and up into the electronic racks.

9.8 Precision placement and alignment with respect to the reactor cores

Precise knowledge of the 'global' location of each hall (with respect to the reactor cores) will be captured in permanent survey markers in each experiment hall. These survey markers will be placed and known to a precision of better than tens of centimeters, with respect to the outside world, even though the halls are hundreds of meters inside underground tunnels.

The Central Detectors will be surveyed into approximate (but precisely known) location on their stands at the bottom of each water pool. The knowledge of the location of each Central Detector, with respect to the fiducial markers in the halls, can be at the level of 100's of μm. The location of the Muon Detector System elements also can be surveyed and understood at this same 100's of μm level. This is both with respect to the Central Detectors and the EH.

Therefore, the precise relationships between the detector elements and the reactor core will be known to the required precision of better than 30 cm.

10 Maintenance & Operations

Routine operations of the Daya Bay experiment will be carried out by a team on shift in the Control Room on the surface. This team will have support from the power plant as the owner, China Guandong Nuclear Power Group (CGNPG), is a collaborator on the experiment.

10.1 Operations Plans

The operations of the detector will consist of online data analysis for monitoring the detector performance and data quality. The operations will also include analysis of data for calibration of the detector. The calibration procedure will include automated calibration runs. The calibration procedure will also include special manual calibration runs.

10.1.1 Calibrations

The operations of the detector will include both automatic as well as manual calibrations as described in Section 6.

10.1.2 Detector Swapping

The purpose of swapping detectors has been described in Sections 1, 2, and 3. A an overview of the swapping procedure has been outlined in Section 5.

The mechanical structure of each detector will be assembled in the SAB (as described in Section 9) and the detectors will be transported underground to the MH (hall #5 in Fig. 4.1 in Section 4.1) empty. The detectors will then be filled in pairs with Gd-LS, LS and mineral oil in hall #5. Each detector will be commissioned in the Daya Bay near hall (hall #1) along with a reference detector. As part of the commissioning procedure each detector will collect antineutrino data at the Daya Bay near site for XXX days. After this initial commissioning one detector of each pair will be moved to the far site and one will be moved to one of the near sites.

After all detectors are commissioned and located at their initial sites the experiment will collect data for approximately six months. After each six month interval two pairs will be swapped far — near (as described in Table 3.3).

The total estimated time for detector swapping in the baseline water pool configuration is 2–4 days.

1. Disconnect large area RPC roof system gas piping and electrical as necessary to ready this portion of muon veto for sliding back and out of the way for central detector lift operation
2. Drain water pool to level below central detector module ($\sim$1000–1500 m^3) and pump water out through tunnels to pond by entrance, replace with fresh filtered water when refilling
3. Install man bridge over open pit to allow safe access to top of central detector
4. Disconnect PMT HV, signal cables, LS overflow plumbing, etc. as require to prepare for move
5. Remove/prepare calibration system & piping as required from top of central detector
6. Down in pool, remove Cherenkov water pool PMT's in frames from locations where damage could occur when lifting central detectors.
7. Attach required lifting devices to central detector
8. Using a 150 T crane, lift the central detector vertically out of pool and translate it horizontally, placing it on a flat bed trailer or transporter
9. Connect tractor to trailer (if using trailer)

10. Drive Central Detector Module ($\sim$1 km/hr) to new location
11. Reverse the operation, at the previously prepared new location

11 Management, Scope and Cost

In this chapter, the overall project plan will be described. This will include an overview of the project organization, schedule, and the concept for international division of scope and cost. Later, the planned US scope and cost range will be outlined. Because this is a joint project with an international collaboration, the cost accounting approach differs substantially from country to country. Project cost accounting in the Peoples Republic of China is quite different than in the US. In the PRC, essentially all labor costs (Physicist, Engineer and technician) do not appear in the cost estimate. The primary cost item in China is materials. For those items in China where labor must be paid for, such as mining, the price of labor is very much less than the price in the US. As a result, it is very difficult to review the cost of a Chinese scope element while applying typical US costing standards. For this reason, while the total project schedule and scope will be discussed, the only cost estimate presented will be that of the US collaboration for the planned US scope.

11.1 Daya Bay Project Organization

The Daya Bay Project will be international in scope, funding and organization. In this section, we will give an overview of the international Project organization as well as some of the management approaches.

An overview of the Project Organization and Management is presented here. We will present a summary of the planning and scheduling process as well as our proposed tools. While there will be many agencies and agency reviews of the Daya Bay Project, here we will only summarize the planned function of our own internal standing and ad-hoc committees and our technical review process. For example, the function of the Project Advisory Panel, the Physics Advisory Committee, as well as the internal/external expert ad-hoc technical reviews will be described.

The need to control change formally after the formal baseline is established (at the time of the US DOE CD-1 review) will be presented in a Project Management Plan.

Looking at the Project from the oversight agency level, the international organization for the Daya Bay Project is shown below in Figure 11.1.

11.1.1 Planning

11.1.2 Reviews

11.1.3 Change Control

11.2 Project Scope Overview

The entire project technical scope has been described in the previous chapters. The total Daya Bay project includes the civil construction of the experimental facility at the Daya Bay site. In addition to the facility construction, detector elements (Central Detectors, Muon System, Calibration System, DAQ/Trigger, online and offline hardware and software) are included. Key to all of these activities are the project integrating elements such as Installation and Test, System Integration and Project Management.

11.2.1 US Project Scope Range

The US Project scope will not be set until a formal MOU is developed and signed between the US, PRC and other countries. Therefore, the present status of discussions within the collaboration is presented.

11.2.2 US Project Cost Range

The US Cost range associated with the above scope is shown in Table.

11.2.3 Project Schedule

Briefly, the first significant construction event of the Daya Bay Experiment schedule begins with the initiation of civil construction on the tunnels in the spring of 2007. The goal is to complete the civil con-

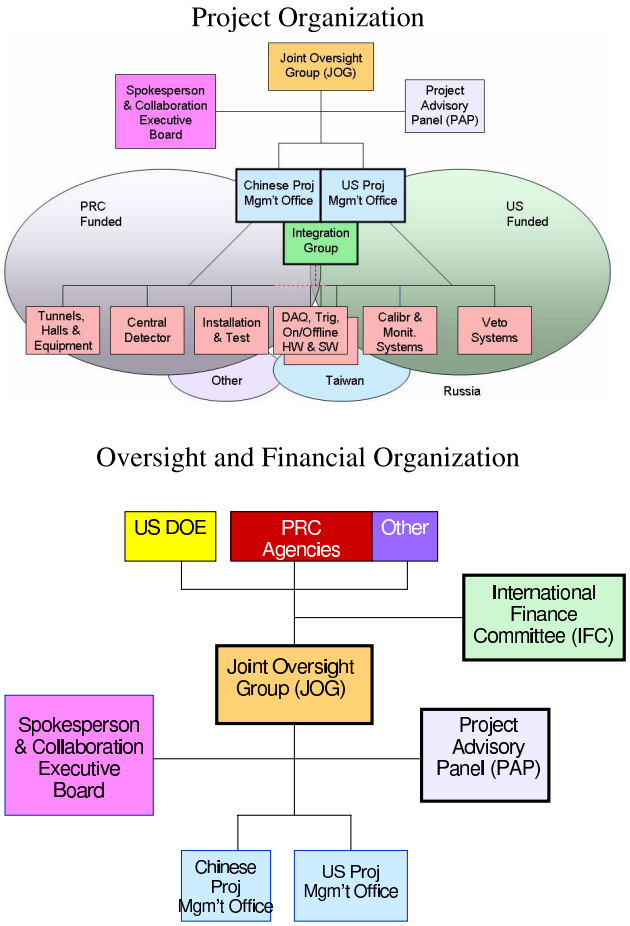

Fig. 11.1. Project organization chart.

Table 11.1. Proposed US project scope.

WBS	Description	Comments on Scope
1.1	Central Detectors	Acrylic inner vessel design, PMTs and PMT testing as well as base/control board design and fabrication. Gd loaded Liquid Scintillator. Installation and Test
1.2	Muon System	System design, PMTs, testing, bases/control boards as well as the support structure
1.3	Calibration and Monitoring	Automated...
1.4	Trig/DAQ/Online	mmmlfajd
1.5	Offline	mmmlfajd
1.7	Installation and Test	Installation as well as test planning and oversight, some onsite testing
1.8	System Integration	Integration planning, documents and management activities
1.9	Project Management	Planning, oversight, regular reporting and review efforts, change control and contingency management

struction of the tunnels, experimental halls and utility infrastructure before the middle of 2009. There is an additional goal to complete the Daya Bay Near Hall 8–10 months earlier than the final (Far) hall. The schedule for the detector elements is therefore driven by the completion of the first two Central Detectors

and a small portion of the Muon System hardware by the fall of 2008 in order to deploy these in this first experimental hall. This first hall will be used as an early opportunity to install, perform system testing and begin partial experiment operations — a chance to debug and gain insight into detector operations. The next hall to follow will be the Mid Hall. This hall and its detectors will most likely be available 4–5 months later (early in calendar 2009). This would then allow us the first opportunity for beginning measurements of θ_{13} by late summer of 2009. The remainder of the detectors will be installed and commissioned by the summer of calendar 2010 so that the full complement of near and far detectors can begin data taking. A more complete view of the project schedule is shown in figure 11.2 below.

Fig. 11.2. Daya Bay Project Summary Schedule.

A Acronyms

AC	alternating current
ADC	analog to digital converter
BES	Beijing Electron Synchrotron
BINE	Beijing Institute of Nuclear Energy
BNL	Brookhaven National Laboratory
CAS	Chinese Academy of Sciences
CDR	Conceptual Design Report
CC	charged current neutrino interactions
CCG	central clock generator
CD	Central Detector
CERN	European Organization for Nuclear Reseach
CL	Confidence Level
CP	Charge, Parity symmetry
CPT	Charge, Parity, Time reversal symmetry
CVS	code versioning system
DAC	digital to analog converter
DAQ	data acquisition
DC	direct current
DCS	detector control system
ES	elastic neutrino scattering
ESH	Environment, safety & health
FADC	Flash ADC
FEC	Front-End Card
FEE	Front-End electronics
FET	field effect transitor
FPGA	field programmable gate array
FY	fiscal year
FWHM	full width at half maximum
Gallex	Gallium Experiment
GEANT	detector discription and simulation tool
GNO	Gallium Neutrino Observatory
GOC	global operation clock
GPS	Global Positioning System
H/C	ratio of hydrogen to carbon
H/Gd	ratio of hydrogen to gadolinium
HV	high voltage
HVPS	high voltage power supplies
IGG	Institute of Geology and Geophysics
IHEP	Institute for High Energy Physics
ILL	Institute Louis Langevin
ISO	International Standards Organization
JTAG	electronic standard for testing & downloading FPGA's
KamLAND	Kamioka Liquid Antineutrino Detector
K2K	KEK to Kamiokanda neutrino oscilaltion experiment

KARMEN	Karlsruhe Rutherford Medium Energy Neutrino experient
KEK	High Energy Accelerator Research Organization
Kr2Det	Two Detector Reactor Neutrino Oscillation experiment at Krasnoyarsk
L/E	Distance divided by energy
L3C	L3 cosmic ray experiment
LAB	Linear Alkyl Benzene
LED	Light emitting diode
LENS	Low Energy Solar Neutrino Spectrometer
LMA	Large Mixing Angle solution
Ln	lanthanides
LS	Liquid scintillator
LSND	Liquid scintillator neutrino detector
LVDS	low voltage differential
m.w.e.	meters of water equivalent
MC	Monte Carlo
MINOS	Main Injector Neutrino Oscillation experiment
MSB	1,4-bis[2-methylstyrl]benzene
MSPS	mega-sample per second
NC	neutral current neutrino interactions
NPP	Nuclear Power Plant
ODH	Oxygen deficiency hazard
OPERA	Oscillation Project with Emulsion-tRacking Aperatus
p.e.	photo-electrons
PC	pseudocumin
PC	personal commputer
PMT	photo multiplier tube
PRD	Pearl River Delta (elevation above sea level)
PVC	Poly Vinyl Cloride

PWR	pressurized water reactors
QA	Quality Assurance
QE	Quantum Efficiency
REE	rare earth elements
R&D	Reseach and developement
RS	Richter scale
RPC	resistive plate chamber
RPVC	Rigid Polyvinyl Chloride
SAGE	Soviet American Gallium solar neutrino Experiment
s.p.e.	single photo-electron
SNO	Sudbury Neutrino Experiment
SNO+	Sudbury Neutrino Experiment
SS	stainless stell
$SU_c(4)$	
$SO(10)$	
SAB	Surface Assembly Building
TDC	time to digital converter
TSY	Fourth Survey and Design Institute of China Railways
UV	ultraviolet light
VME	Versa Module Europa
WBS	work-breakdown structure
YREC	Yellow River Engineering Consulting Co. Ltd.

B Work Breakdown Structure

The Daya Bay work breakdown structure (WBS) has nine major categories as shown in Table B.1. China will take the lead role on 1.1 1.4 and 1.6; the U.S. will take the lead role on 1.2–3. The remaining tasks: 1.5, 1.7–9 will be jointly lead.

Table B.1. Daya Bay Work Breakdown Structure (WBS) shown at level 2.

WBS element	Task Name
1.1	Antineutrino Detector
1.2	Muon Detector
1.3	Calibration and Monitoring Systems
1.4	Trigger, DAQ and Online
1.5	Offline
1.6	Conventional Construction and Equipment
1.7	Installation and Test
1.8	System Integration
1.9	Project Management

WBS Dictionary

The WBS dictionary descriptions at level 2 and the complete WBS down to level 3 are described below. The WBS includes the entire project scope; for details on the US scope see Section 11.2.1.

WBS 1.1: Antineutrino Detector

This element covers labor, materials and equipment associated with the design, further prototyping, construction, assembly and testing of the Central Detector, its tanks, support structures and moving equipment. This element also includes the liquid scintillator, Gd loaded LS, mineral oil buffer and liquid handling/purification systems. The element includes the PMTs, HV and control boards, front-end electronics and associated power supplies and cables. It also includes safety systems needed specifically for these elements. It also includes any special fixtures required to fabricate, assemble and install the Central Detectors at the Daya Bay Site. Note that final assembly in the Surface Assembly Building and installation of the Central Detectors in the experimental halls, plus subsequent in-situ system testing, is included in WBS 1.7. All required management activities associated specifically with the Central Detector are included here. The complete WBS for the Central Detector to level 3 is shown in Table B.2.

Table B.2. Daya Bay WBS for the Central Detector shown to level 3.

WBS	Description
1.1	**Central Detector**
1.1.1	Mechanical Assembly
1.1.2	Liquid Scintillator
1.1.3	Photomultiplier Tubes (PMTs)
1.1.4	Electronics
1.1.5	Safety Systems
1.1.6	Prototypes
1.1.7	Assembly
1.1.8	Subsystem Test
1.1.9	Subsystem Management

WBS 1.2: Muon Detector

This element covers labor, materials and equipment associated with the design, further prototyping, construction, assembly and testing of the Muon Veto system, its tracking chambers, Water Cherenkov system, support structures, gas systems, front-end/readout electronics and associated power supplies and cables. This element also includes the water pool liquid handling/filtering system including plumbing. It also includes safety systems needed specifically for these elements. It also includes any special fixtures required to fabricate, assemble, test and install the Muon systems in their experimental halls. Note that testing of the muon system elements in the Assembly Building, installation of the Muon Detector elements in the experimental hall, and subsequent in-situ system testing, is included in WBS 1.7. All required management activities associated specifically with the Muon Detector are included here. The complete WBS for the Muon Detector to level 3 is shown in Table B.3.

Table B.3. Daya Bay WBS for the Muon Detector, shown to level 3.

WBS	Description
1.2	**Muon Veto**
1.2.1	Mechanical Assembly
1.2.2	Water Cherenkov System Elements
1.2.3	Tracker System Elements
1.2.4	Magnetic Shielding
1.2.5	Readout Electronics
1.2.6	Safety Systems
1.2.7	Muon Detector Prototypes
1.2.8	Assembly
1.2.9	Subsystem Test
1.2.10	Subsystem Management

WBS 1.3: Calibration

This element covers labor, materials and equipment associated with the design, prototyping, construction, assembly and testing of the Calibration system, its mechanisms, plumbing, light/radiation sources, shutters, valves and devices. It also includes the control system, readout electronics and associated power supplies and cables. It also includes safety systems needed specifically for these elements. It includes any special fixtures required to fabricate, assemble and install the Calibration system elements in the Surface Assembly Building or experimental halls. Note that installation of the Calibration System elements while in the Assembly Building, experimental hall, and subsequent in-situ system testing, is included in WBS 1.7. All required management activities associated specifically with the Calibration System are included here. The complete WBS for the Calibration and Monitoring System to level 3 is shown in Table B.4.

WBS 1.4: Trigger/DAQ/online

This element covers labor, materials and equipment associated with the design, prototyping, construction, assembly and testing of the Trigger, DAQ and Online hardware and software. This includes all racks, crates, power supplies, cables, custom and off-the-shelf boards, as well as computers and communication equipment. (Interface documents will be developed with strict interface definitions between this hardware and the front-end/readout systems of each of the major detector elements.) This also includes any air or water cooling systems, plumbing, ducting, fans and heat exchangers that may be required. (The strict definition of the interface with conventional utilities (see WBS 1.6.5) will be documented elsewhere.) It also includes safety systems needed specifically for these elements (in rack smoke detection and fire suppression for example). It includes any special fixtures required to assemble and install these hardware elements in the Surface Assembly Building or experimental halls. Note that installation of the Trigger/DAQ/Online Hardware elements while in the Assembly Building, experimental hall, and subsequent in-situ system testing, is

Table B.4. Daya Bay WBS for the Calibration and Monitoring System, shown to level 3.

WBS	Description
1.3	**Calibration and Monitoring Systems**
1.3.1	Automated Deployment System
1.3.2	Manual Calibration Systems
1.3.3	LED System
1.3.4	Radioactive Calibration Sources
1.3.5	Detector Component Monitoring Systems
1.3.6	Low-Background Source and Materials Counting System
1.3.7	Safety Systems
1.3.8	Prototypes
1.3.9	Assembly
1.3.10	Subsystem Test
1.3.11	Subsystem Management

included in WBS 1.7. All required management activities associated specifically with Trigger/DAQ/online hardware and software are included here. The complete WBS for the Trigger and DAQ to level 3 is shown in Table B.5.

Table B.5. Daya Bay WBS for the Trigger and DAQ, shown to level 3.

WBS	Description
1.4	**DAQ, Trigger and Online**
1.4.1	DAQ
1.4.2	Trigger
1.4.3	Monitoring and Controls
1.4.4	Online
1.4.5	Infrastructure and Safety Systems
1.4.6	Subsystem Test
1.4.7	Subsystem Management

WBS 1.5: Offline Hardware and Software

This element covers all non-physicist labor associated with the specification, design, prototyping, coding, integration and testing of the Trigger, DAQ, On-line and offline software. It also includes code written for controls and monitoring functions. The simulations efforts for each of the subsystems and the overall experiment are also included in this element. All required management activities associated specifically with Trigger/DAQ/online/offline Software are included here. The complete WBS for the Offline Hardware and Software to level 3 is shown in Table B.6.

WBS 1.6: Civil Construction

This element covers all labor, materials and equipment associated with the design and construction of the underground tunnels and caverns. It covers the design and construction of the entrance, the ancillary rooms for LS and water system as well as all underground utilities for the tunnels, halls and experiment. This element also covers the design and construction of the surface buildings at the site. All ‘universal’ or non-detector specific life and equipment safety systems — ventilation, smoke detection, fire suppression, ODH, etc. are included here. Detector specific elements (for example flammable gas and ODH detection) will be

Table B.6. Daya Bay WBS for the Online and Offline Software, shown to level 3.

WBS	Description
1.5	**DAQ, Trigger, Online and Offline Software**
1.4.1	Networking and data transfer
1.4.2	Offline Hardware including Data archiving
1.5.3	Analysis Software
1.5.4	Simulations Software
1.5.5	Subsystem Test
1.5.6	Subsystem Management

included under their WBS costs. All required management activities associated specifically with the Civil Construction and Infrastructure are included here. The complete WBS for the Conventional Construction to level 3 is shown in Table B.7.

Table B.7. Daya Bay WBS for the Conventional Construction, shown to level 3.

WBS	Description
1.6	**Conventional Construction and Equipment**
1.6.1	Tunnels
1.6.2	Tunnel Entrance and Surroundings
1.6.3	Experimenal Halls
1.6.4	Other Underground Rooms
1.6.5	Conventional Utilities
1.6.6	Communication Systems
1.6.7	Surface Buildings
1.6.8	Safety Systems
1.6.9	Subsystem Management

WBS 1.7: Installation

This element supports the overall planning and execution of the final assembly and installation of the experiment on site at Daya Bay. It includes labor, materials and universal (not associated with a single detector subsystem above) equipment required to perform these functions. For example, lift trucks, scaffolding, and rigging equipment. However, it does not include the custom installation and test hardware required for individual detector elements — these are included in the WBS elements above. It also includes the overall system testing and commissioning of the experiment once installed. The element includes activities in the surface storage and assembly buildings as well as in the underground caverns and rooms. It includes all technical and engineering labor required to install the detector elements, but not the physicist and engineering efforts from the subsystems supporting the installation and test activities. All required management activities associated specifically with Installation and Test are included here. The complete WBS for Installation and Test to level 3 is shown in Table B.8.

WBS 1.8: Systems Integration

This WBS element includes the cost of labor and materials for system level detector integration activities. These activities include the following:

1. Creating and maintaining boundary and interface definition drawings between subsystems.

2. Developing and maintaining system level drawings of the experiment.

Table B.8. Daya Bay WBS for Installation and Test, shown to level 3.

WBS	Description
1.7	**Installation and Test**
1.7.1	Installation
1.7.2	Detector Test and Commissioning
1.7.3	Subsystem Management

3. Creating and maintaining experiment plumbing, cabling and safety system space drawings.
4. Creating and maintaining experiment assembly scenario drawings.
5. Creating and maintaining experiment servicing/maintenance scenario drawings.
6. Creating and maintaining detector utility and facility requirements lists and drawings.
7. Planning and scheduling detector installation activities.

The complete WBS for the System Integration to level 3 is shown in Table B.9.

Table B.9. Daya Bay WBS for System Integration, shown to level 3.

WBS	Description
1.8	**System Integration**
1.8.1	Mechanical Integration
1.8.2	Electronics Integration
1.8.3	Software Integration
1.8.4	Common Fund
1.8.5	Subsystem Management

WBS 1.9: Project Management

This WBS element includes the cost of labor and materials necessary to plan, track, manage, maintain effective communications, distribute drawings and documents, and perform necessary EH&S and QA tasks during all phases of the project. However, subsystem related management and support activities for planning, estimating, tracking and reporting as well as their specific EH&S and QA tasks are included in each of the subsystems. The complete WBS for the Project Management to level 3 is shown in Table B.10.

Table B.10. Daya Bay WBS for Project Management, shown to level 3.

WBS	Description
1.9	**Project Management**
1.9.1	Planning
1.9.2	Management
1.9.3	Tracking and Reporting
1.9.4	Meetings and Reviews
1.9.5	Project Contingency Funds